



# THE DESIGN OF POWER COMBINED OSCILLATORS SUITABLE FOR MILLIMETRE-WAVE DEVELOPMENT

by

**Ali Afkari Sayyah, B.Sc, M.Sc**

A thesis submitted in the fulfilment of the requirement for the degree of

Doctor of Philosophy

in

The University of Adelaide  
Department of Electrical and Electronic Engineering  
Faculty of Engineering

November, 1997

To my wife, Jila for her patience and encouragement and my sons,  
Younes and Edris

# Table of Contents

<i>Abstract</i> . . . . .	<i>xi</i>
<i>Statement of Originality</i> . . . . .	<i>xiii</i>
<i>Acknowledgement</i> . . . . .	<i>xiv</i>
<i>List of Author's Related Publications</i> . . . . .	<i>xv</i>
<i>List of Principal Symbols</i> . . . . .	<i>xvi</i>
<i>List of Abbreviations</i> . . . . .	<i>xxiv</i>

---

## Chapter 1

<i>Introduction</i> . . . . .	1
-------------------------------	---

---

## Chapter 2

<i>Review of Solid State Microwave and Millimetre-Wave Sources</i> . . . . .	4
2.1 Introduction . . . . .	4
2.2 The Ideal Microwave or Millimetre Wave Source . . . . .	5
2.3 IMPATT and Gunn Diode Oscillator Operating Modes . . . . .	6
2.4 Single Diode Oscillator Mounting Structures . . . . .	7
2.4.1 <i>Non-Radiating</i> . . . . .	7
2.4.2 <i>Radiating</i> . . . . .	8
2.5 Single Field Effect Transistor Oscillator Mounting Structure . . . . .	10
2.5.1 <i>Non-Radiating</i> . . . . .	10
2.5.2 <i>Radiating</i> . . . . .	11
2.6 Field Effect Transistor Operating Modes . . . . .	12
2.7 Multiple Diode Oscillator Mounting Structures . . . . .	14
2.7.1 <i>Introduction</i> . . . . .	14
2.7.2 <i>Non-Radiating</i> . . . . .	14
2.7.2.1 N oscillators in Corporate Combiners . . . . .	15
2.7.2.2 N diodes in a Single Resonator . . . . .	15

# Table of Contents

2.7.2.3	Planar Arrays of Electric Current Elements in Open Resonator . . . . .	17
2.7.2.4	N diodes in an Open resonator . . . . .	18
2.7.2.5	Diode Oscillators in an Open Resonator . . . . .	19
2.7.3	<i>Radiating</i> . . . . .	20
2.7.3.1	Arrays of Diode Oscillator Patch Antennas . . . . .	20
2.7.3.2	Diode Grid Oscillators . . . . .	21
2.8	Multiple Transistor Oscillator Mounting Structures . . . . .	22
2.8.1	<i>Introduction</i> . . . . .	22
2.8.2	<i>Non-Radiating</i> . . . . .	22
2.8.2.1	N Transistor Oscillators Coupled to a Rectangular Cavity Combiner . . . . .	23
2.8.2.2	N Transistor Oscillators within an Open Resonator . . . . .	25
2.8.3	<i>Radiating</i> . . . . .	26
2.8.3.1	Arrays of Transistor Oscillator Patch Antennas . . . . .	26
2.8.3.2	Transistor Grid Oscillators . . . . .	27
2.9	Practical Design Consequences of Surface Waves on Thick Substrates . . . . .	32

---

## Chapter 3

<i>Design Concepts to Satisfy Practical Constraints</i> . . . . .	34	
3.1	Introduction . . . . .	34
3.2	MMIC Constraints . . . . .	35
3.3	Concepts Arising from the Design Problems . . . . .	36
3.3.1	<i>Concept 1: Shielded Inverted Microstrip</i> . . . . .	36
3.3.2	<i>Concept 2: Oscillator on Dielectric Resonator</i> . . . . .	37
3.3.3	<i>Concept 3: Partially Filled Cavity Resonator</i> . . . . .	37
3.3.4	<i>Concept 4: Quasi-TEM Mode Circuit Decoupling from LSM Resonator</i> . . . . .	38
3.3.5	<i>Concept 5: Output Coupling to LSM Mode Resonator</i> . . . . .	38
3.3.6	<i>Concept 6: Thick Iris Output Coupling to Waveguide</i> . . . . .	39
3.3.7	<i>Concept 7: Coupling Factor Adjustment</i> . . . . .	39
3.3.8	<i>Concept 8: Oscillator Array Positioning on Dielectric Surface</i> .	40
3.3.9	<i>Concept 9: Cavity Resonator as Synchroniser</i> . . . . .	40

# Table of Contents

3.3.10 Concept 10: Individual Oscillator Tuning . . . . .	42
3.3.11 Concept 11: Partially Filled Cavity Resonator Tuning . . . . .	42
3.3.12 Concept 12: Oscillator Assembly as Active Aperture Antenna . . . . .	43
3.3.13 Concept 13: Oscillator Assembly as Active Array Antenna . . . . .	43
3.3.14 Concept 14: Metal Posts as Transistor Heat Sinks. . . . .	43
3.3.15 Concept 15: Metal posts as Unwanted Resonance Suppressors. . . . .	45
3.3.16 Concept 16: Potential for Class C Operation of Oscillators . . . . .	45
3.3.17 Concept 17: Metal Strip Output Coupling to Coaxial Line . . . . .	46
3.4 Oscillator Design for MMIC Development at Millimetre Wavelengths . . . . .	46
3.5 Design Procedure . . . . .	48
3.5.1 Stage I: Selection of Transistor Oscillator Circuit Type and Critical Positioning of Elements. . . . .	49
3.5.2 Stage II: Separation of Parts. . . . .	50

---

## Chapter 4

<i>Design Methods -Part I: Oscillator Circuit</i> . . . . .	53
4.1 Selection of The Type of Transistor Circuit . . . . .	53
4.2 S-Parameter Design of Transistor Oscillator . . . . .	53
4.2.1 Small Signal Design . . . . .	54
4.2.2 Derivation of $Z_d$ . . . . .	55
4.2.3 Series Feedback . . . . .	56
4.3 An Oscillator Design Automation Program . . . . .	56
4.4 Shielded Inverted Microstrip Oscillator . . . . .	61
4.5 Bias Circuit . . . . .	67
4.6 Design Example . . . . .	67

---

## Chapter 5

<i>Design Methods -Part II: Cavity Structure</i> . . . . .	74
5.1 Review of Design Methods . . . . .	74
5.2 The Partially-Filled Cavity Resonator . . . . .	76
5.2.1 Field Expansions . . . . .	77

# Table of Contents

5.3 Surface Integrals . . . . .	79
5.3.1 Continuity of Electric Fields . . . . .	82
5.4 Generalised Admittance . . . . .	84
5.4.1 Source-free Cavity . . . . .	90
5.4.2 Completely Enclosed Cavity . . . . .	90
5.5 Field Distribution on the Interfacial Surface . . . . .	91
5.5.1 The Effect of the Aperture on the Resonant Frequency . . . . .	92
5.6 Probe Excitation . . . . .	96
5.6.1 Source Integrals . . . . .	97
5.6.2 Normalised Source Integrals . . . . .	99
5.6.3 Probe Impedance . . . . .	100

---

## Chapter 6

### *Design Methods -Part III: Coupling Structure . . . . .* 103

6.1 Introduction . . . . .	103
6.1.1 The Cavity Aperture Reflection Coefficient . . . . .	106
6.1.2 Mode-Matching Analysis of Waveguide Junctions . . . . .	109
6.2 Analysis of The First Junction . . . . .	110
6.2.1 Reaction Elements . . . . .	112
6.3 The Second Junction . . . . .	115
6.3.1 Calculation of Reaction Elements . . . . .	118
6.4 Overall S- Matrix . . . . .	120
6.5 Numerical Calculation . . . . .	121
6.5.1 Input Data: . . . . .	122
6.5.2 Cutoff Frequencies . . . . .	124
6.5.3 Eigenvalues . . . . .	127
6.5.4 Mode-Matching of the First Junction . . . . .	128
6.5.5 Mode-Matching of the Second Junction . . . . .	131
6.5.6 Cascade Connection . . . . .	132

# Table of Contents

---

## Chapter 7

<i>Designs and Experiments</i> . . . . .	134
7.1 Oscillator Design Procedure. . . . .	134
7.2 Microwave Test Structure . . . . .	139
7.3 <i>Design Validation Testing: Single-Transistor Oscillator</i> . .	144
7.3.1 <i>Single Transistor Oscillator: Version 1.</i> . . . . .	145
7.3.1.1 Design .....	145
7.3.1.2 Test Results .....	150
7.3.1.3 Conclusion .....	153
7.3.2 <i>Single Transistor Oscillator Version 2: Improved Efficiency</i> . .	153
7.3.2.1 Improving the Oscillator Performance .....	153
7.3.2.2 Design .....	156
7.3.2.3 Test Results .....	164
7.3.2.4 Conclusions.....	167
7.4 Design Validation Testing: Power Combining . . . . .	169
7.4.1 <i>The Dielectric Resonator as a Power Combiner.</i> . . . . .	169
7.4.2 <i>Power Combined Two Transistor Oscillator</i> . . . . .	170
7.4.2.1 Design .....	170
7.4.2.2 Results.....	176
7.4.2.3 Discussion and Conclusions .....	180

---

## Chapter 8

<i>Overall Conclusions &amp; Recommendations</i> . . . . .	182
--	-----

---

## Appendix A

<i>Design of Shielded Inverted Microstrip Line Using Conformal Mapping</i> . . . . .	187
A.1 Design Procedure . . . . .	187
A.2 Calculation of C . . . . .	189
A.3 Structure Dimensions . . . . .	192
A.4 Determination of $Z_0$ and $C_0$ . . . . .	192
A.5 Numerical Result . . . . .	193

# Table of Contents

## Appendix B

<i>Hybrid Modes in Partially-Filled Waveguides</i> . . . . .	194
B.1 Introduction. . . . .	194
B.2 LSE <sup>y</sup> Modes . . . . .	195
B.2.1 Continuity Equation for LSE <sup>y</sup> Modes . . . . .	198
B.2.2 Normalisation of LSE <sup>y</sup> Modes . . . . .	199
B.3 LSM <sup>y</sup> Modes . . . . .	
B.3.1 Continuity Equation for LSM <sup>y</sup> Modes . . . . .	202
B.3.2 Normalisation of LSM <sup>y</sup> Modes . . . . .	202

## Appendix C

<i>Mode Expansion of Maxwell's Equations in Partially-Filled Cavities</i> . . . . .	203
---	-----

## Appendix D

<i>Eigenfunctions of Partially-Filled Cavities</i> . . . . .	213
D.1 Introduction. . . . .	213
D.2 LSE <sub>mnl</sub> <sup>y</sup> Modes . . . . .	214
D.3 LSM <sub>mnl</sub> <sup>y</sup> Modes . . . . .	216
D.4 Irrotational Fields. . . . .	217
D.4.1 Local Electric Fields. . . . .	217
D.4.2 Local Magnetic Fields. . . . .	219

# Table of Contents

## Appendix E

<i>Coefficients of Surface Integral Expansion</i> . . . . .	221
---	-----

## Appendix F

<i>Theory of Mode-Matching Technique</i> . . . . .	224
F.1 Introduction . . . . .	224
F.2 Basic Terminology . . . . .	225
F.2.1 Fields of Guide #1 . . . . .	226
F.2.2 Fields of Guide #2. . . . .	228
F.3 Normalised Mode-Vectors . . . . .	228
F.4 Mode-Matching Equations . . . . .	229
F.4.1 First Equation . . . . .	231
F.4.2 Second Equation . . . . .	232
F.5 Generalised Junction Scattering Matrix . . . . .	234
F.6 Derivation of Reaction Elements . . . . .	237

## Appendix G

<i>A Graphically Oriented Automation of Microstrip Amplifier and Oscillator Design</i> . . . . .	240
1 Introduction . . . . .	241
2 Program Structure. . . . .	242
3 Design Examples . . . . .	244
4 Experimental Results . . . . .	247
5 Conclusion. . . . .	248
6 References . . . . .	249

# Table of Contents

## Appendix H

<i>Transistor Data Sheets</i> . . . . .	262
ATF-13036 Hewlett-Packard MESFET . . . . .	264
NEC GaAs MESFETs series NE-720. . . . .	266
Bibliography . . . . .	272

## Abstract

The development of transistors with useful gain at frequencies up to 100 GHz has created prospects for more efficient power sources at millimetre wave wavelengths than those that are currently available using IMPATT or Gunn diodes. The power handling capability of all solid state devices that need to be physically small compared with the operating wavelength decreases with increasing frequency. For many systems applications, designed to operate in the millimetre wave part of the electromagnetic spectrum, power combined arrays of oscillators are needed to satisfy power source requirements. The research presented in this thesis addresses the problem of designing power sources for operation at millimetre wavelengths using transistors and distributed circuit elements that are all fabricated as a monolithic millimetre wave integrated circuit (MMIC) that is compatible with the physical constraints of current semiconductor materials technology and foundry practice.

Monolithic fabrication appears to be the only cost-effective way to make arrays of extremely small components. It is assumed in this research that the MMICs, on what are relatively fragile gallium arsenide (GaAs) or indium phosphide (InP) substrates, need to be at least 200 microns thick to be physically strong enough to be processed without excessive breakage rates. At 100 GHz the MMIC substrate will be electrically thick (thickness divided by wavelength in the dielectric near 0.25). In this thesis a completely new design for power combined transistor oscillator arrays on electrically thick MMICs is presented.

A review of both diode and transistor oscillator designs, including those that have been claimed to have prospects for monolithic fabrication as arrays at millimetre wave frequencies, reveals the designs that have been investigated in the past and the problems that have been encountered. The problems that arise are due to excitation of surface wave modes in thick substrates on the one hand or the increased losses and extreme fragility of very thin wafers or chips (50 microns or less) on the other.

The main concepts that form the basis of a new design include treating the MMIC rectangular substrate as a dielectric resonator with the transistor oscillators on the surface designed as shielded inverted microstrip component assemblies. The substrate partially fills a closed rectangular metal box. The air gap between the lid, and the surface of the substrate supports the quasi-TEM fields of the inverted microstrip oscillator components. The resonant mode of the partially filled cavity is energised by the output from each oscillator and the combined power output is fed to a load via a coupling structure in one wall of the resonator that is designed to be compatible with the constraints of monolithic fabrication. The transistor oscillators are positioned on the substrate surface so that only the output of each oscillator is coupled to the resonator although feedback within the oscillator circuit via the resonator can be designed.

Analytical methods for solving all of the design problems associated with this new combination of concepts are presented in detail. They include the design of transistor oscillators in shielded inverted microstrip, positioning of oscillator circuits on the surface of a large rectangular dielectric resonator, coupling between the oscillators and the longitudinal section magnetic (LSM) mode in the dielectric resonator and coupling combined power from the resonator into an output waveguide or radiating aperture.

The validity and accuracy of the overall design has been tested. The tests have been conducted on accurately scaled-up models that use packaged transistors in hybrid-type assemblies rather than monolithic assemblies. Technology and resource constraints that apply to most research efforts in this area of work, as revealed in the review, have forced most designers into scale model testing at microwave frequencies. Power combined outputs with good efficiency and spectrum characteristics have been demonstrated. It is concluded that this new design for power combined oscillators offers a means of creating millimetre wave power sources of significance for systems applications.

## **Statement of Originality**

This work contains no material that has been accepted for the award of any other degree or diploma in any university or other tertiary institution and, to the best of the author's knowledge and belief, contains no material previously published or written by another person, except where due reference has been made in the text.

The author gives consent for this copy of his thesis, when deposited in the University Library, being available for loan and photocopying.

Ali A. Sayyah

## Acknowledgement

I would like to express my gratitude to my supervisor Dr. Donald W. Griffin for his creative ideas and tremendous support, without which this research could not have been accomplished. Also I would like to thank Dr. Andrew J. Parfitt for his valuable advice and the time that he has devoted to me during this research.

The work was supported by a major research grant from The Australian Research Council.

I would like to express my thanks to Mr. Geoff Pook for his expert assistance, preparation of controlled cutting and skilful fabrication of the oscillator circuit. Also I thank Mr. Gordon Allison for his work on the fabrication of the precision mechanical parts of the oscillator assembly.

Finally I would like to acknowledge the support of the Iranian Ministry of Science and Higher Education for providing me with a scholarship during the period of my PhD research, August 1993 to February 1997.

## List of Author's Related Publications

A.A. Sayyah and D.W. Griffin, "A new design of microwave and millimetre-wave sources compatible with the constraints of monolithic technology," *Proceedings of Workshop on Applications of Radio Science (WARS97)*, Australian Academy of Science, Barossa Valley, Australia, Sept. 1997, pp. 37-41.

D.W. Griffin and A.A. Sayyah, "Design of Millimeter-Wave Source using Electrically Thick Monolithic Substrate Mode Resonant Combiners," *22nd International Conference on Infrared and Millimeter Waves*, Wintergreen, Virginia, U.S.A., July 1997, pp. 249-250.

A.A. Sayyah and D.W. Griffin, "Thick Substrate Mode Transmitting Antennas for Monolithic Millimeter-Wave Development," *1997 IEEE AP-S International Symposium and URSI Radio Science Meeting*, Montreal, Canada, July 1997, pp.2472-2475.

D.W. Griffin and A.A. Sayyah, "Limitations of Transistorized-Grid Oscillator-Type Quasi-Optical Transmitting Arrays," *Fifth Australian Symposium on Antennas*, CSIRO Division of Radiophysics, Sydney, Australia, February 1996, pp. 48-49.

## Patent

D.W. Griffin and A.A. Sayyah (as inventors), "Thick substrate mode transmitters for microwave or millimetre-wave frequencies", *Filed by Luminus Pty. (a commercial arm of Adelaide of University) on Dec.1996*.

## List of Principal Symbols

Symbol	Definition
$a_0$	junction width offset
$a_{mn}^{k, mode}, b_{mn}^{k, mode}$	normalised wave amplitudes corresponding to a hybrid mode in waveguide # $k$ at the junction where $k$ is 1 or 2
$b_0$	junction height offset
$d$	length of partially-filled cavity
$\tilde{e}_{mnl}^e, \tilde{f}_{mnl}$	normalised field amplitudes corresponding to a unit source
$\bar{e}_k^e, \bar{h}_k^e$	eigenvectors of LSM <sup>y</sup> modes
$\bar{e}_k^h, \bar{h}_k^h$	eigenvectors of LSE <sup>y</sup> modes
$e_n, \bar{E}_n$	amplitude and eigenvector of resonant electric field
$\bar{e}_{mn}^{k, mode}, \bar{h}_{mn}^{k, mode}$	electric and magnetic field eigenvectors for a hybrid mode in waveguide # $k$ at the junction where $k$ is 1 or 2
$\bar{e}_t^{mode}, \bar{h}_t^{mode}$	transverse vector functions of transverse coordinates
$\bar{e}_z^{mode}, \bar{h}_z^{mode}$	axial vector functions of transverse coordinates
$f_c$	cutoff frequency of hybrid mode
$f_n, \bar{F}_n$	amplitude and eigenvector of local electric field
$g$	length of the air-gap
$g_n, \bar{G}_n$	amplitude and eigenvector of local magnetic field
$h$	thickness of the dielectric substrate
$h^i$	height of the dielectric or air-filled region in a partially-filled structure
$[h], [e], [g], [f]$	$(N \times 1)$ vectors of wave amplitudes

Symbol	Definition
$h_n, \bar{H}_n$	amplitude and eigenvector of resonant magnetic field
$k$	medium wave-number of current distribution on the probe
$k_0$	wave number of free space
$k_c$	cutoff wave number of hybrid mode
$k_n, k_{mnl}$	eigenvalue of resonant modes in partially filled cavity
$k_n^d, k_n^a$	partially-filled waveguide eigenvalues in y-direction for dielectric and air-filled regions
$l_0, w$	dimensions of probe strip
$m$	eigennumber in the $x$ -direction
$m_s$	elliptic modulus
$n$	eigennumber in the $y$ -direction
$n'$	virtual eigennumber for $LS^y$ modes
$n_s$	elliptic characteristic
$\hat{n}$	normal unit vector
$x_0, z_0$	driving point coordinates of probe strip
$y_{ij}$	admittance parameters
$A^{d, mode}, A^{a, mode}$	amplitude of scalar mode function in dielectric and air-filled regions
$A_{mn}^{d, mode}, A_{mn}^{a, mode}$	amplitude of $\bar{e}_t^{mode}$ in dielectric and air-filled regions
$A_{mnl}^{i,f}$	normalised amplitude of $\Psi_{mnl}^{i,f}$
$A_{mnl}^{i,g}$	normalised amplitude of $\Psi_{mnl}^{i,g}$
$A_{mnl}^{i, mode}$	normalised amplitude of $\Psi_{mnl}^{i, mode}$
$[B]$ and $[C]$	$(N \times M)$ matrices of surface integral coefficients

Symbol	Definition
$B_{jun}^{e,mn}$	susceptance of cavity aperture for a hybrid propagating mode
$B_{nk}^e, B_{nk}^h, C_{nk}^e, C_{nk}^h$	surface integral coefficients
$C$	capacitance of inhomogeneously filled stripline
$C_0$	capacitance of air-filled stripline
$[D]$	diagonal matrix with elements $D_{ii}$
$D_{ii}$	propagation factor of the $i$ -th hybrid mode in the thick iris
$\bar{E}, \bar{H}$	total electric and magnetic fields in partially filled cavity
$\bar{E}^a, \bar{H}^a$	electric and magnetic fields in air filled region
$\bar{E}^d, \bar{H}^d$	electric and magnetic fields in dielectric region
$\bar{E}_t, \bar{H}_t$	tangential electric and magnetic field components
$\bar{E}_t^{(k)}, \bar{H}_t^{(k)}$	tangential fields of guide # $k$ at the junction, where $k$ is 1 or 2
$\bar{E}_t^{mode}, \bar{H}_t^{mode}$	transverse field components of LS modes
$\bar{E}_z^{mode}, \bar{H}_z^{mode}$	axial field component of LS modes
$\bar{E}_{nt}^y, \bar{F}_{nt}^y$	transverse eigenvectors of electric fields with respect to the y-axis
$[\bar{E}], [\bar{F}]$	$(N \times 1)$ vectors with elements $\bar{E}_n, \bar{F}_n$
$E(m_s)$	complete elliptic integral of the second kind
$E(\phi/m_s)$	incomplete elliptic integral of the second kind
$F(\phi/m_s)$	incomplete elliptic integral of the first kind
$I_{in}$	total driving current evaluated at the probe input
$I_{source}^{e,mn}$	electric current source for a hybrid propagating mode

Symbol	Definition
$I_x$	amplitude of current distribution on the probe strip
$[I]_{norm}$	$(M \times 1)$ vector of normalised waveguide currents
$[I]_{source}$	$(N \times 1)$ vector with elements $I_{source}^{e, mn}$
$\Im m$	imaginary part of a complex term
$\Im_{mnl}^e, \Im_{mnl}^f$	source integral of electric fields on the probe strip
$\tilde{\Im}_{mnl}^e, \tilde{\Im}_{mnl}^f$	normalised source integral of electric fields on the probe strip
$\tilde{J}$	electric current source
$[K]$	diagonal vector of resonant mode eigenvalues
$K(m_s), K'(m_s)$	complete elliptic integrals of the first kind
$M$	number of waveguide modes
$N$	number of cavity modes
$P_x, Q_x$	linear integrals along and across the probe strip
$Q_d$	Q-factor due to dielectric loss
$Q_{mn}^{k, mode}$	normalisation constant corresponding to a hybrid mode in waveguide # $k$ at the junction where $k$ is 1 or 2
$Q_{nm}^{mode}$	orthogonality constant for a hybrid mode
$Q_L$	loaded-Q
$Q'_n$	unloaded-Q factor of the cavity
$Q_{sn}$	Q-factor due to conductivity loss
$\Re e$	real part of a complex term
$\Re_{mnkl}^{mode1, mode2, d}$ , $\Re_{mnkl}^{mode1, mode2, a}$	reaction elements corresponding to the dielectric- and air - filled areas of the junction

Symbol	Definition
$[\mathfrak{R}]$	reaction matrix
$S$	total surface of the cavity walls
$S'$	total surface of conducting walls
$S_k$	cross-section area for waveguide # $k$ at the junction where $k$ is 1 or 2
$S_{ij}$	scattering parameter
$S_0$	surface of cavity aperture
$S_0^d, S_0^a$	surface of dielectric and air filled regions
$[S]$	generalised scattering matrix of the coupling structure
$[S]_I$	generalised scattering matrix for the first junction
$[S]_{II}$	generalised scattering matrix for the second junction
$[S_c]$	conventional scattering matrix of the coupling structure
$U$	unit matrix with dimension $(N \times M)$
$V$	total volume of cavity
$V_{DS}$	drain to source DC voltage
$V_{GS}$	gate to source DC voltage
$V_k^{mode}, I_k^{mode}$	normalised equivalent voltage and current of a hybrid mode at the aperture cross-section
$V_{mn}^{k, mode}, I_{mn}^{k, mode}$	normalised voltage and current corresponding to a hybrid mode in waveguide # $k$ at the junction where $k$ is 1 or 2
$[V], [I]$	$(M \times 1)$ vector of equivalent voltages and currents at the aperture cross-section
$Y_0$	admittance of free space
$Y_{0N}$	wave admittance of waveguide number N
$\bar{Y}_{cav}$	normalised cavity admittance for desired propagating mode

Symbol	Definition
$Y_{nm}^{mode}$	wave admittance of a hybrid mode
$Y_{cav}^{mode, mn}$	cavity admittance for a hybrid propagating mode
$Y_{jun}^{mode, mn}$	aperture admittance for a hybrid propagating mode
$Y_{mn}^{k, mode}$	wave admittance corresponding to a hybrid mode in waveguide # $k$ at the junction where $k$ is 1 or 2
$[Y]$	diagonal matrix of wave admittances
$[Y]_{cav}$	( $N \times 1$ ) vector with elements $Y_{cav}^{mode, mn}$
$[Y]_{jun}$	( $N \times 1$ ) vector with elements $Y_{jun}^{mode, mn}$
$Z_0$	impedance of dielectric filled space
$Z_c$	characteristic impedance of shielded inverted microstrip
$Z_c^a$	characteristic impedance of air-filled stripline
$Z_{ck}$	characteristic impedance of the waveguide number $k$
$Z_d$	device output impedance seen at the drain
$Z_L$	equivalent load impedance connected to drain
$Z_{strip}$	driving point impedance of the probe strip
$Z_w$	surface impedance
$Z_{wave}$	wave impedance
$\alpha_m$	eigenvalue in the $x$ -direction
$\beta_z$	phase constant
$\beta_n^d, \beta_n^a$	partially-filled cavity eigenvalues in the $y$ -direction for dielectric and air-filled regions
$\gamma$	propagation constant
$\gamma_i$	propagation constant of the $i$ -th hybrid mode in the thick iris

Symbol	Definition
$\gamma_{mn}^{k, mode}$	complex propagation constant corresponding to a hybrid mode in waveguide # $k$ at the junction where $k$ is 1 or 2
$\delta$	interlayer gap
$\delta_{nm}$	kronecker's delta
$\epsilon_0$	permittivity of vacuum
$\epsilon_{0k}$	Neumann constant
$\epsilon_{eff}$	effective dielectric constant
$\epsilon_r$	dielectric constant
$\kappa$	relative permittivity
$\lambda_g$	wavelength in the air-filled waveguide
$\lambda_s$	wavelength in shielded inverted microstrip
$\mu_0$	permeability of vacuum
$\rho$	reflection coefficient
$\rho_L$	load reflection coefficient
$\Psi$	normalised wave-amplitude matrix
$\Psi_{mnl}^{i,f}$	scalar electric potential function
$\Psi_{mnl}^{i,g}$	scalar magnetic potential function
$\psi^{mode}$	scalar mode function of LS modes
$\Psi_{mnl}^{i, mode}$	scalar mode function for a LSM <sup>y</sup> <sub>mnl</sub> or LSE <sup>y</sup> <sub>mnl</sub> resonant mode
$\omega$	radian frequency
$\omega_n$	resonant frequency
$\omega'_n$	modified resonant frequency

<b>Symbol</b>	<b>Definition</b>
$\omega''$	exact resonant frequency of cavity
$\Delta_n$	frequency selective term of the resonant field expression
$\Delta h$	thickness of lower layer dielectric slabs
$\Delta h'$	thickness of top layer dielectric slab
$\Delta l$	length of the thick iris
$[\Delta]$	diagonal matrix of $\Delta_n$
$\Pi(n_s, \text{asin}\alpha m_s)$	incomplete elliptic integral of the third kind
$\bar{\Pi}_e$	electric vector potential
$\bar{\Pi}_h$	magnetic vector potential

## List of Abbreviations

<b>Abbreviation</b>	<b>Definition</b>
DC	Direct Current
DH-PHEMT	Heterojunction-PHEMT
FET	Field Effect Transistor
GaAs	Gallium Arsenide
HEMT	High Electron Mobility Transistor
IMPATT	Impact Avalanche and Transit Time
InAlAs	Indium Aluminium Arsenide
InGaAs	Indium Gallium Arsenide
InP	Indium Phosphide
LSA	Limited Space Charge Accumulation
LSE	Longitudinal Section Electric
LSM	Longitudinal Section Magnetic
MESFET	Metal Semiconductor FET
MMIC	Monolithic Microwave (or Millimetre-Wave) Integrated Circuit
PHEMT	Pseudomorphic HEMT
Q	Quality factor
RF	Radio Frequency
S	Scattering
SIE	Surface Integral Equation
SIML	Shielded Inverted Microstrip Line
TEM	Transverse Electromagnetic
TGO	Transistor Grid Oscillator
VIE	Volume Integral Equation



---

## Chapter 1

# *Introduction*

Most systems that are designed for operation at frequencies in the microwave and millimetre wave parts of the electromagnetic spectrum include one or more subassemblies for the generation of power at the operating frequency. Exploitation of the spectrum through the development of new systems has followed advances in technology and the innovative design of practical systems that incorporate the new technology. Prominent amongst the recent advances in technology are developments in transistors that have raised the operating frequency towards 100 GHz [1].

The first systems applications involved vacuum tube type power sources. Those sources are now at an advanced state of development and are well established because of the extent to which they meet the power output and operating life requirements of the systems that are built around them [2]. Power sources based on semiconducting devices have been under development for a shorter period of time and many of the developments in semiconducting materials technology that have a specific effect on increasing the operating frequency and the power output are currently being pursued.

Many of the industrial, military and commercial applications that are yet to be realised

are subject to size, weight, cost, efficiency, etc., constraints that cannot be satisfied by either vacuum tube type sources or currently available solid state sources. In particular, more efficient sources that deliver adequate power at frequencies up to 100 GHz are needed if certain of the systems are going to be small enough and light enough. To be cost effective a high level of integration in the fabrication of the systems for operation at millimetre wavelengths appears necessary and is a major factor driving the further development of monolithic integration of millimetre wave assemblies of active and passive components [3,pp. ix-x].

The oscillation frequency of microwave and millimetre wave oscillators is determined by a passive resonant structure that is modified by an active region where power, supplied by a bias source, is converted partly into the desired oscillator output and partly into unwanted heat. The physical phenomenon that is exploited in the active region imposes physical constraints on the design of the passive structure that incorporates it. The resonant structure for single oscillators is usually a combination of reactances arising from the active region and a distributed component such as a length of transmission line or a cavity with dimensions of the order of one quarter to one half the wavelength of the oscillation frequency in the medium that fills the distributed part. As a consequence the dimensions of oscillators decrease with increasing frequency and this in turn decreases operating power levels. Combining the output from an array of oscillators that operate in synchronism is used to compensate for this effect. It is evident that for a desired level of power output it is likely that more oscillators in combination will be required at higher frequencies and that as an assembly, the overall dimensions will be integral multiples of the dimensions of a single oscillator. This adds considerably to the design task because the passive part of the structure must provide for interaction amongst the active regions or devices so that they synchronise and must also impose phase relationships that result in the combining of all of the oscillator outputs in the load. Because the passive structure will have dimensions that may be of the order of several wavelengths operation in an unwanted mode may occur at a frequency different from that required.

Advances in the materials technology that lead to active devices that have good performance characteristics at frequencies as high as 100 GHz can be pursued in advance of

the design of passive structures external to the active devices. The materials technology will impose constraints on the design of the external passive structure that will join with the active device to form an efficient oscillator. A combination of concepts that solve the problems presented by the constraints is needed for a successful outcome.

The operating principles of the passive structure must be accurately modelled from the beginning so that the combination of concepts that form the proposed design can be subject to practical testing. After the design has been validated it must be developed so that it conforms with specifications with regard to the fabrication process that must be used for producing the active device or devices embedded in the passive structure as well as specifications with regard to operating frequency, output, biasing, packaging, etc.

Fabrication requires access to facilities that are very expensive to operate. Designs that have been tested from the point of view of validating the combination of concepts that together make them innovative and compatible with the main constraints of the materials technology may still need development and re-design before prototype fabrication in a foundry proceeds. The research reported in this thesis is confined to innovative design of power sources that satisfy constraints that arise when the semiconducting wafer essential for transistor fabrication for monolithically formed arrays of oscillators is electrically thick. This occurs for example if a standard GaAs wafer 200 microns thick is used at 100 GHz. The design presented in this thesis is validated by testing hybrid type models that are scaled up 30 times in size at frequencies around 3.5 GHz.

---

## Chapter 2

# *Review of Solid State Microwave & Millimetre-Wave Sources*

### **2.1 Introduction**

The development of transistors with impressive gain, power output and efficiency at frequencies up to 100 GHz has created prospects for more efficient millimetre wave oscillators than those that use IMPATT or Gunn diodes. Oscillators that have been described in the literature may be classified as either conventional or unconventional in design. The conventional designs embed the transistor in a microstrip type circuit whereas the unconventional designs embed the transistor in a different type of transmission line or structure involving metallisation on dielectric. A critical review of these designs is presented so that some of the origins of the combination of concepts that form what is set out in this thesis as a new design are clarified. Three books [3], [4] and [45] that comprehensively review the published literature have been used in this review of the concepts that have been utilised in the circuits or structures for sources.

## 2.2 The Ideal Microwave or Millimetre Wave Source

No source is ideal in all aspects and for most applications only a subset of all of the ideal qualities is needed to make a source acceptable. Figure 2-1 shows the properties of a source that would be ideal for use in many of the microwave and millimetre-wave systems that have been visualised but not yet realised.

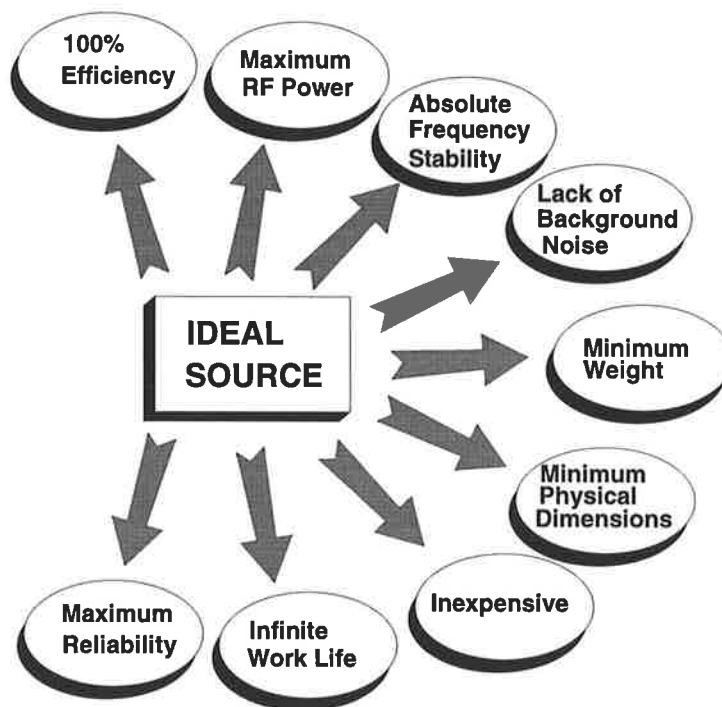


Figure 2-1. Properties of an ideal source

Although, an ideal source cannot be realised, a definition of the ultimate features of a microwave or millimetre wave source is a guide in identifying goals and evaluating the nature of the work to be done to achieve a satisfactory result. The DC to RF efficiency of real sources is much less than 100% and, depending on the specific source, may vary from a fraction of one percent in vacuum tubes to as high as 50% in modern solid-state sources. The RF power is an important design parameter specified according to the system application. In practice, microwave and millimetre wave sources are classified according to their RF power level, namely: low, medium, and high power sources. The

frequency stability of a source, as a measure of the frequency drift during a long period of steady-state operation, is a technical figure that depends upon the quality of the oscillator circuitry. The presence of background noise which is a critical factor in the design of local oscillators, may be of less importance in general purpose microwave and millimetre wave sources.

Non-electrical properties such as weight, physical dimensions and fabrication cost, are major considerations in the development of millimetre wave systems. Indeed, recent advances in monolithic microwave integrated circuit (MMIC) technology have promised excellent opportunities for the development of new systems using small size, inexpensive and compact solid-state microwave and millimetre-wave sources. There are more general engineering factors such as reliability and working life, which should be considered once a comparison amongst different sources is carried out.

## **2.3 IMPATT and Gunn Diode Oscillator Operating Modes**

IMPATT and Gunn diodes are characterised as two terminal broadband negative resistance devices with some reactance. To make an oscillator, they are mounted in a resonant type of structure. The resonant structure is usually formed from a length of suitable transmission line or waveguide. The length and terminations are usually chosen so that oscillation occurs at the lowest resonant frequency of the structure. An important part of the design is minimising the extent to which the broadband negative resistance may excite oscillations at a higher frequency resonance or at the second and higher harmonics.

An exception to this is the type of the structure designed to make IMPATT type diodes operate in a high efficiency mode by trapping harmonics of the oscillation frequency within the structure. This operating mode and the particular type of diode developed for the purpose are given the acronym TRAPATT. The concept basic to this design is modification of the current and voltage waveforms at the diode so that the percentage of input bias power lost as heat is minimised. Considerable efforts has also been expended developing Gunn diodes and resonant mounting structures that oscillate in the limited space

charge accumulation (LSA) mode. By suppressing domain formation in relatively thick layers of gallium arsenide (GaAs) higher RF peak voltage and output power has been obtained but only for very short duty cycles of pulsed bias. Neither the TRAPATT nor the LSA modes of operation appear to have been exploited in practical systems at microwave or higher frequencies.

## 2.4 Single Diode Oscillator Mounting Structures

### 2.4.1 Non-Radiating

Coaxial line and waveguide structures are used almost exclusively for single diode oscillators that have non-radiating output ports [4, pp. 223-301]. Structures that resonate in conjunction with the diode include coaxial resonators with coaxial output ports like that shown in Figure 2-2, coaxial structures coupled into rectangular cross-section waveguide, post-gap mounted diodes across rectangular waveguide, top hat type posts across a rectangular waveguide and either single or double entry coaxial junctions at the broad face of rectangular waveguide.

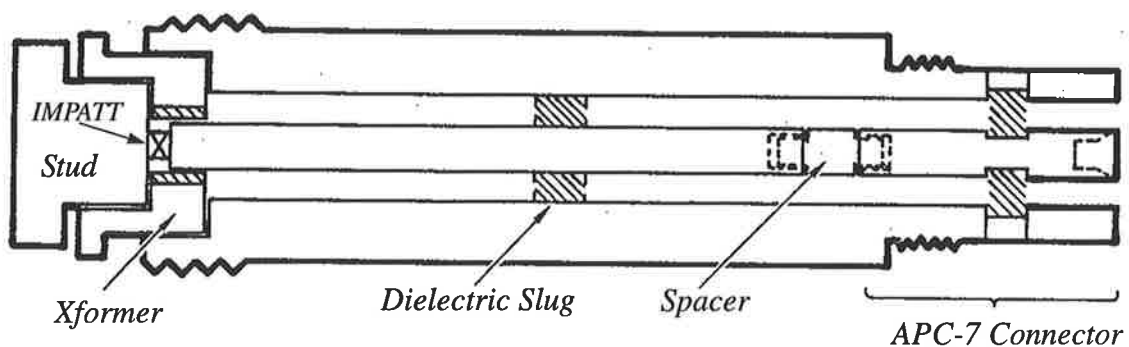


Figure 2-2. Coaxial oscillator circuit for a packaged IMPATT diode.

None of the structures are compatible with the constraints of planar geometry and in particular with monolithic fabrication of both the active device and its resonating mount coupled to the output load.

### 2.4.2 Radiating

The most recently developed single diode oscillators are those designed so that the output power is radiated directly into space. The passive structure external to the diode acts as both a resonator and an antenna as well as providing appropriate bias circuitry for the diode.

The microstrip patch antenna is used almost exclusively in these oscillators with the diode connected between the patch and the ground plane as shown in Figure 2-3 [3, pp. 133 to 135 and 140 to 155].

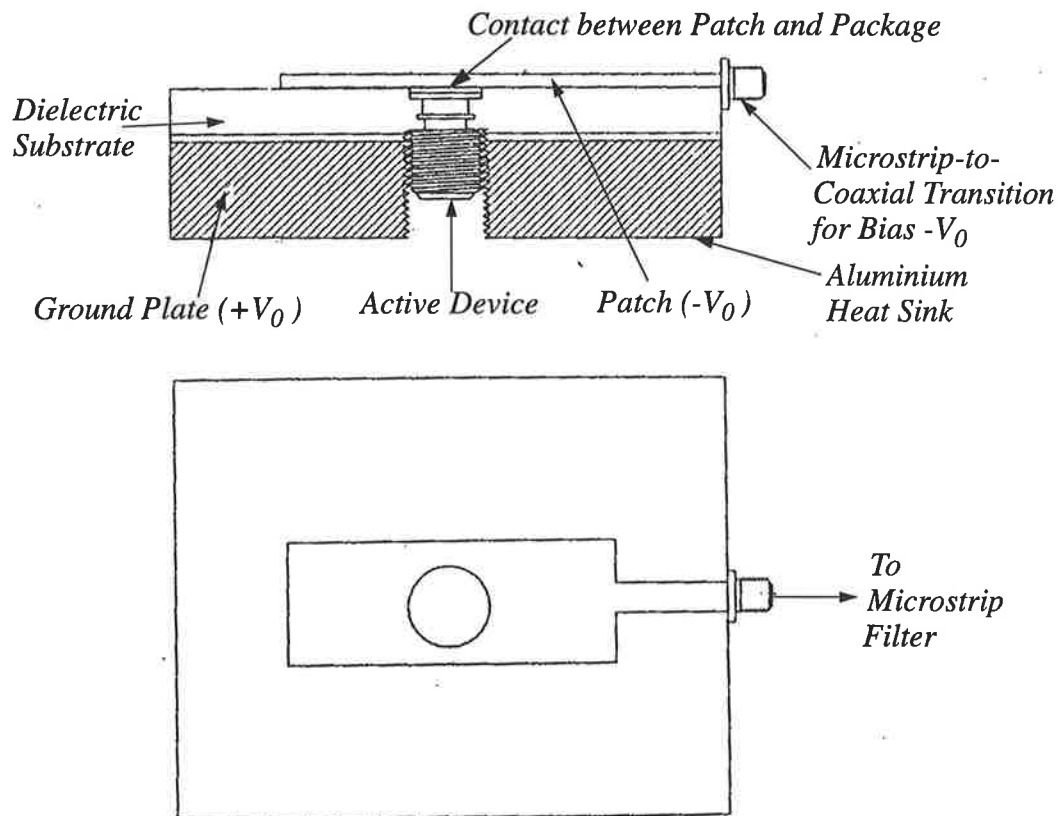
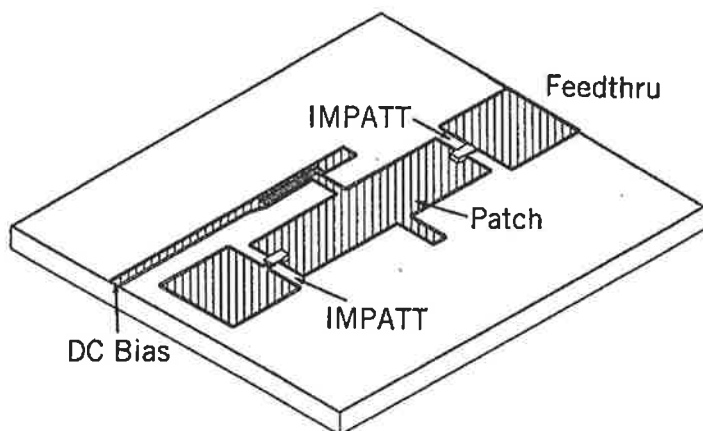


Figure 2-3. A microstrip patch antenna excited by a diode oscillator

When fabricated in conventional microstrip a hole must be formed through the dielectric to accommodate the diode or other means must be designed for providing the return path to the ground plane for diode bias current such as that shown in Figure 2-4 [5]. The substrate must be electrically thin to minimise the proportion of output power that may excite surface waves that lead to consequential pattern degradation and losses, although thin substrates cause increased conductor losses in microstrip [6].



*Figure 2-4. An IMPATT oscillator patch antenna with diodes mounted on the dielectric surface*

The concept of using inverted microstrip has been exploited in the active patch antenna shown in Figure 2-5 [7].

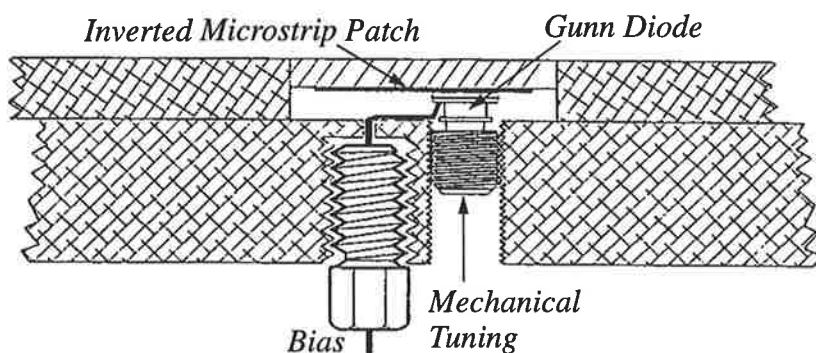


*Figure 2-5. Inverted microstrip patch antenna excited by a Gunn oscillator*

This structure will have lower internal losses but the major advantage is the mechanical tuning of the resonant frequency that can be achieved by varying the air gap between the patch and the top of the diode package that acts as an electric field coupling probe.

## 2.5 Single Field Effect Transistor Oscillator Mounting Structures

### 2.5.1 Non-Radiating

Conventional microstrip structures are used almost exclusively for simple transistor oscillators whether the active device is in packaged form, or in chip form that has to be wire bonded to the circuit, or is part of a complete monolithically formed oscillator [4, pp. 172 to 214]. Figure 2-6 is an illustration of one of the simplest microstrip type mounting structures for a packaged MESFET.

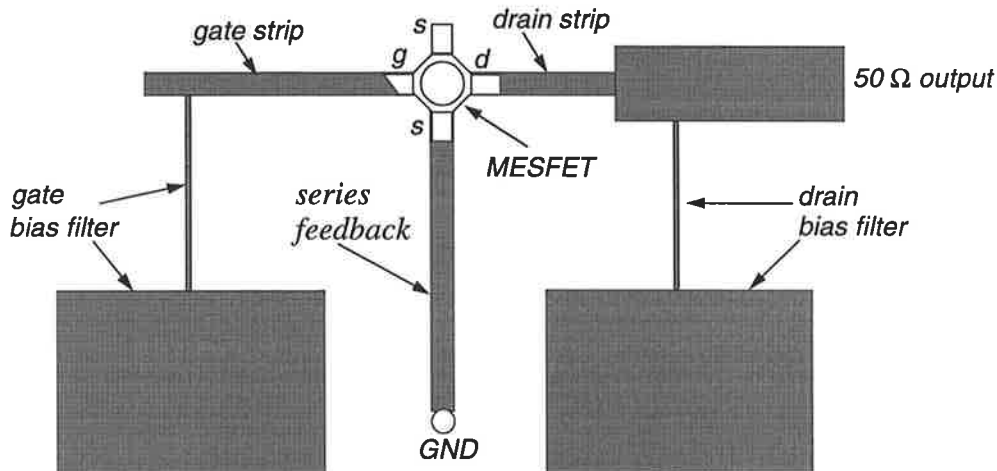


*Figure 2-6. Typical layout of a microstrip MESFET oscillator with series feedback*

It is normally classified as a series feedback type of circuit with the microstrip connected to the source designed to provide a level of feedback that will result in spontaneous growth of oscillation at a frequency determined mainly by the microstrip connected to the gate. Power transfer to the load is optimised mainly by the design of the microstrip matching structure that connects the drain to the load. A dielectric resonator may be cou-

pled to the output microstrip to improve the frequency stability [4, pp. 199 to 206]. At microwave frequencies this component is made small relative to the wavelength on the microstrip line by the use of a dielectric constant of 40 or more. It is essentially a lumped component at a localised position in the distributed circuit structure but this restricts the practice to frequencies in the microwave band.

### 2.5.2 Radiating

As with single diode oscillators the most recent developments in single transistor oscillators are structures that radiate directly into space. These structures are almost exclusively microstrip arrangements that incorporate both transistors and patch antenna radiating elements, as illustrated in Figure 2-7 [8].

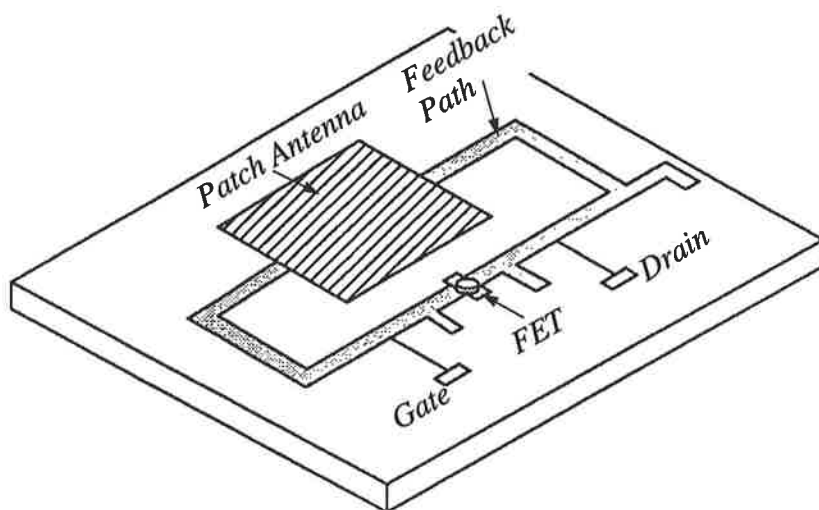
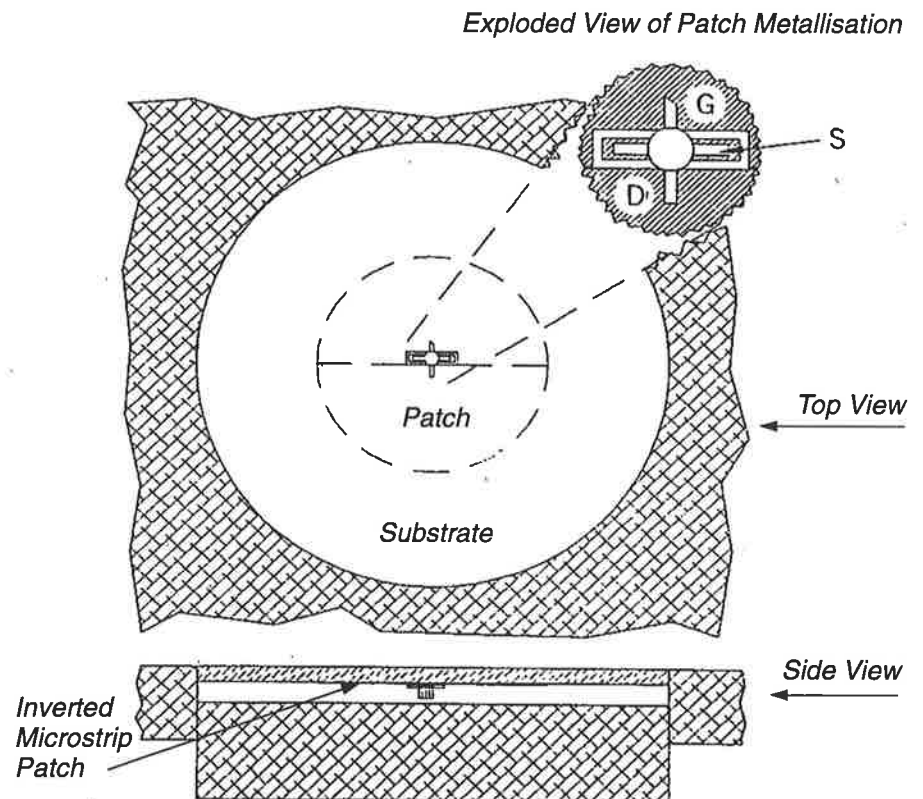


Figure 2-7. A patch antenna in the feedback path of a microstrip FET oscillator

A less conventional structure incorporates the transistor in an inverted microstrip type radiating patch as shown in Figure 2-8 [9].



*Figure 2-8. Typical FET oscillator feeding an inverted microstrip patch antenna*

By connecting the patch type resonant circuit in series with the drain of the MESFET as shown in Figure 2-9 [10] and designing the feedback to the gate and the bias supplies appropriately a DC to RF conversion efficiency in excess of 50 percent has been achieved. This high efficiency transistor operating mode is explained below.

## 2.6 Field Effect Transistor Operating Modes

The metal-semiconductor field effect transistor (MESFET) has its gate in the form of a Schottky barrier diode that can act as a clamping diode when the MESFET is the active device in an oscillator. With appropriate circuit design the peak of the gate-to-source voltage will be clamped to a level corresponding to a small positive voltage at the gate relative to the common bias supply lead.

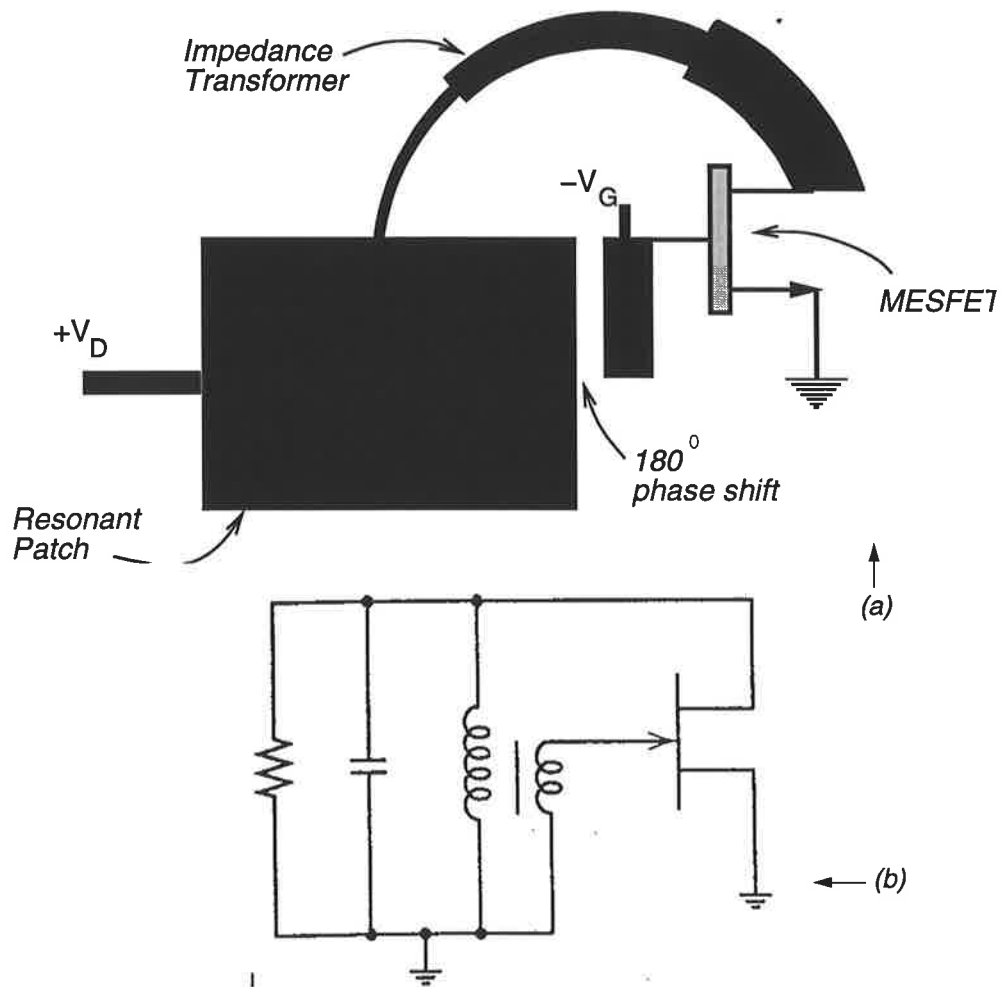


Figure 2-9. A high efficiency FET patch oscillator: (a) layout (b) equivalent circuit

As a consequence of this clamping action and the small DC component of gate current, a DC gate-to-source bias may be developed that pinches off the channel for part of the oscillation cycle. Thus the potential exists for high efficiency class C mode operation but an appropriate circuit like that shown in Figure 2-9 is required.

Improvements in carrier transport properties of the channel and reduction in the length of the gate electrode result in extension of the operation of the transistor up to frequencies near 100 GHz and also to increases in power output capability. These improvements arise from advances in semiconducting materials technology and the progressive development of high electron mobility transistors (HEMTs), pseudomorphic HEMTs

(PHEMTs), heterojunction-PHEMTs and double heterojunction-PHEMTs (DH-PHEMTs). A gate length of 0.15 microns on layers of indium gallium arsenide (InGaAs), and indium aluminium arsenide (InAlAs) formed on an indium phosphide (InP) substrate is used in a state-of-the-art MMIC power amplifier that delivers an output power of 130 mW at 94 GHz with 13 percent power added efficiency and 4 dB associated gain [1]. These figures are for what appears to be class A operation but no data are given regarding distortion.

## 2.7 Multiple Diode Oscillator Mounting Structures

### 2.7.1 *Introduction*

The main aim in designing multiple diode oscillator mounting structures is to generate a required level of output power by combining the power output capability of a sufficient number of IMPATT or Gunn effect diodes. Interaction amongst the diodes in one way or another is essential if the output power is to be at a single stable frequency.

Mounting structures may be non-radiating or radiating and there are major differences between these two categories due to the means and level of interaction that occurs between the diodes.

### 2.7.2 *Non-Radiating*

Two alternatives are possible in designing a non-radiating multiple diode oscillator mounting structure. Either a resonant structure can be provided for each of N diodes in which case there are N oscillators to be synchronised and power combined, or, the N diodes can be mounted in a single resonator, in which case the N wide band negative resistances contributed by the diodes must be effectively combined to cancel the load resistance and mounting structure losses at a specified frequency. The main problem in this latter case is that the single resonator has to be large enough to accommodate the N diodes and as a consequence it will have a multiplicity of resonances that will be more closely spaced the larger the number N.

### 2.7.2.1 N oscillators in Corporate Combiners

Figure 2-10 illustrates schematically the components and the function to be performed in a corporate combiner that includes 8 separate diode oscillators. Coupling between the oscillators that results in synchronisation and required relative phasing must be provided. Next a corporate combining structure, shown in Figure 2-10 symbolically as a tree of hybrids, can be used to add the individual oscillator output powers together.

Apart from the difficulty and cost of fabricating corporate combiners the losses become excessive as the operating frequency approaches the millimetre wave band.

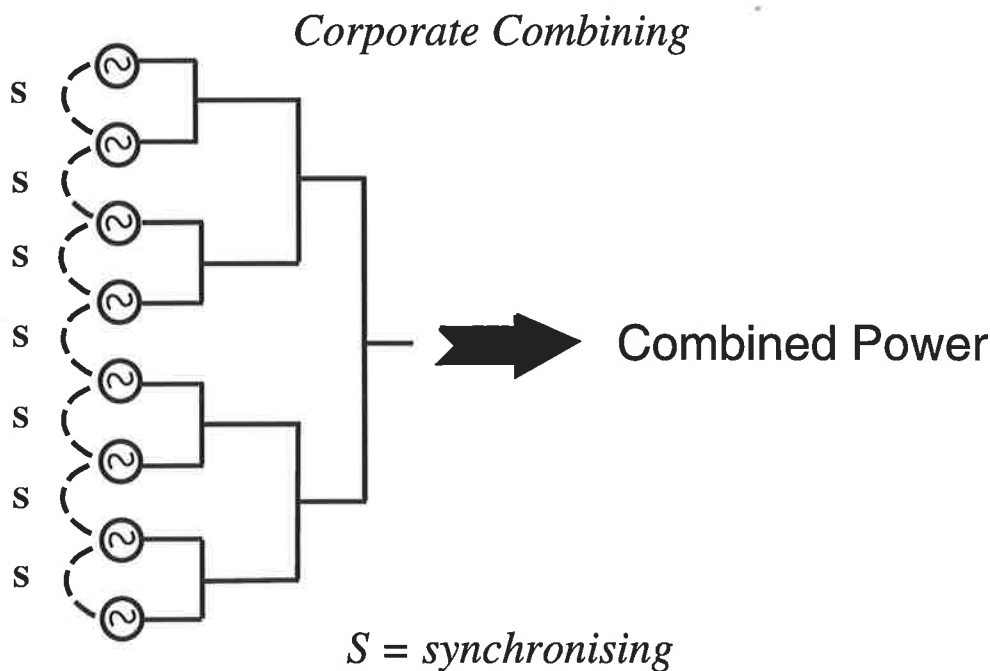


Figure 2-10. Diagram of the corporate combining

### 2.7.2.2 N diodes in a Single Resonator

The structure shown in Figure 2-11 [11] qualifies as an example of N diodes in a single resonator for the following reasons. Each diode is mounted at one end of a coaxial line that is coupled through an aperture to the magnetic field at the side wall of a  $TE_{01n}$  rectangular waveguide cavity resonator where  $n = N/2$  with  $N$  even.

Each coaxial line structure is terminated by an absorptive load so that the only resonant structure in the assembly is the waveguide cavity. The coupling apertures in the side walls are at positions of maximum resonant magnetic field.

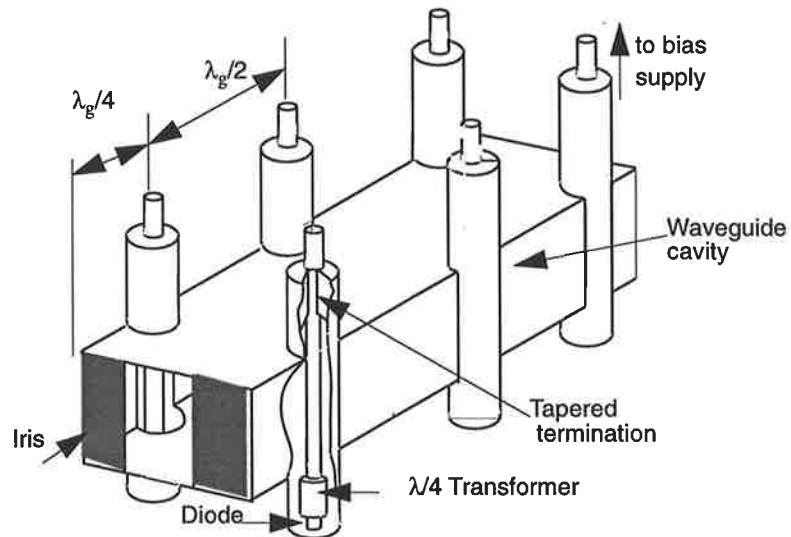


Figure 2-11. Kurokawa's resonant cavity power combiner

The effect of this is to connect the equivalent circuits that represent the coaxial mounted diodes in parallel as shown in Figure 2-12.

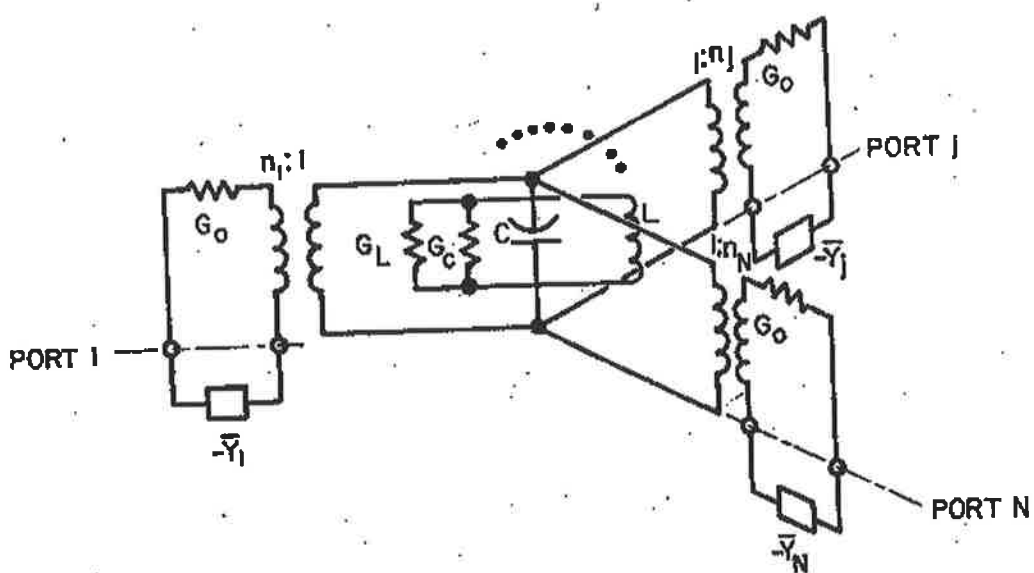


Figure 2-12. Equivalent circuit of the Kurokawa's oscillator where 3 of N branches are shown

The negative conductances add together and increase the power that passes to the load that is coupled into the cavity at the iris type output port. They are amplitude dependent and there is reactance but no resonance. A circular  $\text{TM}_{010}$  mode resonator can also be used as a combining structure.

### 2.7.2.3 Planar Arrays of Electric Current Elements in an Open Resonator

In principle this may be classified with the structure of section 2.7.2.2. The main differences are the type of resonator and the analytical approach in design. The idealising assumptions that are made in the analysis [12] of quasi-optical power combining of current elements in an open resonator are such that  $N$  elements are placed in a single resonator where the elements are not assumed to be individual resonators but are simply sources [3, pp. 80 to 60]. The assumed current elements do not have any associated impedance or admittance but it is implied that they are synchronous and in phase and also form a planar array that is normal to the axis of the open resonator as illustrated in Figure 2-13. The analysis determines the fraction of the total power from the array of sources that is coupled into the fundamental mode of the open resonator as a function of the amplitude distribution across the array and the spacing between the elements of the array.

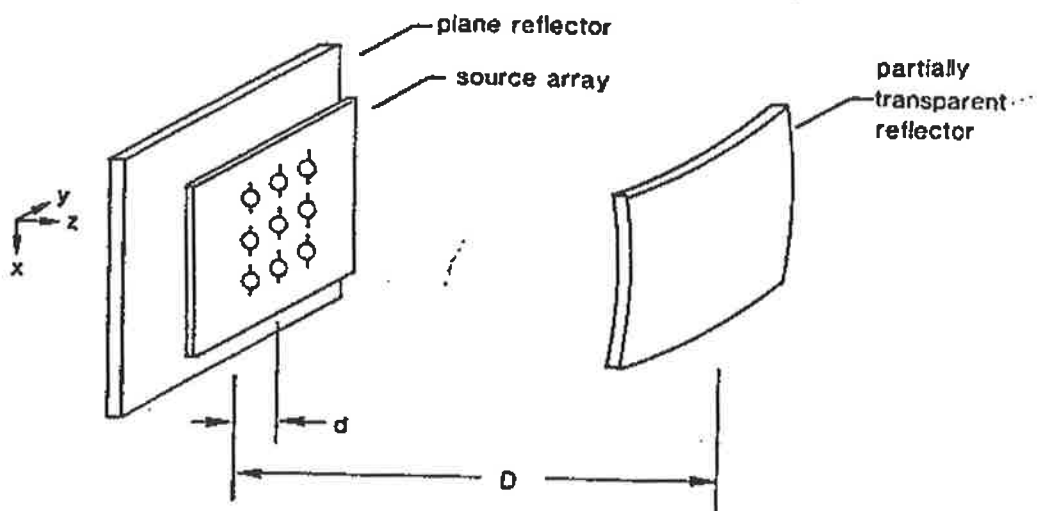


Figure 2-13. Quasi-optical array system

Thus power combining efficiency is the main consideration and it is assumed that the analysis indicates one way toward generating high power output at millimetre wavelengths by combining the outputs of large numbers of low power solid state sources. The design problems associated with creating a suitable array of sources at millimetre wavelengths are not addressed. In practice the sources may be oscillators in which case a means of synchronising and phasing all the oscillators in the array is essential. This aspect of the open resonator as a power combiner will be examined in detail in the major section on multiple transistor oscillator mounting structures.

#### 2.7.2.4 N diodes in an Open resonator

The power combining function of an open resonator has been tested with diodes mounted in grooves in the flat mirror reflector of the open resonator as shown in Figure 2-14 [13] and coupled to it so that oscillation only occurs via connection with the open resonator, [3, pp. 94 to 96].

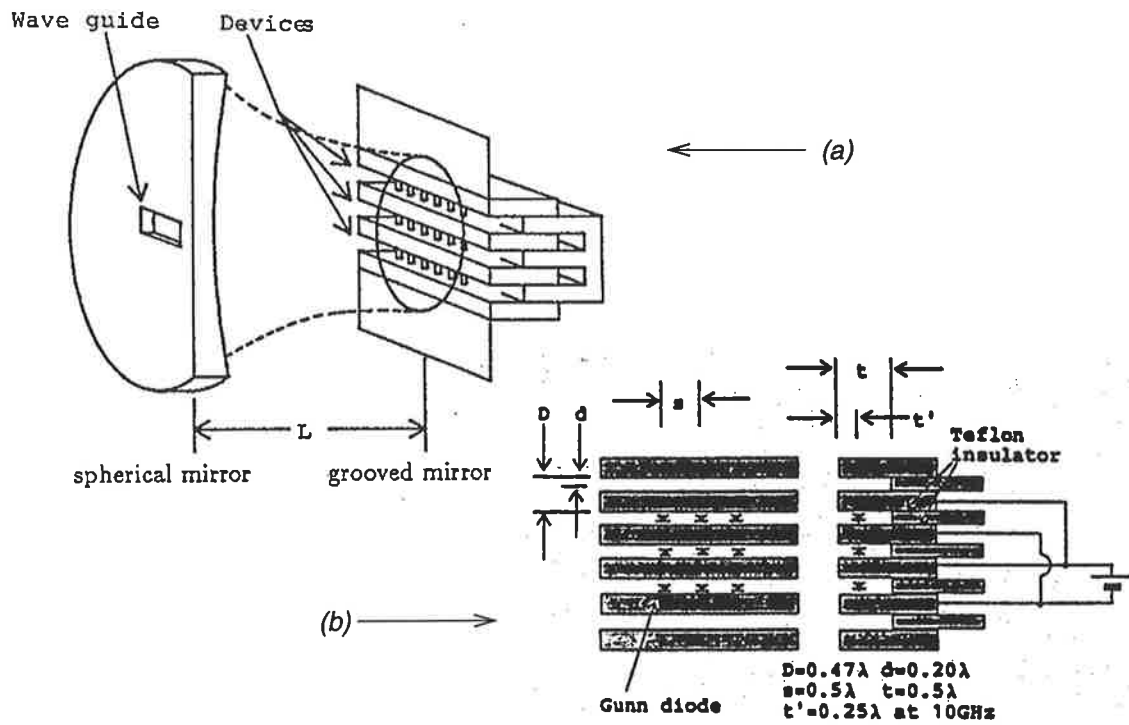


Figure 2-14. Grooved mirror type Fabry-Perot oscillator: (a) overall structure; (b) grooved mirror

These tests demonstrate efficient combining and very good spectrum characteristics. However the assembly of the diodes and their coupling to the power combiner does not appear to be suitable for monolithic fabrication and is not likely to be cost effective or efficient overall as a millimetre-wave power source.

This test of the open resonator as a power combiner has an important feature that other tests lack. No material or structure is placed within the volume between the reflecting surfaces that define the resonator. The effects of the grooves at the flat mirror surface may be represented by equivalent impedances that will include negative resistance parts.

Thus the reflective surfaces that define the open resonator are both modified, one by a negative surface resistance (as well as a surface reactance) due to the diodes, and the other by a positive surface resistance (as well as a surface reactance) due to the coupling to the load that may be free space or the input aperture of a cascade of quasi-optical components.

#### **2.7.2.5 Diode Oscillators in an Open Resonator**

Initial tests of open resonator power combining were conducted with diode oscillators symmetrically placed around the resonator's axis. One of the first tests, [3, pp. 94], [14], coupled the output from two Gunn diode oscillators into the resonator by means of dielectric wedge launchers. All of the tests in this category involved relatively few oscillators but they clearly demonstrated that the open resonator synchronised the oscillators as well as power combining them. The interaction necessary for synchronisation to occur was due to the direct connection via the open resonator. It may be regarded as the highest level of injection locking that can be arranged and an important concept for the design of a power combining structure.

## 2.7.3 Radiating

### 2.7.3.1 Arrays of Diode Oscillator Patch Antennas

The active patch antenna oscillators reviewed in section 2.4.2 have all been used in planar arrays to create power combined output power as a beam radiated normal to the plane of the array as illustrated in Figure 2-15. Mutual coupling between the elements of the array causes interaction throughout the array of oscillators that leads to synchronisation at a frequency that is within the range of oscillator free running frequencies.

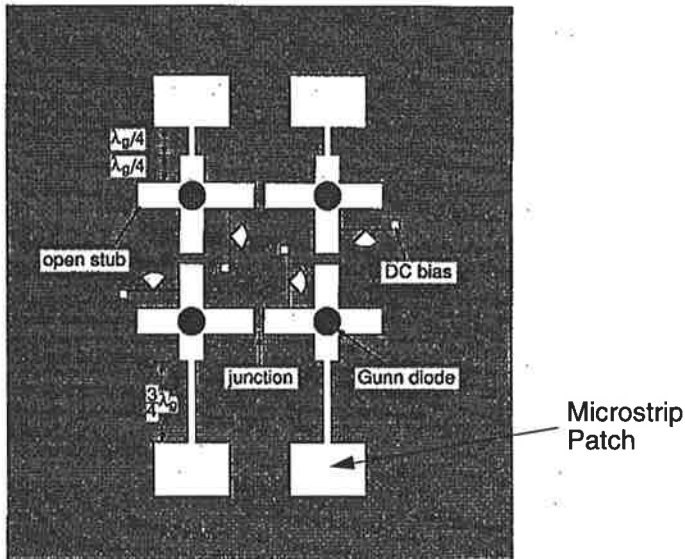


Figure 2-15. Typical array of diode oscillator patch antennas

The oscillators should ideally deliver equal amplitude in-phase outputs by means of the injection locking. However the weaker the level of mutual coupling the closer the free running frequencies must be for synchronisation to occur. A simple means of tuning individual oscillators like that shown in Figure 2-5 appears desirable but is only practical at microwave frequencies where packaged diodes are suitable in this particular example.

Interaction throughout the array to ensure synchronous operation is achieved in a variety of ways including direct connection via microstrip lines [15], mutual coupling via space or surface waves and broadcast of an injection locking signal. The losses in patch

antennas and microstrip lines increase with frequency particularly as the substrate is made thinner to maintain the condition that it be electrically thin ( $t/\lambda_d < 0.05$ , where  $t$  is the physical thickness and  $\lambda_d$  is the wavelength in the dielectric medium). Monolithic fabrication for operation at millimetre wave frequencies does not appear to be practical.

### 2.7.3.2 Diode Grid Oscillators

The essential features of a diode grid oscillator assembly are shown in Figure 2-16. Gunn diodes are mounted on a rectangular metal strip grid formed on a thin dielectric plate [16].

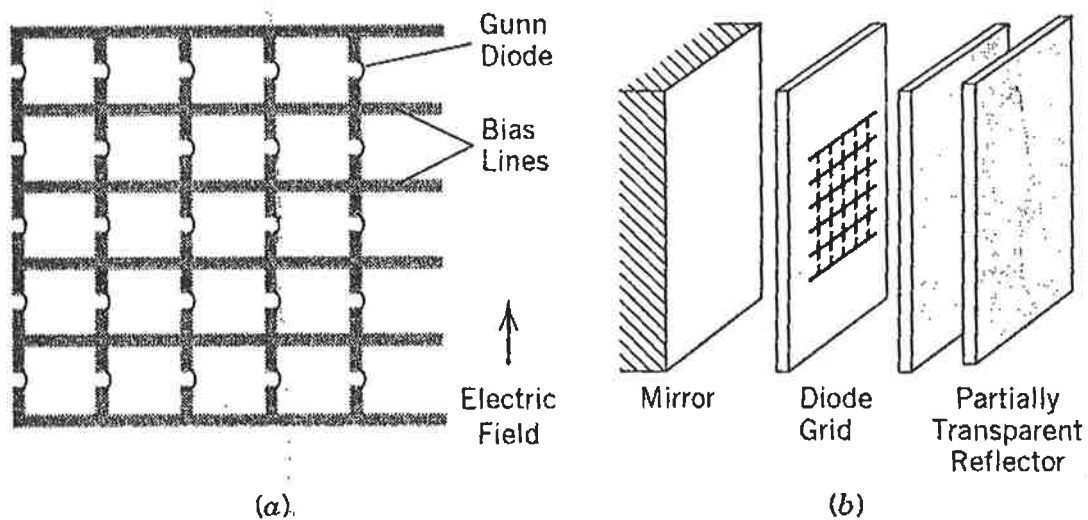


Figure 2-16. Diode grid oscillator: (a) Gunn-diode loaded grid; (b) power combiner configuration.

The diodes are connected across gaps in the vertical grid strips and the horizontal strips are used as DC bias supply lines to the diodes. The flat grid is placed about a quarter of a wavelength in front of a flat perfect reflector and a partial reflector is placed on the other side of the grid as shown in Figure 2-16 (b).

In the desired mode of operation the diodes all oscillate in phase and the RF electric currents that flow in the vertical metal strips connected to the diodes radiate electromagnetic waves polarised parallel to those strips. The wavefront that propagates towards the

mirror is reflected and returns in phase with the wavefront that propagates towards the partial reflector. The grid is commonly regarded as being within a Fabry-Perot cavity which is an open resonator defined with flat reflective boundaries. However the main function of the partial reflector in Figure 2-16 appears to be synchronisation of output power. The quality factor of the parallel plate structure may be too low for it to be regarded as an open resonator. The array of active antennas in this assembly are effectively electric current elements about a quarter wavelength in front of a perfect reflector whereas the array of active patch elements of Section 2.7.3.1 may be regarded as an array of magnetic current elements close to a perfect reflector.

Even though diode grid oscillators are planar structures monolithic fabrication constraints, that will be explained in detail in the review of transistor grid oscillators below, appear to create insoluble design problems at millimetre wave frequencies. Diode arrays are simpler but less efficient than transistor oscillator arrays.

## 2.8 Multiple Transistor Oscillator Mounting Structures

### 2.8.1 *Introduction*

The main advantage sought by using transistors rather than diodes is improved efficiency. Two additional aspects of transistor operation that lead to quite different circuit designs are the three terminal nature of the transistor and the fact that invariably the microwave and millimetre wave circuits that develop negative resistance (or conductance) are narrowband oscillators. Broadband negative resistance is not an equivalent circuit concept in transistor design in the way that it appears when analysing diode assemblies as explained in Section 2.7.2.2 in particular.

### 2.8.2 *Non-Radiating*

Because corporate combiners introduce excessive loss at millimetre-wave frequencies as explained in Section 2.7.2.1 only resonator type power combiners with arrays of transistor oscillators have been studied.

### 2.8.2.1 N Transistor Oscillators Coupled to a Rectangular Cavity Combiner

Microstrip-type MESFET oscillators have been coupled to a rectangular resonant cavity [17] by means of extensions of the oscillator output lines that enter the cavity at positions of maximum electric field intensity as shown in Figure 2-17.

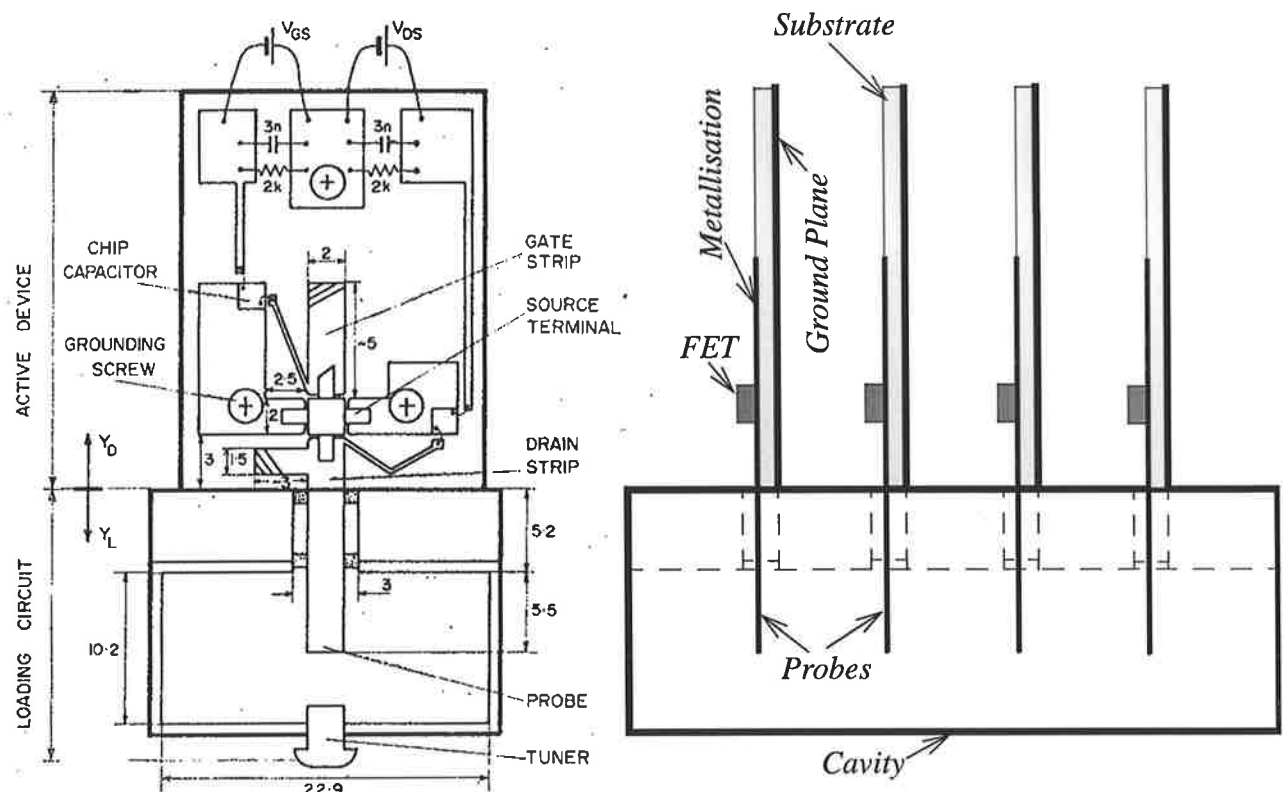
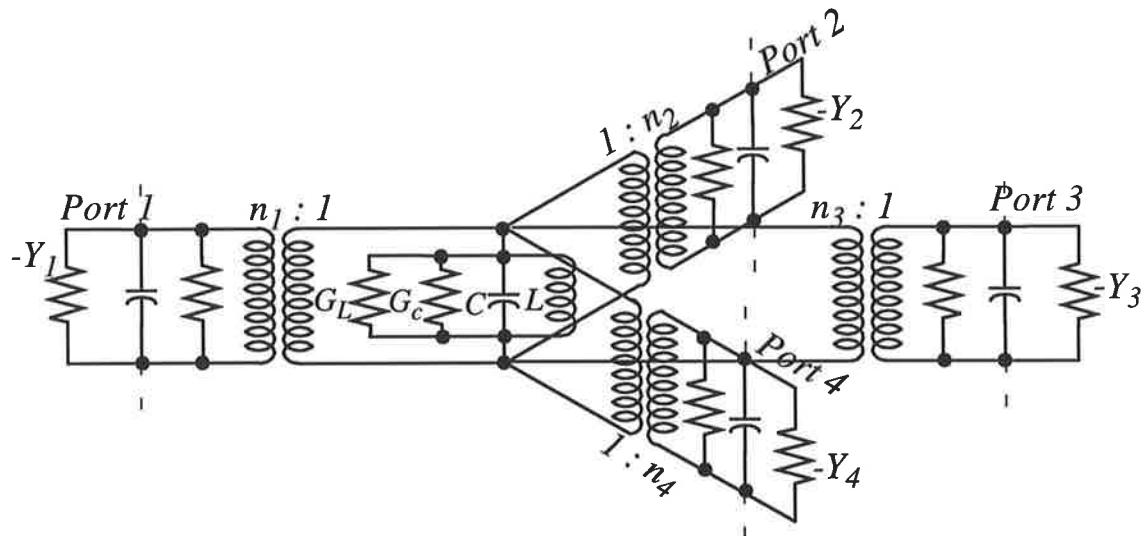


Figure 2-17. A power combiner consisting of 4 microstrip MESFET oscillators coupled to a resonant cavity

The effect of this arrangement in equivalent circuit terms is similar to that of Figure 2-12 and is shown in Figure 2-18. It is evident from the point of view of interaction that the oscillators are all directly connected to each other. Thus a high level of injection locking exists and the maximum load presented to each oscillator will occur at a frequency that is mainly determined by the resonance of the cavity combiner.



*Figure 2-18. Equivalent circuit of 4-transistor oscillators coupled to a rectangular cavity combiner*

The main difference between having  $N$  diodes coupled to a rectangular cavity combiner and having  $N$  transistor oscillators is that the diodes contribute wideband negative resistance whereas the transistor oscillators contribute narrowband negative resistance. The larger the rectangular cavity the smaller the frequency separation between resonances. In the case of narrowband negative resistance the cavity can be larger and accommodate more sources before an unwanted resonance appears within the frequency bandwidth of the negative resistances.

Problems relevant to the design of this kind of resonant cavity combiner that do not appear to have received attention in research are as follows.

- (a) The locking characteristics of transistor oscillators that are effectively connected in parallel to a single load need to be known so that the largest acceptable differences between the free running frequencies within a group of oscillators can be determined.

(b) The relationship between oscillator bandwidth, cavity combiner bandwidth and the number of oscillators needs to be known so that an achievable maximum number of oscillators in a combiner can be determined.

### 2.8.2.2 N Transistor Oscillators within an Open Resonator

This type of structure is non-radiating in the sense that the open resonator is the power combining structure and the output power may be either radiated as a beam from the partially transmitting reflector or focused onto the input aperture of a quasi-optical component or a waveguide. The structure reviewed in Section 2.7.2.4 that has diodes mounted in grooves in the flat mirror reflector of an open resonator has also been tested with MESFETs mounted on a similar grooved type of mirror as shown in Figure 2-19.

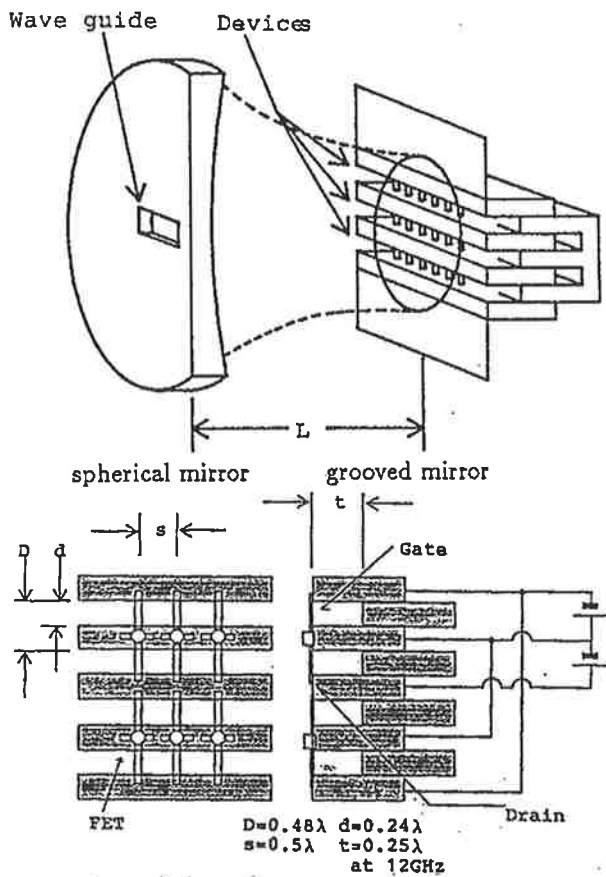


Figure 2-19. FET transistors mounted on a grooved type mirror reflector

Each MESFET oscillates in an external mounting structure formed from the drain and gate leads and the grooves in the mirror. The output frequency of the array depends on the length of the open resonator and can be tuned over a range of frequencies by it. It appears therefore that the open resonator synchronises the otherwise different free running oscillators and delivers the power combined output to a load coupled into it. The groove type structure makes the mutual coupling between rows in the array smaller than the coupling within the rows. It is possible therefore that synchronisation of each row with the next is all that the open resonator has to achieve for power combining to occur.

The particular type of structure incorporated with this open resonator does not conform with the constraints of monolithic fabrication and so is not considered suitable for millimetre wave development.

### ***2.8.3 Radiating***

#### **2.8.3.1 Arrays of Transistor Oscillator Patch Antennas**

The transistor oscillator patch antennas reviewed in Section 2.5.2 have been developed for used either singly or with others in arrays. The elements in an array can be fabricated on a common planar substrate and ground plane in which case synchronisation across the entire array may be achieved either by interconnecting microstrip components or by mutual coupling or a broadcast injection locking signal. One of the most recently adopted arrays is a 26 MESFET spatial power combining oscillator [18] designed to radiate combined power normal to the plane of the array at 10 GHz as shown in Figure 2-20. A common introductory theme of most of the papers on research on this topic are the millimetre wave systems that require sources of power that may only be produced by efficient power combining of power from many solid state sources. Almost without exception design proposals are tested at microwave frequencies using relatively low dielectric constant materials in mounting structures and array assemblies that cannot be scaled for monolithic fabrication on GaAs and millimetre wave frequency operation.

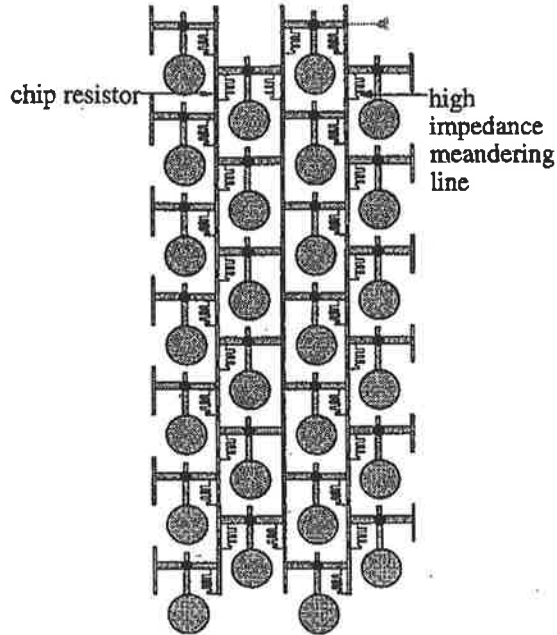


*Figure 2-20. Typical array of transistor oscillator patch antennas*

### 2.8.3.2 Transistor Grid Oscillators

Figure 2-21 illustrates the main features of the transistor grid oscillator [19]. Comparison with Figure 2-16 for the diode grid oscillator reveals similarity of detail with the main difference arising from the need to introduce metal strips that pass underneath the transistors and provide electrical connection for the third electrode for all of the transistors that lie on its path. In the earliest transistor grid oscillators using packaged MESFETs [19] the sources were connected to these strips and the drains and gates were connected to vertical strips that extended to bias lines parallel and either side of the source connection strip. Chip transistors in later assemblies had their gates connected to the strips that passed along the parallel lines of transistors and the bias lines provided supply for the drains and the sources in the transistors [20].

The basis of design is to assume that all transistors oscillate in phase with equal amplitude and that the array is uniform and infinite in extent throughout the plane. The

RF currents that flow in the metal strips that connect the transistor electrodes to the bias lines radiate in phase to either side of the grid plane.

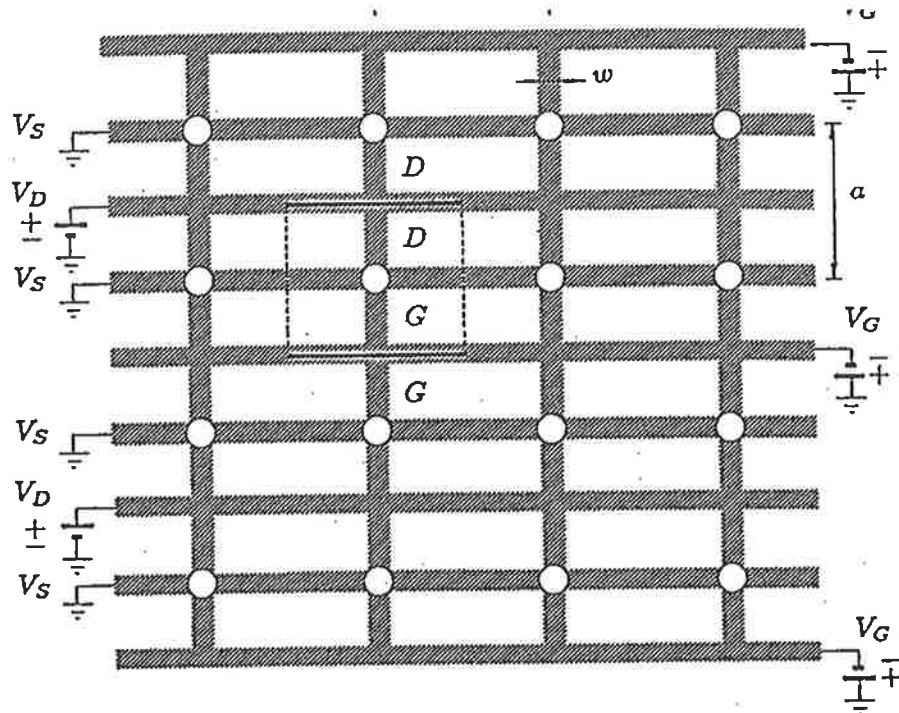


Figure 2-21. Transistor grid oscillator

A perfectly reflecting mirror is placed parallel to the grid plane to one side and a partially reflecting plane is placed parallel to the grid on the other side to act as a matching structure between the plane wave source and unobstructed half space as the load. One unit cell of this uniform, periodic, laterally infinite structure is analysed as a waveguide [19] with its axis normal to the grid plane, perfect electric conducting planes through the bias line positions and perfect magnetic conducting planes half way between the positions of transistors.

The uniform transverse electromagnetic (TEM) waves radiated on either side of the grid plane are the only non-evanescent propagating modes assumed in the analysis that determines the components of an equivalent circuit for the transistor mounting structure. In practice a dielectric wafer is needed as a physical support structure for the grid and the

transistors but it is assumed that only TEM waves propagate normal to the plane faces of this wafer. The wafer is finite rather than infinite in lateral extent but it is assumed that the edges can be terminated in such a way that the assumptions that underlie the analysis are still valid.

The design procedure, based on all of these idealising assumptions, yields dimensions for the metal strips that form the grid such that for specified transistor small signal scattering parameters the unit cells will oscillate at the frequency required in the design. The frequency can be tuned by altering the spacing between the grid and the mirror behind it and the radiated output can be varied by the selection of partially reflecting plate and its position in front of the grid. The radiation pattern beamwidths in the E-plane and the H-plane are related to the rectangular dimensions of the grid and the RF power output and the DC to RF conversion efficiency can be determined by integration of the radiated power pattern.

Uniform amplitude of oscillation across the grid should yield an E-plane radiation pattern that has a main beam with equal amplitude sidelobes tapering down from about -12 dB. Results obtained from transistor grid oscillators at both 5 GHz and 10 GHz exhibit these features and both papers [19, 20] conclude that transistor grid oscillators are suitable for the monolithic integration of possibly “thousands of millimetre-wave devices for large scale power combining”. The mirror and the grid are regarded as forming a Fabry-Perot cavity that effectively synchronises the array of oscillators in the grid and so causes the power combined radiated output.

Results are also presented for a grid designed to oscillate at 17 GHz [20]. The DC to RF conversion efficiency was determined to be 7% compared with 20% for the grid operated at 10 GHz. Also a noticeable feature of the E-plane radiation pattern was a sidelobe level of -5 dB. Subsequent to this, results have been published for a monolithically fabricated transistor grid oscillator [21] that is formed on a GaAs substrate with dielectric constant 12.8. It oscillates at 34.7 GHz and is claimed as the first report of a successful monolithic grid oscillator. The E-plane radiation pattern reproduced in Figure 2-22

clearly shows three beams of approximately equal amplitude. This indicates that radiation from this grid is from two equal amplitude sources along the edges of the wafer that are parallel to the E-plane.

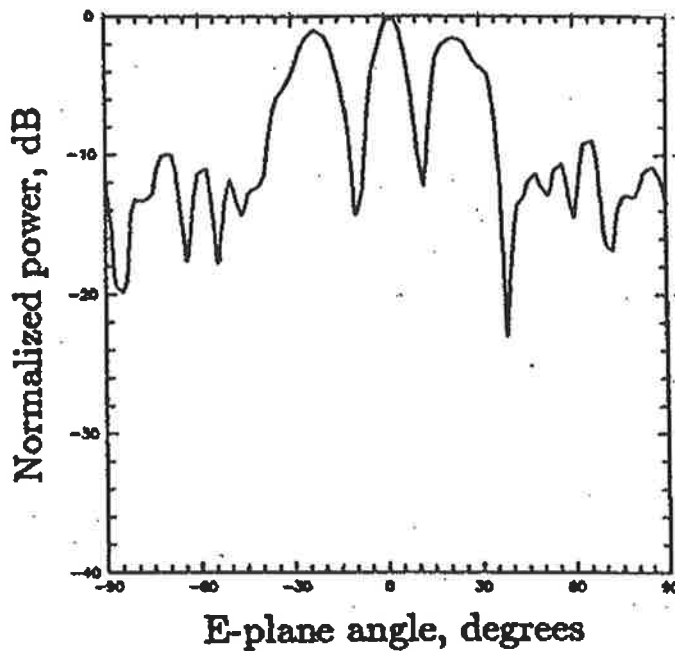


Figure 2-22. E-plane radiation pattern of the 34.7 GHz monolithic grid oscillator

The angular separations between these beams accurately agree with that calculated from the edge-to-edge dimension of the GaAs wafer and the oscillation frequency. It is a simple interference pattern. It is evidence of the presence of a fundamentally different mode of oscillation in this grid, a mode that the design method assumes not to exist, [23].

The dielectric slab that supports the monolithically formed active devices and the metal grid mounting structure is within the Fabry-Perot cavity. In the case of the grid that oscillates at 34.7 GHz the GaAs substrate is 740 microns thick and as a percentage of the wavelength in GaAs is 31 percent. The RF oscillator currents on the surface will radiate most of their power [22] on a primary wave basis into the dielectric as surface waves. These will propagate towards the edges and after partial radiation and partial reflection will create a partial standing wave pattern throughout the GaAs substrate. The oscillators

in the grid are coupled to the standing wave pattern and if the coupling is strong enough then this will be the dominant cause of interaction amongst the oscillators. The reflection at the edges of the substrate may be closer to the maximum value of +1 than the value of 0 that corresponds to complete radiation of the primary incident wave. That being the case there will be a periodic phase change as well as amplitude change throughout the standing wave pattern. If this injection locks the array of oscillators then there will be differences in phase between adjacent elements. The unit cells of the array are about one half wavelength square as measured in the substrate dielectric material. In a standing wave pattern the difference in phase at positions one half wavelength apart has its greatest value and that value approaches 180 degrees as the standing wave ratio approaches infinity. Thus in the extreme case of surface wave injection locking of a transistor grid oscillator array adjacent elements will be reversed in phase, radiation normal to the plane of the array will be minimal and most power will be coupled into the substrate and leak from the edges. In the case of the monolithically fabricated grid that oscillated at 34.7 GHz the mirror of the Fabry-Perot cavity extended beyond the edges of the wafer. This caused the radiation maximum from each edge to be normal to the mirror as in a patch antenna on a large ground plane.

Failure of a transistor grid oscillator due to surface wave injection locking may be avoided by making the substrate electrically thin so that the Fabry-Perot cavity is almost uniformly filled with the same medium as that external to it, usually air or vacuum. For the substrate to be electrically thin, e.g. 5 percent of the wavelength in the dielectric, its physical thickness at 100 GHz would need to be no more than 40 microns. This would be too fragile to sustain the mechanical forces that would arise due to bias line connections and other edge support items for grid assemblies of moderate size. Monolithic integration of “thousands of millimetre-wave devices for large scale power combining” [20] would appear to be quite impractical.

The fundamental concepts that are the basis for grid design are the creation of uniform plane TEM waves using a planar uniform array of identical oscillators embedded on a planar uniform radiating structure. The dielectric slab that is essential for the fabrication

of the active devices and physical support of the array violates the ideal assumptions by introducing the possibility of modes of propagation being excited in directions transverse to the direction of the TEM waves. Practical constraints that become important at millimetre wave frequencies result in a structure that is more likely to operate in a way that the original assumptions regarded as non-existent. This outcome invites study of ways whereby surface waves in thick monolithic millimetre wave integrated circuits might be exploited in the design of power combined arrays of oscillators.

## **2.9 Practical Design Consequences of Surface Waves on Thick Substrates**

Radiation of output power via the edges of an electrically thick substrate that supports a planar array of oscillators may be prevented by placing perfectly reflecting walls against those edges. Complete reflection of the primary waves created by oscillators in the substrate will produce a complete standing wave pattern corresponding to a resonant mode if the excitation wavelength is appropriate for the wafer and circuit dimensions. The conditions that prevail in any unit cell of the overall resonance pattern will be quite different from those assumed in the design of transistor grid oscillators [19] and arrays of transistor patch antennas [18].

In practice high conductivity metal walls can be placed on the edges of the substrate and they will be a good approximation to perfectly reflecting walls that may be assumed in developing a design procedure. The planar oscillator array on the thick substrate would still present a difficult design problem because of a combination of a half-space to one side of the active array and a dielectric slab enclosed by metal walls on the other side.

The electromagnetic field distribution at the plane of the active array needs to be known accurately for the oscillators to be designed accurately. The half-space can be removed by extending the metal walls above the edges of the substrate so that they are joined to a metal plate that is spaced above and parallel to the planar array of oscillators. A uniform gap between a ground plane and the planar array of active devices and circuit

elements replaces the half-space and if the gap is electrically thin quasi-TEM mode fields replace the fields associated with radiation into the half-space.

Thus the practical consequence of using an electrically thick substrate that supports surface waves and has the potential to radiate in an unwanted way is to enclose it within a cavity that has high conductivity walls. The substrate partially fills the cavity so that the surface waves give rise to longitudinal section magnetic (LSM) mode resonances and between metal strips on the substrate surface and a ground plane separated from it by an electrically thin air gap quasi-TEM mode propagation may occur.

Power may be coupled out of the cavity via an aperture in one of the walls in such a way that it either propagates along a single mode waveguide or is radiated into free space. An assembly such as this has the potential to be more versatile than the transistor grid oscillator that is a radiating aperture only.

---

## Chapter 3

# *Design Concepts to Satisfy Practical Constraints*

### **3.1 Introduction**

Critical examination of the existing design methods for the generation of millimetre-wave power using semiconductor diodes and transistors has been given in Chapter 2. It has been a common practice to develop a design prototype at microwave frequencies and once the experiments proved successful, then, it has been assumed that the same method could be applied to millimetre-wave design by simply scaling up the frequency. While most of the power combining methods have been successfully examined at microwave frequencies, only a few of them have been tested as millimetre-wave designs and the practical results in the case of transistor grid oscillators appear to be unsatisfactory [21].

The reason is that by scaling up the frequency to the millimetre-wave spectrum, the fabrication technology should be changed from conventional hybrid MIC to MMIC, in order to reach a cost-effective solution. The review suggests that, while the recent power combining methods are compatible with hybrid MIC techniques, they will not satisfy the practical constraints of monolithic integrated circuit technology. At millimetre-wave fre-

quencies, conventional hybrid MIC fabrication is hardly feasible due to the small circuit dimensions, the device mounting problem and the effect of the device package parasitics. MMIC technology overcomes these hybrid integration problems by fabricating solid-state devices and circuits on a single substrate. Since the device and circuit share the same substrate, there are no bonding or hybrid integration discontinuities, or package parasitics to take into account, resulting in low-cost production. Consequently, MMIC fabrication will be the most attractive technology at millimetre-wave frequencies, and the success of a new method of power combiner design in this spectrum will rely on whether the method satisfies the MMIC fabrication constraints.

## 3.2 MMIC Constraints

Monolithic MICs require substrates on which devices and circuits can be grown through fabrication processes. Among the available materials for monolithic fabrication, gallium arsenide (GaAs) is the preferred microwave substrate with a high dielectric constant (12.8) and low loss. GaAs wafers with sufficient area to accommodate an array of oscillators at 100 GHz need to be at least 200 microns thick to be mechanically strong enough for processing. With a dielectric constant of 12.8 these wafers are almost  $\lambda_d/4$  thick at 100 GHz, where  $\lambda_d$  is the wavelength in the dielectric medium. In this research it is assumed that the substrate thickness is the most critical constraint of MMIC fabrication that should be addressed in the development of a design methodology for millimetre-wave sources and power combiners.

Most of the proposed methods for spatial power combining as reviewed in Chapter 2, involve the use of electrically thin dielectric sheet material as the support structure for the active devices, the radiating elements and the interconnecting metal strips. In order to be electrically thin in the millimetre-wave spectrum, the substrate thickness would be too fragile for current MMIC processing; whereas the minimum substrate thickness of 200 microns would yield an electrically thick substrate that is not compatible with the original assumption, and would lead to erroneous results.

### 3.3 Concepts Leading to a Design Solution

In this chapter the concepts of a new design are developed on the basis of this wafer thickness constraint of MMIC technology, with the aim of producing a new millimetre-wave source that is fully compatible with monolithic technology. These concepts are described in the following sections.

#### 3.3.1 Concept 1: Shielded Inverted Microstrip

Design the oscillator in inverted microstrip so that the GaAs wafer is a superstrate that may be electrically thick. The configuration of wafer and ground plane is shown in Figure 3-1 (b) compared with conventional microstrip in Figure 3-1 (a).

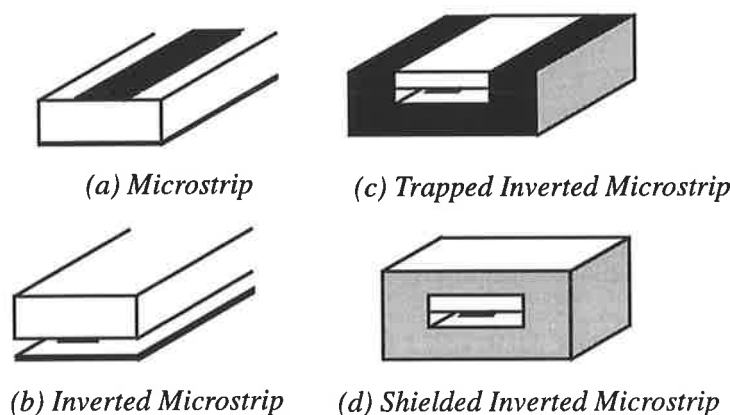


Figure 3-1. Development of shielded inverted microstrip transmission line

The medium between the metal strip and the ground plane may be air or vacuum or a low dielectric constant layer and will have a dominant effect on the effective dielectric constant of the inverted microstrip lines used in the design of the oscillator circuit. The distance between the metal strip and the ground plane may be comparable with the GaAs wafer thickness but still be electrically thin because the effective dielectric constant of that layer may be close to unity compared with 12.8 for GaAs. Shielding the inverted microstrip as shown in Figure 3-1 (d) will reduce the losses for quasi-TEM mode operation.

### 3.3.2 Concept 2: Oscillator on Dielectric Resonator

Use the high dielectric constant wafer as a millimetre-wave resonator and in so doing, design the oscillator circuits so that they are entirely on the surface of that resonator as shown in Figure 3-2.

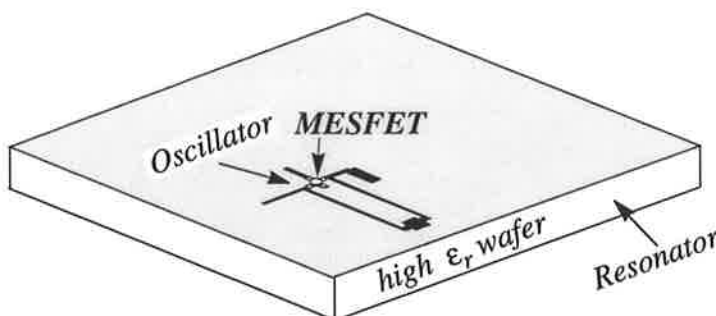


Figure 3-2. GaAs wafer as a rectangular dielectric resonator

### 3.3.3 Concept 3: Partially Filled Cavity Resonator

Shield the superstrate with perfect electric conducting walls as in Figure 3-3, to form a cavity resonator that is partially filled by the superstrate and supports longitudinal section magnetic (LSM) resonant modes. Select the cavity dimensions so that the resonant frequency of the desired LSM mode resonance is the same as the required oscillator frequency.

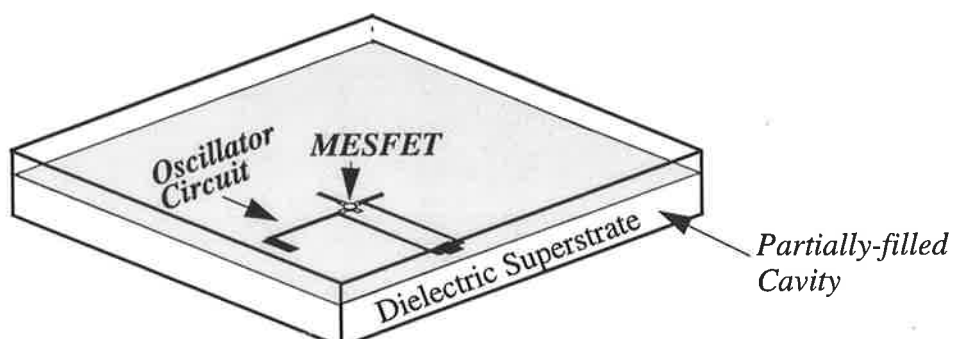


Figure 3-3. Formation of partially-filled cavity from shielded inverted microstrip oscillator

### 3.3.4 Concept 4: Quasi-TEM Mode Circuit Decoupling from LSM Resonator

Position the transistors at zeros in the LSM resonant mode surface electric field and place metal strips from the electrodes transverse to these fields created by the oscillators,

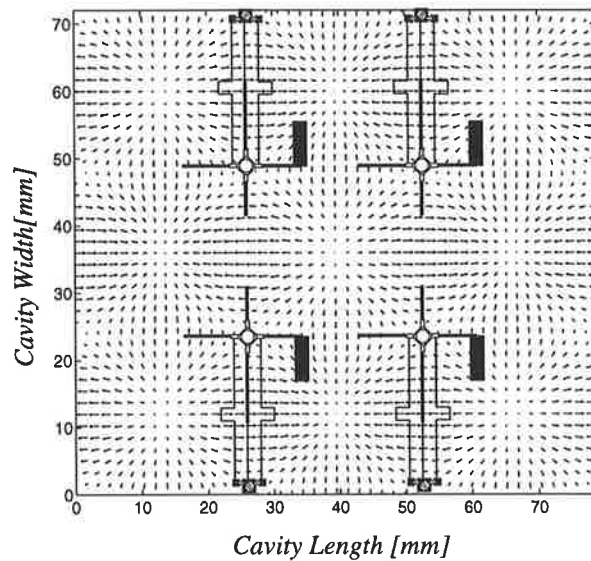
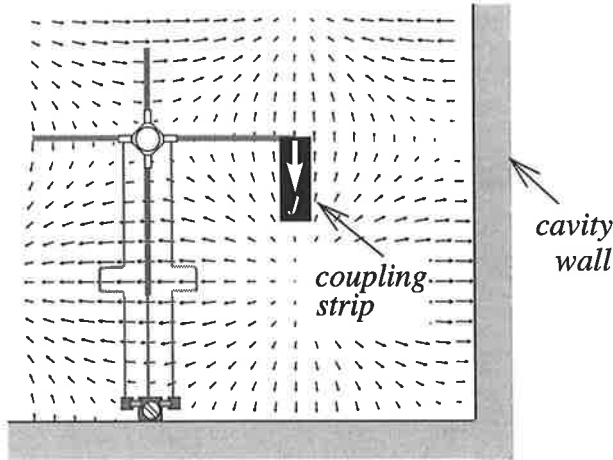


Figure 3-4. Positioning of the transistors at zero surface E-fields

except where the output is coupled from each oscillator quasi-TEM mode to the resonator LSM mode as shown in Figure 3-4.

### 3.3.5 Concept 5: Output Coupling to LSM Mode Resonator

Design the coupling between the oscillator and the LSM mode resonance for maximum power transfer using details of the LSM mode electric field distribution (Figure 3-5) and the electric current on the metal strip coupling probe.



*Figure 3-5. Coupling between the oscillator and partially-filled cavity*

### 3.3.6 Concept 6: Thick Iris Output Coupling to Waveguide

Couple the partially-filled cavity to standard air-filled waveguide via a section of  $\text{LSM}_{10}$  partially-filled waveguide compatible with simple monolithic technology by simply extending part of the wafer to form what is shown as the thick iris in Figure 3-6.

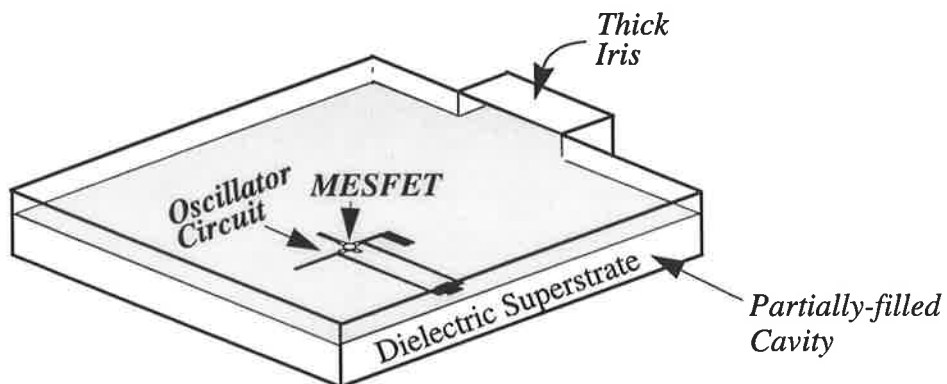


*Figure 3-6. Coupling the partially-filled cavity via a thick iris.*

### 3.3.7 Concept 7: Coupling Factor Adjustment

Follow the section of  $\text{LSM}_{10}$  partially-filled waveguide by a section of reduced height standard air-filled waveguide that has the same cutoff frequency and is connected

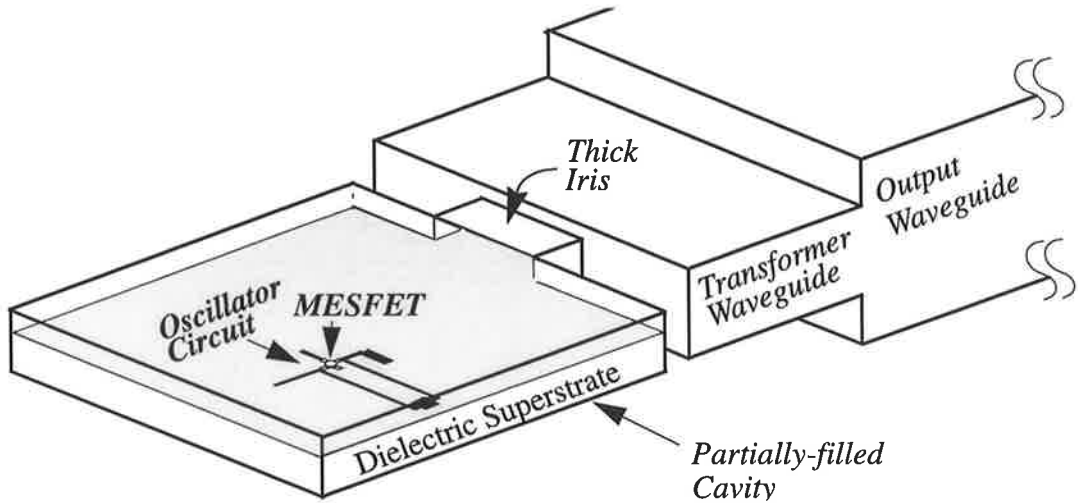


*Figure 3-7. Connection of the iris to the output air-filled waveguide*

in turn to full height air-filled waveguide as shown in Figure 3-7.

### *3.3.8 Concept 8: Oscillator Array Positioned on Dielectric Surface*

Form an array of  $2(N - 1)$  oscillators as shown in Figure 3-8 within a partially-filled cavity that resonates in the  $\text{LSM}_{30N}$  mode by positioning transistors at the  $2(N - 1)$  nulls found in the surface electric field excluding those at the side walls.

### *3.3.9 Concept 9: Cavity Resonator as Synchroniser*

In such an oscillating array the resonance in the  $\text{LSM}_{30N}$  mode couples all of the oscillators to each other forcing them to synchronise with relative phasing so that all of the oscillators couple output power through the resonance of the cavity, and combines it in the load that is connected to the cavity via the coupling structure. This coupling mechanism is shown symbolically by the equivalent circuit in Figure 3-9.

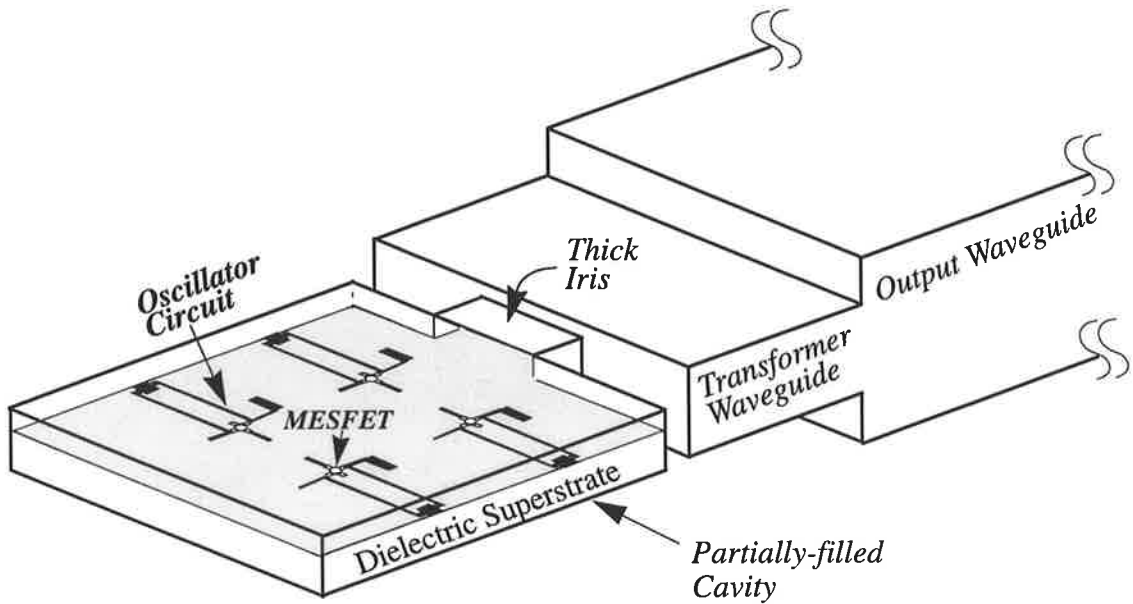


Figure 3-8. Positioning a 4-oscillator array within a partially-filled cavity LSM<sub>303</sub> resonance.

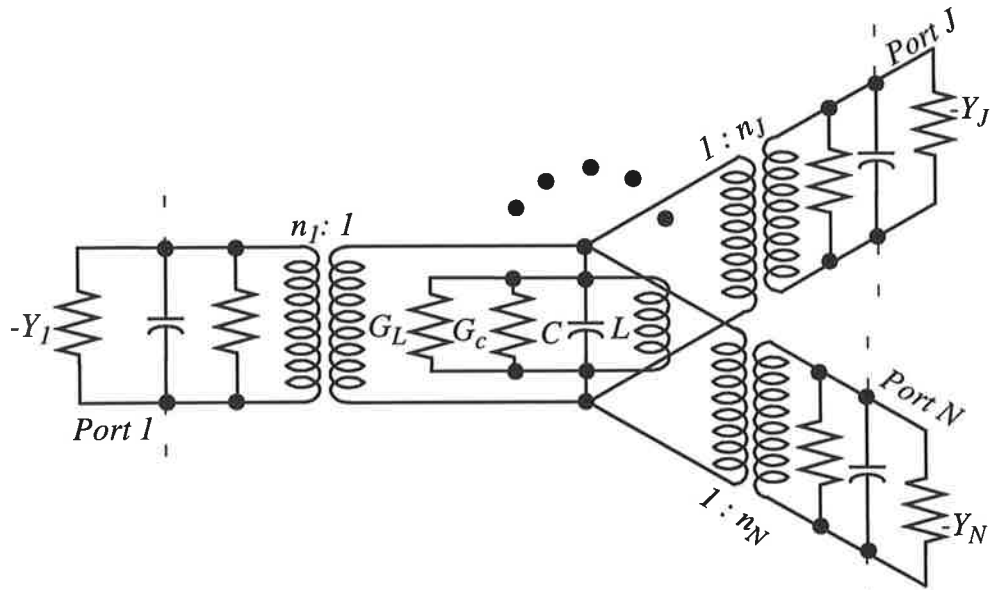


Figure 3-9. An equivalent circuit representation of the power combined oscillators

### 3.3.10 Concept 10: Individual Oscillator Tuning

Individual oscillators can be tuned as shown in Figure 3-10, by altering the gap between the ground plane and the metal strip connected to the gate of the transistor by means of a metal screw.

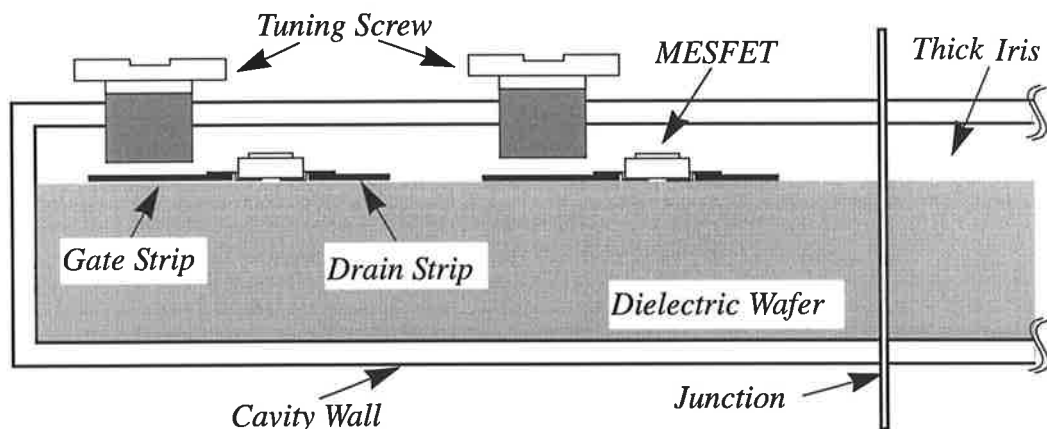


Figure 3-10. Oscillator tuning by adjusting the gap between the gate strip and ground

### 3.3.11 Concept 11: Partially Filled Cavity Resonator Tuning

The resonant frequency of the LSM<sub>30N</sub> partially-filled cavity mode can be tuned by moving an end wall to create an air gap in which the evanescent fields effectively present an inductive reactance at the surface of the dielectric slab as shown in Figure 3-11.

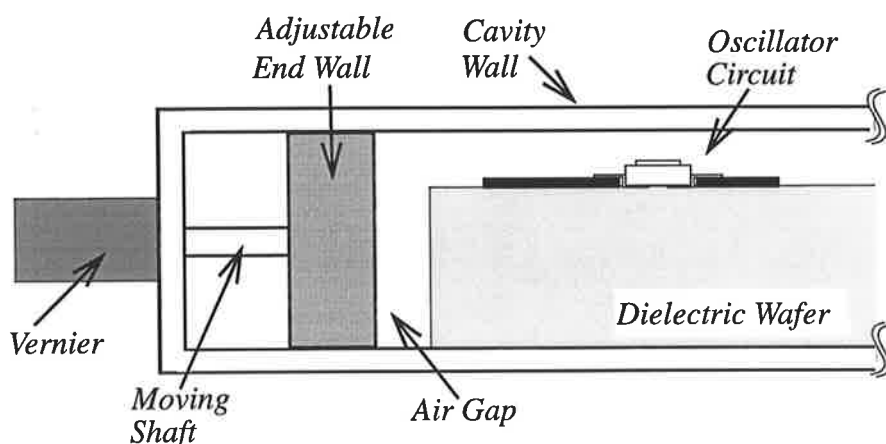


Figure 3-11. Tuning the resonant frequency of the cavity by adjusting the end wall

### 3.3.12 Concept 12: Oscillator Assembly as Active Aperture Antenna

The air-filled waveguide may feed a radiating aperture, in which case the assembly

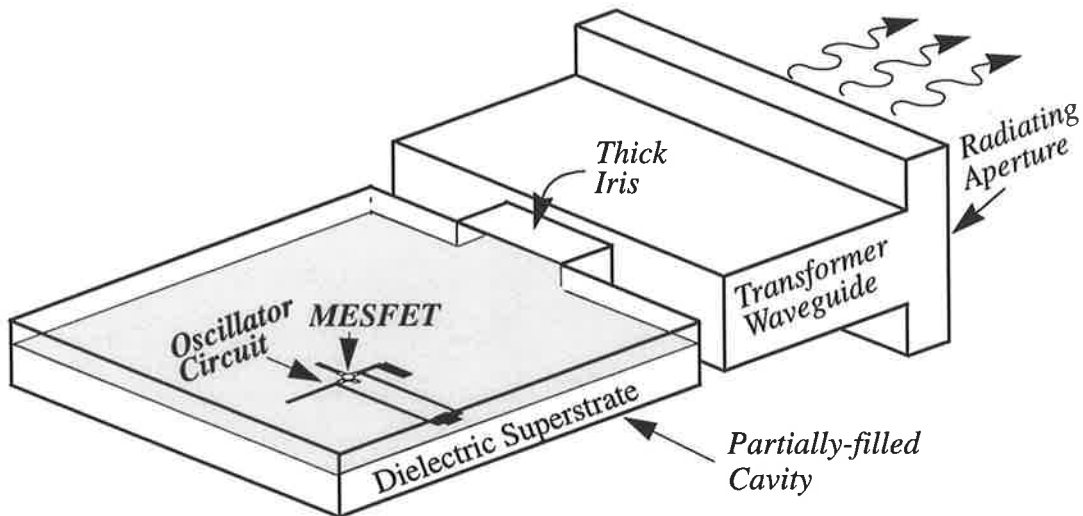


Figure 3-12. Application of the oscillator assembly as an active antenna

may be regarded as an active antenna. This concept is illustrated in Figure 3-12.

### 3.3.13 Concept 13: Oscillator Assembly as Active Array Antenna

Instead of coupling to an air-filled waveguide via one end of the cavity, apertures spaced  $\lambda_g$  apart, may be formed along one side-wall of a  $LSM_{20N}$  resonator to give a linear array of  $(N-1)$  radiators as shown in Figure 3-13.  $\lambda_g$  is the wavelength within the resonator parallel to the row of oscillators.

### 3.3.14 Concept 14: Metal Posts as Transistor Heat Sinks

The electric field at the position of each transistor is zero normal to the dielectric surface and as a result a metal post can be formed through the dielectric slab to form a heat sink for the transistor. A longitudinal cross-section of the oscillator assembly is shown in Figure 3-14, where the metal posts are exactly positioned at the nulls of the E-field distribution and extend to the underneath surface of the transistors.

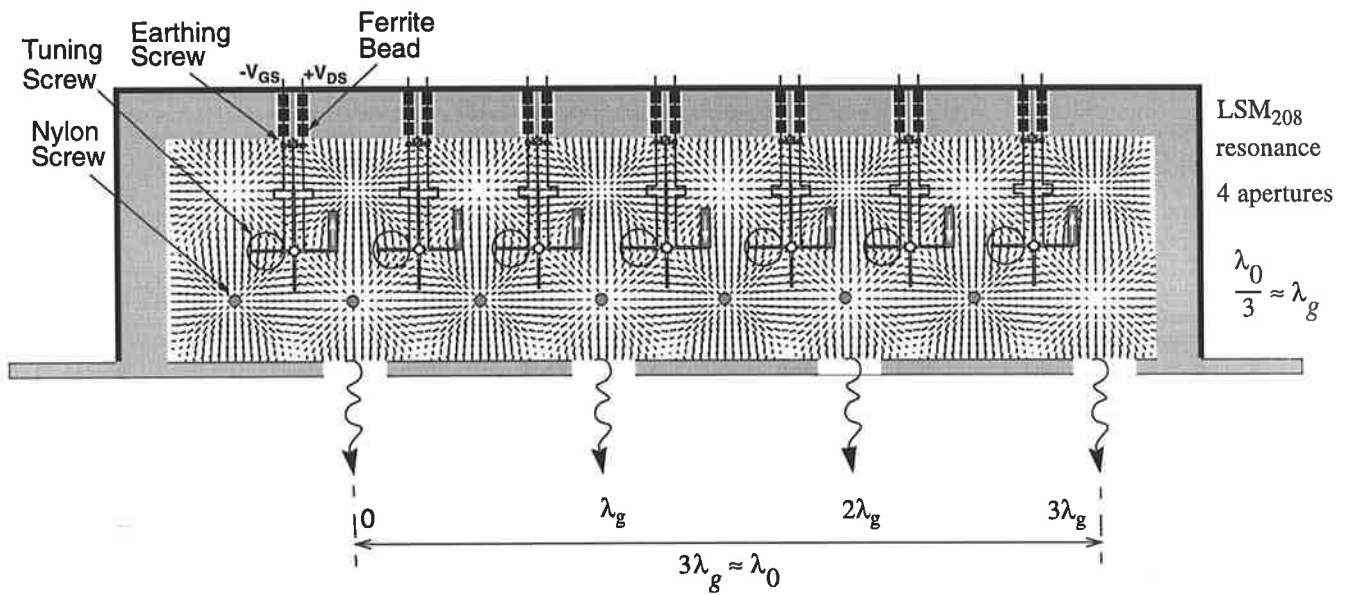


Figure 3-13. An active antenna using apertures in the side-wall of the cavity

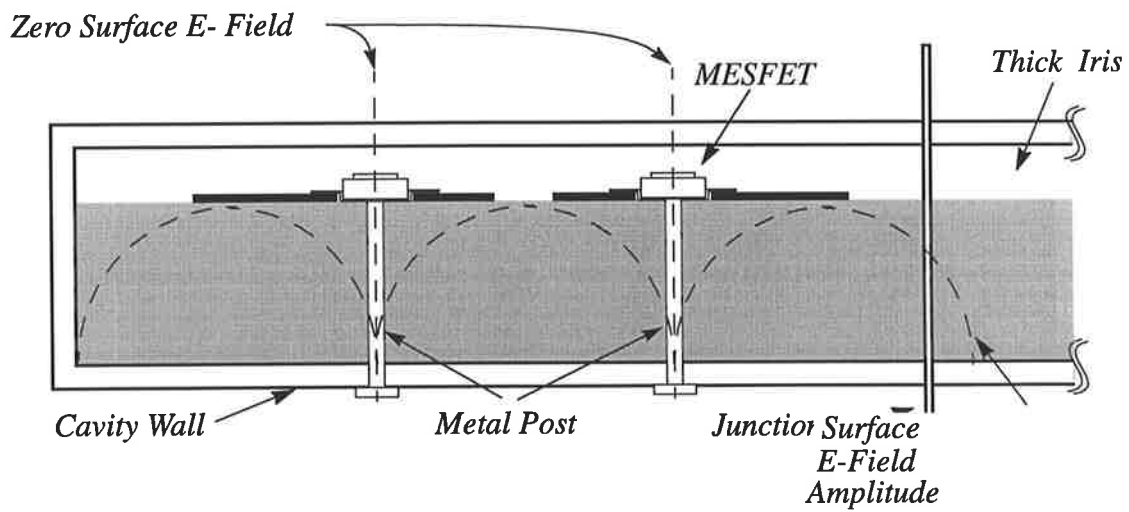


Figure 3-14. Positioning of the metal posts under the transistors for heat sink operation

### 3.3.15 Concept 15: Metal Posts as Unwanted Resonance Suppressors

Metal posts that penetrate the dielectric slab at zero electric field positions also tend to suppress resonances in unwanted modes. Figure 3-15 shows a transverse cross-section of

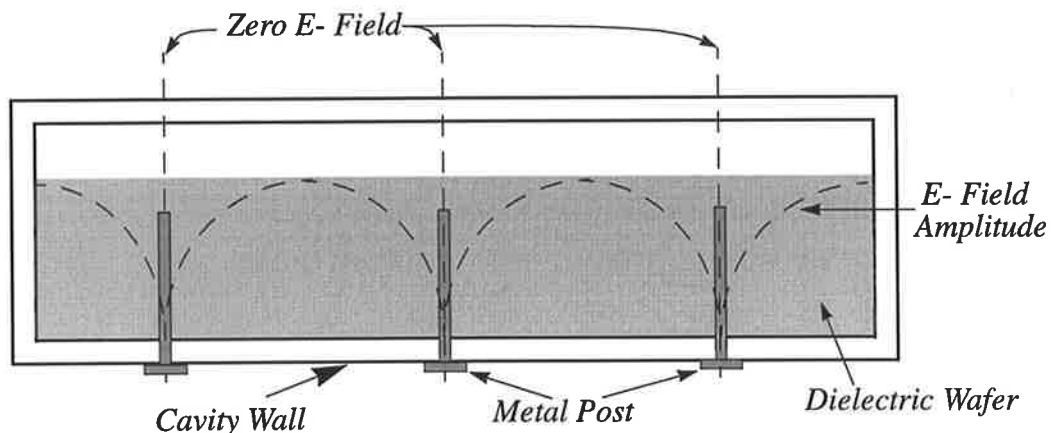


Figure 3-15. Penetration of metal posts at nulls of E- field of the desired mode to suppress the unwanted modes

the partially-field cavity with the total E- field amplitude of the designed mode depicted in the plane through the positions of transistors. Penetration of metal posts at the null electric-field points in the dielectric substrate will not affect the field distribution of the desired resonant mode, but will suppress any unwanted resonant modes that may be excited.

### 3.3.16 Concept 16: Potential for Class C Operation of Oscillators

The concept of coupling the output from the drain of the MESFET oscillator into the LSM mode resonance of the partially-filled cavity resonator, set down as concept 5, creates a circuit like that shown schematically in Figure 2-9 on page 13, in which the concept of high frequency class C operation may be realised.

### 3.3.17 Concept 17: Metal Strip Output Coupling to Coaxial Line

Coaxial line output instead of rectangular cross-section waveguide output appears possible by extending the inner conductor of the coaxial line in the form of a metal strip probe like that described as concept 5.

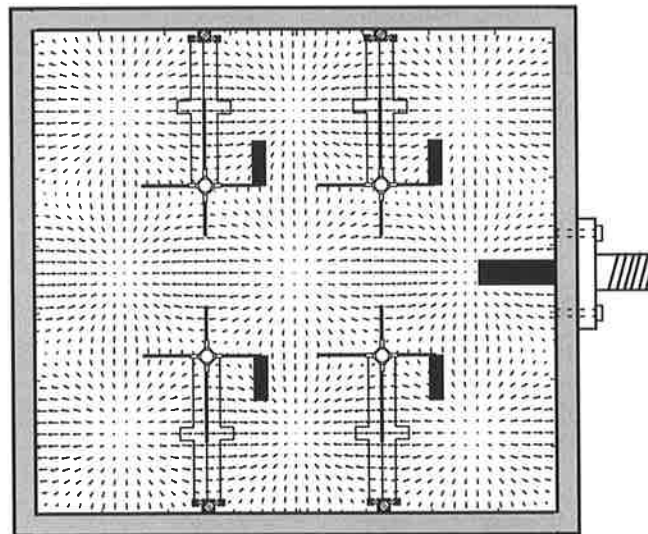
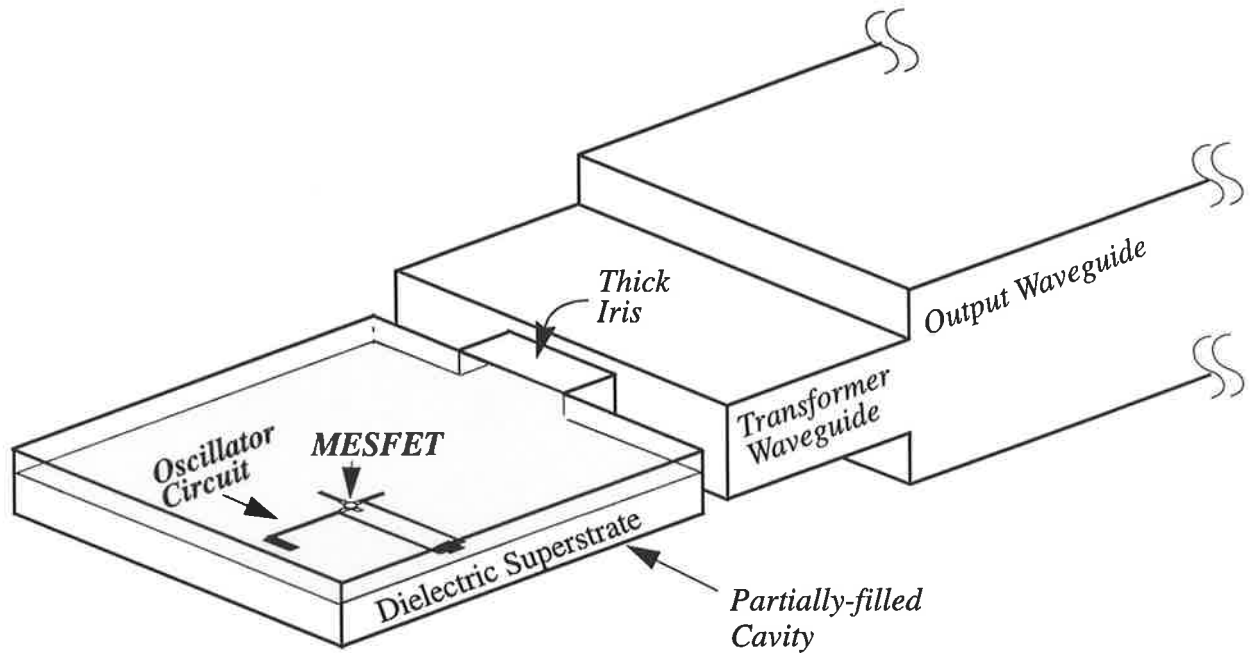


Figure 3-16. Coaxial line output coupling structure

## 3.4 Oscillator Design for MMIC Development at Millimetre Wavelengths

An overall design that combines basic concepts set out in Section 3.3 is shown in Figure 3-17. The main parts forming this assembly are as follows.

- (i) The microstrip MESFET oscillator is formed on the surface of a GaAs wafer that may be as thick as three eighths of the operating wavelength as measured in the dielectric substrate.



*Figure 3-17. New oscillator design compatible with monolithic fabrication at millimetre-waves*

- (ii) The GaAs wafer is placed within a metal-walled cavity resonator of rectangular shape so that it partially fills the cavity with a uniform gap between the surface of the wafer where the microstrip circuit is formed and the top wall of the cavity.
- (iii) An iris that is compatible with monolithic fabrication constraints connects the cavity to a transformer section of air-filled waveguide.
- (iv) The transformer waveguide is a section of air-filled waveguide with adjustable height that introduces a different characteristic impedance. The length of this section is approximately  $\lambda_g/4$ , at the operating frequency. Adjustment of the coupling between the cavity and the output waveguide is easily obtained with the aid of this transformer waveguide.
- (v) Output is to either a standard air filled rectangular waveguide or an aperture antenna fed by such a waveguide.

Several of the concepts set down in Section 3.3 have formed part of the oscillator designs reviewed in Chapter 2 while others appear to be new. The combination of concepts in the assem-

bly of Figure 3-17 makes it quite different from any previously published microwave or millimetre wave power combined oscillator. The new concepts introduce new design problems that do not appear to have been addressed in any previously published work. Solution to these problems are presented in Chapters 4, 5 and 6. Not all of the concepts may be incorporated in a MMIC oscillator array for millimetre wave operation. Concepts such as numbers 10 and 15 are easily built into microwave test structures where the physical dimensions are large enough and packaged transistors with differing parameters may make it necessary that the circuits be tuned. However monolithic millimetre wave circuits may be too small for such mechanical attachments to be practical. In that case the test data on physically large lower frequency assemblies may be used to indicate how tight the tolerances on MMICs would need to be for operation to occur within frequency specifications.

### 3.5 Design Procedure

The mounting structure shown in Figure 3-17 may be regarded as a cascade of components that need to be accurately designed if the transistors are to be presented with impedances (or admittances) that give optimum operation with regard to specified power and frequency quantities and qualities. A design procedure is required that is applicable to any transistor that is deemed suitable for operation in the planar geometry of Figure 3-17.

In order to test the validity and accuracy of the design procedure that has been developed a packaged transistor has been selected for use in this research. Resource limitations have prevented access to monolithic fabrication and testing at millimetre wave frequencies. Inexpensive packaged MESFETs soldered onto metal strip type circuits on the surface of dielectric slabs that have a dielectric constant, 10.6, as close to that of GaAs or InP as can be readily obtained, are the items that have been used in the partially filled cavity. As a consequence of these practical limitations the major source of error in comparing design with test results is identified as the difference between the actual operating parameters of each transistor used and the S-parameters specified by the manufacturer. The lat-

ter have been used in design even though under oscillation conditions non-linear large signal parameters will apply. The mounting structure is a passive linear assembly and the test results that validate its overall design pertain to oscillation frequency and power output of assemblies involving one or more transistors. Optimisation of power output and efficiency of various size arrays would require detailed knowledge of characteristics of a relatively uniform batch of transistors. This information would be needed in the design of prototype MMIC oscillators using the structure of Figure 3-17 and the procedure presented in this thesis. The solution of all of the design problems have been combined to form the following design procedure.

### ***3.5.1 Stage I: Selection of Transistor Oscillator Circuit Type and Critical Positioning of Elements***

The partially-filled cavity resonator is tuned to resonate at the desired operating frequency of the transistor oscillator. At this resonant frequency an electric field intensity distribution will exist on the surface of the wafer where the transistor oscillator microstrip circuit is formed and the detail of that distribution governs the type of transistor oscillator circuit that should be chosen as well as the positioning of all of the parts and connecting metal strips in the circuit as shown in Figure 3-18. The transistor is positioned at one of the null points of the field distribution. Except for the coupling probe all microstrip lines in Figure 3-18 are normal to the field distribution and their couplings to the resonator are negligible. However the coupling probe is parallel to a component of the field lines and therefore it is coupled to the cavity. The type of circuit is one that has series feedback by means of a microstrip line in series with the transistor source electrode.

This is a crucial part of the design. The positioning of the transistor and the microstrips must be accurately determined with respect to the surface electric field distribution so that only the desired component is significantly coupled to the cavity whereas the remaining parts are left effectively uncoupled. This method avoids complication that would arise due to the unwanted interaction between the cavity and microstrip components. As an important consequence of this critical positioning it will be possible to

design the microstrip oscillator using the conventional S-parameter technique without considering the effect of the resonant cavity fields. Only the impedance of the coupling probe is required as an equivalent load for the microstrip oscillator. Such impedance will be calculated using Harrington's variational theory of cavity probes [24, pp. 434-436].

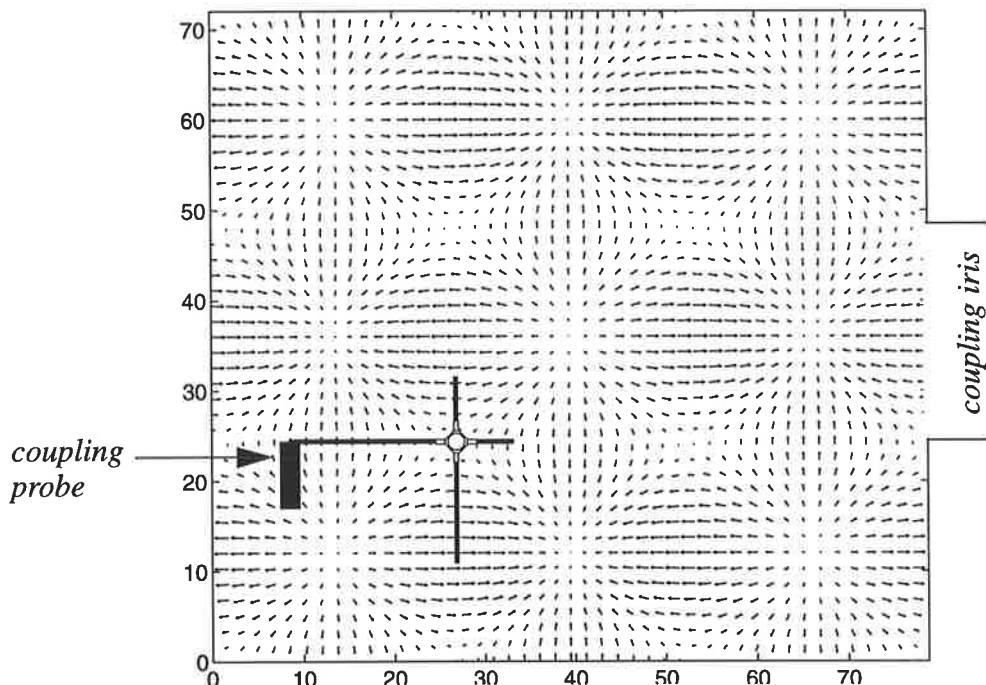


*Figure 3-18. Positioning of oscillator circuit with respect to the surface electric field distribution*

### 3.5.2 Stage - II: Separation of Parts

The design methodology for the overall assembly of Figure 3-17 is a combination of numerous analytical and numerical techniques applied to various parts of the cascade of components. Therefore it is important to identify and analyse the different parts of the oscillator assembly and develop a suitable design method for each part. Such individual methods should be used in a correct sequence as will be specified by a general procedure.

Using the above critical positioning one can separate the microstrip oscillator circuit from the cavity without affecting the overall function. Nonetheless the coupling probe will be an integrated part of the cavity, in the form of an introduced current source. Also

the waveguide coupling structure may be separated from the cavity and replaced by an equivalent aperture impedance. These are all illustrated in Figure 3-19. Each part numbered (1) to (3) will be described briefly although the detailed analyses will be given later on.

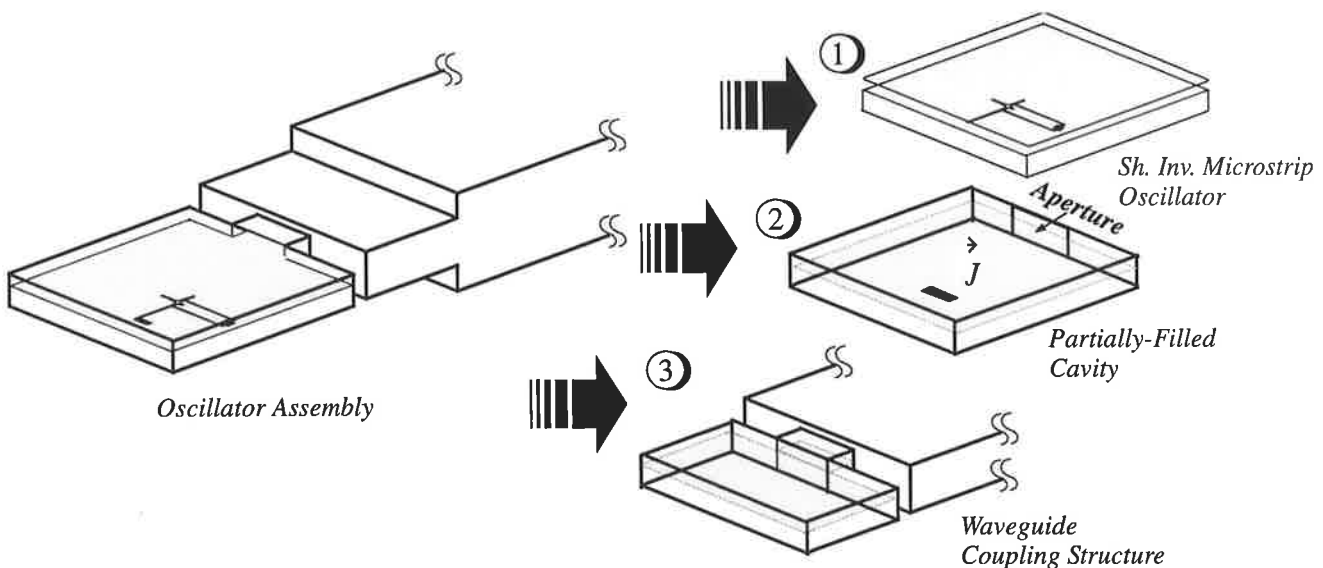


Figure 3-19. Decomposition of the oscillator assembly to its key parts will simplify the design

- (i) The shielded inverted microstrip oscillator circuit is designed on a GaAs wafer that is shielded by a top plate and metal side walls. The substrate thickness is about a quarter to three eighth of the wavelength in the dielectric medium. The air gap is small (typically less than half of the dielectric thickness) in the case of hybrid fabrication for microwave testing and provides adequate clearance for accommodating the circuit elements such as transistors, chip capacitors, microstrips, etc. on the substrate surface. In the design of the shielded inverted microstrip circuit elements practically the side walls may be disregarded if the strips are relatively narrow and distant from the substrate edges. A simple perturbation based on image theory is used to modify the characteristics of those strips that are close to the side walls [25, pp. 73 to 75]. Such a transmission medium as *shielded inverted microstrip line* is classified as an *inhomogeneous asymmetric stripline*.

(ii)The partially-filled cavity has a rectangular shape and encloses the GaAs wafer. It includes the coupling probe, that is simply an accurately positioned metal strip that is joined to the output line of the microstrip oscillator. An aperture in the transverse wall permits coupling of power to the output waveguide. To simplify the analysis the coupling structure is replaced by its equivalent aperture impedance for each propagating mode. As the oscillation frequency is dominated by the resonant frequency of the required cavity mode, full wave analysis of the cavity resonator is very important in the design of the oscillator circuit.

(iii)The coupling structure is the part of the assembly that can be rigorously analysed using the *Mode-Matching Technique* which is a standard method for treating waveguide discontinuities. The structure comprises three different junctions that are connected in cascade. The first junction between the cavity and the thick iris is a partially-filled to partially-filled waveguide discontinuity. The second junction between the thick iris and the air-filled transformer waveguide is a partially filled to air filled waveguide junction. Due to the double step nature of this junction higher order waveguide modes should be taken into account and as a consequence the convergence of mode-matching is relatively slow. The third junction is a simple step in the height of air-filled waveguide. The overall S-matrix of the coupling structure is calculated by cascading the generalised S-matrices of the junctions. The reflection coefficients of the cavity aperture for all possible propagating modes inside the cavity are extracted from the overall S-matrix. An exact knowledge of the aperture reflection coefficient in a particular propagating mode is extremely important to determine the following:

- (i) *the shift of resonant frequency of the cavity with respect to its eigenmode value,*
- (ii) *the influence of the aperture on the cavity field distribution which in turn will affect the impedance of the coupling probe or the load impedance of the microstrip oscillator, and*
- (iii) *the coupling from the cavity to the output waveguide which determines the loaded quality factor of the cavity.*

A detailed design analysis for each part of the oscillator assembly is set out in the following chapters.

---

## Chapter 4

# *Design Methods*

## *Part I: Oscillator Circuit*

### **4.1 Selection of The Type of Transistor Circuit**

As explained in Section 3.5.1 and illustrated in Figure 3-18 a series feedback type microstrip circuit with metal strips connected to all three electrodes and orientated with right angles between adjacent strips is required so that the oscillator functions entirely by means of the quasi-TEM mode in shielded inverted microstrip. The partially filled cavity LSM mode is only connected to the oscillator as a load and hence the well established S-parameter design method can be used to determine the dimensions of the metal strip circuit elements without the complications of contributions to feedback via the LSM mode resonance.

### **4.2 S-Parameter Design of Transistor Oscillator**

Oscillator design is inherently a problem in which there is no external driving source. This adds complexity to the design because the frequency of the oscillator is a specification that the circuit design must satisfy. The development of a high performance source

with emphasis on high efficiency and output power depends on a more comprehensive design approach in which the nonlinear effects are taken into account. As explained in Section 3.5 this research is focused on the new type of power combining mounting structure and the simpler S-parameter approach to the active part of the oscillator design suffices for validation testing of the mount design.

#### 4.2.1 Small Signal Design

Classical design of microwave solid-state oscillators using the negative-resistance approach has been commonly used as a reliable method for guaranteeing that oscillations will begin at the desired frequency [26]. It is based on the negative-resistance model in which the oscillator is regarded as a one port impedance with negative resistance. The model consists of device impedance  $Z_d(I_0, \omega)$  and load  $Z_L(\omega)$  as shown in Figure 4-1 with  $V(t)$  representing noise or a turn-on transient voltage that starts up oscillations [27, pp. 449-469].

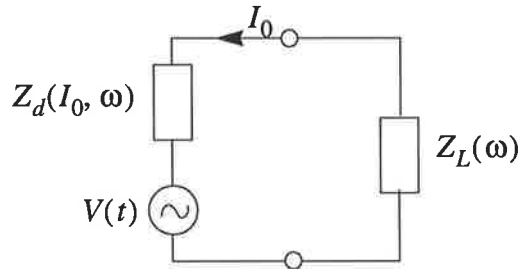


Figure 4-1. Negative-resistance model of oscillator

$I_0$  is the device current at the fundamental frequency of oscillation. For small signal oscillation  $Z_d$  is a linear function of  $\omega$  and independent of  $I_0$ . As the oscillation amplitude grows,  $Z_d$  gradually changes with  $I_0$  and is no longer a linear function of  $\omega$ . The device must have negative resistance, i.e.,

$$\Re e\{Z_d\} < 0 \quad (1)$$

Usually such negative resistance decreases with increasing oscillation amplitude. To start up oscillations the following conditions must be satisfied,

$$\Im m\{Z_d\} = -\Im m\{Z_L\} \quad (2)$$

$$\Re e\{Z_d\} + \Re e\{Z_L\} < 0 \quad (3)$$

$Z_d$  in equations (2) and (3) is calculated from small-signal S-parameters. From (2) the net circuit reactance is zero. Also from (3) overall loop resistance is negative which causes the oscillation amplitude to increase. This will reduce  $|\Re e\{Z_d\}|$  until the loop resistance vanishes giving steady state oscillation conditions represented by,

$$Z_d(I_{ss}, \omega_{ss}) = -Z_L(\omega_{ss}) \quad (4)$$

where  $\omega_{ss}$  and  $I_{ss}$  are steady-state oscillation frequency and current. Equations (2) and (3) establish the small-signal design and guarantee that oscillations will start at the desired frequency. However the steady-state frequency is determined from equation (4).

#### 4.2.2 Derivation of $Z_d$

$Z_d$  is commonly taken to be the output impedance of the transistor but it may be defined at the input port of the device. A small-signal model of a FET oscillator is shown in Figure 4-2.

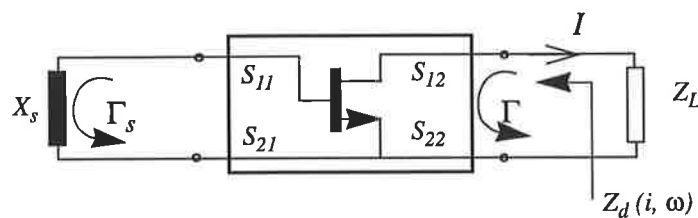


Figure 4-2. Small-signal model for FET oscillator

$Z_d$  is easily determined from network theory as,

$$Z_d = \frac{(1 + \Gamma)}{(1 - \Gamma)} Z_0 \quad \text{with } Z_0 = 50 \Omega \quad (5)$$

and in Figure 4-2 where  $\Gamma = S_{22} - \frac{S_{12}S_{21}}{S_{11} + \Gamma_s}$  (6)

and  $\Gamma_s = \frac{X_s - Z_0}{X_s + Z_0}$  (7)

If  $|\Gamma| > 1$ , the device is unstable and  $\Re e\{Z_d\}$  is negative. Equations (5) to (7), show the effect of gate reactance on the device impedance and hence it follows that both (2) and (3) depend on  $X_s$ . To satisfy equation (3)  $X_s$  should be selected from the unstable region on the Smith chart which is specified by drawing the device source stability circle at the oscillation frequency [28, ch. 12]. The exact value of  $X_s$  will be determined from (2).

#### 4.2.3 Series Feedback

Generally the level of negative resistance depends on the device stability at the operating frequency and in a detailed sense the exact value is affected by the gate reactance. Usually microwave transistors have stable performance in the frequency bands up to 6 GHz. Consequently the negative resistance may not be high enough to yield a good design in this frequency range. One method of enhancing the instability is to connect a suitable reactance in series with the common terminal (i.e. emitter or source) of the device so that the overall S-parameters will be modified resulting in a higher negative resistance at the frequency of interest [29].

### 4.3 An Oscillator Design Automation Program

The clarity and reliability of classical microwave S-parameter design procedures have been exploited in a new simulation program which has been developed for the design of microstrip amplifier and oscillator circuits [30].<sup>\*</sup> This mini software is equipped

---

\* Reproduced as Appendix G

with graphical tools that enable the designer to, (a) visualise the device stability criteria and the design constraints on an automated Smith chart, (b) extract the load and source impedances of his own choice from the Smith chart as the best starting point for the optimisation routine and, (c) check the result by monitoring the optimisation trace. The program is interactive, microstrip-oriented and well suited for educational purposes. The program has been exploited for numerous undergraduate projects and typical amplifier and oscillator circuits have been built based on this program using NE-72084 NEC and ATF-13036 Hewlett-Packard GaAs FET transistors and their bias and small signal specifications given in Appendix H. Test results have shown excellent agreement with this theoretical design procedure. The design automation has been developed on a UNIX<sup>1</sup> workstation, using the MATLAB<sup>2</sup> mathematical software [31]. The primary aim has been to develop an interactive and user-friendly program for the design of MESFET amplifiers and oscillators. Figure 4-3 shows the block diagram of this program.

The major functions that it performs in producing an optimised oscillator design are:

1. **Design information:** such as the MESFET configuration i.e. common-source or common-gate etc., oscillation frequency, and the optional value of series feedback are entered by the designer. The modified S-parameters are calculated and the new stability circles are depicted on the automated Smith chart.
2. **Initialisation:** initial source reactance ( $X_s$ ) and load impedance ( $Z_L$ ) are graphically selected by the designer from the unstable areas of the Smith chart. These areas are defined by the device stability circles. The analytical formulae are available in the literature [28], [32] and [33]. Once the initial  $X_s$  and  $Z_L$  are determined, they are used in a specific program to synthesise appropriate matching sections. For this purpose the actual initial values for the length and characteristic impedance  $Z_C$  of each synthesised matching section would be used as initial values for optimisation.

---

1. UNIX is a trademark of Bell Laboratories and denotes a standard operating system for use on computer networks.  
 2. MATLAB is a trademark of Math Work, Inc.

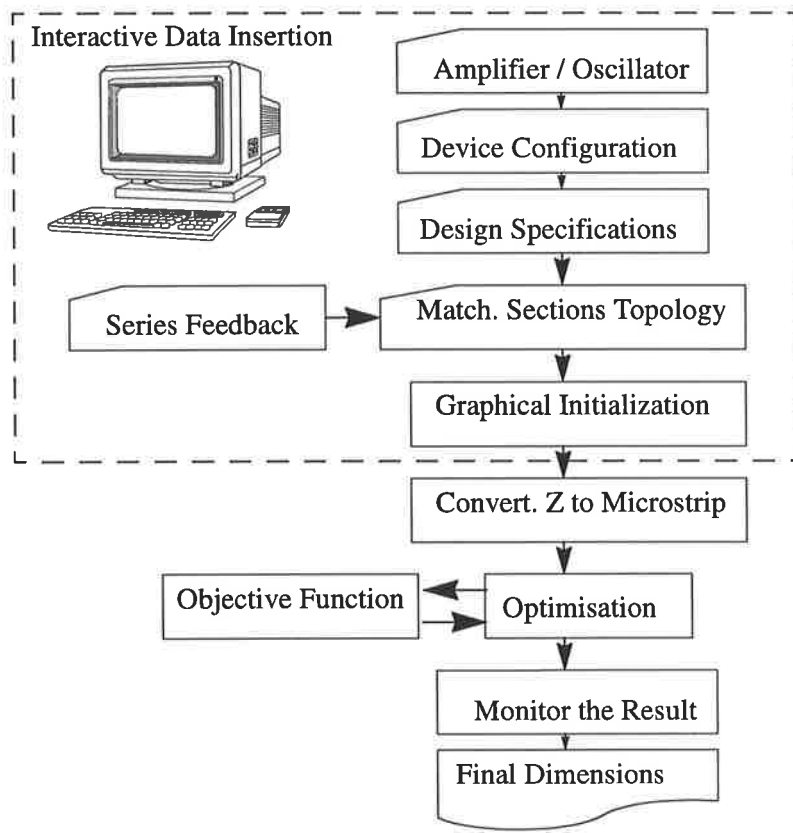


*Figure 4-3. Block diagram of the design automation. The interactive sections are shown in the dashed-line box.*

3. **Optimisation:** various routines may be used in the program such as: direct search, gradient-descent and random techniques. Both direct search<sup>1</sup> and gradient-descent<sup>2</sup> routines have been used in this software [34]-[35]. Each technique has its own advantage. The gradient techniques appear to be better for finding the global minimum, however they appear to be much slower than direct search techniques, particularly in the case of microstrip oriented design with non-trivial objective functions. As mentioned above, the optimisation variables are the transmission-line parameters of the circuit matching sections, namely: length and  $Z_C$ . Therefore the total number of variables depends on the topological complexity of the matching sections. When the optimisation process

1. Hooke and Jeeves optimisation algorithm.

2. Fletcher and Powell optimisation technique.

comes to an end, the final impedances appear on the Smith chart and the physical dimensions of microstrip sections are also displayed on the screen. Typical design automation for a 5 GHz FET oscillator which has been implemented by this program is shown in Figures 4-4 and 4-5.

DESIGN OF MICROWAVE MESFET TRANSISTOR OSCILLATOR  
USING  
ATF -13036 FET TRANSISTOR

```
ENTER Oscillator frequency in GHz = 5
SELECT common-source/ common-gate [cs/ cg] : cs
Series Feedback ? [ y/ n]: y
Length of feedback strip in degree = 135
Width of feedback strip in millimetre = 1
Graph - A is displayed
Do you want to initialize from origin ? [y/ n]: n
Starting from the last minimum point ? [y/ n]: n
ENTER the normalised initial source reactance [ j*Xs ] : j
ENTER the normalised initial load resistance: [ RL ] : 1

<< THE Hooke & Jeeves Optimization ROUTINE >>
Minimum error function is Fmin = 0.0047
Number of function evaluations: 400
Zdevice = -8.7928 - 1.1279i      Zload = 2.4816 + 1.1279i
Graph - B is displayed
<<< Optimization Result for Microstrip MESFET Oscillator >>>
oscillation frequency = 5 GHz
length of gate strip = 11.93 mm
width of gate strip = 1 mm
length of drain strip = 6.664 mm
width of drain strip = 1 mm
Type of Series Feedback : Short Circuit Stub
length of source strip = 13.39 mm
width of gate strip = 1 mm
```

Figure 4-4. Program messages and the designer's selections followed by optimisation results.

The detail is typical of that for microwave oscillators used in testing the validity of the overall design.

In Figure 4-4 following the program messages, the design specifications are inserted. The initial values are selected from the unstable area of the feedback MESFET as shown in graph - A of Figure 4-5.

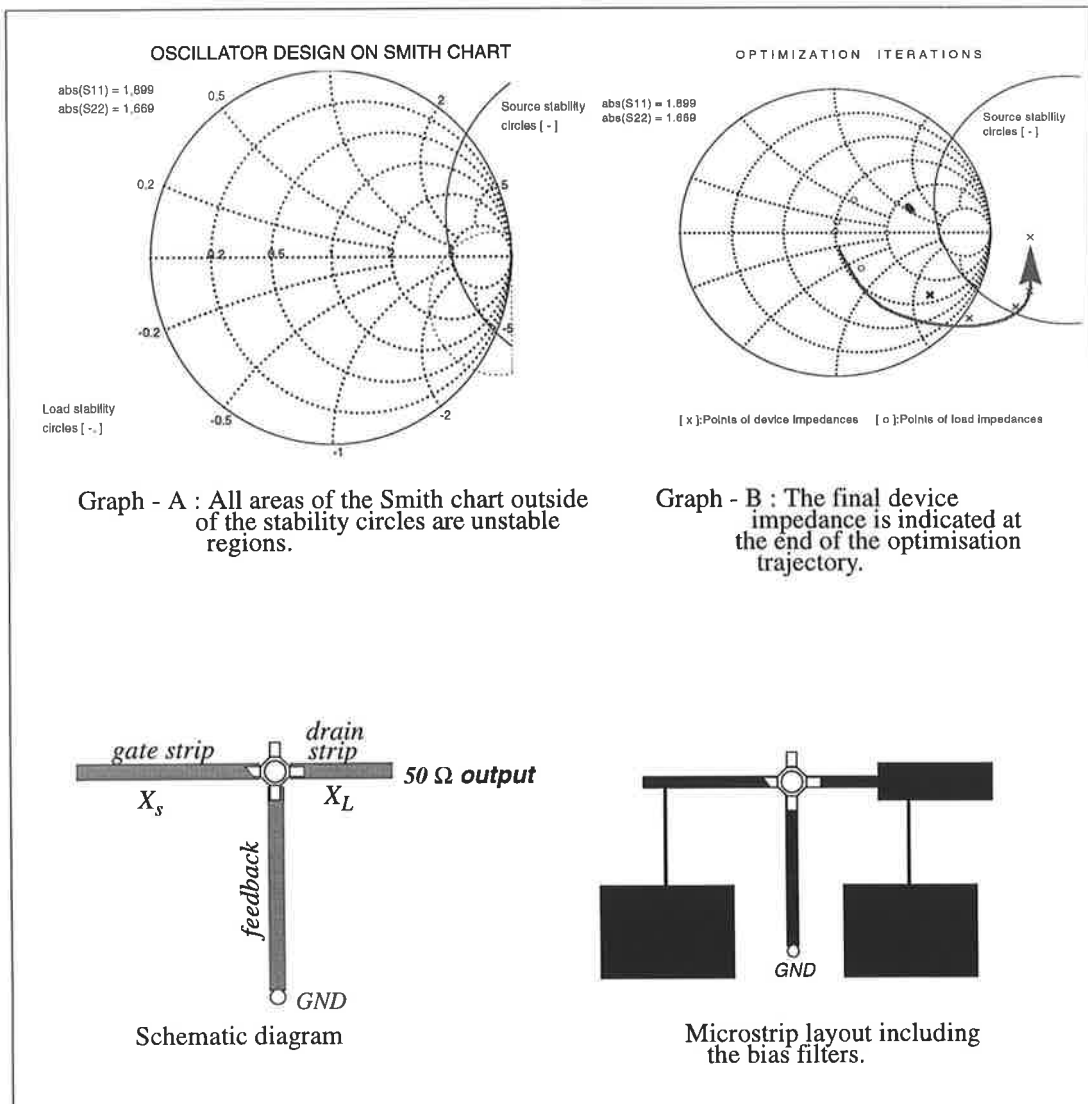


Figure 4-5. Graph - A for initialisation, graph - B showing the final impedances, schematic diagram and microstrip layout of the design

After about 400 error-function evaluations the optimised dimensions of the microstrip circuits are printed out as shown in Figure 4-5. Also the optimisation iterations are shown in graph - B where the final device and load impedance are checked on the Smith chart. The schematic diagram of the designed oscillator and the microstrip layout including the bias filters are illustrated in Figure 4-5.

## 4.4 Shielded Inverted Microstrip Oscillator

The design of a microstrip oscillator on a thick dielectric substrate which is covered by a metal sheet as shown in Figure 4-6 is the first part of the novel oscillator design. The dielectric constant is very high ( $\epsilon_r > 10$ ) and the top plate clearance ( $g$ ) is much less than the substrate thickness ( $h$ ). The design method for MESFET oscillators as described in the preceding section is still valid for this circuit. However the formulae for conventional microstrip lines are no longer valid for this particular geometry.

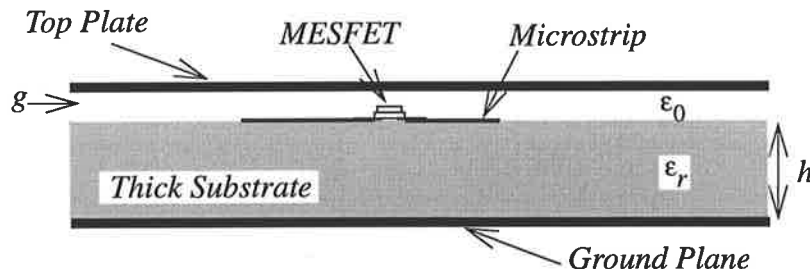


Figure 4-6. MESFET oscillator circuit on the shielded inverted microstrip

To describe the transmission medium of Figure 4-6 we simply remove the ground plane. The resultant would be an inverted microstrip where the dielectric thickness ( $h$ ) is greater than the air-filled region ( $g$ ) as shown in Figure 4-7 (a).

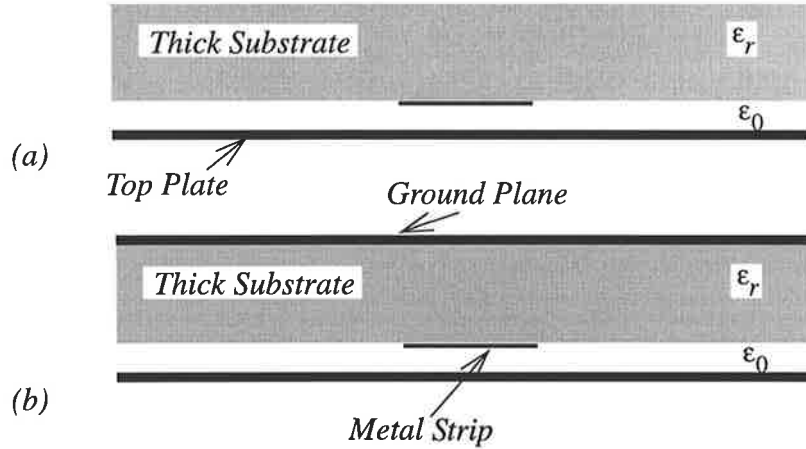


Figure 4-7. Geometry of (a) inverted microstrip and (b) shielded inverted microstrip

Now adding the ground plane to the back of the substrate will result in a *shielded inverted microstrip* line (SIML) as shown in Figure 4-7 (b). There is no simple design expression for this type of transmission medium. Generally it falls in the category of shielded microstrip lines which have been widely studied in treatments of the microwave packaging problem and have resulted in accurate empirical formulae [36]. But the geometry of interest for packaging problems is a relatively thin substrate inside a high air-filled enclosure (i.e.  $g/h \gg 1$ ). There are rigorous methods of analysis such as the variational method [37, 38] and modified residue calculus [39, 40] which are based on numerical calculations. Both methods provide sufficiently accurate results, although they require a comparatively long computation time. A common disadvantage of these methods, as with all numerical methods, is that they do not provide a clear analytic review of the effect of geometrical dimensions and technological line constants on the electrical parameters of microstrips. This disadvantage is removed by an analytical method using conformal mapping.

Generally for the planar transmission lines such as microstrips and striplines, the conformal mapping method has been successfully used with excellent accuracy. The principle of using this method for the solution of microstrip lines has been described in detail in many publications e.g. [41, 42] and in particular the analysis of inhomogeneously-filled

asymmetric stripline (shielded inverted microstrip line) [43, 44] which is used in this chapter. The design procedure including the mathematical relations is given in Appendix A.

It should be noted that the analysis involves a number of numerical integrations with unknown parameters which cannot be obtained explicitly. Consequently the method has been implemented with a computer program using MATLAB. A recursive approach using optimisation has been exploited to determine the characteristic impedance and effective dielectric constant for a given geometry. As an example the parameters of a shielded inverted microstrip line with the geometry shown in Figure 4-7 (b) have been computed for a range of strip widths. The design specifications are:  $\epsilon_r = 10.61$ ,  $h = 8.41$  mm and  $g = 3.0$  mm and the numerical results are shown in Figure 4-8. These results are typical of those for fabrication of oscillators used to test the validity of the overall oscillator design at microwave frequencies.

These graphs are obtained from the numeric data of the conformal mapping program. Obviously the data can be easily handled by the oscillator design program explained in Section 4.3 for the design of shielded inverted microstrip oscillators as shown in Figure 4-4. It should be noted again that this model assumes relatively narrow microstrips with respect to the substrate dimensions and that the side walls are non-existent. The first condition is usually satisfied in practice because the widths of the microstrips are kept as narrow as possible to reduce unnecessary interaction with the electric field distribution on the dielectric surface. The effect of the side walls is negligible as long as the strips are not close to the cavity walls. However a simple perturbation based on image theory and parallel-coupled lines can be employed to determine the change of effective dielectric constant and the characteristic impedance of any metal strip that may happen to be located close to a side wall [25].

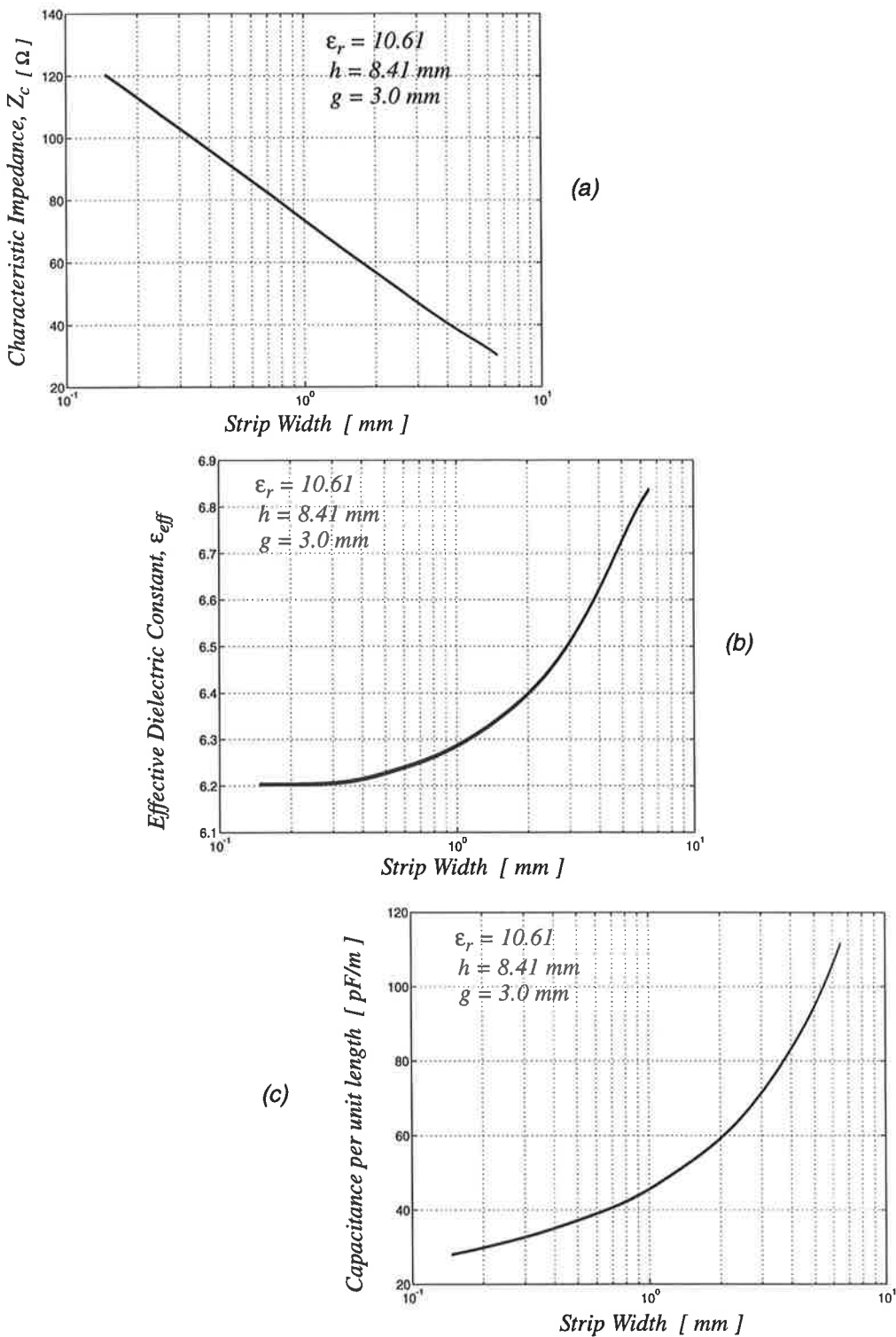


Figure 4-8. Parameters of shielded inverted microstrip line: (a)  $Z_c$ , (b)  $\epsilon_{eff}$  and (c) capacitance

The design of shielded inverted microstrip oscillators is not basically different from the conventional ones as stated earlier. However there are special problems associated with this unique oscillator due to the LSM mode cavity fields that have never been encountered in any other circuit. To demonstrate these problems we consider the oscillator circuit apart from the cavity structure as illustrated in Figure 3-19. Details of the circuit components are clearly illustrated in Figure 4-9. It should be noted that the condition of critical positioning as explained in Section 3.5.1 should be satisfied thoroughly, i.e., the coupling between the circuit components and the cavity field distribution on the surface of the dielectric should be kept to a negligible value. To achieve this, the following design constraints are applied:

- The transistors are positioned on the null area of the electric field distribution on the dielectric surface of the partially-filled cavity.
- The number of circuit components is kept to a minimum.
- The microstrips are as narrow as possible.

In the simplified layout of Figure 4-9 the MESFET is positioned on the null point where electric field is zero.

The number of circuit components are three, namely, gate, phasing(drain) and feed-back (source) strips with the bias lines excluded. The coupling probe is assumed to be an integral part of the cavity as explained in Section 3.5.2 . The gate and phasing strips are coincident with the axis of zero axial electric field ( $E_z = 0$ ) whereas the feedback strip is exactly positioned on the axis of zero transverse electric field ( $E_x = 0$ ). The strips are narrow enough to have negligible coupling due to width and therefore all components are effectively uncoupled from the cavity. The coupling probe is exposed to significant electric fields and is strongly coupled to the cavity thus giving rise to an impedance  $Z_{strip}$  at the input point  $\alpha$  on Figure 4-9.

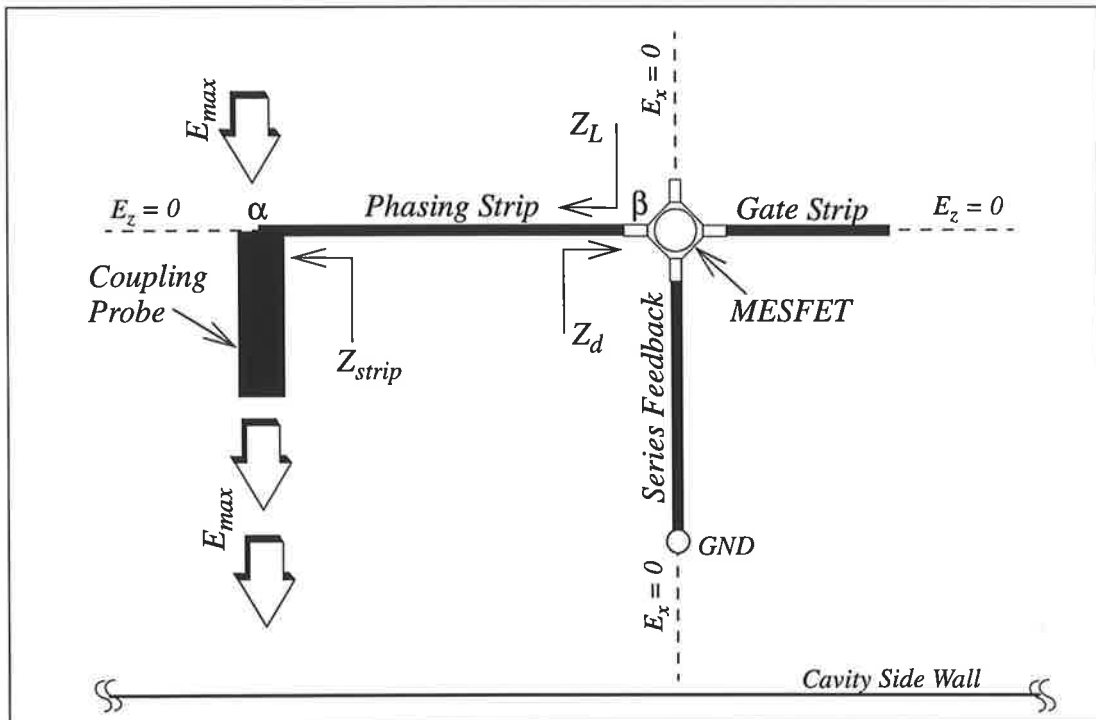


Figure 4-9. Typical layout of a shielded inverted microstrip oscillator for design testing at microwave frequencies

This impedance is transformed through the phasing strip to its output point  $\beta$  where it appears as the load impedance  $Z_L$  for the MESFET. The device impedance  $Z_d$  as specified depends on the length of the gate and feedback strips. The oscillation condition as given by equations (2) and (3) is thus established between  $Z_d$  and  $Z_L$ .

A practical problem in the circuit of Figure 4-9 is the microwave ground connection of the feedback strip. It is very difficult to provide a ground using a via connection because of the thick substrate. An alternative method is to make the ground connection with the aid of a metal post or screw extended from the cavity lid to the surface of the substrate. This option adds to the structural complexity. In addition the post or screw itself introduces excessive inductance as well as perturbing the field distribution inside the partially-filled cavity. This problem is avoided by choosing the feedback strip as an open stub thus eliminating a microwave ground connection. However a DC return is needed for the source terminal as will be explained below.

## 4.5 Bias Circuit

In order to satisfy the design constraints, the bias lines should be located in the lowest intensity field regions. The lines are very narrow and usually  $\lambda/4$  or  $3\lambda/4$  long. They are grounded either directly or via a capacitor. A complete layout of the oscillator is illustrated in Figure 4-10 where two open stubs are used for series feedback and the bias lines are included. The total series feedback is the parallel combination of reactances that are introduced by the open stubs. The DC return is a  $\lambda/4$  line that provides DC current to the source terminal. It is obvious that the length of the lower stub cannot be changed and the level of the feedback is mainly determined by the upper stub.

The narrow bias strips for gate and drain are  $3\lambda/4$  long and for RF are bypassed to ground by the chip capacitors in the case of this microwave test model. These strips are positioned as close to the null field axis as possible. Part of each bias line is meandered to increase the length of the line in order that the overall length be equal to  $3\lambda/4$ . The meanders should be symmetrically positioned with respect to the maximum field axis ( $E_{max}$ ) so that the induced electric fields in the segments along the  $z$ -axis, i.e.,  $+\epsilon$  and  $-\epsilon$  will cancel out. The  $V_{GS}$  and  $V_{DS}$  supply voltages are provided by the wires that are fed through the ferrite beads inside the cavity wall. These wires are connected to the corresponding solder patches on the circuit layout. The combination of chip capacitors and ferrite beads are an effective filter structure for microwave test models up to 4 GHz or thereabouts.

## 4.6 Design Example

The automation program described in Section 4.3 has been modified to include the design of shielded inverted microstrip oscillators. The design process relies on the following information:

- I. The distribution of electric field on the interface of the partially-filled cavity as derived in Chapter 5,
- II. The parameters of shielded inverted microstrip line such as  $Z_c$  and  $\epsilon_{eff}$  shown in Figure 4-8, and,

III. The input impedance of the coupling probe,  $Z_{strip}$  as derived in Chapter 5.

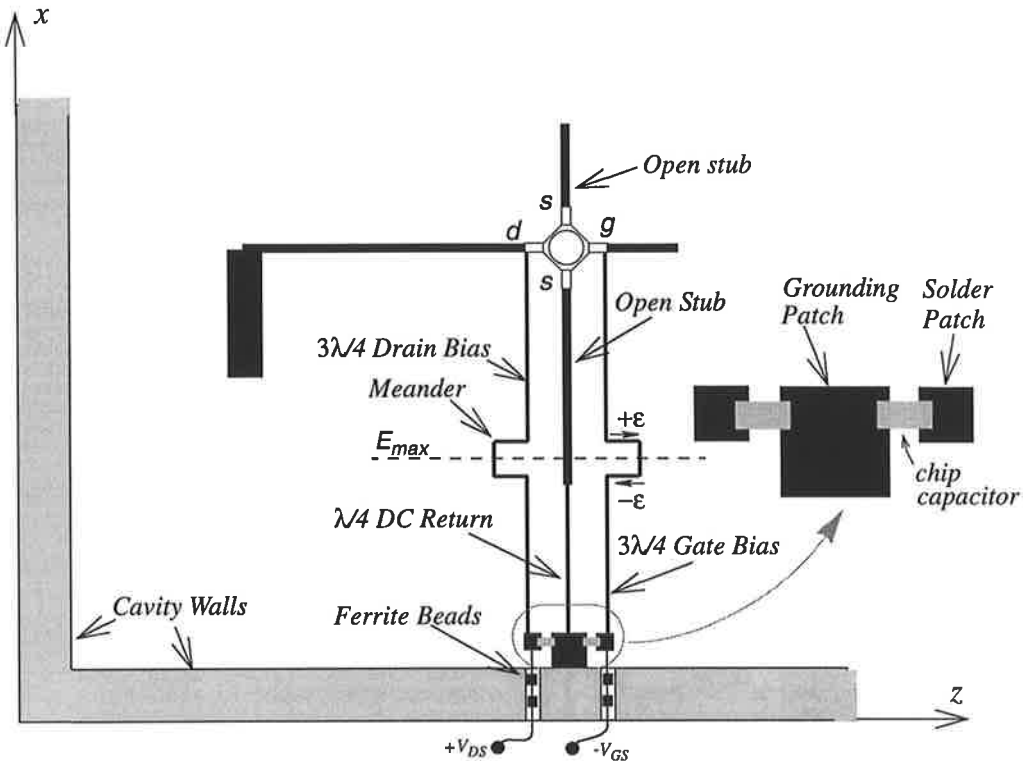


Figure 4-10. Design of bias circuit and their critical positioning in the microwave test oscillator

A knowledge of the field distribution on the dielectric surface is necessary for accurate positioning of the circuit components. Numerical data for  $Z_c$  and  $\epsilon_{eff}$  as shown in Figure 4-8 are easily handled by the oscillator design program. Calculation of the probe impedance is usually made for a wide range of strip lengths and specific width as well as strip coordinates. Details on the calculation of probe impedance will be given in the discussion of the partially-filled cavity in Chapter 5.

It is obvious from the above that the dimensions of the partially-filled cavity and the coupling structure should be specified prior to obtaining this information. Also a detailed analysis of the cavity structure including determination of the resonant frequencies and the field distribution are necessary before the stage of oscillator design. In addition the

oscillation frequency itself is determined from a knowledge of the resonant modes that are excited by the coupling probe.

A design example is given based on the above knowledge and using the cavity analysis given in a separate section. For a given partially-filled cavity with the following specifications a test oscillator will be designed for operation at 3.5 GHz.

**TABLE 1. Specifications of partially-filled cavity. Dimensions in millimetres**

Length.....	80 mm	Dielectric Thickness.....	8.41 mm	Cavity Mode	LSM <sup>y</sup> <sub>303</sub>
Width.....	72 mm	Air-Gap.....	3.0 mm	Frequency....	3.5043 GHz
Height.....	11.41 mm	Average Dielectric Constant....	10.61		

Typical design using the modified oscillator program is explained in Figure 4-11. The desired oscillator frequency should be used to determine the cavity dimensions. The type of series feedback chosen is an open stub connected to the MESFET source as explained previously. The correct amount of feedback is selected by graphical analysis in which the stability circles of the device plus feedback are shown for different lengths of the feedback line. Referring to Figure 4-12, Graph -A is the stability criterion of the device for a selected length of feedback stub. The range of the load coupling probe lengths is specified from Graph -B for the purpose of optimisation. Also the minimum and maximum length of the gate strip is chosen from Graph -C. The optimisation routine will change the lengths of the probe and gate strip to find the correct values of  $Z_L$  and  $Z_d$  which satisfy the oscillator conditions of equations (2) and (3) at the operating frequency. In fact these selected ranges confine the field of optimisation excursion and are chosen with regard to optimum possible design such as achieving maximum negative resistance and minimum length of gate strip. The latter is important in order to keep the layout of each oscillator compact and so make multiple device power combining layouts possible.

DESIGN OF MICROWAVE MESFET OSCILLATOR  
ON  
SHIELDED INVERTED MICROSTRIP  
USING  
ATF -13036 FET TRANSISTOR

ENTER Oscillator frequency in GHz = 3.5  
SELECT common-source/ common-gate [cs/ cg] : cs  
-----<< Selection of series feedback >>-----  
If you want a short circuit stub choose : s  
If you want a open circuit stub choose : o  
If you do not need a feedback choose : n  
ENTER your choice: [ s, o, n ] o  
Graphical analysis of series feedback?? [y/n] n  
Length of the feedback strip in degree = 65  
Width of the feedback strip in millimetre = 0.5  
Graph - A is displayed  
-----<< Initialisation >>-----  
Starting from the last minimum point ? [y/ n]: n  
Graph - B and C are displayed  
ENTER the min. length of Gate strip [mm]: 7  
ENTER the max length of Gate strip [mm]: 10  
ENTER the width of Gate strip [mm]: 0.5  
ENTER min. length of Probe strip [mm]: 2  
ENTER max length of Probe strip [mm]: 4  
ENTER the width of Phasing strip [mm]: .5

Figure 4-11. Program messages including specifications, series feedback and initialisation.

The length of the phasing line is chosen in order to transform the probe impedance to an appropriate level of  $Z_L$ . The optimisation result is shown in Figure 4-13 including dimensions of all microstrip components where SIML stands for shielded inverted microstrip lines.

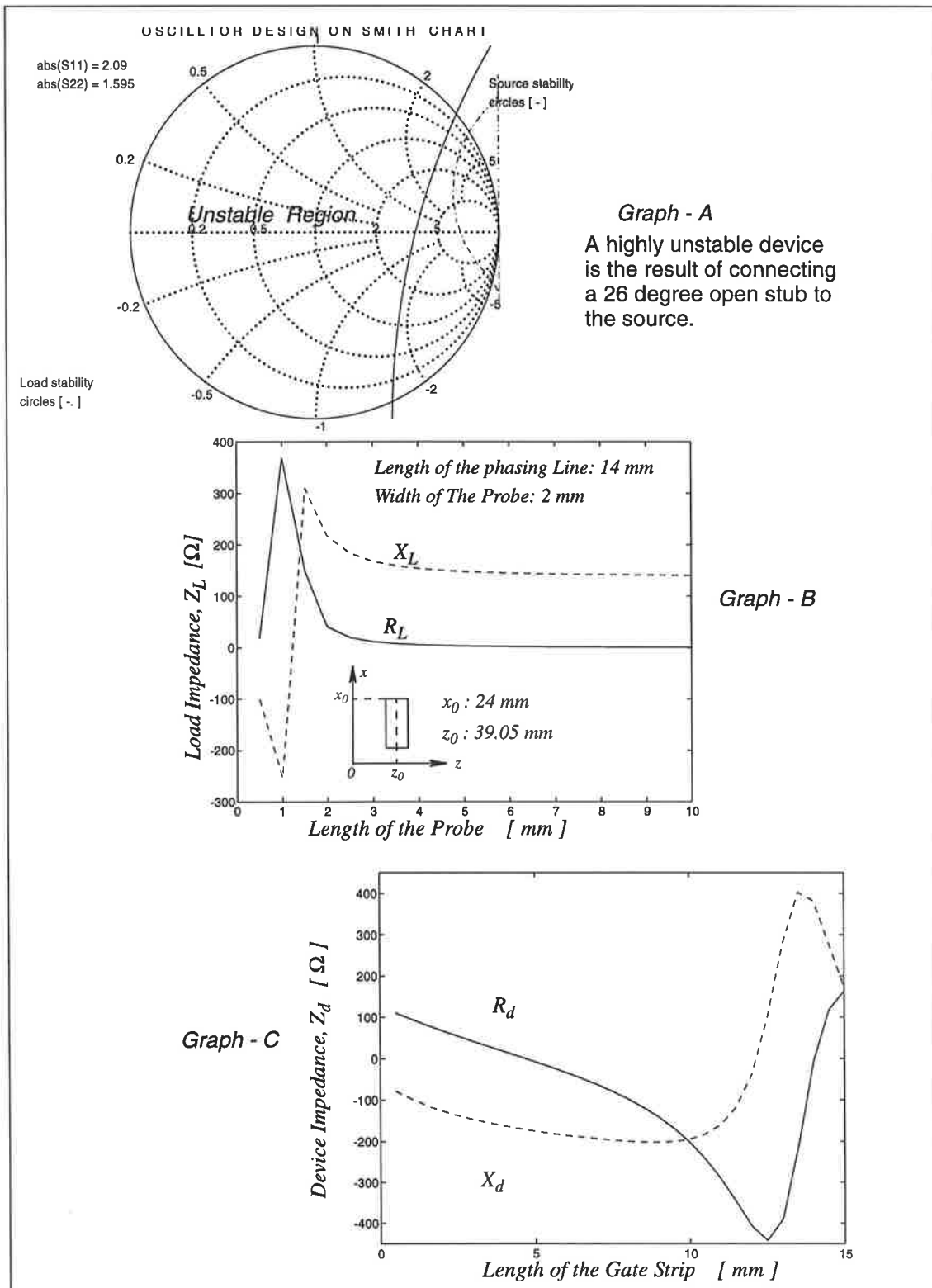


Figure 4-12. Graph - A: stability circles, Graph - B:  $Z_L$ , and Graph - C:  $Z_d$

```
<< THE Hooke & Jeeves Optimization Routine >>
Minimum error function is Fmin = 7.7169 e-005
Number of function evaluations: 400
Zdev = -1.3125 - 3.88361i Zload = 0.5153 + 3.8836i
```

```
<<< Optimization Result for The Shielded Inverted Oscillator Design >>>
transistor: ATF-13036 MESFET
oscillator frequency = 3.5 GHz
length of gate strip = 7.08 mm
width of gate strip = 0.5 mm
length of current strip = 2.25 mm
width of current strip = 2 mm
type of series feedback : open circuit stub
length of equivalent single source-strip = 65 degree
length of upper source-strip = 6.95 mm
length of lower source-strip = 12.6 mm
width of source-strips = 0.5 mm
length of DC-return strip = 8.598 mm
width of DC-return strip = 0.2 mm
length of phasing strip = 14 mm
```

Figure 4-13. Optimisation results including the dimensions of circuit components

The critical positioning of circuit components with respect to the field distribution of the specified cavity is clearly shown in Figure 4-14. Detailed discussion of the circuit layout will be given in Chapter 7.

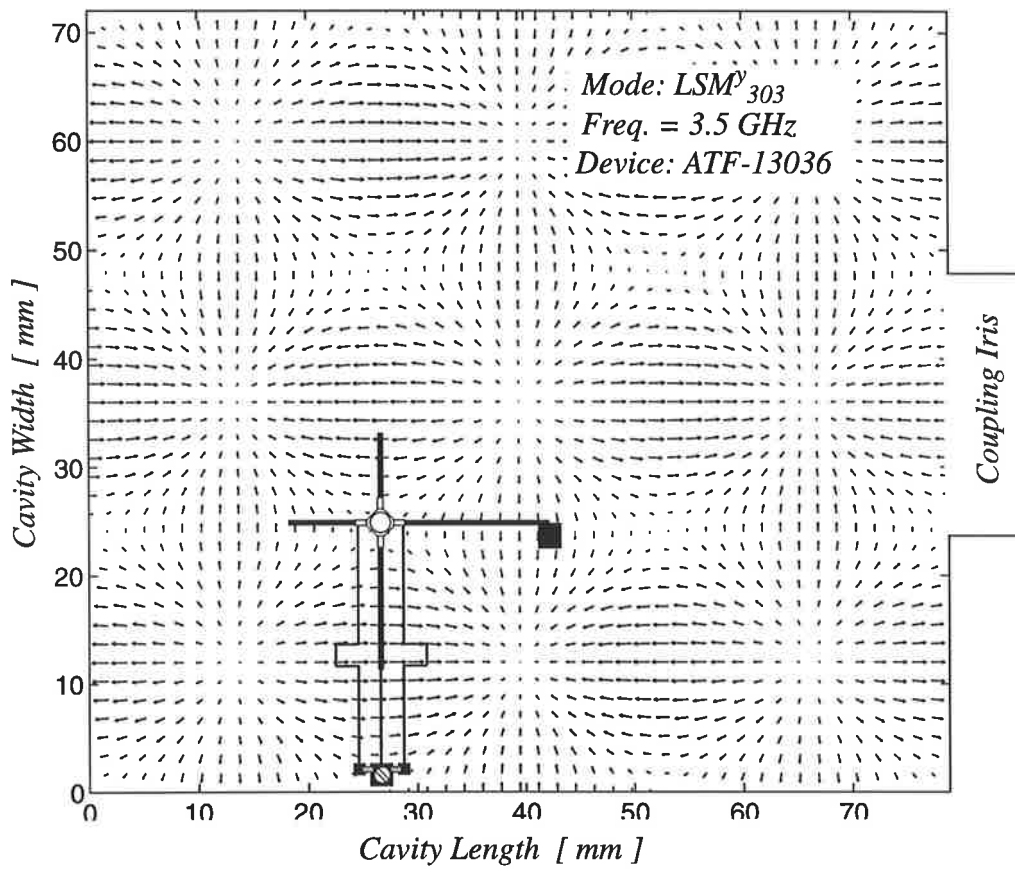


Figure 4-14. Positioning of components w.r.t. surface E-fields of the partially-filled cavity

---

## Chapter 5

# *Design Methods*

## *Part II: Cavity Structure*

### **5.1 Review of Design Methods**

In order to simplify the design of the overall oscillator structure it has been virtually decomposed into three constituent parts. These parts have been clearly illustrated in Figure 3-19. The first part, the MESFET oscillator on shielded inverted microstrip line has been designed in Chapter 4. This chapter deals with the design of the partially-filled cavity resonator with a coupling aperture in the wall. In the case of coupled cavities the accurate evaluations of the resonant frequency, the port impedance (here at either the oscillator output probe or the aperture) and the coupling factor have always been problematic in the design of cavity oscillators and power combiners. For partially-filled cavities in particular no comprehensive analysis has been reported for determining these parameters.

In the past the accurate characterisation of waveguide-coupled cavities has been difficult to analyse precisely. In fact the classical treatment has been twofold: (i) approximate design based on assumed ideal geometry and (ii) provision of adjustments such as tuning

screws and other perturbations in the cavity to compensate for design errors. Such approximate methods appeared to be adequate for the design of conventional microwave sources. However no similar adjustments are feasible in the design of millimetre-wave sources that must be compatible with monolithic fabrication. In addition the technique of critical positioning which has been described in Section 3.5.1 requires an exact knowledge of the field distribution on the dielectric surface of the partially-filled cavity. This will not be achieved unless an accurate analysis of the cavity structure is performed.

Several numerical studies have been reported using versatile methods such as finite difference [46], finite elements [47] and the transmission line matrix approach [48]. These methods are efficiently applied to the complex geometries and inhomogeneously filled structures where analytical techniques are non-existent. Nevertheless, for simple geometries, they are tedious methods and do not provide analytical expressions of field distributions.

Analytical approaches that are available in the literature consist of the following.

- (i) Solution of Helmholtz equation for a source-free cavity [49].
- (ii) Solution of Maxwell's equations for a source-impressed cavity using dyadic Green's functions [49].

No magnetic currents are assumed in the above analyses, and so, there can be no large apertures in the cavity walls. The problem of small apertures<sup>1</sup> is usually solved using Bethe's small hole theory [49].

- (iii) An updated analysis of an arbitrary-shaped cavity resonator associated with a large aperture was published by Kurokawa [50], [51] in which he expanded Maxwell's equations in terms of source-free eigenfunctions. The effect of the aperture on the cavity fields is expressed by two surface integrals. Kurokawa did not give a general treatment for these integrals except for the simple geometry shown in Figure 5-1 where he determined the input admittance of a short-circuit terminated waveguide. The refer-

---

1. Small aperture refers to a hole whose diameter is less than 10% of the medium wavelength.

ence plane  $S_0$  is  $l_z$  away from the short-circuited end and the cavity extends from the shorted end up to  $S_0$  where it is connected to an infinite waveguide. In this simple model there is no discontinuity and no iris reflection. A cavity such as this is not a high quality factor resonator.

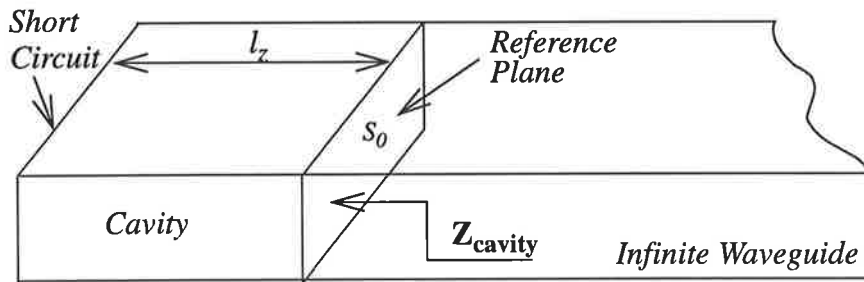


Figure 5-1. A short-circuited waveguide was analysed by Kurokawa's field expansion.

Recently some efforts have been made to develop versatile analytical methods for complex inhomogeneously-filled cavities as better alternatives to finite element and finite difference methods from the viewpoint of numerical efficiency. These analyses, similar to Kurokawa's, are based on the expansion of the cavity fields with respect to a complete set of eigenmodes of the empty, short-circuited cavity [52]. In one of the methods the surface magnetic currents of the aperture were formulated in terms of equivalent polarisation currents, thus, leading to a set of volume integral equations (VIE) [53]. In an improved method called the SIE formulation, the effect of the magnetic currents on the cavity field distribution has been expressed by surface integral equations [54]. The VIE and SIE formulations have been developed to solve the scattering problem of dielectric bodies. However one can obtain an idea from this for the treatment of the aperture problem in the cavity field expansion that will be presented later in this chapter.

## 5.2 The Partially-Filled Cavity Resonator

As described in Chapter 4, the core of the new oscillator assembly is a partially-filled cavity resonator enclosing the oscillator circuit. The cavity is coupled to an air-filled waveguide through a thick iris so that the oscillator power flows out by means of sub-

strate mode or surface wave propagation. The design of the oscillator circuit depends primarily on the accurate analysis of the cavity resonator. Such analysis is crucial to provide the following quantities.

- (i) The appropriate resonant mode that dominates the oscillator frequency.
- (ii) The exact field distribution on the dielectric interfacial surface so that the critical positioning technique can be used to locate the oscillator circuit components inside the cavity enclosure.
- (iii) The exact analytical expressions of the cavity fields to determine the input impedance of the coupling probe which will appear as an effective load on the oscillator circuit.
- (iv) The physical dimensions of the partially-filled cavity that are used to determine the characteristics of the shielded inverted microstrip line.

Figure 5-2 shows detail of the typical partially-filled cavity under consideration. Logically, due to the simple rectangular geometry, an analysis can be developed similar to the one that exists for hollow rectangular cavities. However the field expansion should be performed in terms of hybrid modes rather than conventional  $TE^z$  and  $TM^z$  modes. However such analysis is not available for the structure of Figure 5-2 and needs to be developed in the following section.

### 5.2.1 Field Expansions

A method based on Kurokawa's approach [51] can be used to expand the cavity fields in terms of the LSE<sup>y</sup> and LSM<sup>y</sup> eigenfunctions. These eigenfunctions are derived from the field expressions of the partially filled rectangular waveguide as given in Appendix B. Due to the two-fold nature of the structure, each medium is associated with a separate field configuration. This is mainly due to the different  $y$ -eigenvalues which are interrelated by transcendental equations. For the cavity of Figure 5-2 one can define the electric and magnetic fields,  $\bar{E}$  and  $\bar{H}$ , as follows:

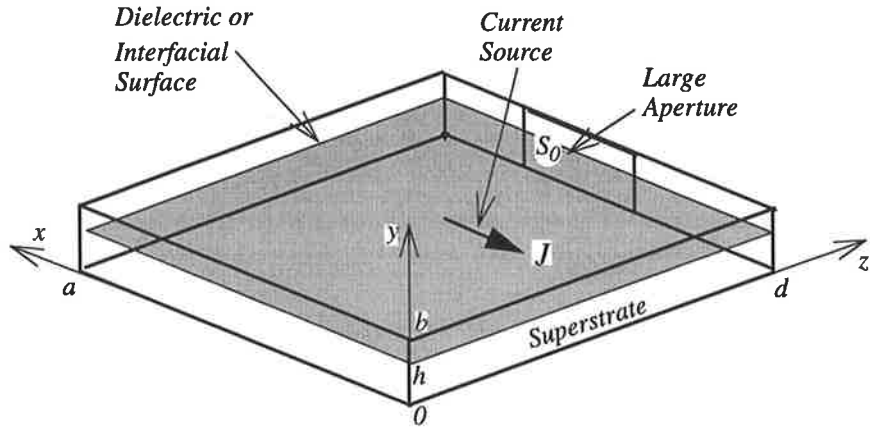


Figure 5-2. Partially-filled cavity with current source and aperture.

$$\bar{E} = \begin{cases} \bar{E}^d & \text{for } 0 < y < h \\ \bar{E}^a & \text{for } h < y < b \end{cases} \quad \bar{H} = \begin{cases} \bar{H}^d & \text{for } 0 < y < h \\ \bar{H}^a & \text{for } h < y < b \end{cases} \quad (5-1)$$

The fields should satisfy the following Maxwell's equations that include an electric current source as set out below:

$$\bar{\nabla} \times \bar{E} = -j\omega\mu_0 \bar{H} \quad (5-2)$$

$$\bar{\nabla} \times \bar{H} = -j\omega\kappa\epsilon_0 \bar{E} + \bar{J} \quad (5-3)$$

where  $\kappa$  is the relative permittivity and is defined as:

$$\kappa = \begin{cases} \epsilon_r & \text{for } 0 < y < h \\ 1 & \text{for } h < y < b \end{cases} \quad (5-4)$$

It can be shown [49] that the electromagnetic fields can be expanded in terms of eigenfunctions of the fully enclosed cavity. Thus let

$$\bar{E} = \sum_n (e_n \bar{E}_n + f_n \bar{F}_n) \quad (5-5)$$

$$\bar{H} = \sum_n (h_n \bar{H}_n + g_n \bar{G}_n) \quad (5-6)$$

where  $\bar{E}_n$  and  $\bar{H}_n$  are the resonant fields corresponding to the  $n$ th resonant eigenmode.  $\bar{F}_n$  and  $\bar{G}_n$  are the local fields that are produced by electric and magnetic currents respectively. Detail of the field expansion is given in Appendix C.

$\bar{E}_n$  and  $\bar{H}_n$  should satisfy Maxwell's equations for the source-free and fully enclosed cavity. Thus let

$$\bar{\nabla} \times \bar{E}_n = k_n \bar{H}_n \quad (5-7)$$

$$\bar{\nabla} \times \bar{H}_n = k_n \bar{E}_n \quad (5-8)$$

where  $k_n$  is the eigenvalue for the  $n$ th resonant mode inside a fully enclosed cavity.

Also the eigenfunctions  $\bar{F}_n$  and  $\bar{G}_n$  are found from the following wave equations:

$$\bar{\nabla}^2 \bar{F}_\alpha + k_\alpha^2 \bar{F}_\alpha = 0, \quad \hat{n} \times \bar{F}_\alpha = 0 \quad \text{on } S \quad (5-9)$$

$$\nabla^2 \psi_\lambda + k_\lambda^2 \psi_\lambda = 0, \quad k_\lambda^2 \bar{G}_\lambda = \bar{\nabla} \psi_\lambda, \quad \hat{n} \cdot \bar{G}_\lambda = 0 \quad \text{on } S \quad (5-10)$$

These eigenfunctions are completely determined as described in Appendix D.

The unknown amplitudes  $e_n$ ,  $h_n$ ,  $f_n$ , and  $g_n$  in (5-5) and (5-6) are determined from the Maxwell's equations (5-2) and (5-3) by using equations (5-5) to (5-8). However the procedure is described in Appendix C and is not brought into this chapter.

### 5.3 Surface Integrals

By expanding the Maxwell's equations as described in Appendix C the fundamental equations of wave amplitude are obtained as below:

$$\Delta_n e_n + Z_0^2 \iiint_V \bar{J} \cdot \bar{E}_n dV = \frac{k_n}{j\omega\kappa\epsilon_0} \iint_{S_0} \hat{n} \times \bar{E} \cdot \bar{H}_n dS \quad (5-11)$$

$$\Delta_n h_n = \frac{k_n}{j\omega\kappa\epsilon_0} \int_V \bar{J} \cdot \bar{E}_n dS + \int_{S_0} \hat{n} \times \bar{E} \cdot \bar{H}_n dS \quad (5-12)$$

$$j\omega\mu_0 g_n = \int_{S_0} \hat{n} \times \bar{E} \cdot \bar{G}_n dS \quad (5-13)$$

$$-\int_V \bar{J} \cdot \bar{F}_n dV = j\omega\kappa\epsilon_0 f_n \quad (5-14)$$

where

$$\Delta_n \equiv \mu_0 \omega_n \left[ \left\{ \frac{\omega}{\omega'_n} - \frac{\omega'_n}{\omega} \right\} j + \frac{1}{Q'_n} \right] \quad (5-15)$$

$\omega'_n$  is the modified resonant frequency of the fully enclosed cavity, and  $Q'_n$  is the unloaded-Q as defined in Appendix C. The surface integrals involved in (5-11) to (5-13) can be determined using the tangential electromagnetic fields on the surface of the large aperture  $S_0$  as will be explained later in this chapter and Appendix E. As the cavity is connected to a dissimilar waveguide, these fields depend on the field distribution on both sides of the junction. Therefore an exact determination of the aperture fields requires an elaborate method such as the mode-matching technique. This method has been applied to the coupling structure that is used in the novel oscillator assembly. A comprehensive discussion of the mode matching analysis will be given in the treatment of the coupling structure in Chapter 6.

Generally the tangential fields on the aperture can be expanded in terms of the waveguide modes as below:

$$\bar{E}_t = \sum_k V_k^e \bar{e}_k^e + \sum_k V_k^h \bar{e}_k^h \quad (5-16)$$

$$\bar{H}_t = \sum_k I_k^e \bar{h}_k^e + \sum_k I_k^h \bar{h}_k^h \quad (5-17)$$

where  $\bar{E}_t$  and  $\bar{H}_t$  are the tangential electric and magnetic fields on the surface of the aperture  $S_0$ . This surface is clearly divided into  $S_0^d$  and  $S_0^a$ , as shown in Figure 5-3. The normalised mode vectors  $\bar{e}_k^e$ , and  $\bar{h}_k^e$  are the eigenvectors of LSM<sup>y</sup> modes of the partially-filled waveguide. Similarly  $\bar{e}_k^h$ , and  $\bar{h}_k^h$  are the eigenvectors of LSE<sup>y</sup> modes. The coefficients  $V_k^{mode}$  and  $I_k^{mode}$  are the normalised equivalent voltage and current corresponding to the  $k$ th LSM<sup>y</sup> or LSE<sup>y</sup> mode. These coefficients are determined using the mode matching method that will be described in Chapter 6.

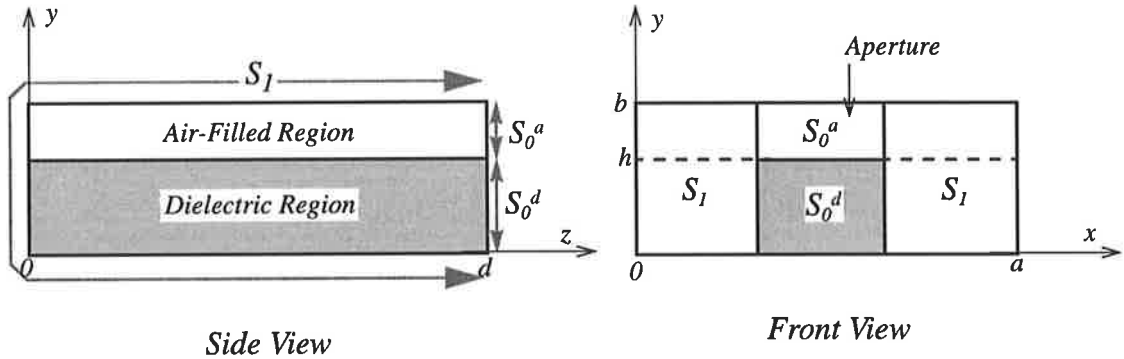


Figure 5-3. Views of the partially-filled cavity, showing the surface of walls and the aperture.

The normalised mode vectors should satisfy the following orthogonality condition:

$$\int_{S_0^d} \bar{e}_n^e \times \bar{h}_m^e \cdot \hat{a}_z ds = Q_{nm}^e \delta_{nm} \quad \text{where } \delta_{nm} = \begin{cases} 1 & , n = m \\ 0 & , n \neq m \end{cases} \quad (5-18)$$

$$\text{and} \quad \int_{S_0^a} \bar{e}_n^h \times \bar{h}_m^h \cdot \hat{a}_z ds = Q_{nm}^h \delta_{nm} \quad (5-19)$$

where  $Q_{nm}^e$  and  $Q_{nm}^h$  are the normalisation constants for LSM<sup>y</sup> or LSE<sup>y</sup> modes respectively. As will be explained later, in mode matching analysis these constants are assumed equal to the wave admittances of the corresponding hybrid modes. Thus let

$$Q_{nm}^e = Y_{nm}^e \quad \text{and} \quad Q_{nm}^h = Y_{nm}^h \quad (5-20)$$

### 5.3.1 Continuity of Electric Fields

The tangential electric field at the aperture is related to the cavity field as below:

$$\hat{n} \times \bar{E}|_{S_0} = \hat{n} \times \bar{E}_t|_{S_0} \quad (5-21)$$

where  $\bar{E}_t$  is the tangential electric field at the aperture surface and  $\bar{E}$  is the cavity field. Substitution of  $\bar{E}_t$  from (5-16) into the continuity equation (5-21) yields the following:

$$\hat{n} \times \bar{E}|_{S_0} = \sum_k V_k^e (\hat{n} \times \bar{e}_k^e) + \sum_k V_k^h (\hat{n} \times \bar{e}_k^h) \quad (5-22)$$

where the equivalent voltages have been previously defined on the aperture surface  $S_0$  at the junction.

By substituting (5-22) into the surface integrals involved in equations (5-11) to (5-13) and noting that  $\hat{n} = -\hat{a}_z$  and using a vector identity<sup>1</sup> we obtain the complete expansion of the surface integrals. Thus let

$$-\int \int_{S_0} \hat{n} \times \bar{E} \cdot \bar{H}_n dS = \sum_k V_k^e B_{nk}^e + \sum_k V_k^h B_{nk}^h \quad (5-23)$$

$$-\int \int_{S_0} \hat{n} \times \bar{E} \cdot \bar{G}_n dS = \sum_k V_k^e C_{nk}^e + \sum_k V_k^h C_{nk}^h \quad (5-24)$$

where  $B_{nk}^e$ ,  $B_{nk}^h$ ,  $C_{nk}^e$ , and  $C_{nk}^h$  are determined from the reaction integrals between the cavity and waveguide eigenfunctions:

$$B_{nk}^e = \int \int_{S_0} (\bar{e}_k^e \times \bar{H}_n) \cdot \hat{a}_z dS \quad (5-25)$$

---

1.  $\bar{A} \times \bar{B} \cdot \bar{C} = \bar{A} \cdot \bar{B} \times \bar{C}$

$$B_{nk}^h = \iint_{S_0} (\bar{e}_k^h \times \bar{H}_n) \cdot \hat{a}_z dS \quad (5-26)$$

$$C_{nk}^e = \iint_{S_0} (\bar{e}_k^e \times \bar{G}_n) \cdot \hat{a}_z dS \quad (5-27)$$

$$C_{nk}^h = \iint_{S_0} (\bar{e}_k^h \times \bar{G}_n) \cdot \hat{a}_z dS \quad (5-28)$$

Derivation of the above coefficients will be straightforward using the relevant eigenfunctions of waveguide and cavity and the analytical expressions are given in Appendix E. By substituting (5-23) and (5-24) into (5-11) and (5-12), and (5-13), we obtain the final equations:

$$\Delta_n e_n + Z_0^2 \iiint_V \bar{J} \cdot \bar{E}_n dV = -\frac{k_n}{j\omega\kappa\epsilon_0} \sum_k (V_k^e B_{nk}^e + V_k^h B_{nk}^h) \quad (5-29)$$

$$\Delta_n h_n = \frac{k_n}{j\omega\kappa\epsilon_0} \iint_V \bar{J} \cdot \bar{E}_n dS - \sum_k (V_k^e B_{nk}^e + V_k^h B_{nk}^h) \quad (5-30)$$

$$j\omega\mu_0 g_n = -\sum_k (V_k^e C_{nk}^e + V_k^h C_{nk}^h) \quad (5-31)$$

$$j\omega\kappa\epsilon_0 f_n = -\iint_V \bar{J} \cdot \bar{F}_n dV \quad (5-32)$$

where  $Z_0 = \sqrt{\mu_0/\kappa\epsilon_0}$  and  $\kappa$  is given by (5-4). The above equations provide the field amplitudes of the  $n$ th cavity mode. These equations can be presented in matrix form to include all possible cavity modes. This is advantageous for multimode manipulations such as derivation of the generalised admittance of the cavity. Thus the matrix representations of (5-29) to (5-32) are given by the following expressions,

$$[\Delta][h] = \frac{1}{j\omega\kappa\epsilon_0} [K] \iiint_V \bar{J} \cdot [\bar{E}] dV - [B][V] \quad (5-33)$$

$$[\Delta][e] = -Z_0^2 \iiint_V \bar{J} \cdot [\bar{E}] dV - \frac{1}{j\omega\kappa\epsilon_0} [K][B][V] \quad (5-34)$$

$$j\omega\mu_0[g] = -[C][V] \quad (5-35)$$

$$j\omega\kappa\epsilon_0[f] = -\iiint_V \bar{J} \cdot [\bar{F}] dV \quad (5-36)$$

where we assume  $N$  cavity modes and  $M$  waveguide modes are considered.  $[h]$ ,  $[e]$ ,  $[g]$ , and  $[f]$  are  $(N \times 1)$  vectors of wave amplitudes.  $[B]$  and  $[C]$  are  $(N \times M)$  matrices of surface integral coefficients as described by (5-25) to (5-28).  $[\bar{E}]$ ,  $[\bar{F}]$  are  $(N \times 1)$  vectors with elements  $\bar{E}_n$ ,  $\bar{F}_n$ , and  $[\Delta]$  is a diagonal matrix of  $\Delta_n$ .  $[V]$  is the  $(M \times 1)$  vector of equivalent voltages at the aperture cross-section. This vector is determined using generalised junction admittance as given in the following section.

## 5.4 Generalised Admittance

The second boundary condition on the aperture surface is the continuity of tangential magnetic fields as expressed by:

$$\hat{n} \times \bar{H} \Big|_{S_0} = \hat{n} \times \bar{H}_t \Big|_{S_0} \quad (5-37)$$

Using the mode matching expansion for the tangential fields at the aperture we get:

$$\bar{H}_t = \sum_k I_k^e \bar{h}_k^e + \sum_k I_k^h \bar{h}_k^h \quad (5-38)$$

where  $I_k^{mode}$  is the normalised equivalent current for the  $k$ th waveguide mode. By substituting (5-6) and (5-38) into (5-37) we obtain:

$$\hat{n} \times \left\{ \sum_n h_n \bar{H}_n + \sum_n g_n \bar{G}_n \right\} \Big|_{S_0} = \hat{n} \times \left\{ \sum_n I_n^e \bar{h}_n^e + \sum_k I_k^h \bar{h}_k^h \right\} \quad (5-39)$$

Multiplying the above relation by the waveguide eigenvector  $\bar{e}_m^{mode}$  and integrating over the surface  $S_0$  and noting that  $\hat{n} = -\hat{a}_z$  we obtain:

$$\sum_n h_n B_{nm}^{mode} + \sum_n g_n C_{nm}^{mode} = \sum_k \left[ I_k^e \int_{S_0} \bar{e}_k^{mode} \times \bar{h}_k^{mode} \cdot \hat{a}_z dS + I_k^h \int_{S_0} \bar{e}_k^{mode} \times \bar{h}_k^{mode} dS \right]$$

where *mode* means either *e* or *h*. Considering the orthogonality conditions of (5-18) and (5-19) and using (5-20), the integral series on the right-hand side will reduce to one term. Thus let

$$\sum_n h_n^i B_{nm}^{mode} + \sum_n g_n^i C_{nm}^{mode} = Y_m^{i, mode} I_m^{mode} \quad (5-40)$$

where  $I_m^{mode}$  is the normalised current for the  $m$ th waveguide mode evaluated at the aperture cross-section and  $Y_m^{mode}$  is the wave admittance of the corresponding waveguide mode. Equation (5-40) can be expressed in matrix form as below:

$$[B]^T[h] + [C]^T[g] = [Y][I]_{norm} \quad (5-41)$$

where  $[I]_{norm}$  is a  $(M \times 1)$  vector of normalised waveguide currents evaluated at the aperture and  $[Y]$  is a diagonal matrix of wave admittances for  $M$  waveguide modes. The right-hand side of (5-41) indicates the actual currents as below:

$$[I] = [Y][I]_{norm} \quad (5-42)$$

Now if we substitute  $[h]$  and  $[g]$  from (5-33) and (5-35) into (5-41) and use (5-42) we obtain a direct expression between the current and voltage vectors at the aperture cross-section. To avoid a long expression we perform two steps:

**Step- 1:** we remove the electric current source, i.e. put  $\bar{J} = 0$ . In this case we obtain:

$$[I] = - \left[ [B]^T [\Delta]^{-1} [B] + \frac{1}{j\omega\mu_0} [C]^T [C] \right] [V] \quad (5-43)$$

The minus sign accounts for the change of current direction which will be inward in the absence of an internal source. Therefore the generalised cavity admittance will be determined from (5-43). Let

$$[Y]_{cav} = -[I][V]^T = [B]^T[\Delta]^{-1}[B] + \frac{1}{j\omega\mu_0}[C]^T[C] \quad (5-44)$$

A symbolic representation of  $I$ ,  $V$ , and  $Y_{cav}$  for an arbitrary waveguide mode is illustrated in Figure 5-4. The cavity is assumed to be coupled to a dissimilar waveguide at  $z = d$ .

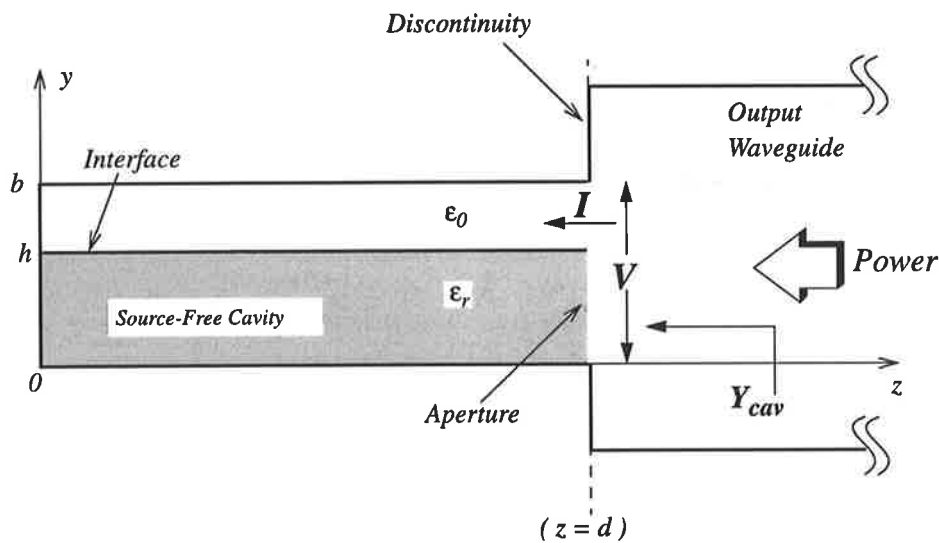


Figure 5-4. Illustration of step-1. The equivalent current is directed toward the cavity

**Step-2:** retaining the current source, we repeat the calculation of (5-43). The result is as below:

$$[I] = [I]_{source} - [Y]_{cav}[V] \quad (5-45)$$

$$[I]_{source} = \frac{1}{j\omega\kappa\epsilon_0} [B]^T [\Delta]^{-1} [K] \iint_V \bar{J} \cdot [\bar{E}] dV \quad (5-46)$$

In this case  $[I]$  represents the propagating mode currents inside the partially-filled waveguide that are evaluated at the  $z = d$  plane and directed toward the output waveguide. This situation is shown in Figure 5-5. For a typical  $LSM^y_{mn}$  propagating mode the matrix equation will be reduced to the following:

$$I_{mn}^e = I_{source}^{e,mn} - Y_{cav}^{e,mn} V_{mn}^e \quad (5-47)$$

where

$$I_{source}^{e,mn} = \frac{1}{j\omega\kappa\epsilon_0} \sum_{\lambda=1}^L \frac{B_{mn\lambda}^e k_{mn\lambda}}{\Delta_{mn\lambda}} \iiint_V \bar{J} \cdot \bar{E}_{mn\lambda}^e dV \quad (5-48)$$

and the cavity admittance is given from (5-44) to be:

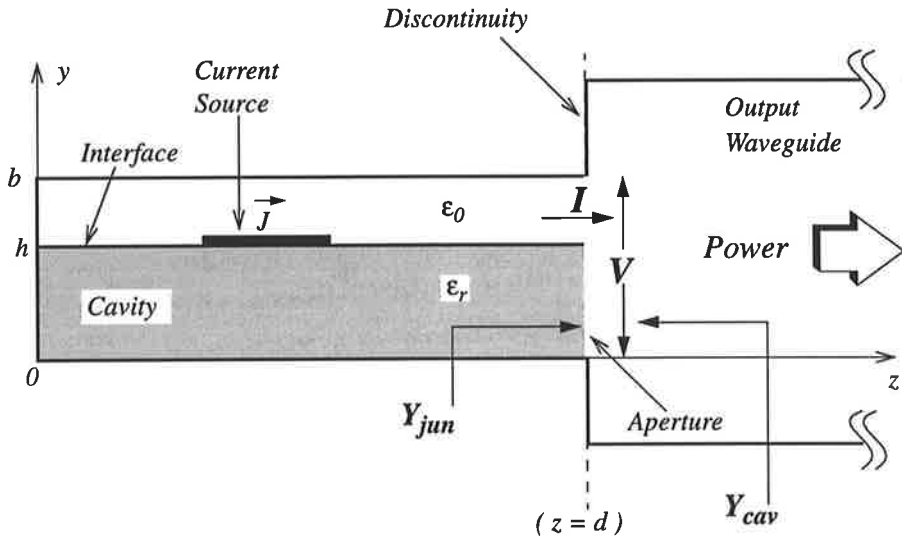


Figure 5-5. Illustration of a source-impressed cavity. All transmission line components are defined at the discontinuity plane.

$$Y_{cav}^{e,mn} = -I_{mn}^e / V_{mn}^e = \sum_{p=1}^L \frac{(B_{mnp}^e)^2}{\Delta_{mnp}} + \sum_{q=0}^L \frac{(C_{mnq}^e)^2}{j\omega\mu_0} \quad (5-49)$$

$L$ , the number of cavity modes is theoretically infinite. However in practice it is made sufficiently high for accurate calculations.  $\Delta_{mnp}$  is the frequency selective term as defined by equation (C-47):

$$\Delta_{mnp} \equiv \mu_0 \omega_{mnp} \left[ \left\{ \frac{\omega}{\omega'} - \frac{\omega'_{mnp}}{\omega} \right\} j + \frac{1}{Q'_{mnp}} \right] \quad (5-50)$$

where  $\omega_{mnp}$  is the resonant frequency of the  $\text{LSM}^Y_{mnp}$  mode and  $\omega'_{mnp}$  and  $Q'_{mnp}$  are the modified resonant frequency and the unloaded-Q respectively. Obviously  $\Delta_{mnp}$  denotes a resonant effect corresponding to the  $\text{LSM}^Y_{mnp}$  mode. Therefore the series that involves  $\Delta_{mnp}$  accounts for the resonant modes, whereas the series with  $j\omega\mu_0$  terms is relevant to the local fields and presents an inductance. If the operating frequency  $\omega$  is close to one of the resonant modes, say  $\omega_{mnl}$ , then from (5-50) the  $|\Delta_{mnl}|^{-1} \gg 1$  and the remaining resonant terms are dominated by the  $\text{LSM}^Y_{mnl}$  mode. The junction admittance  $[Y]_{jun}$  that is presented to the propagating modes is derived from the scattering matrix of the waveguide discontinuity as will be explained below. The relationship between the current and voltage vectors at the junction would be as follows:

$$[I] = [Y]_{jun}[V] \quad (5-51)$$

An equivalent circuit for  $Y_{cav}^{e,mn}$  and  $Y_{jun}^{e,mn}$ , based on (5-49) to (5-51) evaluated at the intersection plane ( $z = d$ ), is shown in Figure 5-6.

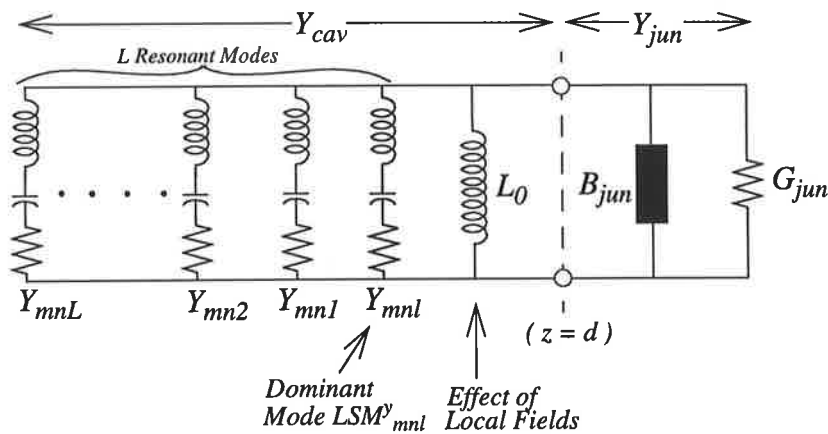


Figure 5-6. Equivalent circuit of the cavity in terms of resonant modes and local fields

Now substituting (5-51) into (5-45) results in the voltage vector that has been unknown in equations (5-33) to (5-35). Let

$$[V] = \{[Y]_{cav} + [Y]_{jun}\}^{-1} [I]_{source} \quad (5-52)$$

where  $[V]$  is a  $M \times 1$  vector with elements  $V_{mn}^{mode}$  and  $M$  is the number of waveguide propagating modes.  $[Y]_{cav}$ , and  $[Y]_{jun}$  are  $M \times M$  diagonal matrices and  $[I]_{source}$  is defined from (5-46) with elements the same as  $I_{source}^{e,mn}$  given by (5-48). An equivalent circuit based on equations (5-45), (5-51), and (5-52) for an arbitrary propagating mode is shown in Figure 5-7.

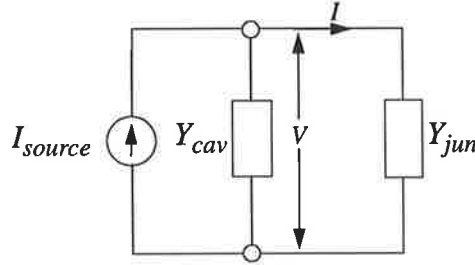


Figure 5-7. Equivalent circuit of the cavity evaluated at the intersection  $z = d$

By substituting  $[V]$  from (5-52) into the cavity equations (5-33) to (5-35), for a typical LSM $^y_{mnl}$  cavity mode we obtain the following expressions:

$$e_{mnl}^e = -\frac{Z_0^2}{\Delta_{mnl}} \int_V \bar{J} \cdot \bar{E}_{mnl}^e dV - \frac{1}{j\omega\kappa\epsilon_0} \frac{k_{mnl}B_{mnl}^e}{\Delta_{mnl}} (Y_{cav}^{e,mn} + Y_{jun}^{e,mn})^{-1} I_{source}^{e,mn} \quad (5-53)$$

$$h_{mnl}^e = \frac{1}{j\omega\kappa\epsilon_0} \frac{k_{mnl}}{\Delta_{mnl}} \int_V \bar{J} \cdot \bar{E}_{mnl}^e dV - \frac{B_{mnl}^e}{\Delta_{mnl}} (Y_{cav}^{e,mn} + Y_{jun}^{e,mn})^{-1} I_{source}^{e,mn} \quad (5-54)$$

$$g_{mnl}^e = -\frac{1}{j\omega\mu_0} C_{mnl}^e (Y_{cav}^{e,mn} + Y_{jun}^{e,mn})^{-1} I_{source}^{e,mn} \quad (5-55)$$

where  $I_{source}^{e,mn}$  is given by (5-48). By changing the superscript  $e$  to  $h$ , the above expressions will be valid for LSE $^y_{mnl}$  modes. Equations (5-53) to (5-55) together with (5-32) establish a complete solution for the source-impressed partially-filled cavity coupled

to a waveguide. The source integrals in (5-53), (5-54), (5-48) and (5-32) are determined by assuming an appropriate current distribution on the coupling probe. Detailed discussion will be given in Section 5.6 .

#### 5.4.1 Source-free Cavity

In this case the cavity is excited by the aperture and the direction of the current is reversed compared with the source-impressed cavity, as shown in Figure 5-4. The voltage at the intersection plane ( $z = d$ ) is constant and specified from the air-filled waveguide. Therefore from the general equations (5-29) to (5-31) we obtain the following for the  $\text{LSM}^y_{mn1}$  cavity mode:

$$e_{mn1}^e = -\frac{k_{mn1}}{j\omega\kappa\epsilon_0\Delta_{mn1}} \frac{1}{V_{mn}^e} B_{mn1}^e \quad (5-56)$$

$$h_{mn1}^e = -\frac{1}{\Delta_{mn1}} V_{mn}^e B_{mn1}^e \quad (5-57)$$

$$g_n = -\frac{1}{j\omega\mu_0} V_{mn}^e C_{mn1}^e \quad (5-58)$$

where  $V_{mn}^e$  is the equivalent voltage of the  $\text{LSM}^y_{mn}$  propagating mode evaluated at the intersection plane ( $z = d$ ) and is mainly determined from the voltage level inside the air-filled waveguide by transferring it through the S-parameters of the waveguide discontinuity. Obviously no  $F$ -field is excited in this case.

#### 5.4.2 Completely Enclosed Cavity

The effect of closing the aperture is the same as setting the aperture surface voltage to zero. This is equivalent to dropping the series terms in (5-29) to (5-31) and results in the following for a  $\text{LSM}^y_{mn1}$  cavity mode:

$$e_{mn1}^e = -\frac{Z_0^2}{\Delta_{mn1}} \iiint_V \bar{J} \cdot \bar{E}_{mn1}^e dV \quad (5-59)$$

$$h_{mnl}^e = \frac{k_{mnl}}{j\omega\kappa\epsilon_0\Delta_{mnl}} \iiint_V \bar{J} \cdot \bar{E}_{mnl}^e dS \quad (5-60)$$

$$f_{mnl} = \frac{-1}{j\omega\kappa\epsilon_0} \iiint_V \bar{J} \cdot \bar{F}_{mnl} dV \quad (5-61)$$

where  $\bar{J}$  is the vector electric current source embedded on the dielectric interface as shown in Figure 5-5. No  $G$ -field is excited as there is no aperture.

## 5.5 Field Distribution on the Interfacial Surface

The LSM<sup>y</sup> electric field on the dielectric interface is determined from equation (C-5) as:

$$\bar{E}_t^y \Big|_{y=h} = \sum_{\lambda} (e_{mn\lambda}^e \bar{E}_{mn\lambda t}^y + f_{mn\lambda} \bar{F}_{mn\lambda t}^y) \Big|_{y=h} \quad (5-62)$$

where  $\bar{E}_t^y \Big|_{y=h}$  is the transverse component with respect to the  $y$ -axis evaluated at the interface.  $e_n$  and  $f_n$  are determined from equations (5-53) and (5-32) and  $\bar{E}_{nt}^y$  and  $\bar{F}_{nt}^y$  are the transverse eigenvectors obtained from (D-18) to (D-20), and (5-26) to (5-28) respectively. A computer program has been developed to calculate and plot the electric and magnetic fields inside the cavity. For example the specifications of cavity number I is detailed in Table 5-1. It incorporates a current source and an aperture.

**Table 5-1. Specifications of partially-filled cavity- I.**

Length.....	80 mm	Dielectric Thickness.....	8.41 mm	Cavity Mode	LSM <sup>y</sup> <sub>303</sub>
Width.....	72 mm	Air-Gap.....	3.0 mm	Frequency....	3.503 GHz
Height.....	11.41 mm	Average Dielectric Constant....	10.61	Status.....	Source, and Aperture

The field pattern on the dielectric interface is plotted based on the computer calculations of (5-62) and is shown in Figure 5-8 (a). The field amplitudes  $e_{mn\lambda}^e$  and  $f_{mn\lambda}$  are generally obtained from (5-53) and (5-32). For the fully enclosed cavity number II the

field distributions are similarly obtained from (5-62) and the field amplitudes are given by (5-59) and (5-61). Table 5-2 specifies this cavity and the field pattern is plotted in Figure 5-8 (b).

**Table 5-2. Specifications of short-circuited partially-filled cavity- II.**

Length.....	120 mm	Dielectric Thickness.....	8.41 mm	Cavity Mode	$LSM^y_{305}$
Width.....	72 mm	Air-Gap.....	3.0 mm	Frequency....	3.621 GHz
Height.....	11.41 mm	Average Dielectric Constant....	10.61	Status.....	Source, and No Aperture

Also for the source-free cavity number III with specifications set out in Table 5-3 the field distribution is plotted in Figure 5-8 (c).

The field amplitude  $e_{mn\lambda}^e$  is calculated from (5-56) and no  $F$ - field is excited.

**Table 5-3. Specifications of a source-free partially-filled cavity- III**

Length.....	84.6 mm	Dielectric Thickness.....	7.62 mm	Cavity Mode	$LSM^y_{103}$
Width.....	22.86 mm	Air-Gap.....	2.54 mm	Frequency....	3.696 GHz
Height.....	10.16 mm	Average Dielectric Constant....	10.61	Status.....	Source-free, Aperture

### 5.5.1 The Effect of the Aperture on the Resonant Frequency

The aperture introduces a reactance that is determined from the admittance of the junction namely:

$$B_{jun}^{e,mn} = \Im m\{Y_{jun}^{e,mn}\} \quad (5-63)$$

where a  $LSM^y_{mn}$  propagating mode is assumed. For a cavity that is coupled to either an air-filled or a partially-filled waveguide, the resonance condition is generally established as a particular frequency at which the net cavity reactance at the intersection ( $z = d$ ) is zero. This condition leads to the exact resonant frequency ( $\omega = \omega''$ ) that is slightly different from the dominant mode fully enclosed frequency  $\omega_{mnl}$ .

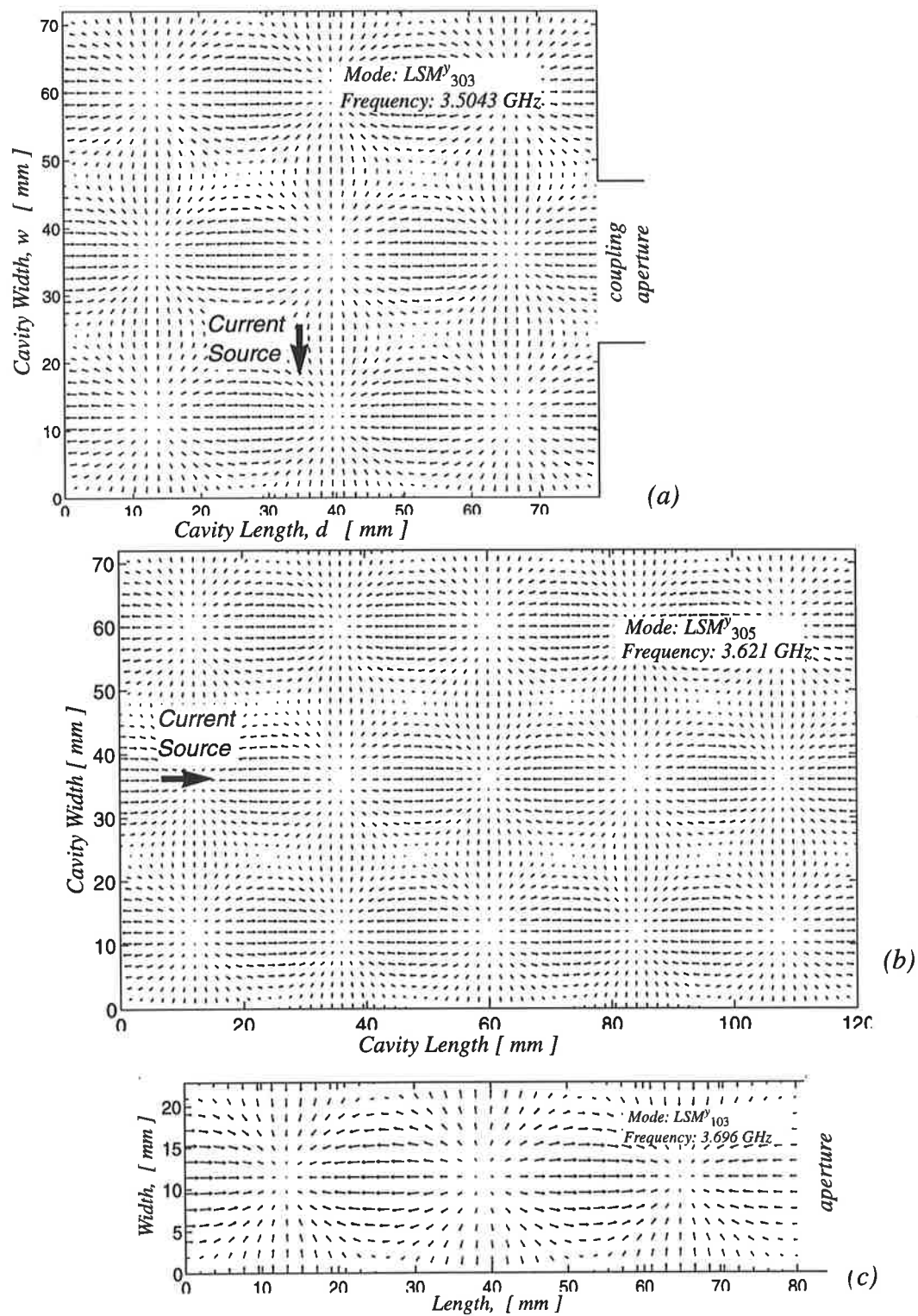


Figure 5-8. Plot of electric field pattern on the dielectric interface of: (a) cavity -I with source and aperture, (b) cavity -II with source and without aperture and (c) cavity -III with aperture and without source

With regard to the equivalent circuit of Figure 5-6, the junction reactance should be cancelled out by the cavity reactance, namely [56]:

$$B_{jun}^{e,mn} + \Im m\{Y_{cav}^{e,mn}\} = 0 \Big|_{\omega = \omega''} \quad (5-64)$$

Calculation of  $\omega''$  from the above equation could be very difficult because  $B_{jun}^{e,mn}$  is frequency dependent and should be calculated from mode matching analysis of the waveguide discontinuity, and also the cavity reactance is determined from equation (5-49). For simplicity  $B_{jun}^{e,mn}$  is substituted by its pre-determined value at  $\omega_{mnl}$  without significant error. This is because the junction S-parameters are only slowly dependent on the frequency. Thus let:

$$B_{jun}^{e,mn}(\omega_{mnl}) + \Im m\{Y_{cav}^{e,mn}\} \Big|_{\omega = \omega''} \cong 0 \quad (5-65)$$

Once the exact resonant frequency is calculated from (5-65), the coupling factor can be determined by transforming the cavity admittance to the output of the coupling structure as shown in Figure 5-9. The new admittance that is seen from the output waveguide is obtained from the following equation:

$$Y_{in} = Y_{03} \left( y_{22} - \frac{y_{12}y_{21}}{y_{11} + \bar{Y}_{cav}} \right) \quad (5-66)$$

where  $\bar{Y}_{cav}$  is the normalised cavity admittance as obtained from (5-49) at  $\omega = \omega''$ , and  $Y_{03}$  is the wave admittance of  $LSM^y_{10}$  (or  $TE^z_{10}$ ) in the air-filled waveguide.  $y_{ij}$ , the admittance parameters, are obtained from the mode matching calculation of the coupling structure that will be explained in Chapter 6.

Therefore the coupling factor can be defined by:

$$\beta = Y_{03}/\Re e(Y_{in}) \quad (5-67)$$

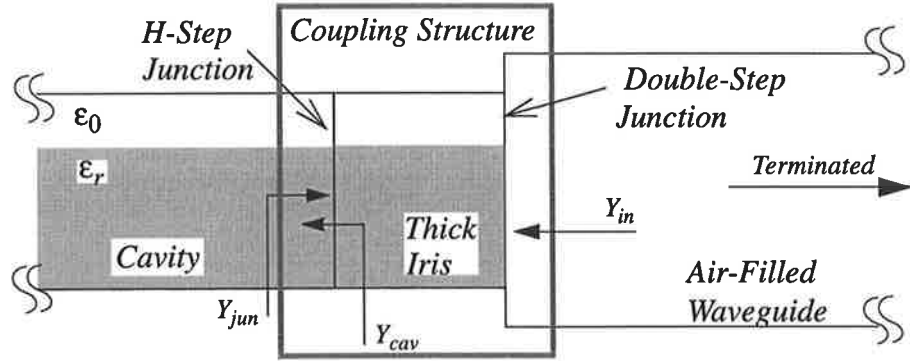


Figure 5-9. Diagram of the coupling structure connecting the cavity to the air-filled waveguide

Unfortunately the solution of (5-65) is not straightforward due to the complicated expression for  $Y_{cav}^{e,mn}$ . A computer program has been developed using optimisation techniques for numerical calculation of  $\omega''$  from equation (5-65). Typical results for the cavity number I, as specified in Table 5-2, is given below.

Closed Cavity Resonant Freq at $TM^y_{303} = 3.503$ GHz
Exact Resonant Freq at $TM^y_{303} = 3.561$ GHz
Coupling Factor = 2.2813
Cavity Impedance at the Intersection is $Z_{cav} = 27.65+237.4i$ ohm
Impedance of the Coupling Structure is $Z_{jun} = 118.2-142.6i$ ohm
Normalised cavity Admittance is $y_{cav} = 0.06162-0.529i$
Normalised Port Admittance is $y_{jun} = 0.4384+0.529i$
Normalised Input Admittance is $y_{in} = 0.7423 - 0.0740i$
Minimum Error = 1.775e-026

Figure 5-10. Numerical solution of equation (5-65) for the cavity number I

Also the results of calculation for the coupled cavity number III is given for different resonant modes from the solutions of (5-65) and (5-67) as set out in the table below:

Mode	$LSM^y_{101}$	$LSM^y_{102}$	$LSM^y_{103}$	$LSM^y_{104}$
Mode Res. Freq.	3.116 GHz	3.322 GHz	3.612 GHz	3.953 GHz
Exact Res. Freq.	3.136 GHz	3.378 GHz	3.694 GHz	4.063 GHz
Coupling	1.575	0.9882	1.162	0.4999
$Y_{cav}$ [norm.]	0.176+j1.03	0.047+j0.48	0.034+j0.21	0.027+j0.20
$Y_{jun}$ [norm.]	0.112--j1.03	0.048--j0.48	0.029--j0.21	0.053--j0.20

## 5.6 Probe Excitation

In the novel oscillator assembly, the excitation of the partially-filled cavity by the transistor oscillator is accomplished by a probe comprising a metal strip embedded on the air-dielectric interface. The probe should be properly positioned with respect to the surface electric field distribution so that it will 1) be strongly coupled to the fields and excite the cavity, and 2) introduce the required load impedance at the output of the MESFET oscillator. Figure 5-11 shows the probe positioned on the dielectric interface of cavity number I, where the location of the probe is specified with respect to the cavity walls.

The direction of the current source  $\bar{J}$  is shown symbolically on the strip flowing in the direction of the surface electric field component that is parallel to it, but it will be  $180^\circ$  different in phase to feed power into the cavity.

The performance of the probe as a link between the transistor oscillator circuit and the cavity has been generally explained in Section 3.5.1 . A detailed analysis should be done in two steps:

- (i) The effect of the probe as a current source inside the cavity. This gives rise to the volume integrals in the field equations (5-53), (5-54), (5-48) and (5-32). These integrals should be determined in order to find the field distribution inside the cavity.
- (ii)The probe acts as a load impedance with respect to the transistor oscillator circuit.

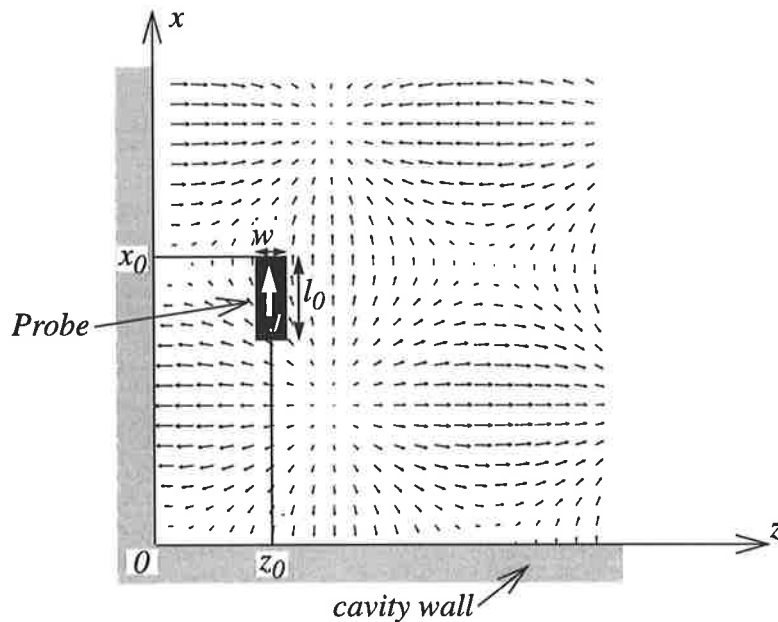


Figure 5-11. Positioning of the probe strip on the air-dielectric interface

A complete analysis relevant to these effects is set out below.

### 5.6.1 Source Integrals

The ambiguity in the field amplitude expressions stems from the volume integrals involving the current source  $\bar{J}$  as given below:

$$\mathfrak{I}_{mnl}^e = \int_V \bar{J} \cdot \bar{E}_{mnl}^e dV \quad (5-68)$$

$$\mathfrak{I}_{mnl}^f = \int_V \bar{J} \cdot \bar{F}_{mnl}^e dV \quad (5-69)$$

where  $\bar{E}_{mnl}^e$  and  $\bar{F}_{mnl}^e$  are eigenfunctions for the LSMY<sub>mnl</sub> mode. The procedure is the same for LSE<sub>mnl</sub> cavity modes and the eigenfunctions are provided from Appendix C.  $\bar{J}$  is the electric current density on the probe strip as shown in Figure 5-11, that is:

$$\bar{J} = J_x \hat{a}_x \quad (5-70)$$

Assuming a uniform current distribution across the width of the strip as given by Harrington [24] we obtain:

$$J_x = I_x \frac{\sin k(x_0 + l_0 - x)}{\sin k l_0} \delta(y - h) \text{ with } x_0 \leq x \leq x_0 + l_0, z_0 - \frac{w}{2} \leq z \leq z_0 + \frac{w}{2} \quad (5-71)$$

which is clearly illustrated in Figure 5-12.  $k$  is the medium wave-number and is defined in terms of operating frequency and the medium constants:

$$k = \omega \sqrt{\epsilon_{eff} \epsilon_0 \mu_0} \quad (5-72)$$

where  $\epsilon_{eff}$  is the effective dielectric constant of the partially-filled medium as obtained from the analysis of the shielded inverted microstrip line. This is because the current strip is located exactly on the air-dielectric interface. Typical values of  $\epsilon_{eff}$  for the cavity number I are obtained from Figure 4-8 (b).

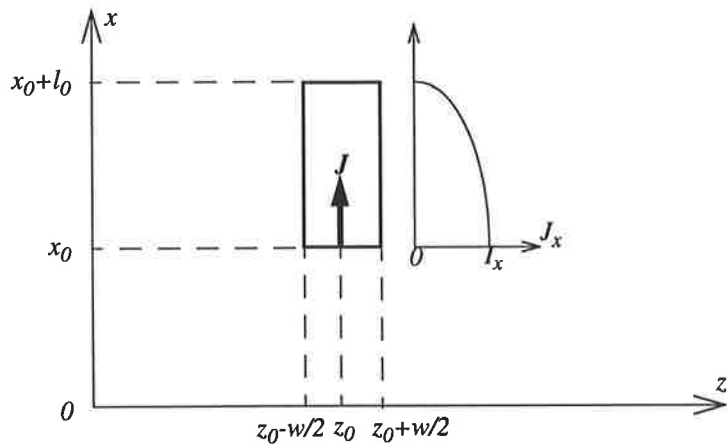


Figure 5-12. Current distribution on the surface of the probe strip

By substituting  $\bar{J}$  and  $\bar{E}_{mn}^e$  from (5-70) and (5-71), and (D-18) into (5-68) and noting that the tangential electric field is continuous at the interface we obtain the analytical solution as below:

$$\mathfrak{I}_{mn}^e = -\frac{I_x}{\sin k l_0} A_{mn}^{d,e} (k_{mn})^{-1} \{ \alpha(\beta_n^d) \sin(\beta_n^d h) \} P_x Q_x \quad (5-73)$$

where

$$P_x = \frac{\sin \alpha x_0 (k \sin \alpha l_0 - \alpha \sin k l_0) + k \cos \alpha x_0 (\cos k l_0 - \cos \alpha l_0)}{\alpha^2 - k^2} \quad (5-74)$$

$$Q_x = \frac{2}{\gamma} \sin \gamma l_0 \sin \gamma \frac{w}{2} \quad (5-75)$$

Also  $\alpha = \frac{m\pi}{a}$  and  $\gamma = \frac{l\pi}{d}$ .

It should be noted that for a probe strip located in the  $z$ - direction i.e.  $\bar{J} = J_z \hat{a}_z$ , the result is exactly the same as (5-73) except that  $\alpha$  and  $x_0$  should be replaced by  $\gamma$  and  $z_0$  respectively and vice versa.

Similarly by substituting  $\bar{J}$  and  $\bar{F}_{mnl}$  from (5-70) and (D-26) into equation (5-69) we obtain the following analytical solution:

$$\mathfrak{I}_{mnl}^f = \frac{I_x}{\sin k l_0} A_{mnl}^{d,f} (k_{mnl})^{-1} \{ \alpha \sin(\beta_n^d h) \} P_x Q_x \quad (5-76)$$

where  $P_x$  and  $Q_x$  are obtained from (5-74) and (5-75) respectively.

For a probe strip in the  $z$ - direction i.e.  $\bar{J} = J_z \hat{a}_z$ , the solution of the volume integral will be easily obtained by simply swapping  $\alpha$  with  $\gamma$  and  $x_0$  with  $z_0$  in equations (5-76), (5-74) and (5-75).

### 5.6.2 Normalised Source Integrals

We can define normalised source integrals corresponding to a current source with unit amplitude, that is:

$$\mathfrak{I}_{mnl}^e = I_x \tilde{\mathfrak{I}}_{mnl}^e \quad (5-77)$$

$$\mathfrak{I}_{mnl}^f = I_x \tilde{\mathfrak{I}}_{mnl}^f \quad (5-78)$$

Similar expressions can be defined in terms of  $I_z$  for z-directed probe strips. By substituting the above volume integrals into equations (5-48), (5-53) and (5-32) we can easily obtain:

$$e_{mnl}^e = I_x \cdot \tilde{e}_{mnl}^e \quad (5-79)$$

$$f_{mnl} = I_x \cdot \tilde{f}_{mnl} \quad (5-80)$$

where  $\tilde{e}_{mnl}^e$  and  $\tilde{f}_{mnl}$  are the normalised field amplitudes corresponding to a unit current source and are given by:

$$\tilde{e}_{mnl}^e = -\frac{Z_0^2}{\Delta_{mnl}} \tilde{\mathfrak{I}}_{mnl}^e - \frac{1}{(j\omega\kappa\epsilon_0)^2} \frac{k_{mnl} B_{mnl}^e}{\Delta_{mnl}} (Y_{cav}^{e,mn} + Y_{jun}^{e,mn})^{-1} \sum_{\lambda=1}^L \frac{k_{mn\lambda} B_{mn\lambda}^e}{\Delta_{mn\lambda}} \tilde{\mathfrak{I}}_{mn\lambda}^e \quad (5-81)$$

$$\tilde{f}_{mnl} = -\frac{1}{j\omega\kappa\epsilon_0} \tilde{\mathfrak{I}}_{mnl}^f \quad (5-82)$$

### 5.6.3 Probe Impedance

A variational formula for the input impedance of a cavity probe is given by Harrington [24]. Thus let:

$$Z_{in} = -\frac{1}{I_{in}^2} \iiint_V \bar{E} \cdot \bar{J} dV \quad (5-83)$$

where  $\bar{E}$  is the overall source-impressed electric field inside the cavity,  $\bar{J}$  is the current density on the probe surface, and  $I_{in}$  is the total driving current evaluated at the probe input as shown in Figure 5-13.

Substituting  $\bar{E}$  from equation (5-5) into the impedance formula (5-83) results in:

$$Z_{in} = -\frac{1}{I_{in}^2} \left[ \sum_{l=1}^L e_{mnl}^e \iiint_V \bar{E}_{mnl} \cdot \bar{J} dV + \sum_{l=1}^L f_{mnl} \iiint_V \bar{F}_{mnl} \cdot \bar{J} dV \right] \quad (5-84)$$

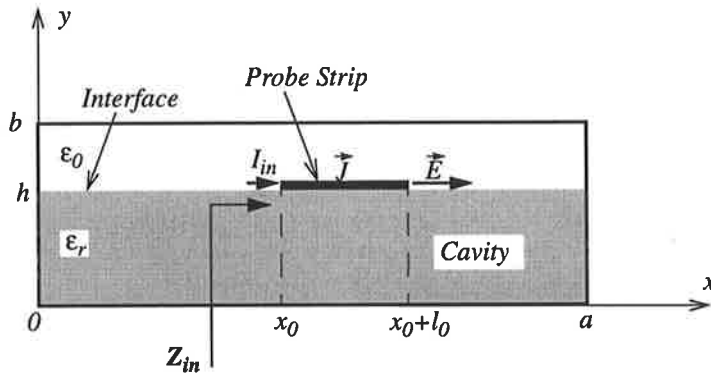


Figure 5-13. Input impedance of the probe strip

The current density  $\bar{J}$  on the probe strip is of critical importance. For a simple geometry of probe such as shown in Figure 5-12, with negligible metal thickness, the current distribution that is uniform across the strip width is still valid. The driving point current  $I_{in}$  is obtained by integration of  $\bar{J}$  as given by (5-70) and (5-71) across the strip width as below:

$$I_{in} = \int_{z_0 - w/2}^{z_0 + w/2} J_x dz = w I_x \quad (5-85)$$

Substituting the volume integrals and  $I_{in}$  from (5-68), (5-69) and (5-85) into (5-84) and using the normalised relations (5-77) to (5-80) will give:

$$Z_{strip} = Z_{in} = -\frac{1}{w^2} \sum_{l=1}^L \{ \tilde{e}_{mnl}^e \tilde{\mathfrak{I}}_{mnl}^e + \tilde{f}_{mnl} \tilde{\mathfrak{I}}_{mnl}^f \} \quad (5-86)$$

where  $\tilde{e}_{mnl}^e$  and  $\tilde{f}_{mnl}$  are determined from (5-81) and (5-82),  $\tilde{\mathfrak{I}}_{mnl}^e$  and  $\tilde{\mathfrak{I}}_{mnl}^f$  are given by equations (5-73) to (5-76), and  $w$  is the width of the probe strip.  $L$  is the number of modes that is high enough to give an accurate calculation.

Equation (5-86) has been implemented on a computer and calculated for a probe strip with the following specifications that are relevant to the design of a microwave oscillator test assembly.

**Table 5-4. Specification of the probe strip inside the cavity no. I**

Cavity	Driving Point Coordinate	Strip Width	Current
No. I by Table 5-2	$x_0$ 24 mm	$z_0$ 40.95 mm	2 mm $-\hat{a}_x$

The probe is extended along the  $x$ -direction as illustrated in Figure 5-11. A plot of calculated probe impedance as shown in Figure 5-14 reveals a strong capacitive reactance apparently transferred from the coupling aperture reactance which is also capacitive. This phenomena will be discussed in more detail through Chapters 6 and 7. The probe reactance has a dominant effect on the layout of the oscillator circuit.

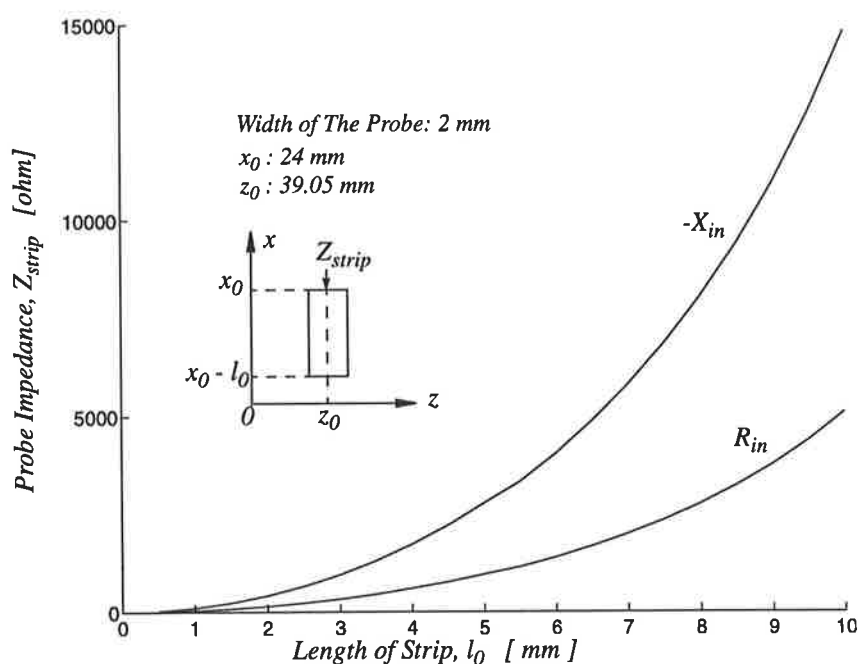


**Figure 5-14.** Plot of probe impedance versus the strip length for cavity number I relevant to a 3.5 GHz microwave assembly for design testing.

---

## Chapter 6

# *Design Methods*

## *Part III: Coupling Structure*

### **6.1 Introduction**

This chapter deals with the third constituent part of the novel oscillator assembly: *the coupling structure*. This part allows the oscillator power to be effectively propagated into the output waveguide. The structure incorporates four dissimilar waveguides as shown in Figure 6-1 (a). Oscillator power is generated in the main partially-filled waveguide (#1) and is propagated through the dielectric substrate toward the output (#4). Coupling to the output waveguide is accomplished by a thick iris that is designed to conform to the constraints of monolithic millimetre-wave fabrication. From the engineering point of view, the presence of the thick iris may appear to increase the overall complexity. However the mechanical joint of the two dissimilar waveguides (#1) and (#3) is only obtained by placing a flange between the two guides. Therefore a thick iris is formed inside the flange, constituting an intermediate waveguide (#2) that may be partially-filled by an extension of the dielectric substrate.

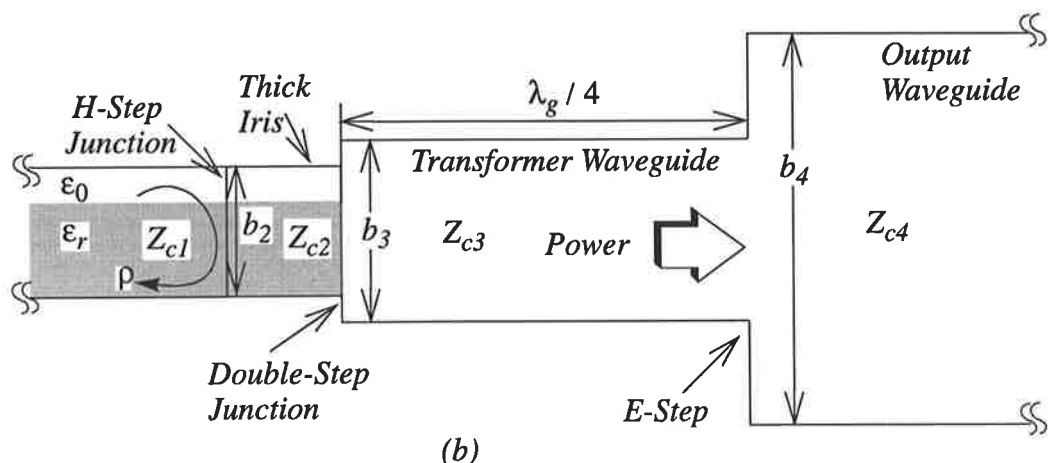
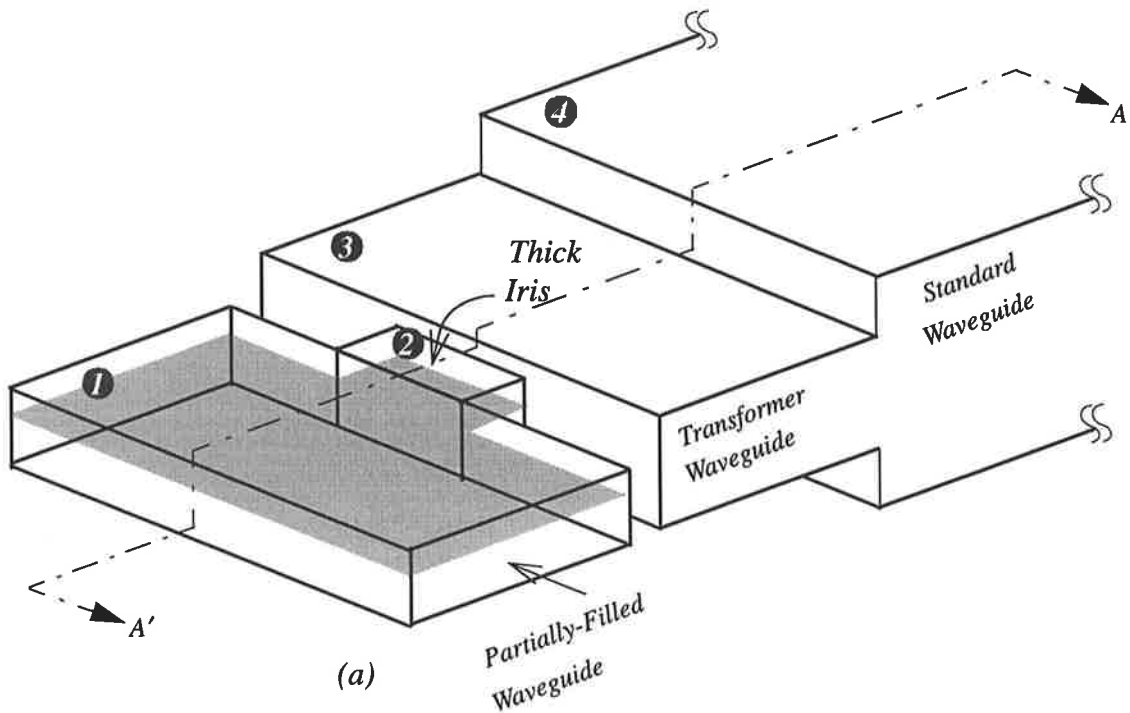


Figure 6-1. The coupling structure: (a) 3-D view (b) Cross-section A - A'

A view of the longitudinal cross-section is shown in Figure 6-1 (b) in which the discontinuities are clearly shown. The first discontinuity is an H-step between the input waveguide and the thick iris and the second is a double-step junction, connecting the iris

to the transformer waveguide. The third is an E-step junction which is assumed to be far away from the iris to simplify the design.

The effect of the transformer waveguide is to provide a means of adjusting the overall coupling factor, by altering the mismatch between the input and output waveguides. The length of the transformer waveguide should be about a quarter of a wavelength at the frequency of interest. Although both transformer and output waveguides have the same width and consequently the same wave impedance ( $Z_{wave}$ ), the characteristic impedance ( $Z_c$ ) will be different because it is defined to be proportional to the height [57] so that

$$Z_c = \frac{b}{a} Z_{wave} \quad (6-1)$$

where  $a$  and  $b$  are the guide's width and height respectively. The oscillator output load  $Z_{c4}$  will be changed by the transformer waveguide to a lower value at the double-step junction given simply by,

$$Z_{in} = \frac{Z_{c3}}{Z_{c4}} \quad (6-2)$$

if the transformer waveguide is a quarter of a wavelength long.

Therefore by reducing the height of guide #3, one can reduce the load at the thick iris and increase the overall coupling factor between the partially filled oscillator cavity and its output load.

Adjustment of the coupling factor in physically large microwave test assemblies can be practically achieved by attaching metal blocks to the top and bottom wall of the standard output waveguide as shown in Figure 6-2. The blocks may be identical and about a quarter of a wavelength long. The height of the output waveguide ( $b_4$ ) minus the height of the blocks ( $2H$ ) determines the height of the transformer waveguide ( $b_3$ ). Therefore the adjustment of the transformer waveguide is a matter of changing the metal blocks.

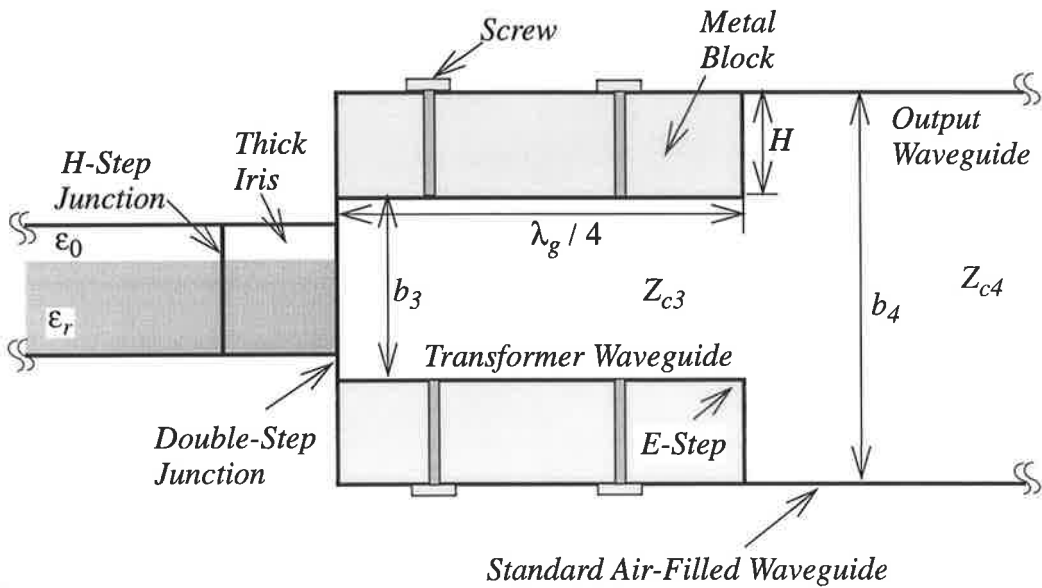


Figure 6-2. Formation of the transformer waveguide by attaching metal blocks inside the output waveguide

### 6.1.1 The Cavity Aperture Reflection Coefficient

Assume that the output waveguide is sufficiently long or connected to a matched termination. The most important parameter is the reflection coefficient  $\rho$  at the aperture in the cavity wall as shown in Figure 6-1 (b) and is related to its normalised admittance through the relationship:

$$Y_{jun} = \frac{1 - \rho}{1 + \rho} \quad (6-3)$$

where  $Y_{jun}$  has been widely used in the analysis of the partially-filled cavity as discussed in Chapter 5. However derivation of  $\rho$  is not easy and relies on the combination of both H-step and double-step discontinuities, transformed through the thick iris and the overall effect is very complicated. The E-step discontinuity of the air-filled waveguide is assumed to be far enough from the iris so that any fringing influence is negligible on the reflection coefficient. Therefore the critical section that should be analysed in detail is shown in Figure 6-3, comprising a section of thick iris and two junctions that are close

to each other ( $\Delta l \ll \lambda_g$ ). The first junction is an H-step discontinuity between two partially filled waveguides and the second is a double-step between a partially filled and an air-filled waveguide.

As far as the analysis of the partially-filled cavity is concerned ( Chapter 5) a knowledge of the cavity aperture admittance is adequate for the design of the oscillator assembly. However the following peculiarities make the derivation of  $Y_{jun}$  very difficult.

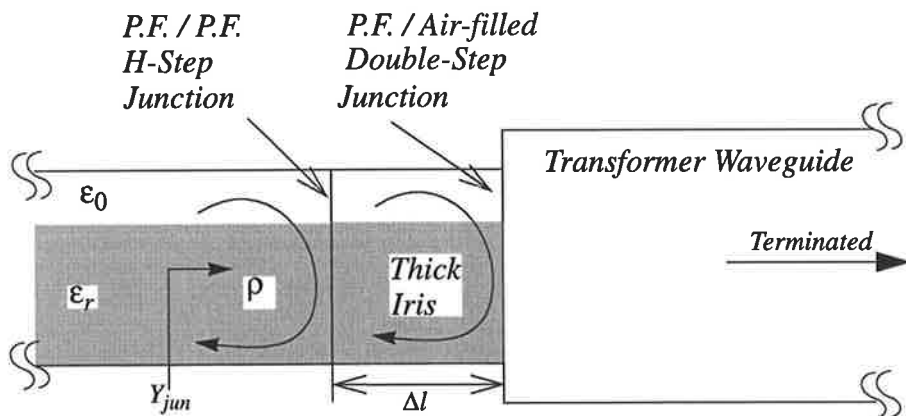


Figure 6-3. Critical part of the coupling structure comprising the thick iris and the junctions at each end

1. The evanescent hybrid modes that are excited in the vicinity of the junctions will store significant energy that contributes to the overall cavity aperture reactance ( $\Im m\{Y_{jun}\}$  ).
2. For the double-step junction, in particular, this energy is substantially carried by the higher order hybrid modes.
3. As the distance between the junctions ( $\Delta l$ ) is short enough with respect to the wavelength, these evanescent modes around the two junctions will react with each other in a complex manner.

4. In addition the cavity aperture is assumed to be very large, typically one third of the cavity cross-section, to give a strong coupling to the output waveguide and maximum transfer of power from the oscillator to the load. The coupling factor of most oscillator resonators is significantly greater than unity.
5. The cavity aperture admittance has a key influence on such design parameters as resonant frequency and the E-field distribution on the cavity dielectric interface.

These effects will eliminate any approximate solution for  $Y_{jun}$ . In fact the problem with waveguide junctions is that the higher order modes that are usually excited below cutoff frequency carry significant energy. Therefore an accurate method based on multi-mode analysis will be an appropriate solution in which these evanescent modes are taken into account. The structure of Figure 6-3 may be decomposed into the primary sections that are represented by the transmission-line models shown in Figure 6-4.  $[p]_J$  and  $[p]_L$  are diagonal matrices with elements  $p^i_J$  and  $p^k_L$  that are reflection coefficients corresponding to  $i$ -th and  $k$ -th excited modes.

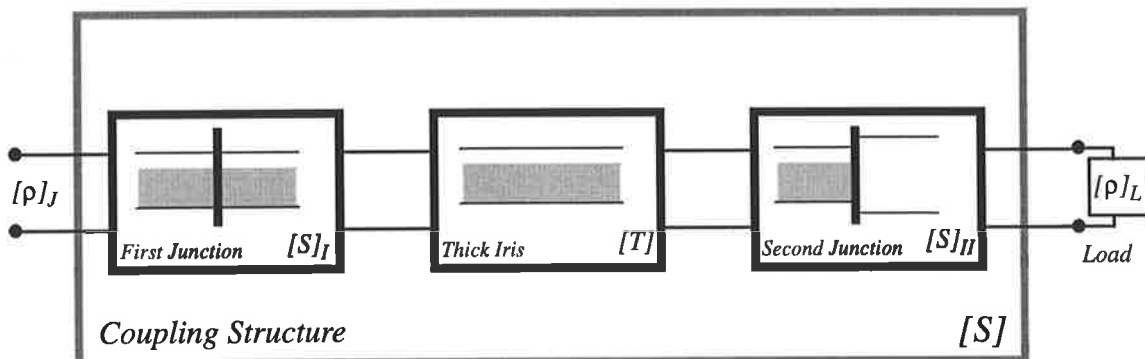


Figure 6-4. Decomposition of the coupling structure to cascaded transmission-line models

On this basis a systematic approach can be developed comprising the following:

- A generalised scattering matrix of the partially filled to partially filled waveguide junction,

- A multimode transmission-line matrix of the intermediate partially filled waveguide, and
- A generalised scattering matrix of the partially filled to air-filled waveguide junction.

The generalised scattering matrix incorporates S-parameters of all modes excited at the junction. Mathematically an infinite number of modes should be considered, but in practice, a finite number will give sufficiently accurate results. From Figure 6-4 the step-wise procedure for calculation of  $Y_{jun}$  would be as follows.

1. The generalised scattering matrices  $[S]_I$  and  $[S]_{II}$  are determined by numerical calculation at the frequency of interest.
2. The overall S-matrix of the coupling structure  $[S]$  is calculated by cascade connection using  $[S]_I$ ,  $[S]_{II}$  and the partially filled waveguide section in appropriate calculations.
3. The conventional scattering matrix  $[S_c]$  that relates the particular propagating modes between the input and output guides of the thick iris is extracted from the generalised S-matrix  $[S]$ . This is achieved by simply selecting the elements from  $[S]$  which correspond to the specified modes.
4. The cavity aperture reflection coefficient  $\rho$  is easily obtained from the  $[S_c]$  matrix as follows:

$$\rho = S_{c11} - \frac{S_{c12} \cdot S_{c21}}{S_{c22} + \rho_L} \quad (6-4)$$

where  $\rho_L$  is the load reflection coefficient at the double step junction. Then  $Y_{jun}$  is calculated from (6-3)

### 6.1.2 Mode-Matching Analysis of Waveguide Junctions

The mode-matching method has been recognised as a standard treatment of waveguide discontinuities and has been repeatedly used in the design of single-steps [58], double-steps [59], [60] and multiple-junctions [59], [61]. The method incorporates multi-

mode excitation and consequently avoids the disadvantages of classical approaches [62], [63] which are based on the assumption that only the dominant mode is propagating along the guide.

Looking to the published works pertinent to rectangular structures reveals that it has been common practice to expand the mode-matching equations in terms of conventional TE<sup>Z</sup> and TM<sup>Z</sup> eigenfunctions. However this is not always possible because the boundary conditions of the waveguide structure do not necessarily support such an expansion. Particularly in the structure of Figure 6-4, it will be more convenient to apply longitudinal section (LS) mode expansion due to the partially-filled boundary conditions. A new approach to mode-matching theory with LS mode expansion is presented in Appendix F where the formulae developed there will be used throughout the following sections.

## 6.2 Analysis of The First Junction

Referring to the block diagram of Figure 6-4 the first junction is located between the partially-filled resonant cavity waveguide and the thick iris. The cavity aperture should be large enough to allow substantial power out. A three dimensional view of the junction is shown in Figure 6-5. where the longitudinal and transversal cross-sections are marked by guide lines  $A - A'$  and  $B - B'$ .

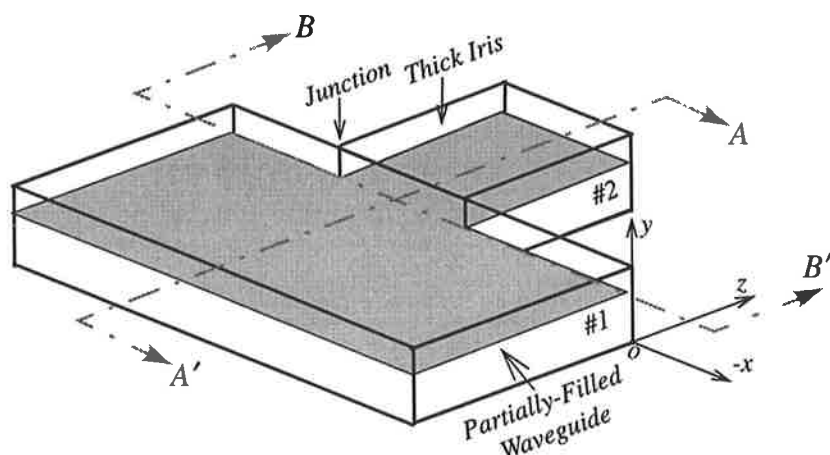


Figure 6-5. A view of the first junction with positions of its cross-sectional lines

The junction is clearly an H-step in which the height of the guides #1 and #2 are equal i.e.  $b_1 = b_2 = b$  and the offsets are defined by:

$$a_0 = \frac{a_1 - a_2}{2}, \quad b_0 = 0 \quad (6-5)$$

The tangential electric and magnetic fields at both sides of the junction are shown in Figure 6-6 (a) and the cross-section areas of guides #1 and #2 in Figure 6-6 (b). Cross-sectional areas  $S_1$  and  $S_2$  are subdivided into dielectric- and air- filled areas  $S_1^d$ ,  $S_1^a$  and  $S_2^d$ ,  $S_2^a$  as shown in Figure 6-6 (b).

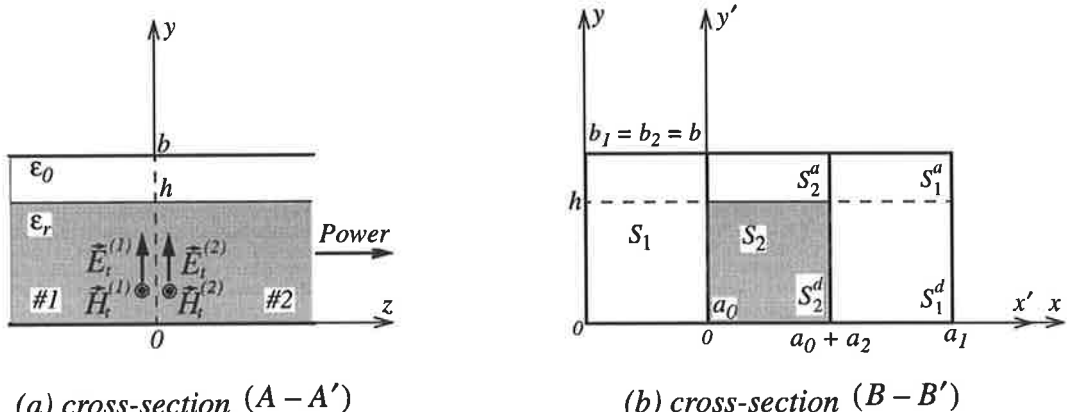


Figure 6-6. Cross-sections of the first junction: (a) longitudinal (b) transversal

$S_1$  is laid out in the  $z = 0$  plane of  $xyz$  coordinates whereas  $S_2$  is shown in the same plane of the  $x'y'z'$  coordinates. The two coordinates are related by equations (F-1) and (F-2) with offsets given by (6-5). Although the waveguides are inhomogeneously-filled, their boundary conditions remain continuous across the junction (cross-section  $A - A'$ ) and consequently the theory of Appendix F can be equally applied without loss of generality. However it should be kept in mind that every eigenfunction or wave admittance will be associated with two different expressions corresponding to dielectric- and air- filled regions. Accordingly the tangential fields of Figure 6-6 (a) are determined from equations

(F-5), (F-7), (F-9) and (F-10) and finally the junction scattering matrix  $[S]_I$  is obtained from equation (F-57) of Appendix F which is repeated here:

$$[S]_I = \begin{bmatrix} S_{11} & S_{12} \\ \dots & \dots \\ S_{21} & S_{22} \end{bmatrix}_{(M+N) \times (M+N)} = \begin{bmatrix} U^T & \Psi^T \\ \dots & \dots \\ -\Psi & U \end{bmatrix}^{-1} \cdot \begin{bmatrix} U^T & \Psi^T \\ \dots & \dots \\ \Psi & -U \end{bmatrix} \quad (6-6)$$

where  $U$  is a unit matrix with dimension  $(N \times M)$  and  $\Psi$  is the normalised wave-amplitude matrix and is given from (F-51) and (F-52):

$$\Psi = [Y^{(2)}]^{-1/2} \cdot [\Re] \cdot [Y^{(1)}]^{-1/2} \quad (M \times N) \quad (6-7)$$

$$\Psi^T = [Y^{(1)}]^{1/2} \cdot [\Re]^T \cdot [Y^{(2)}]^{-1/2} \quad (N \times M) \quad (6-8)$$

$[Y^{(v)}]$  is the diagonal matrix of the guide #v with elements  $Y_k^{v, mode, i}$  where the superscript “mode” stands for the  $e$ - ( $LSM^y_k$ ) or  $h$ - ( $LSE^y_k$ ) mode and “ $i$ ” indicates “ $d$ ” or dielectric- and “ $a$ ” or air- filled medium. The wave admittances for  $LSE^y$  and  $LSM^y$  modes are given respectively by (B-26), (B-27) and (B-55), (B-56) of Appendix B. The ambiguous reaction matrix  $[\Re]$  is generally defined in (F-31) and its elements should be determined from the set of reaction integrals given by (F-34) to (F-37). In fact  $[\Re]$  is a concept which is directly relevant to the junction topology and the reaction elements are to be determined for the junction of Figure 6-5.

### 6.2.1 Reaction Elements

Beginning with equations (F-34) to (F-37) and using the eigenfunctions of partially-filled waveguides from Appendix B we can follow the method of Section F.6 and finally obtain the reaction elements corresponding to the dielectric- filled area of the junction *i.e.*

$S_2^d$  as in Figure 6-6 (b):

$$\Re_{mnkl}^{e, e, d} = A_{kl}^{1, e, d} A_{mn}^{2, e, d} Y_{mn}^{2, e, d} \int_{S_2^d} (e_y^{1, e, d} h_x^{2, e, d}) dS = A_{kl}^{1, e, d} A_{mn}^{2, e, d} Y_{mn}^{2, e, d} J_x J_y^d \quad (6-9)$$

$$\begin{aligned} \Re_{mnkl}^{h, e, d} &= A_{kl}^{1, e, d} A_{mn}^{2, h, d} Y_{mn}^{2, h, d} \int_{S_2^d} (-e_x^{1, e, d} h_y^{2, h, d} + e_y^{1, e, d} h_x^{2, h, d}) dS \\ &= A_{kl}^{1, e, d} A_{mn}^{2, h, d} Y_{mn}^{2, h, d} \left[ \frac{-\alpha_k \beta_l^d}{\varepsilon_r k_0^2 - \beta_l^d} I_x I_y^d + \frac{\alpha_m \beta_n^d}{\varepsilon_r k_0^2 - \beta_n^d} J_x J_y^d \right] \end{aligned} \quad (6-10)$$

$$\Re_{mnkl}^{e, h, d} = \int_{S_2^d} (\bar{e}_{kl}^{1, h, d} \times \bar{h}_{mn}^{2, e, d}) dS = 0 \quad (6-11)$$

$$\Re_{mnkl}^{h, h, d} = A_{kl}^{1, h, d} A_{mn}^{2, h, d} Y_{mn}^{2, h, d} \int_{S_2^d} (e_x^{1, h, d} h_y^{2, h, d}) dS = A_{kl}^{1, h, d} A_{mn}^{2, h, d} Y_{mn}^{2, h, d} I_x I_y^d \quad (6-12)$$

where the primary integrals  $I_x$  and  $J_x$  are given by:

$$I_x = \int_0^{a_2} \cos(\alpha_k x') \cdot \cos(\alpha_m x) dx' = \int_0^{a_2} \cos(\alpha_k x') \cdot \cos \alpha_m(x' + a_0) dx' \quad (6-13)$$

$$J_x = \int_0^{a_2} \sin(\alpha_k x') \cdot \sin(\alpha_m x) dx' = \int_0^{a_2} \sin(\alpha_k x') \cdot \sin \alpha_m(x' + a_0) dx' \quad (6-14)$$

whereas  $I_y^d$  and  $J_y^d$  are defined as:

$$I_y^d = \int_0^h \cos(\beta_l^d y) \cdot \cos(\beta_n^d y) dy \quad (6-15)$$

$$J_y^d = \int_0^h \sin(\beta_l^d y) \cdot \sin(\beta_n^d y) dy \quad (6-16)$$

The eigenvalues in the  $x$ - direction are defined from (F-70):

$$\alpha_k = \frac{k\pi}{a_1}, \quad \alpha_m = \frac{m\pi}{a_2} \quad (6-17)$$

However  $\beta_l^d$  and  $\beta_n^d$  are not easy to obtain. They are related to corresponding air-filled eigenvalues  $\beta_l^a$  and  $\beta_n^a$  by:

*I. eigenvalue equations:*

$$\epsilon_r k_0^2 - \beta_l^{d2} = k_0^2 - \beta_l^{a2} \quad (6-18)$$

$$\epsilon_r k_0^2 - \beta_n^{d2} = k_0^2 - \beta_n^{a2} \quad (6-19)$$

*II. transcendental equations:*

$$\beta_l^d \cot(\beta_l^d h) = -\beta_l^a \cot(\beta_l^a g) \quad \text{for} \quad LSE_{kl}^y$$

$$\beta_l^d \tan(\beta_l^d h) = -\epsilon_r \beta_l^a \tan(\beta_l^a g) \quad \text{for} \quad LSM_{kl}^y \quad (6-20)$$

$$\beta_n^d \cot(\beta_n^d h) = -\beta_n^a \cot(\beta_n^a g) \quad \text{for} \quad LSE_{mn}^y$$

$$\beta_n^d \tan(\beta_n^d h) = -\epsilon_r \beta_n^a \tan(\beta_n^a g) \quad \text{for} \quad LSM_{mn}^y \quad (6-21)$$

Therefore at the frequency of interest, by numerical solution of equations (6-18) and (6-20) one can obtain  $\beta_l^d$  and  $\beta_l^a$ . Similarly  $\beta_n^d$  and  $\beta_n^a$  are determined from simultaneous solution of (6-19) and (6-21). In practice the numerical calculation is achieved by a computer program which has been developed based on the minimisation technique. Detailed explanation will be given later on. Also it should be noted that generally for a guide #v we have:

$$A_{kl}^{v, mode} = \begin{cases} A_{kl}^{v, mode, d} & 0 \leq y \leq h \\ A_{kl}^{v, mode, a} & h \leq y \leq b_v \end{cases} \quad (6-22)$$

$$Y_{kl}^{v, mode} = \begin{cases} Y_{kl}^{v, mode, d} & 0 \leq y \leq h \\ Y_{kl}^{v, mode, a} & h \leq y \leq b_v \end{cases} \quad (6-23)$$

where  $Y_{kl}^{v, mode}$  is determined from (B-26), (B-27) and (B-55), (B-56) of Appendix B.

However the normalised amplitude  $A_{kl}^{v, mode}$  is determined from (B-35), (B-64) and using assumption (F-15) is given by:

$$A_{kl}^{v, e, i} = \left( \frac{4}{ah^i} \right)^{\frac{1}{2}} [1 + \text{sinc}(2\beta_l^i h^i / \pi)]^{-\frac{1}{2}} \quad (6-24)$$

$$A_{kl}^{v, h, i} = \left( \frac{2\epsilon_{0k}}{ah^i} \right)^{\frac{1}{2}} [1 - \text{sinc}(2\beta_l^i h^i / \pi)]^{-\frac{1}{2}} \quad (6-25)$$

$$\text{where } h^i = \begin{cases} h & i \rightarrow d \\ g & i \rightarrow a \end{cases} \quad \begin{array}{ll} \text{dielectric-filled region} \\ \text{air-filled region} \end{array}$$

The reaction elements corresponding to the fields inside the air-filled regions can be derived in the same manner. However using equations (6-18) to (6-21), it can be proved that two sets of reaction elements for the dielectric- and air-filled regions are exactly the same. Thus the reaction elements given by (6-9) to (6-12) are uniquely determined and can be used for calculation of the junction scattering matrix  $[S]_J$  from equations (6-6) to (6-8).

### 6.3 The Second Junction

This junction is formed between the thick iris and the transformer waveguide as shown in Figure 6-7. It is a double-step and the offsets are defined by:

$$a_0 = \frac{a_2 - a_1}{2}, \quad b_0 = \frac{b_2 - b_1}{2} \quad (6-26)$$

From Figure 6-7 (b) the continuity of tangential fields at the iris opening results in:

$$E_t^{(1)} = \begin{cases} E_t^{(1), d} = E_t^{(2)} & \text{on } S_1^d \\ E_t^{(1), a} = E_t^{(2)} & \text{on } S_1^a \end{cases} \quad (6-27)$$

$$H_t^{(1)} = \begin{cases} H_t^{(1),d} = H_t^{(2)} & \text{on } S_1^d \\ H_t^{(1),a} = H_t^{(2)} & \text{on } S_1^a \end{cases} \quad (6-28)$$

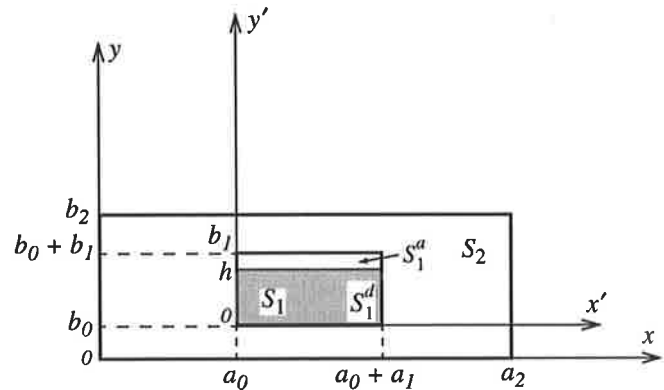
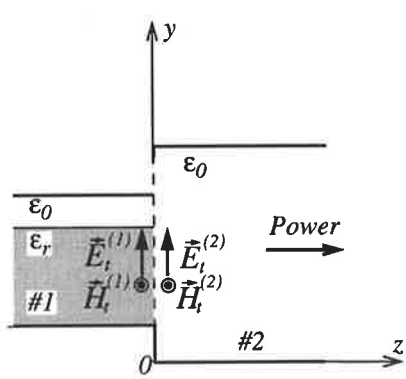
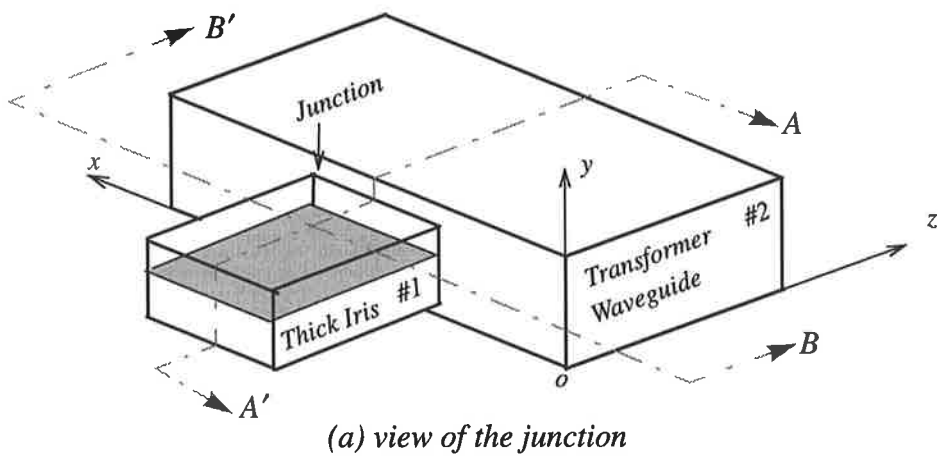


Figure 6-7. Second junction: (a) 3-D view, (b) longitudinal cross-section, (c) transversal cross-section

These conditions require that the surface integrals involved in the mode-matching theory to be separated into integrals over the dielectric- and air-filled areas  $S_1^d$  and  $S_1^a$  respectively.

Therefore the reaction integral (F-34) is divided into the following terms:

$$\begin{aligned}
\mathfrak{R}_{mnkl}^{e,e} &= \int_{S_1} (\bar{e}_{kl}^{1,e} \times \bar{h}_{mn}^{2,e}) \cdot \hat{a}_z dS = \int_{S_1^d} (\bar{e}_{kl}^{1,e,d} \times \bar{h}_{mn}^{2,e}) \cdot \hat{a}_z dS + \int_{S_1^a} (\bar{e}_{kl}^{1,e,a} \times \bar{h}_{mn}^{2,e}) \cdot \hat{a}_z dS \\
&= \mathfrak{R}_{mnkl}^{e,e,d} + \mathfrak{R}_{mnkl}^{e,e,a}
\end{aligned} \tag{6-29}$$

where the reaction element  $\mathfrak{R}_{mnkl}^{e,e}$  corresponding to the whole iris aperture surface  $S_1$  is decomposed into reaction elements relevant to the dielectric- and air-filled regions  $S_1^d$  and  $S_1^a$  respectively. Similarly from (F-35) to (F-37) we obtain:

$$\mathfrak{R}_{mnkl}^{h,e} = \mathfrak{R}_{mnkl}^{h,e,d} + \mathfrak{R}_{mnkl}^{h,e,a} \tag{6-30}$$

$$\mathfrak{R}_{mnkl}^{e,h} = \mathfrak{R}_{mnkl}^{e,h,d} + \mathfrak{R}_{mnkl}^{e,h,a} \tag{6-31}$$

$$\mathfrak{R}_{mnkl}^{h,h} = \mathfrak{R}_{mnkl}^{h,h,d} + \mathfrak{R}_{mnkl}^{h,h,a} \tag{6-32}$$

Also the surface integral in the orthogonality relation for the guide #1 of Figure 6-7 (a) will be broken into two separate terms. Thus recalling from (F-14):

$$\begin{aligned}
Q_{kl}^{1,mode} &= \int_{S_1} (\bar{e}_{kl}^{1,mode} \times \bar{h}_{kl}^{1,mode}) \cdot \hat{a}_z dS = \int_{S_1^d} (\bar{e}_{kl}^{1,mode,d} \times \bar{h}_{kl}^{1,mode,d}) \cdot \hat{a}_z dS \\
&+ \int_{S_1^a} (\bar{e}_{kl}^{1,mode,a} \times \bar{h}_{kl}^{1,mode,a}) \cdot \hat{a}_z dS = Q_{kl}^{1,mode,d} + Q_{kl}^{1,mode,a}
\end{aligned} \tag{6-33}$$

Now using the assumption of (F-15) in equation (6-33) we finally obtain:

$$Q_{kl}^{1,mode} = Y_{kl}^{1,mode,d} + Y_{kl}^{1,mode,a} \tag{6-34}$$

Therefore the matrix  $[Y^{(1)}]$  which appeared in the mode-matching equations should be replaced by:

$$[Y^{(1)}] = [Y^{(1)}]_d + [Y^{(1)}]_a \quad (N \times N) \tag{6-35}$$

where  $[Y^{(1)}]_d$  and  $[Y^{(1)}]_a$  are diagonal matrices with elements  $Y_{kl}^{1, mode, d}$  and  $Y_{kl}^{1, mode, a}$  respectively.

### 6.3.1 Calculation of Reaction Elements

According to equations (6-29) to (6-32) each reaction element of the second junction is a combination of two separate terms that are defined by the fields in the sub-areas  $S_1^d$  and  $S_1^a$  of the aperture as shown in Figure 6-7 (c). Following the procedure of Section F.6 and using the eigenfunctions of Appendix B we obtain:

$$\begin{aligned}\Re_{mnkl}^{e, e, d} &= \int_{S_1^d} (\bar{e}_{kl}^{1, e, d} \times \bar{h}_{mn}^{2, e}) \cdot \hat{a}_z dS = A_{kl}^{1, e, d} A_{mn}^{2, e} Y_{mn}^{2, e} \int_{S_1^d} (e_y^{1, e, d} h_x^{2, e}) dS \\ &= A_{kl}^{1, e, d} A_{mn}^{2, e} Y_{mn}^{2, e} J_x J_y^d\end{aligned}\quad (6-36)$$

$$\Re_{mnkl}^{h, e, d} = A_{kl}^{1, e, d} A_{mn}^{2, h} Y_{mn}^{2, h} \left[ \frac{-\alpha_k \beta_l^d}{\varepsilon_r k_0^2 - \beta_l^d} I_x I_y^d + \frac{\alpha_m \beta_n}{k_0^2 - \beta_n^2} J_x J_y^d \right] \quad (6-37)$$

$$\Re_{mnkl}^{e, h, d} = \int_{S_1^d} (\bar{e}_{kl}^{1, h, d} \times \bar{h}_{mn}^{2, e}) dS = 0 \quad (6-38)$$

$$\Re_{mnkl}^{h, h, d} = A_{kl}^{1, h, d} A_{mn}^{2, h} Y_{mn}^{2, h} I_x I_y^d \quad (6-39)$$

where  $A_{kl}^{1, mode, d}$ ,  $A_{mn}^{2, mode}$  are given by equations (6-24), (6-25) and (F-63) respectively.  $Y_{mn}^{2, mode}$  is obtained by modification from (B-26) and (B-55). The primary integrals are:

$$I_x = \int_0^{a_1} \cos(\alpha_k x') \cdot \cos \alpha_m(x' + a_0) dx' \quad (6-40)$$

$$J_x = \int_0^{a_1} \sin(\alpha_k x') \cdot \sin \alpha_m(x' + a_0) dx' \quad (6-41)$$

$$I_y^d = \int_0^h \sin(\beta_l^d y') \cdot \sin \beta_n(y' + b_0) dy' \quad (6-42)$$

$$J_y^d = \int_0^h \cos(\beta_l^d y') \cdot \cos \beta_n(y' + b_0) dy' \quad (6-43)$$

where  $\alpha_k$  and  $\alpha_m$  are defined from (6-17) and  $\beta_l^d$  should be calculated from equations (6-18) and (6-20). Finally  $\beta_n$  is given by:

$$\beta_n = \frac{n\pi}{b_2} \quad (6-44)$$

Similarly the reaction elements corresponding to surface  $S_1^a$  are obtained as:

$$\mathfrak{R}_{mnkl}^{e, e, a} = A_{kl}^{1, e, a} A_{mn}^{2, e} Y_{mn}^{2, e} J_x J_y^a \quad (6-45)$$

$$\mathfrak{R}_{mnkl}^{h, e, a} = A_{kl}^{1, e, a} A_{mn}^{2, h} Y_{mn}^{2, h} \left[ \frac{-\alpha_k \beta_l^a}{k_0^2 - \beta_l^a} I_x I_y^d + \frac{\alpha_m \beta_n}{k_0^2 - \beta_n^2} J_x J_y^a \right] \quad (6-46)$$

$$\mathfrak{R}_{mnkl}^{e, h, a} = 0 \quad (6-47)$$

$$\mathfrak{R}_{mnkl}^{h, h, a} = A_{kl}^{1, h, a} A_{mn}^{2, h} Y_{mn}^{2, h} I_x I_y^a \quad (6-48)$$

where  $A_{kl}^{1, mode, a}$  is given by (6-24) and (6-25) and the primary integrals  $I_y^a$  and  $J_y^a$  are defined as:

$$\begin{aligned} I_y^a &= \int_h^{b_1} \sin \beta_l^a (b_1 - y') \cdot \sin \beta_n(y' + b_0) dy' \\ &= \int_0^g \sin(\beta_l^a u) \cdot \sin \beta_n(b_1 + b_0 - u) du \quad , g = b_1 - h \\ J_y^a &= \int_h^{b_1} \cos \beta_l^a (b_1 - y') \cdot \cos \beta_n(y' + b_0) dy' \end{aligned} \quad (6-49)$$

$$= \int_0^g \cos(\beta_l^a u) \cdot \cos \beta_n(b_1 + b_0 - u) du \quad , g = b_1 - h \quad (6-50)$$

The reaction elements thus obtained by (6-29) to (6-32) are used to set up the  $[\mathfrak{R}]$  matrix that is used in equations (6-7) and (6-8) and finally (6-6) to obtain the junction S-matrix  $[S]_{II}$ .

## 6.4 Overall S- Matrix

Having determined the scattering matrices of the first and the second junctions, next comes the matter of obtaining the overall scattering matrix of the coupling structure by combining the S-matrix of the cascaded blocks as shown in Figure 6-4. In circuit theory such a cascade combination is commonly treated by transmission matrix parameters. But these parameters are not suitable for multi-mode schemes in which higher-order evanescent modes are present because the transmission-matrix models of the evanescent modes involve parameters with large positive exponents that may lead to numerical instability [61]. A direct treatment of the block diagram shown in Figure 6-4 has been suggested in the literature [59] in which the junction scattering matrices  $[S]_I$  and  $[S]_{II}$  are directly used in a complex combination containing exponential functions with negative arguments:

$$\begin{aligned} [S] &= \begin{bmatrix} [S_{11}]_I & 0 \\ 0 & [S_{11}]_{II} \end{bmatrix} + \begin{bmatrix} [S_{12}]_I[D] & 0 \\ 0 & [S_{21}]_{II} \end{bmatrix} \\ &\times \begin{bmatrix} [E][S_{11}]_{II}[D] & [E] \\ [F] & [F][S_{22}]_I[D] \end{bmatrix} \begin{bmatrix} [S_{21}]_I & 0 \\ 0 & [S_{12}]_{II} \end{bmatrix} \end{aligned} \quad (6-51)$$

where  $[S_{ij}]_I$  and  $[S_{ij}]_{II}$  are sub-matrices of  $[S]_I$  and  $[S]_{II}$  respectively as defined in equation (F-56). The size of  $[S]_I$  is  $(N_I \times M_I)$  where  $N_I$  and  $M_I$  are the number of LS modes in the partially-filled waveguide and thick iris respectively. Also the size of

$[S_{ij}]_{II}$  is  $(N_{II} \times M_{II})$  where  $N_{II}$  and  $M_{II}$  are the number of LS modes in the thick iris and the air-filled waveguide respectively. Evidently  $M_I = N_{II}$  the number of modes inside the thick iris.  $[D]$  is a diagonal matrix with elements  $D_{ii}$  as defined by:

$$D_{ii} = e^{-\gamma_i \Delta l} \quad (6-52)$$

where  $\gamma_i$  is the propagation constant of the  $i$ -th mode inside the thick iris. For evanescent modes  $\gamma_i$  will be real. Also  $\Delta l$  is the physical length of the thick iris as shown in Figure 6-3. The matrices  $[E]$  and  $[F]$  are defined as:

$$[E] = ([U] - [S_{11}]_{II}[D][S_{22}]_I[D])^{-1} \quad (6-53)$$

$$[F] = ([U] - [S_{22}]_I[D][S_{11}]_{II}[D])^{-1} \quad (6-54)$$

where  $[U]$  is a unit matrix.

## 6.5 Numerical Calculation

This section deals with the computer implementation of the methods set out above to achieve the exact numerical treatment of the coupling structure. The procedure is lengthy and cannot be accommodated in a one-step computer program. This is due to the involved nature of partially-filled structures where an additional condition is imposed by the air-dielectric interface leading to the ambiguous eigenvalues  $\beta_n^d$  and  $\beta_n^a$  for the dielectric- and air-filled regions. These eigenvalues should be determined for every contributing mode prior to execution of the mode-matching programs. In fact the accuracy of the overall calculation depends on the number of modes and the faultlessness of the eigenvalues. Consequently a number of computer programs need to be executed in order to work out the S-matrix of the coupling structure. There are different steps throughout the calculation procedure that will be explained later on but obviously the input data is the preliminary step that is now discussed in detailed.

### 6.5.1 Input Data:

Two sets of data are required for the mode-matching calculations:

- Physical specification of the coupling structure including the dimensions of the partially-filled resonant cavity waveguide (#1), the thick iris (#2) and the air-filled waveguide (#3).
- Input parameters that are: (i) the operating frequency ( $\omega$ ), (ii) the number of LS modes  $N_I$ ,  $M_I$ , and  $M_{II}$  in guides #1, #2, and #3 respectively and (iii) the choice of propagating mode corresponding to each waveguide.

The specification of the coupling structure for a microwave test assembly is shown in Table 6-1. The cavity and the thick iris constitute two partially-filled waveguides with the same height and air-gap and consequently the same dielectric thickness of 8.41 mm.

The dielectric region is filled by four Duroid slabs with dielectric constant of 10.8 as

**Table 6-1. Typical specifications of the coupling structure. Dimensions are in millimetres.**

Name of Wavguide	Type of Waveguide	Width	Length	Height	Air-Gap	Average Diel. Const.
Cavity (#1)	Partially-Filled	72	80	11.41	3	10.61
Thick Iris (#2)	Partially-Filled	24	9	11.41	3	10.61
Transformer Guide (#3)	Air-Filled	72	35.9	18.2 <sup>a</sup>	18.2	1

a. Two metal blocks are used as shown in Figure 6-2 with  $H = 7.9$  mm

shown in Figure 6-8. The top layer is a thin slab with  $\Delta h' = 0.63\text{mm}$  (0.025 inch), whereas the underneath layers consist of three thick slabs with  $\Delta h = 2.54\text{mm}$  (0.100 inch). Commercial availability controlled this combination of slabs to act as the partial filling for the cavity and iris.

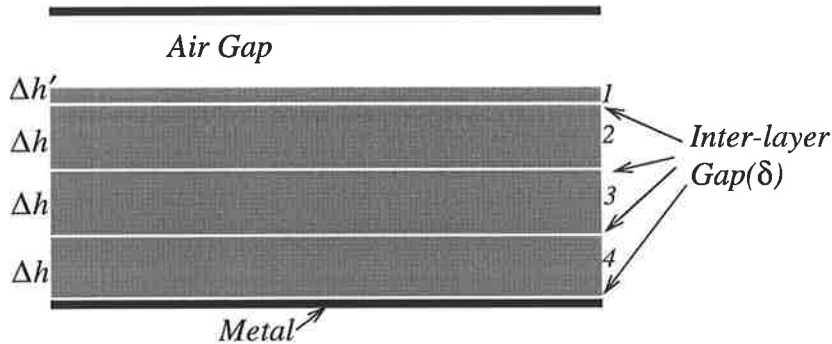


Figure 6-8. Detail of dielectric-filled region including the dielectric slabs and inter-layer gaps

The inter-layer gaps of Figure 6-8 have been measured with a high precision microscopic vernier and the average gap is  $\delta \cong 0.04$  mm. Therefore the overall dielectric thickness would be

$$h = \Delta h' + 3\Delta h + 4\delta \cong 8.41 \text{ mm} \quad (6-55)$$

The inter-layer gaps will change the material's permittivity to:

$$\epsilon_r|_{average} \cong \frac{1}{2}[(\Delta h' + 3\Delta h)\epsilon_r + 4\delta] = 10.61 \quad (6-56)$$

or a reduction of about 1.76% in the dielectric constant that cannot be ignored in accurate calculations.

The other type of data, the operating parameters, can be determined from the cavity dimensions. For example for this oscillator design at 3.5 GHz, the appropriate resonant mode of the partially-filled cavity would be LSM<sup>y</sup><sub>303</sub> with a resonant frequency of 3.503 GHz as given in Table 5-1 of Chapter 5. Thus the appropriate propagating mode inside

the cavity would be  $LSM^y_{30}$  with operating frequency of 3.503 GHz as shown in Table 6-2

**Table 6-2. Typical input parameters for the coupling structure specified in Table 6-1**

Input Parameters	Waveguide #1 (Cavity)	Waveguide #2 (Thick Iris)	Waveguide #3 (Transformer)
Operating Frequency	3.503 GHz	3.503 GHz	3.503 GHz
Number of LS Modes	100	100	150
Propagating Mode	$LSM^y_{30}$	$LSM^y_{10}$	$LSM^y_{10} = TE^z_{10}$

Thanks to the low frequency-sensitivity of the coupling structure, the slight change of the oscillator frequency discussed in Section 5.5.1 will not create any significant errors in the overall S-matrix of the structure.

Figure 6-9 illustrates the procedure for mode-matching calculations in block diagram form, where the input data are the operating conditions shown as the preliminary step in calculation. Once the data files are created the next step would be calculation of the cutoff frequencies for each waveguide.

### 6.5.2 Cutoff Frequencies

Similar to ordinary waveguides, the cutoff frequency of each partially-filled structure is basically determined from the eigenvalue equation by setting  $\gamma_z = 0$ .

$$\beta_n^d = \sqrt{\epsilon_r k_c^2 - \alpha_m^2} \quad , \quad \beta_n^a = \sqrt{k_c^2 - \alpha_m^2} \quad (6-57)$$

Now substituting  $\beta_n^d$  and  $\beta_n^a$  from (6-57) into (6-21) will result in:

$$\begin{aligned} \beta_n^d \cot(h\sqrt{\epsilon_r k_c^2 - \alpha_m^2}) &= -\beta_n^a \cot(g\sqrt{k_c^2 - \alpha_m^2}) && \text{for } LSE_{mn}^y \\ \beta_n^d \tan(h\sqrt{\epsilon_r k_c^2 - \alpha_m^2}) &= -\epsilon_r \beta_n^a \tan(g\sqrt{k_c^2 - \alpha_m^2}) && \text{for } LSM_{mn}^y \end{aligned} \quad (6-58)$$

and the cutoff frequency is defined by  $f_c = 2\pi k_c / \sqrt{\mu_0 \epsilon_0}$ .

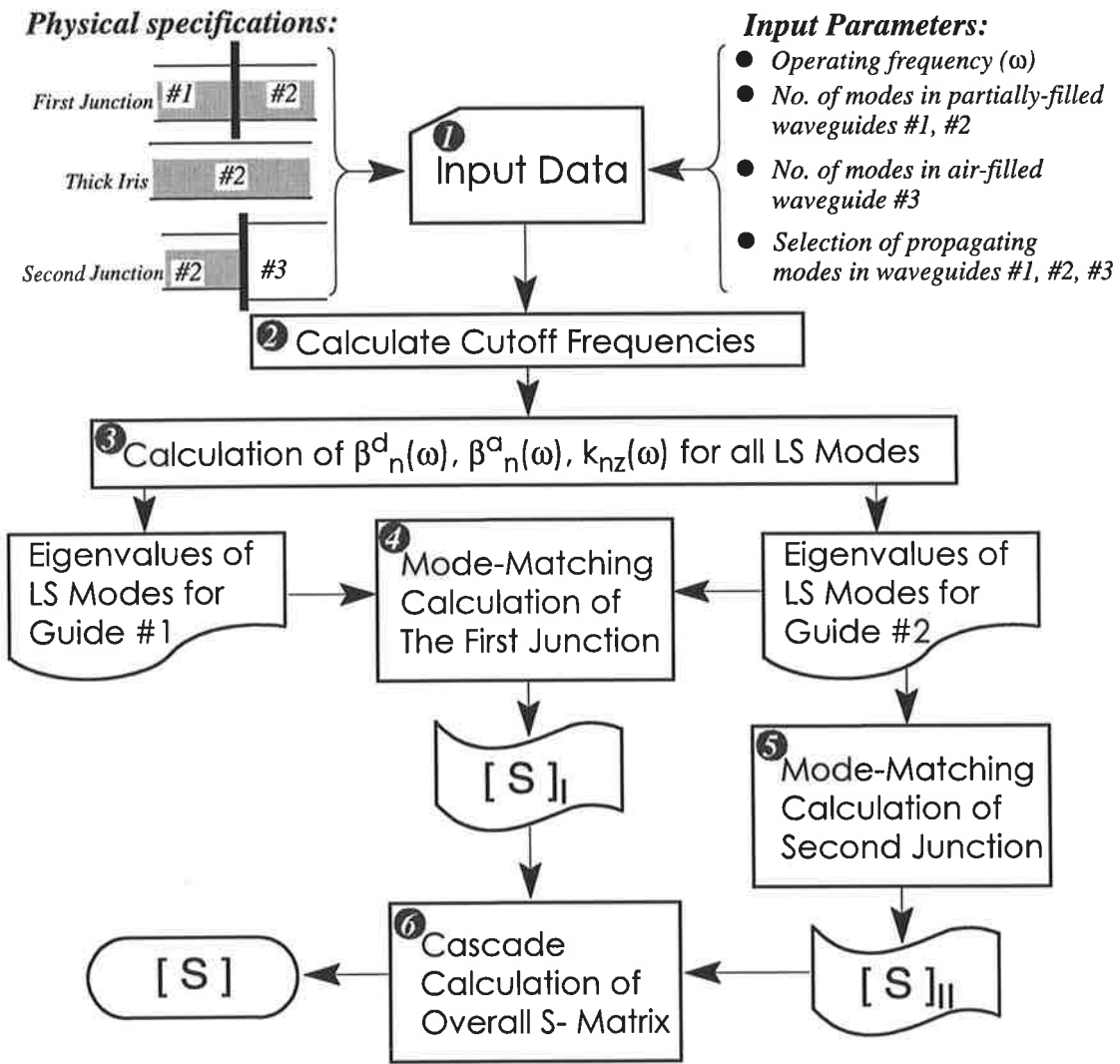


Figure 6-9. Computer implementation for mode-matching calculation of coupling structure

Solution of (6-58) will be laborious and is achieved by optimisation methods. A computer program has been developed to calculate the cutoff frequencies of partially-filled waveguides for different modes and store the results in separate data files for further exploitation. Part of the program results for 100 LS modes (*i.e.* 50 LSM<sup>y</sup> and 50 LSE<sup>y</sup>) in the partially-filled waveguide #1 of the microwave test assembly is shown in Figure 6-10.

Also the cutoff-frequencies of the same waveguide when it is completely air-filled or dielectric-filled are listed for comparison.

Mode	Air <i>Filled</i>	Partially <i>Filled</i>	Dielectric <i>Filled</i>
<b><math>LSM^y_{10}</math></b>	<b>2.0819</b>	<b>1.1640</b>	<b>0.6390</b>
$LSM^y_{11}$	13.3036	4.4232	4.0836
$LSM^y_{12}$	26.3618	9.0509	8.0918
$LSM^y_{13}$	39.4741	14.1332	12.1166
$LSM^y_{14}$	52.6001	19.3653	16.1457
<b><math>LSM^y_{20}</math></b>	<b>4.1638</b>	<b>2.1372</b>	<b>1.2781</b>
$LSM^y_{21}$	13.7837	5.0540	4.230
$LSM^y_{22}$	26.6072	9.2351	8.1671
$LSM^y_{23}$	39.6384	14.2115	12.1671
$LSM^y_{24}$	52.7235	19.4116	16.1836
<b><math>LSM^y_{30}</math></b>	<b>6.2457</b>	<b>2.8757</b>	<b>1.9171</b>
$LSM^y_{31}$	14.5486	5.9859	4.4657
$LSM^y_{32}$	27.0114	9.5841	8.2912
$LSM^y_{33}$	39.9109	14.3493	12.2507
.....	.....	.....	.....
$LSE^y_{01}$	13.1397	4.2119	4.0333
$LSE^y_{02}$	26.2794	8.9933	8.0665
$LSE^y_{03}$	39.4191	14.1078	12.0998
$LSE^y_{04}$	52.5588	19.3501	16.1330
$LSE^y_{05}$	65.6986	24.6372	20.1663
.....	.....	.....	.....

← Propagating mode

← Propagating mode


**Selected Propagating Mode**  
 Cut-Off Freq. = 2.8757 GHz

Figure 6-10. Typical computation of the cutoff-frequencies for the partially-filled waveguide #1

Four propagating modes are found including  $LSM^y_{40}$  which is not shown in the above. Similarly cutoff frequencies of 100 LS modes have been found for the thick iris specified in Table 6-1 in which  $LSM^y_{10}$  mode is the only propagating mode at 3.5 GHz. This is the only explicit application of cutoff frequencies. However they are indirectly used for obtaining the eigenvalues at a particular frequency, the third step in the flowchart of Figure 6-9.

### 6.5.3 Eigenvalues

This part of the calculation is crucial and the eigenvalues of all LS modes are numerically determined from the laborious solution of the eigenvalue and transcendental equations (6-18) to (6-21). By computer solution of these equations one can find the frequency variation of a selected propagating mode. For example a frequency-response of the selected propagating mode in partially-filled waveguide #1 of the microwave test assembly is plotted in Figure 6-11.

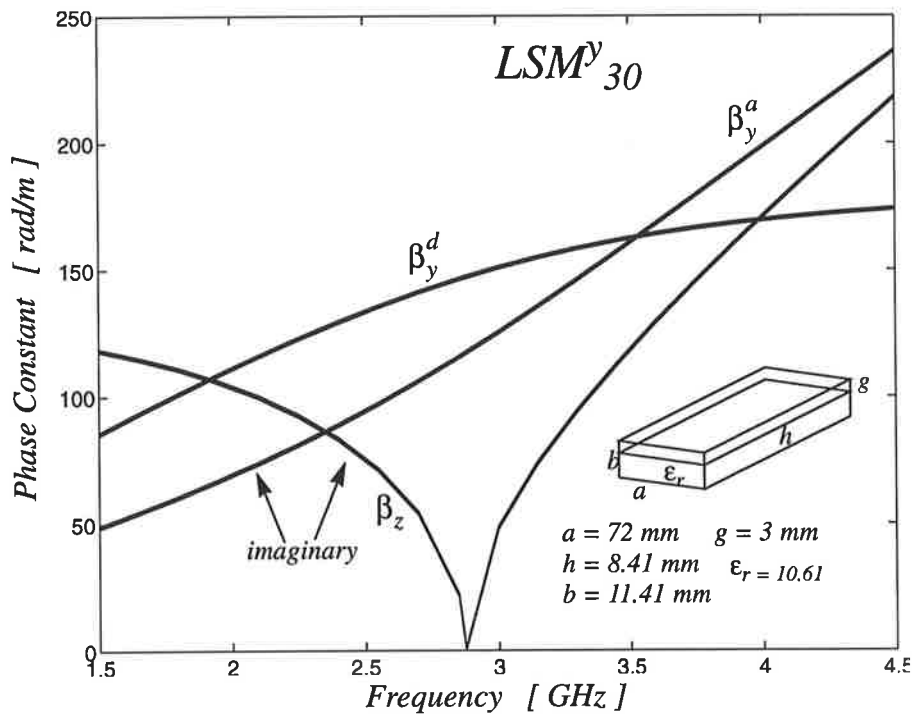


Figure 6-11. Frequency variation of the eigenvalues of  $LSM^y_{30}$  propagating mode

A computer program has been developed for step 3 of Figure 6-9 and the cutoff frequencies are used for correct initialisation of the program for each mode. This will dramatically reduce the number of *irrelevant results*<sup>1</sup> when the program is subsequently executed for a range of modes. These irrelevant results stem from the periodic nature of the transcendental equations (6-20) to (6-21) and can be checked by calculating virtual eigennumber  $n'$  defined as:

1. The irrelevant results are the correct eigenvalues but belong to lower or upper modes.

$$n' = \frac{b}{\pi} \beta_n^d \quad (6-59)$$

and comparing it with the eigennumber of the equivalent homogeneously-filled waveguide  $n$ . Although  $n'$  is not an integer it must change in the same manner as  $n$  is changed. Once the calculations for 100 modes are completed then it is possible to detect the irrelevant eigenvalues by comparing the values of  $n$  and  $n'$  for sequences of modes. Typical output for 100 modes of the partially-filled waveguide #1 are shown in Figure 6-12. All eigenvalues are computed at the operating frequency of 3.5 GHz. By comparing the first two columns, one can observe that as the integer  $n$  is increased the virtual eigen-number  $n'$  grows up until  $n$  is reset again. The eigenvalues  $\beta_n^d$ ,  $\beta_n^a$  and  $\beta_z$  are given in columns 3 to 5, where  $\beta_z = -j\gamma$  is real for propagating modes.

Also the eigenvalues of the partially-filled waveguide #2 have been computed using the same program for 100 LS modes at the same frequency. The results are stored in appropriate data-files that are frequently called by the mode-matching programs.

#### 6.5.4 Mode-Matching of the First Junction

A mode-matching program has been implemented based on the analysis of Section 6.2 for the computation of the generalised S-matrix  $[S]_I$  of the first junction.

Using the pre-determined eigenvalues of guides #1 and #2, the program calculates the reaction elements and  $\Psi$  matrix from (6-9) to (6-12) and (6-7) to (6-8) respectively. Then the junction S-matrix is finally calculated from (6-6) and stored in a data-file to be called by the cascade program. It should be noted that due to the nature of the first junction which is an H-step as shown in Figure 6-6, there is no discontinuity in the y-direction. Therefore only  $LSM_{m0}^y$  modes are practically excited by such a junction.

<i>Mode</i>	<i>n'</i>	$\beta_n^d$	$\beta_n^a$	$\beta_z$	$f_{cutoff}$
$LSM^y_{m\ n}$		[radian/s]	[radian/s]	[radian/s]	[GHz]
$LSM^y_{10}$	0.59	161.83	j160.09	170.63	1.16
$LSM^y_{11}$	0.92	253.16	110.78	j93.73	4.42
$LSM^y_{12}$	3.31	912.66	883.81	j881.84	9.05
$LSM^y_{13}$	3.93	1082.24	1058.03	j1056.38	14.13
$LSM^y_{14}$	4.79	1319.72	1299.94	j1298.60	19.37
$LSM^y_{20}$	0.59	161.83	j160.09	152.98	2.14
$LSM^y_{21}$	0.92	253.16	110.78	j120.41	5.05
$LSM^y_{22}$	3.31	912.66	883.81	j885.07	9.24
$LSM^y_{23}$	3.93	1082.24	1058.03	j1059.08	14.21
$LSM^y_{24}$	4.79	1319.72	1299.94	j1300.80	19.41
$LSM^y_{30}$	0.59	161.83	j160.09	117.83	2.88
$LSM^y_{31}$	0.92	253.16	110.78	j154.97	5.99
.....	.....	.....	.....	.....	.....
$LSE^y_{01}$	1.03	284.21	170.17	j153.51	4.21
$LSE^y_{02}$	2.05	563.22	515.17	j 509.91	8.99
$LSE^y_{03}$	3.04	836.14	804.56	j801.20	14.11
$LSE^y_{04}$	4.02	1107.55	1083.90	j1081.42	19.35
$LSE^y_{05}$	5.02	1381.32	1362.43	j1360.46	24.64
$LSE^y_{11}$	1.03	284.21	170.17	j159.59	4.26
.....	.....	.....	.....	.....	.....

Figure 6-12. Part of the computed eigenvalues for 100 modes of waveguide #1 at 3.5 GHz

It has been found that inclusion of unnecessary modes that are not practically excited, will not only increase the size of the matrices and computation time, but also limit the number of effective modes and lead to poor convergence and incorrect results. Typical output of the program is shown in Figure 6-13 for 50  $LSM^y_{m0}$  modes for each waveguide of the microwave test assembly. The programs have access to the complete set of eigenvalues that have been pre-determined for each waveguide during step 3 of Figure 6-9.

### Mode-Matching between Two Partially-Filled Waveguides

No. of  $\text{LSM}^y_{m0}$  modes in Guide #1 N = 50

No. of  $\text{LSM}^y_{m0}$  modes in Guide #2 M = 50

<<< Specifications of Junction >>>

$$a_1 = 72 \text{ mm} \quad b_1 = b_2 = 11.408 \text{ mm}$$

$$a_2 = 24 \text{ mm} \quad h = 8.408 \text{ mm}$$

$$a_0 = 24 \text{ mm} \quad b_0 = 0 \text{ mm}$$

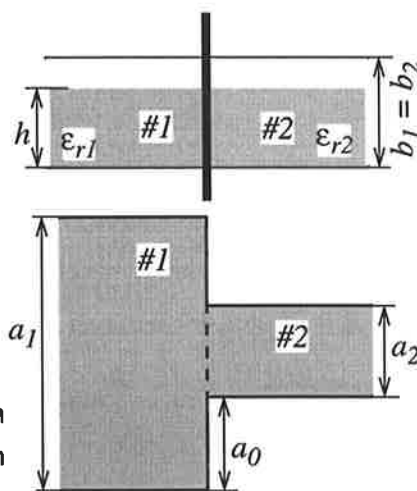
$$\text{esr1} = 10.61 \quad \text{esr2} = 10.61$$

Freq of operation = 3.503 GHz

Wave Impedance of the Guides:

$$Y_{01} (\text{LSM}^y_{30}) = 0.007857 \text{ mho}, Z_{01} = 127.3 \text{ ohm}$$

$$Y_{02} (\text{LSM}^y_{10}) = 0.007857 \text{ mho}, Z_{02} = 127.3 \text{ ohm}$$



<< S-parameters of modes  $\text{LSM}^y_{30}$  of guide #1 and  $\text{LSM}^y_{10}$  of guide #2 >>

$$S_{11} = 0.3919 < 7.088 \quad S_{12} = 0.7433 < 175.7$$

$$S_{21} = 0.7433 < 175.7 \quad S_{22} = 0.1228 < 34.65$$

Figure 6-13. Result of the mode-matching program (step 4) for the first junction

During each cycle the eigenvalues of the selected modes are automatically extracted from the relevant data files. This will greatly enhance the speed of the program, particularly in the typical calculation shown in Figure 6-13 which is composed of 2500 cycles and will end up with a huge S-matrix of  $(100 \times 100)$  elements.

As the generalised S-matrix  $[S]_I$  is too large to be shown, the conventional S-matrix between the  $\text{LSM}^y_{30}$  mode of guide #1 and  $\text{LSM}^y_{10}$  mode of guide #2 is given in Figure 6-13. However the  $[S]_I$  matrix is stored in a data file to be exploited later in the cascade program.

### 6.5.5 Mode-Matching of the Second Junction

Similar to the preceding section, a program has been developed for the mode-matching calculation of the second junction. This program which is step 5 of the procedure is established from the analysis of Section 6.3 for the treatment of a partially-filled to air-filled waveguide junction.

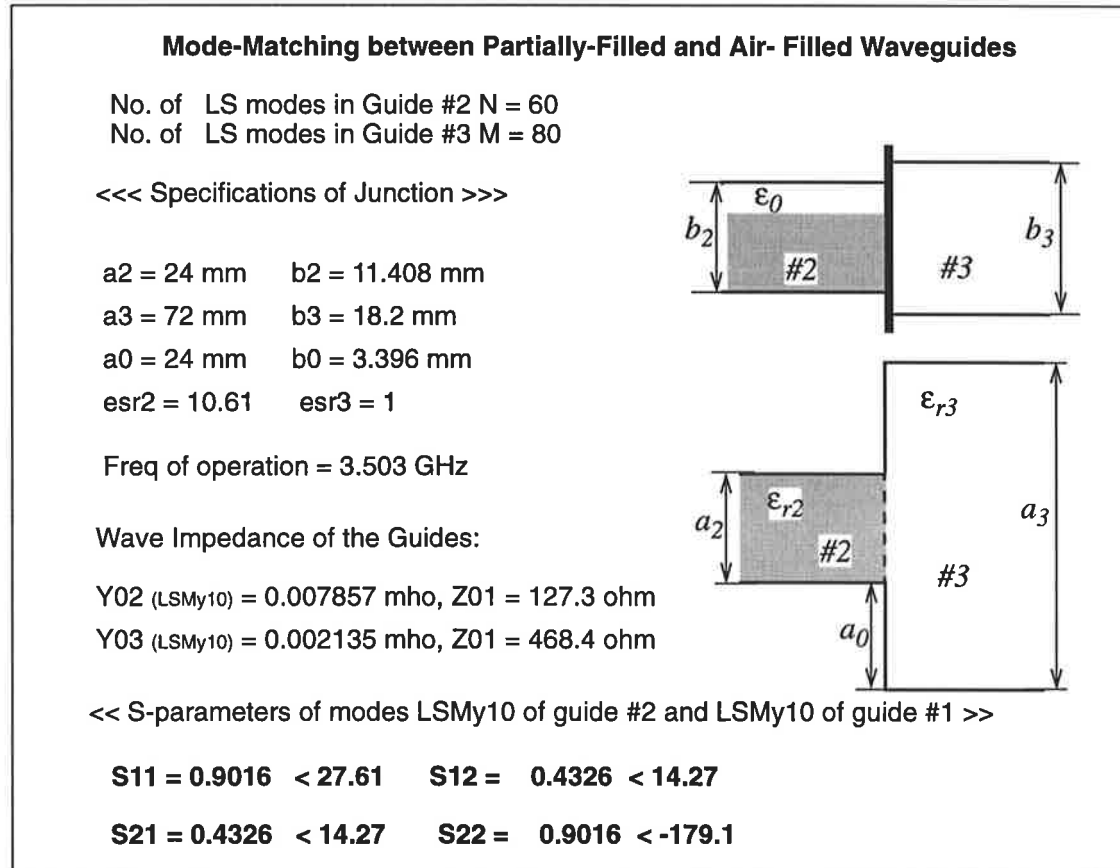


Figure 6-14. Result of the mode-matching program for the second junction, step 5

Typical computation for the structure of Table 6-2 is given in Figure 6-14 including the junction specification. Although the program algorithm is the same as that mentioned in Section 6.5.4 the reaction elements are composed of air and dielectric terms that should be calculated from (6-36) to (6-39) and (6-45) to (6-48) respectively. For unsymmetrical double-step junctions, all LS modes are excited, however in Figure 6-7, due to the symmetrical nature of the second junction in x- and y- directions, it has been verified that only the  $LSM^y_{mn}$  and  $LSE^y_{mn}$  modes that are odd numbered in the x- direction

( $m = 1, 3, 5, \dots$ ) and even numbered in the  $y$ -direction ( $n = (0), 2, 4, \dots$ ) are considered, where  $n = 0$  is only applicable for LSM modes. Inclusion of unnecessary modes will lead to poor convergence and incorrect results. Throughout the calculation, the program extracts the required eigenvalues of the waveguide #2 from the relevant date file in each cycle. Similar to the previous program, the generalised scattering matrix is stored in a data file for the next program. From the above specification  $[S]_{II}$  is a huge matrix of  $(140 \times 140)$  elements and is not shown in Figure 6-14. Instead the conventional S-parameter matrix between the  $\text{LSM}^y_{10}$  propagating modes of the two waveguides is given. It should be noted that  $\text{LSM}^y_{10}$  in the air-filled waveguide is equivalent to the well-known  $\text{TE}^z_{10}$  mode which is the only propagating mode at 3.5 GHz.

### 6.5.6 Cascade Connection

The last step in the procedure of Figure 6-9 is the cascade combination of the scattering matrices corresponding to the first and second junctions (see Figure 6-4) in order to obtain the overall S-matrix of the coupling structure. According to the theory of Section 6.4 all evanescent modes of the thick iris will contribute to the cascade connection. In practice depending on the distance between the two junctions (length of the thick iris), only a few modes need be selected in the order of their cutoff frequencies, and these will be sufficient to yield excellent convergence. Once the necessary modes are selected in the thick iris, the cascade program extracts the corresponding terms for the generalised S-matrices  $[S]_I$  and  $[S]_{II}$  from the data files and substitutes them into the complicated cascade expression of (6-51) to obtain the overall S-matrix of the coupling structure  $[S]$ . However only the conventional propagating mode S-matrix is needed ( $S_c$ ). It is defined between the main propagating mode of guide #1 ( $\text{LSM}^y_{30}$ ) and the dominant mode of the guide #3 ( $\text{LSM}^y_{10} = \text{TE}^z_{10}$ ). Figure 6-15 shows the result of the cascade program as well

as the detailed specification of the coupling structure for the microwave test assembly that has been used as an example throughout this research.

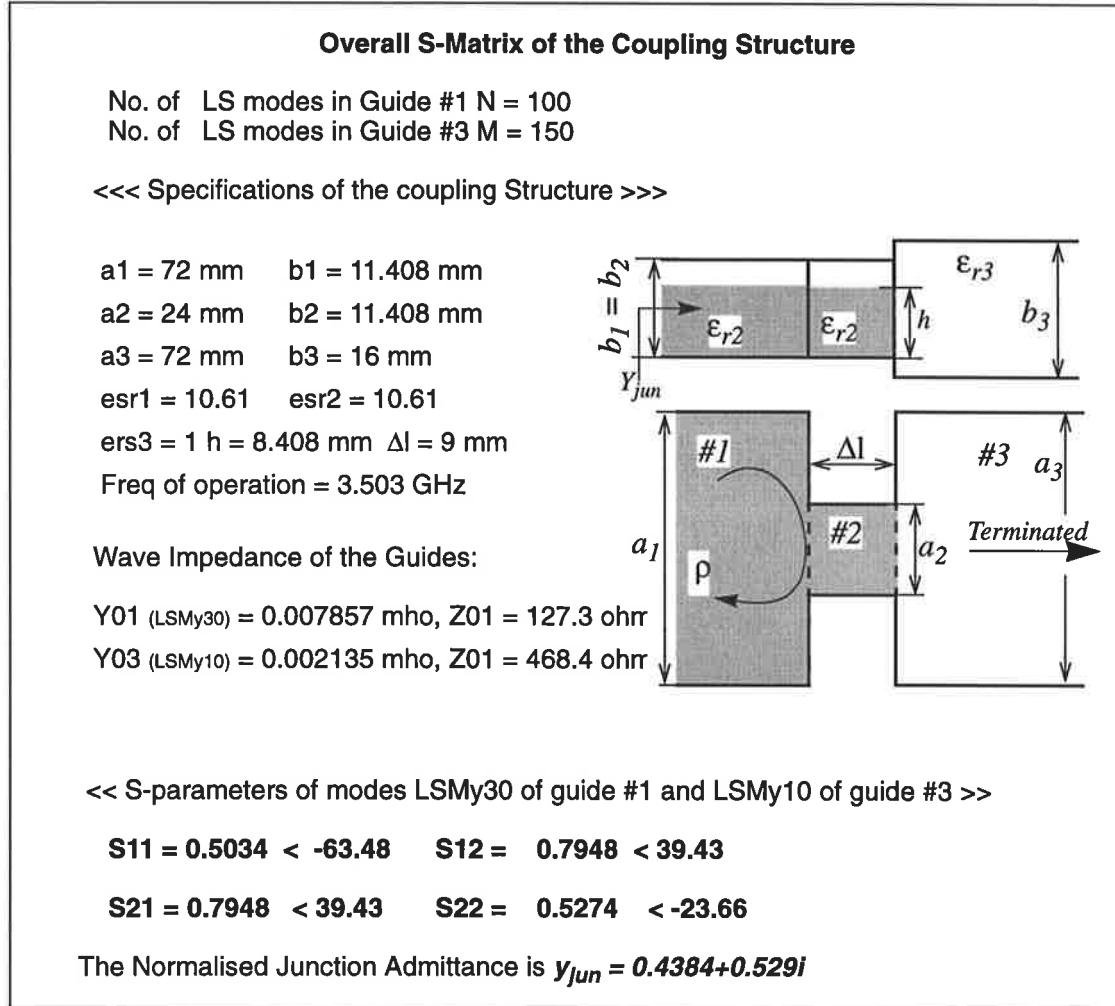


Figure 6-15. Result of the cascade program including the overall S-matrix and the junction admittance

Also the  $S_c$ - matrix is given which is easily extracted from the generalised  $[S]$  matrix. The conversion has been achieved with only one cascading mode in the thick iris,  $\text{LSMy}_{10}$ , and inclusion of higher order evanescent modes do not affect the result. The cavity aperture reflection coefficient is obtained from (6-4) and by substituting in equation (6-3) the cavity aperture admittance  $Y_{jun}$  is finally determined. The normalised cavity aperture admittance is given in Figure 6-15.

---

## Chapter 7

# *Designs and Experiments*

### **7.1 Oscillator Design Procedure**

The new design that has been presented in Chapters 3 to 6 has its origin in what appear to be insoluble problems due to surface wave excitation on thick substrates that have appeared in attempts by various research workers to build oscillator arrays that may be fabricated monolithically and operated at millimetre wave frequencies.

Since the development cost of MMIC prototypes is usually very high, it is necessary to design, fabricate and test models of new designs at microwave frequencies in order to verify the validity of the method and prove the feasibility of the novel structure. However the design should be MMIC compatible, i.e., by scaling up the frequency into the millimetre-wave spectrum, the physical specifications of the design prototype, that are scaled accordingly, should satisfy the MMIC constraints.

In this chapter typical designs in the microwave frequency band are presented and the test results on the fabricated circuits are demonstrated.

The design methods for the essential parts of the novel oscillator assembly have been explained in the foregoing chapters and owing to the complexity, numerous analyses have

been necessarily developed for the different parts. In practice, each design procedure has been implemented on the computer, resulting in several programs for execution in the course of a comprehensive design strategy as shown in Figure 7-1. The overall procedure includes twelve steps that are explained in turn.

**Step 1.** The substrate is solely determined with regard to the monolithic wafer specifications. Usually a GaAs dielectric wafer with high permittivity (12.8), and a thickness range of 200 to 500 microns is used for monolithic fabrication of high-frequency circuits. Because the initial test assembly is designed to operate at a microwave frequency, the substrate thickness ( $h$ ), should be chosen such that, upon scaling up the frequency to the millimetre-wave spectrum, the scaled thickness will fall in the range 200 to 500 microns. The substrate permittivity ( $\epsilon_r$ ) should be high enough to be compared with that for GaAs and most likely will be a commercially supplied composite material suitable for use in hybrid assembly.

**Step 2.** Having the height of the dielectric-filled region ( $h$ ) already specified in step 1, the air-gap ( $g$ ), of the partially-filled cavity is determined from the requirement of minimum clearance for accommodating the circuit components such as transistor, chip capacitors and metallisation on the top of the dielectric surface. The width ( $a$ ), and length ( $d$ ), of the cavity is determined from the number of oscillators and the array configuration. Also the area of the dielectric surface (i.e.  $a \times d$ ) should satisfy both the limitation of the commercially available material and when scaled up in frequency the maximum area of GaAs wafer that may be processed as a MMIC.

**Step 3.** Once the partially-filled cavity is specified the propagating modes should be identified by executing the cutoff frequency and eigenvalue programs that are explained in Sections 6.5.2 and 6.5.3 . The choice of the resonant mode depends on the required oscillator array configuration and the operating frequency. In order to adjust the modes, the cavity dimensions need to be re-specified.

**Step 4.** The resonant frequency for each  $LSM^Y_{mn1}$  mode, is calculated by simultaneous solution of the following eigenvalue and transcendental equations:

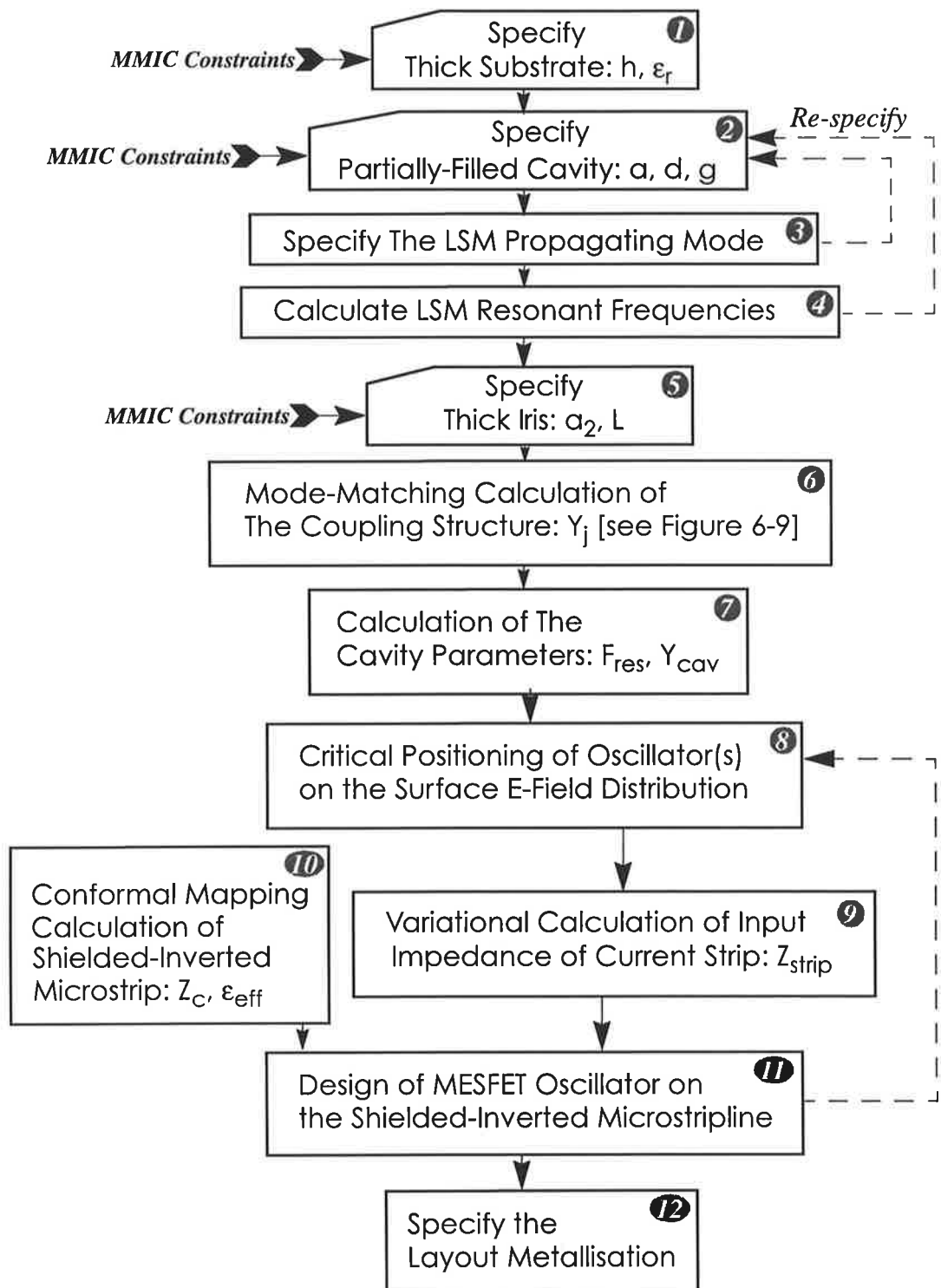


Figure 7-1. General design procedure of the novel oscillator assembly

$$\beta_n^d = \sqrt{\epsilon_r k_0^2 - \alpha_m^2 - \gamma_l^2} \quad , \quad \beta_n^a = \sqrt{k_0^2 - \alpha_m^2 - \gamma_l^2} \quad (7-1)$$

$$\beta_n^d \tan(h\beta_n^d) = -\epsilon_r \beta_n^a \tan(g\beta_n^a) \quad (7-2)$$

where the resonant frequency is defined by:

$$f_0 = k_0 / 2\pi\sqrt{\mu_0\epsilon_0} \quad (7-3)$$

and  $\gamma_l = \frac{l\pi}{d}$ . The resonant mode that is selected at this stage, will dominate the oscillator frequency and the array configurations. It may be required to change the cavity dimensions in order to provide the necessary adjustments. Nonetheless the operating frequency of the assembly is finalised in this step.

**Step 5.** A thick iris is needed for coupling the partially-filled cavity to the output waveguide which should be a standard air-filled waveguide suitable for use at the operating frequency. The concept of thick iris directly stems from the constraint of monolithic fabrication, where a thin walled aperture may not be practical but a relatively high coupling factor is needed for transferring most of the oscillator power to the output load. The thick iris is compatible with monolithic constraints if it is a partially-filled waveguide with the same dielectric and air-gap dimensions as the cavity ( $h$ , and  $g$ ). The iris cross-section is chosen such that only the dominant mode of the partially-filled waveguide is excited at the frequency of interest. Also the thick iris excites the dominant mode of the air-filled waveguide as the only propagating mode. For tight coupling the thickness dimension is chosen to be about one sixth of a wavelength in the partially filled waveguide.

**Step 6.** In this stage of the design the mode-matching calculation of the coupling structure (Figure 6-9) is performed. During this procedure that is described in Chapter 6, the admittance at the wall aperture,  $Y_{cav}$ , is finally determined for the desired propagating mode and frequency of interest.

**Step 7.** The susceptance at the cavity aperture ( $\Im m(Y_{jun})$ ) will shift the resonant frequency slightly higher or lower than the fully closed cavity resonant frequency ( $f_0$  in step 4), depending on whether it is capacitive ( $\Im m(Y_{jun}) > 0$ ) or inductive ( $\Im m(Y_{jun}) < 0$ ). The exact resonant frequency is obtained by numerical solution of equation (5-65). Also the

cavity admittance ( $Y_{cav}$ ) is determined from this calculation.

**Step 8.** Having obtained the exact resonant frequency and the other parameters, it is possible to calculate the accurate surface E-field distribution from (5-62), for critical positioning of the key oscillator components such as the transistor and the coupling probe current strip on the substrate surface.

**Step 9.** Once the position of the current strip is specified from step 8, the driving point impedance will be computed from the variational method of section 5.6.3 .

The impedance values are calculated for different strip lengths and stored in a data file to be used by the oscillator design program.

**Step 10.** The parameters of shielded inverted microstrip, i.e.  $Z_c$  and  $\epsilon_{eff}$ , should be calculated for different strip widths by the conformal mapping method as described in Appendix A. The numerical results are stored in a data file and used by the oscillator design program.

**Step 11.** The structure of the oscillator design program in shielded inverted microstripline has been fully described in Chapter 4. To obtain a satisfactory result, in terms of the metal strip layout and the negative resistance relative to the load at the drain of the transistor, the oscillator design may be re-calculated for various lengths of phasing line and modified lengths and positions of the current strip. This may be done by returning to step 8 and assuming a new position for the coupling strip.

**Step 12.** Once the best combination of lengths of the current strip, gate strip and the series feedback (source strips) is determined from step 11, the bias circuit is designed as explained in section 4.5 , and the layout of metallisations is finally prepared.

It should be noted that the design procedure set out in Figure 7-1 and explained in steps 1 to 12 does not yield a single ideal solution. Indeed the procedure may have to be implemented two or more times before an acceptable result is obtained from step 11. The positioning of the input to the coupling probe on the dielectric surface and the subsequent design of the shielded inverted microstrip oscillator may need to be repeated before an os-

cillator that appears to be good with regard to both performance and metallisation layout is obtained. It may be necessary to select a different value for the iris thickness in step 5 before a good design is obtained.

## 7.2 Microwave Test Structure

It is evident that errors associated with each step in the design procedure will have a cumulative effect on the overall design. Consequently it may appear to be prudent to test the accuracy of the design of each main component that forms the cascade from the transistor through to the load port. This would involve fabrication of special test sections with special input and output port adaptors for making connections to measuring instruments. The measurements would have to be processed so that the actual test component results are de-embedded from the effects of the special adaptors.

Apart from the additional effort involved in such testing there would still be some uncertainty arising from the possibility of errors associated with the adaptors. These are not present if the overall cascade is tested although a different set of problems that affect the interpretation of the test results and the reconciliation of them with the design expectations is unavoidable. In this research these problems arise mainly from limitations on the accuracy of the construction of the test assembly that are imposed by the equipment available for mechanical fabrication of all of the items that form the assembly.

A test structure, based on the specifications of Table 7-1 and Section 6.5.1, is shown in Figures 7-2 and 7-3 for operation in the 3 to 4 GHz range with sufficient versatility so that it may be used for testing either single transistor oscillators or arrays of two or more oscillators.

**Table 7-1 Specifications of the microwave test assembly internal dimensions.**

Name of Waveguide	Type of Waveguide	Width	Length	Height	Air-Gap	Average Diel. Const.
Partially-filled Cavity	Partially-Filled	72 mm	adjustable	11.41 mm	3 mm	10.61
Thick Iris	Partially-Filled	24 mm	9 mm	11.41 mm	3 mm	10.61
Transformer Guide	Air-Filled	72 mm	35.9 mm	adjustable		1
Output Guide	Air-Filled	72 mm		34 mm		1

This test structure incorporates a decision that affects all arrays that may be tested in it. The width of the partially filled cavity is chosen so that at particular cross-sections there will be two null points in the surface electric field distribution at positions  $a/3$  from each side wall. Hence only arrays configured with 1 or 2 by N transistors may be tested. This decision forms part of design step 2. In these arrays each transistor may be separately biased via lines from apertures in the side walls.

Figure 7-2 shows the exterior features of the adjustable partially-filled cavity including,

- (i) the cavity lid with three sets of screws apart from those used to fasten it to the walls of the cavity body,
- (ii) plastic screws uniformly spaced along the centre-line of the lid for the purpose of pressing the Duroid slabs that form the dielectric filling on to each other and the floor of the cavity,
- (iii) tuning screws for adjusting the frequency of individual oscillator circuits as explained in Section 3.3.10 on page 42,
- (iv) grounding screws for providing DC return paths for transistor drain current because of the impracticality of making a soldered connection to the thick brass cavity wall,
- (v) tunnels that accommodate ferrite beads threaded on to the transistor drain and gate bias supply leads with the aim of presenting a high series impedance at microwave frequencies,

(vi)socket boards on either side of the cavity for connecting supplies to otherwise relatively fragile wires that emerge from the internal filter structure,

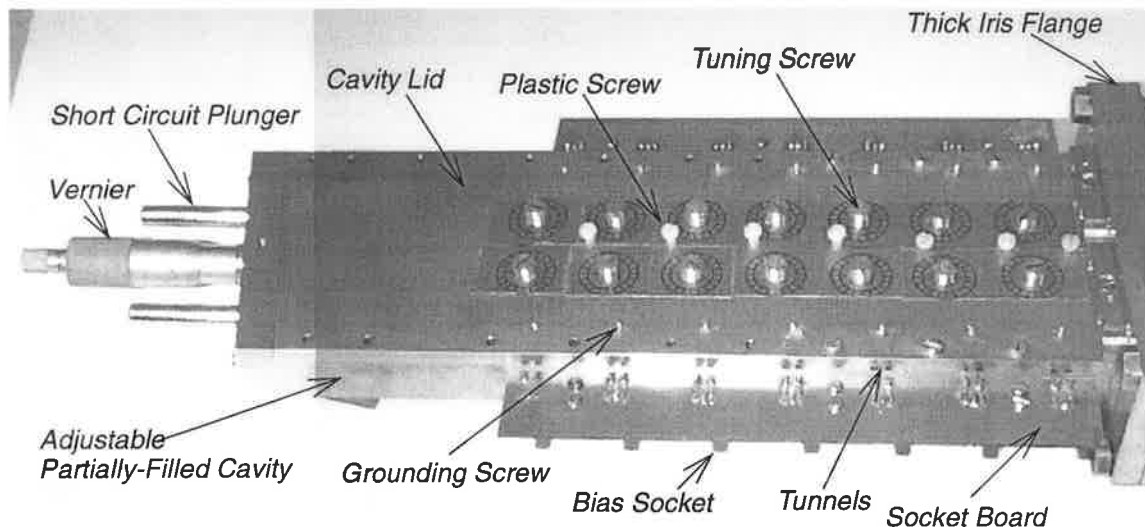


*Figure 7-2. A picture of the fabricated assembly based on specifications of Table 7-1. The air-filled waveguide is not shown in the picture*

(vii)the vernier micrometer head and guide rods for the short circuit plunger that acts as the cavity end wall and can be used to tune the cavity resonant frequency as explained in Section 3.3.11 on page 42 as well as set the length inside the cavity in keeping with the size of the  $LSM_{30N}$  mode in use, and,

(viii)the thick iris flange that is bolted on to the cavity flange and accommodates an extension of the dielectric superstrate and supports  $LSM_{10}$  mode propagation.

Figure 7-3 shows interior features and helps in the identification of the places where limitations on the accuracy of fabrication of parts of the assembly may cause differences between design and measured test results. Constructional limitations of significance include,

(i) fastening of the lid with screws to the top edges of the cavity walls and to the rear surface of the flange on the cavity body, that gives, as a result of surface finish, imperfect contact between the faces so causing some loss in the cavity that may be different each time the parts are reassembled,

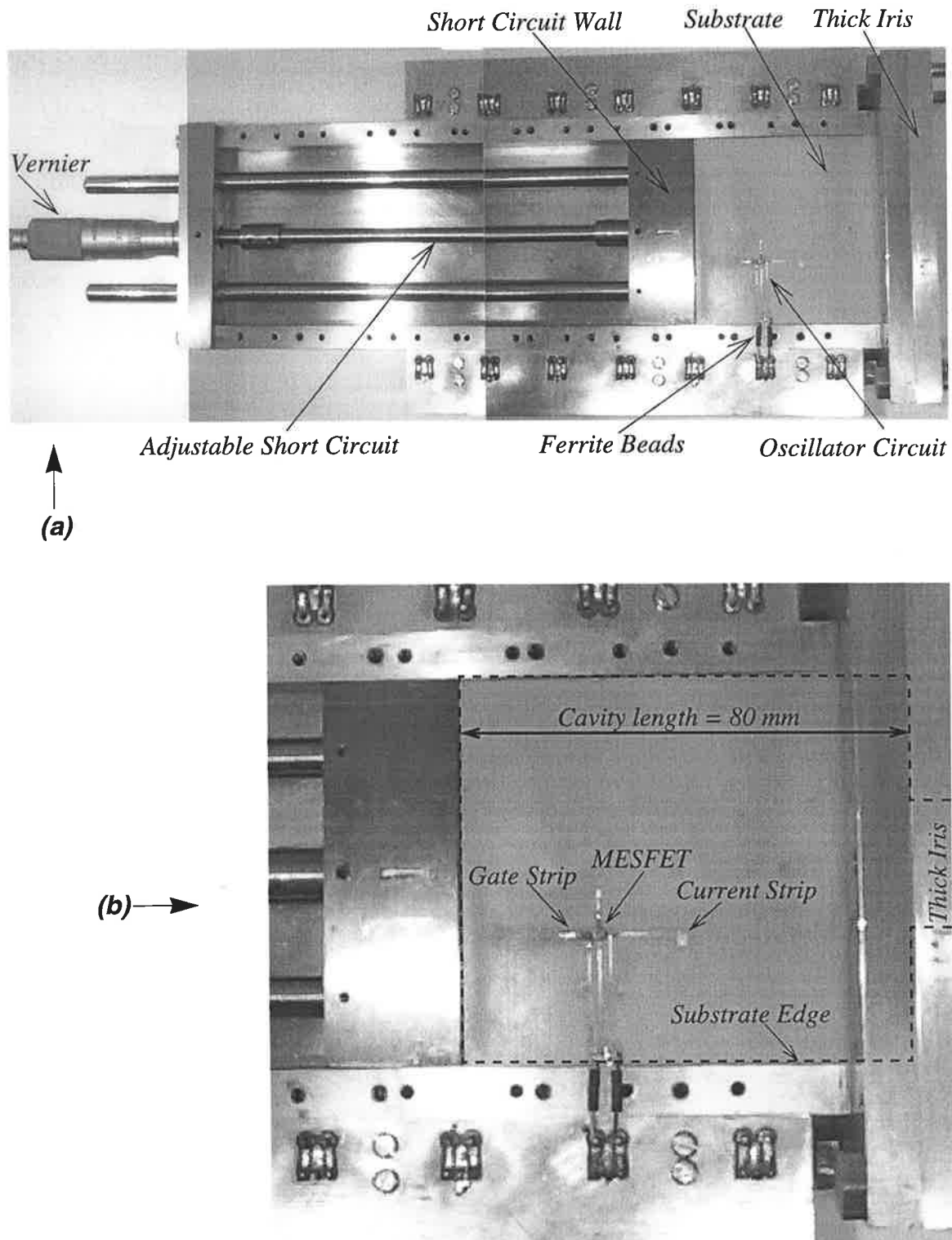


Figure 7-3. (a) Internal picture of the assembly. (b) A close-up view of the oscillator circuit relevant to version 1

- (ii)a gap between the edges of the dielectric slabs and the side walls of the cavity that depends upon surface finishes and a need for an easy sliding fit for slabs that may easily buckle and circuits that are relatively fragile and easily strained,
- (iii)gaps between the dielectric slabs as discussed in Section 6.5.1 on page 122, that are minimised by means of plastic screws and to some extent the grounding screws along the edges close to the cavity side walls but may vary from one assembly to another especially within the thick iris, and,
- (iv)dimensional tolerances in cutting out the metal stripline circuit layout using the Quick Circuit Milling Machine by T-TAK Inc., with Graphic Code Co. software, and positioning the dielectric slab accurately in the partially-filled cavity and thick iris and soldering transistors and bias wires in place.

The thick substrate consists of four Duroid dielectric slabs as shown in Figure 6-8, with total thickness of 8.41 mm and average dielectric constant 10.61. Assuming an operating frequency of 3.5 GHz, the substrate thickness would scale down to about 840 microns at 35 GHz and 210 microns at 140 GHz and still less in changing from Duroid<sup>1</sup> to the dielectric constant of the GaAs wafer. The air-gap is assumed to be 3 mm thick to provide the necessary clearance for the packaged transistors that are mounted on the top layer. In monolithic fabrication the air-gap may be replaced by a layer of low dielectric-constant material to ensure uniformity of clearance.

The cavity length can be changed from zero to 214 mm, by means of the adjustable short circuit wall with various extension rods on the micrometer drive. Also the height of the transformer waveguide can be adjusted by attaching appropriate metal blocks to the upper or lower wall of the guide, as shown in Figure 6-2. Thus a versatile assembly has been fabricated based on the specifications of Table 7-1.

A single transistor oscillator in a LSM<sub>303</sub> mode resonator is shown in Figure 7-3. Referring to the layout of Figure 4-10, the two tunnels to be cut through the cavity wall for each oscillator for bias lines that connect via ferrite beads and chip capacitors to the drain and gate electrodes are clearly shown. Also the grounding patch for the source return path

---

1. Duroid is a manufacturer of dielectric materials

that is connected via an earthing screw that passes across the air gap from the top wall of the cavity is also shown. This circuit layout should be positioned accurately in the cavity field and also adjusted with respect to the wiring tunnels and the grounding screw.

In the fabricated assembly of Figure 7-2, two rows of tunnels and grounding screws have been symmetrically placed in and near the walls of the cavity so that up to fourteen oscillator circuits could be accommodated spaced 26.75 mm apart although it is not necessary to test an array as large as that to validate the overall new design. The cavity length can be adjusted by the short-circuit plunger to provide the necessary space for any number of oscillators up to 14. A spacing of 26.75 mm has been ideally chosen from the surface E-field distribution of a LSM<sub>308</sub> resonant mode within a 214 mm long closed cavity.

The practical limitations in the test assemblies that have been identified above will affect certain aspects of the performance of oscillators. In particular adjustment of the frequency of the oscillator circuit and / or the cavity resonant frequency may be necessary to obtain measurable output and the resulting frequency may differ from the design value. Agreement between measurement and design within one percent should be regarded as a good result and evidence of the validity of the oscillator circuit and cavity resonator design.

The other major effect of the practical limitations is likely to be apparent in power output measurements and DC to RF conversion efficiency results. Differences amongst transistors within the same type number are likely to be the primary cause of inconsistent output characteristics. But even for a particular oscillator different results may be anticipated each time the circuit board is removed and then reassembled with the cavity due to small changes in the cavity internal losses and the thick iris. The reduced height air-filled waveguide coupling section may be changed but only in finite steps.

Oscillator designs that have been fabricated for testing within this cavity will be described in the following sections.

### 7.3 Design Validation Testing: Single-Transistor Oscillator

A single transistor oscillator in a LSM<sub>303</sub> resonant mode partially filled cavity is to be designed according to the specifications of Tables 7-1 and 7-2 and then fabricated and

mounted in the microwave test structure as shown in Figure 7-3 to be the first test of the validity of the concepts and design methods presented in this thesis.

### 7.3.1 Single Transistor Oscillator: Version 1

#### 7.3.1.1 Design

**Steps 1, 2 and 5:** With reference to the 12 step design procedure of Section 7.1 the specification of steps 1, 2 and 5 are given in Tables 7-1 and 7-2.

**Table 7-2 Specifications that are peculiar to version 1 design**

Operating Frequency	Cavity Length	Height of the Transformer	Max. No. of Oscillators
3.5 GHz	80 mm	18.2 mm <sup>a</sup>	4

a. Two metal blocks are used as shown in Figure 6-2 with  $H = 7.9$  mm

These specifications, as indicated in Figure 7-1, arise from MMIC constraints that would apply if the design is to be subsequently scaled down in dimensions by a factor of 30 for operation at a frequency near 100 GHz.

The rest of the design steps are explained below.

**Step 3:** An index of propagating modes of the partially-filled waveguide to be used in forming the cavity can be set up as given in Figure 6-10, and the  $\text{LSM}^y_{30}$  mode selected in order to provide surface electric nulls to accommodate as many pairs of oscillators inside the cavity as required, all fed via bias paths through the side walls, although only one oscillator will be fabricated for this test of the design.

**Step 4 .** The resonant frequencies of the fully enclosed cavity (i.e. no coupling aperture) are then calculated by simultaneous solution of equations (7-1) to (7-3). They are listed in Figure 7-4, where  $\text{LSM}^y_{303}$  is the selected resonant mode that corresponds to the desired operating frequency.

**Step 6 .** The mode matching analysis of the coupling structure with specifications outlined in Tables 7-1 and 7-2, is then applied as described in Chapter 6. The normalised admittance at the cavity wall aperture that is presented to the  $\text{LSM}^y_{30}$  mode as given in Figure

6-15 includes a capacitive reactance as below:

$$\bar{Y}_{jun} = 0.4384 + j0.529 \quad \text{at } 3.503 \text{ GHz} \quad (7-4)$$

It is important to note that while the first junction (H-step) apparently introduces an inductance at the cavity aperture, the effect of the second junction through the thick iris cascade connection will dramatically change the admittance at the cavity aperture to strongly capacitive as given by (7-4). This will have a significant effect on the oscillator design as will be discussed later on. It could be altered by changing the iris thickness assumed in Table 7-1 by using a different extension to the superstrate and a different iris flange in the assembly of Figure 7-3, i.e. several parts would have to be changed.

Mode	Resonant Frequency [GHz]		
	Air Filled	Partially Filled	Dielectric Filled
LSM <sup>y</sup> <sub>301</sub>	6.521	2.961	2.002
LSM <sup>y</sup> <sub>302</sub>	7.284	3.187	2.236
<b>LSM<sup>y</sup><sub>303</sub></b>	<b>8.403</b>	<b>3.503</b>	<b>2.579</b>
LSM <sup>y</sup> <sub>304</sub>	9.759	3.87	2.995
LSM <sup>y</sup> <sub>305</sub>	11.26	4.273	3.456
LSM <sup>y</sup> <sub>306</sub>	12.86	4.704	3.948
LSM <sup>y</sup> <sub>307</sub>	14.53	5.156	4.459
.....	.....	.....	.....



Figure 7-4. Resonant frequencies for the partially-filled cavity with length  $d = 80 \text{ mm}$

**Step 7.** Based on the numerical solution of equation (5-65), the exact resonant frequency is calculated to be 3.56 GHz and the coupling factor to the output load to be 2.2, as outlined in Figure 5-10. These results appear to be very sensitive to the unloaded-Q of the partially filled cavity. Consequently a slight variation of the internal cavity losses that are mainly due to the dielectric and the brass cavity walls will substantially change the results.

**Step 8.** The surface electric field distribution that applies in this cavity is similar to that shown in Figure 5-8 (a), and the zero E-field for transistor positioning is calculated to be at the point  $x_t = 24$  and  $z_t = 25.68$  millimetres from the short-circuit wall (or 54.32 mm from the cavity aperture). The driving point end of the coupling probe strip is assumed

to be positioned at  $x_0 = 24$  and  $z_t = 39.05$  millimetres, and a 14 mm phasing line is needed for transforming it into a load impedance to be presented to the transistor drain.

**Step 9.** Assuming an oscillator frequency of 3.5 GHz, the impedance at the driving point end of the probe strip can be determined by the variational method discussed in Section 5.6. The result exhibits a highly capacitive reactance for all practical lengths as illustrated in Figure 5-14, which is apparently a consequence of the capacitive reactance at the aperture in the cavity wall.

**Step 10.** Numerical calculation of  $Z_c$  and  $\epsilon_{eff}$  for a shielded-inverted microstripline as specified in Table 7-1 is shown in Figure 4-11. The results are stored in data files to be used by the oscillator design program.

**Step 11.** This step has been fully described as a design example in Section 4.6 and the result presented in Figures 4-13 and 4-14. The length of the phasing line has to be long enough to transform the capacitive reactance of the probe ( $X_{strip}$ ) into an inductive reactance  $X_L$  at the transistor drain that is comparable with the conjugate of the device reactance ( $\Im m[Z_d]$ ) as shown in Graph -B and -C of Figure 4-12. A problem that arises is that the magnitude of the small signal device negative resistance ( $\Re e[Z_d]$ ) needs to be large enough compared with the load resistance  $R_L$  to give rise to a strong oscillation at the resonant mode of interest. In this initial design it has been verified, by changing such design parameters as gate, drain and source strips, that the resistance condition does not reach the empirical condition, magnitude  $\Re e[Z_d] \geq R_L/3$ , that is used in oscillator design based on small signal parameters [4, pp. 175]. This problem is overcome in the next oscillator design by making a different choice for the input position of the coupling strip.

**Step 12.** The complete layout of the oscillator circuit including the microstrip dimensions is shown in Figure 7-5. The circuit location with respect to the edges of the dielectric wafer and therefore the cavity walls is readily observed. It is to be noted that the small section of the dielectric layer that extends inside the thick iris will be an integral part of the main substrate in the case of monolithic fabrication.

The dielectric volume comprises four Duroid substrates all with  $\epsilon_r$  of 10.8. Three thick slabs (0.1") are placed underneath a thin layer (0.025") that includes the circuit on the top. From step 8, the accurate position of the transistor along the z-axis is 25.68 mm from the short-circuit wall, which is slightly shifted from the ideal position based on the fully enclosed cavity field distribution (26.5 mm).

As the bias lead tunnels and the grounding screws have been positioned on the basis of the fully enclosed cavity field, a small offset will appear (0.82 mm) that has been accommodated by curving the ends of the bias lines and the DC return. The extent of the meander in the bias lines is calculated so that the total length of the bias lines is  $3\lambda_s/4$ , where  $\lambda_s = \lambda_0/\sqrt{\epsilon_{eff}}$  and  $\lambda_0$  is the wavelength in free space.  $\epsilon_{eff}$  is determined from step 9. Also the total length of the DC return, from the end of the source strip and including the curved section, should be  $\lambda_s/4$  (8.6 mm).

The layout metallisations, particularly the bias lines and the DC return, are chosen thin enough, so that their coupling with the surface electric field is kept to a minimum. Figure 7-3 (a) shows the assembly with the cavity lid removed. The adjustment system is clearly shown, where the cavity length can be varied in the range  $0 < d < 214$  mm.

The cavity length has been adjusted to 80 mm to accommodate the thick substrate with lateral dimensions as given by Figure 7-5. Also the 9 mm substrate extension is placed inside the thick iris to form the intermediate partially-filled waveguide. An enlarged photographs of the oscillator circuit for design version 1 is shown in Figure 7-3 (a) and (b) with the substrate periphery highlighted.

# LAYOUT-1

Oscillator Freq.: 3.5 GHz

Cavity Resonant Freq.: 3.56 GHz

Resonant Mode: LSM<sub>303</sub>

Transistor: ATF-13036 HP MESFET

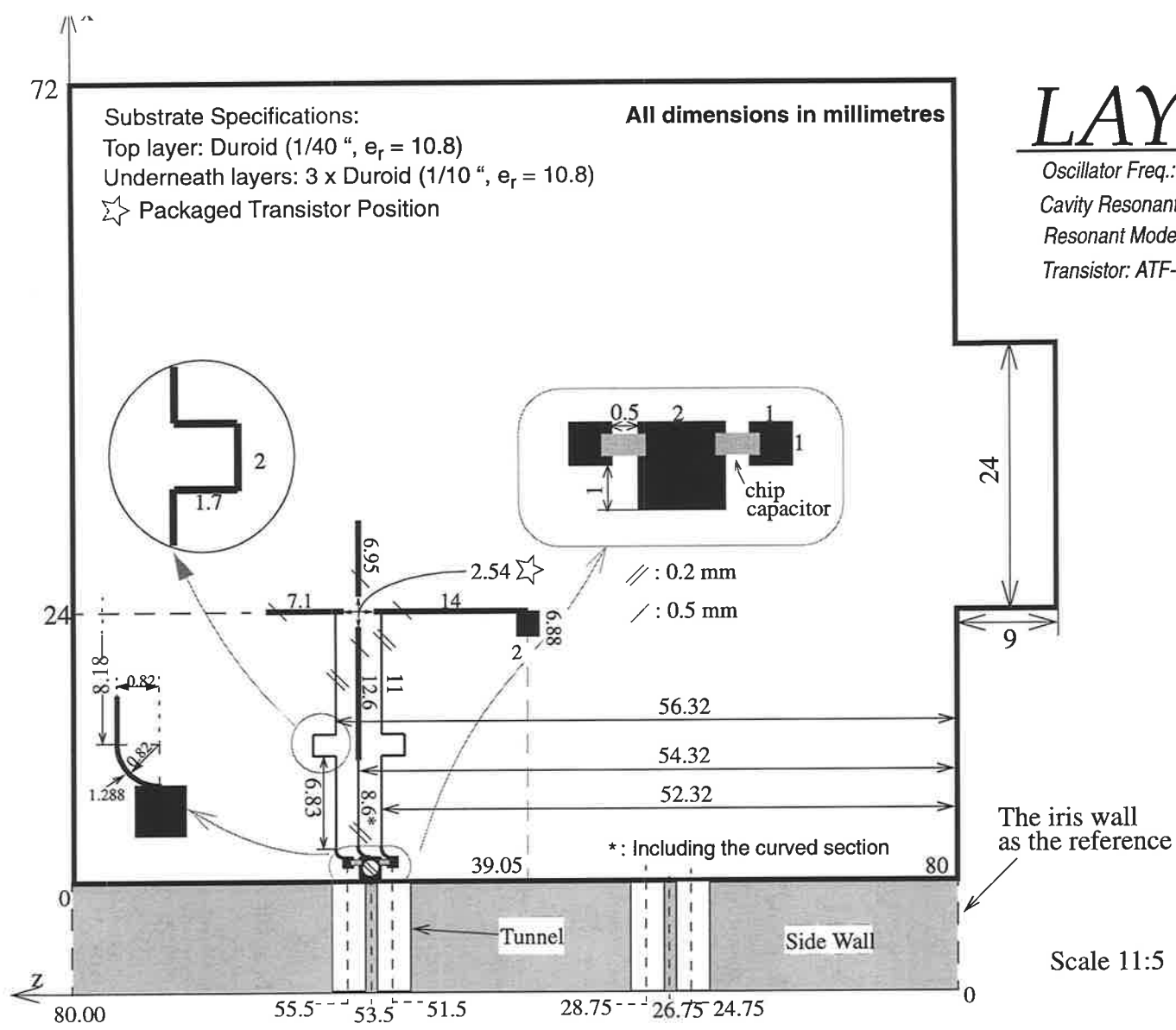
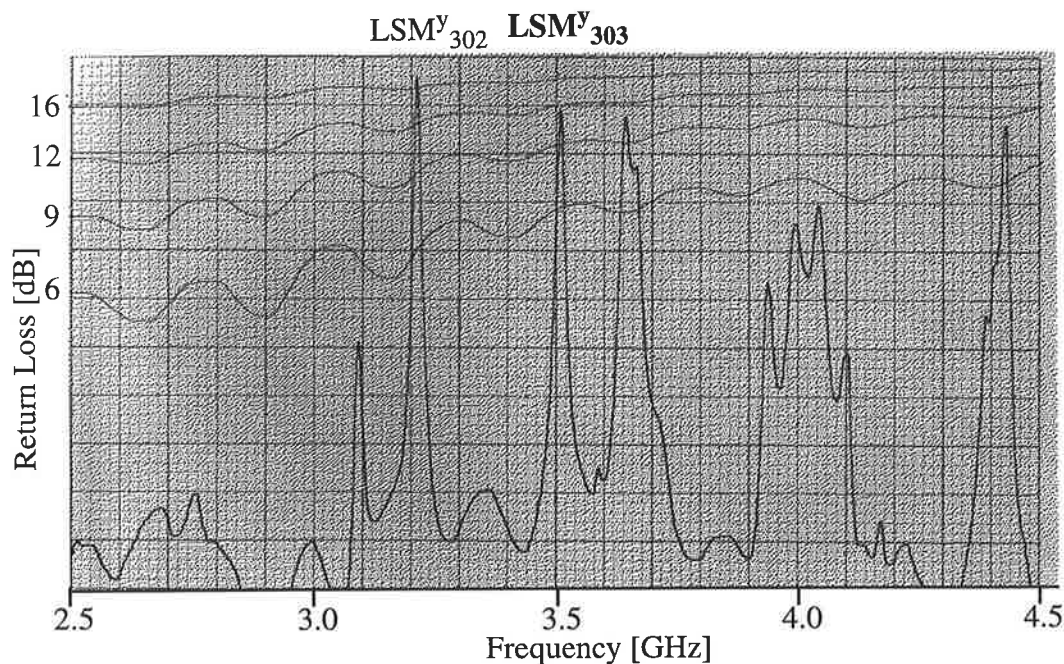


Figure 7-5. Complete layout of the single transistor oscillator: version 1 on the dielectric surface of a cavity with 80 mm length

### 7.3.1.2 Test Results

The single transistor oscillator with its standard air-filled rectangular waveguide output (WG10, inside dimensions 2.840 by 1.340 inches or 72 by 34 mm and operating range 2.60 to 3.95 GHz) can be tested as a passive single-port cavity resonator by connecting the assembly to a swept frequency reflectometer. The return loss characteristic at the output port of the assembly with the version 1 microstrip circuit metallisation in place but with no bias voltages applied to the transistor is shown in Figure 7-6.



*Figure 7-6. Swept frequency measurement of the single transistor oscillator version 1 assembly without bias*

The design resonant mode  $\text{LSM}^y_{303}$  is readily identified in the plot with a frequency of 3.51 GHz and a return loss of 12 dB which is equivalent to a coupling factor of 1.7 [56]. It has been observed that by slight movement of the dielectric filling, particularly the top layer, that may occur by simply removing and replacing the lid, the resonant frequency will change about 1% (3.51 to 3.55 GHz), whereas the change in the return loss may be high (3 to 12 dB) which is evidence of the sensitivity of the resonance equation (5-65) to small cavity perturbations. In fact the extra reactance that is caused by perturbations will disturb the reactance equilibrium required by (5-65) at the cavity aperture junction, leading

to a slightly shifted resonant frequency in order to cancel out the extra reactance. Changes in cavity wall resistance also caused by perturbation of the cavity will change the resultant coupling factor through changes to the unloaded cavity Q. The external -Q of the assembly can be measured from the frequency response of the mode of interest as shown in Figure 7-7, an expanded version of Figure 7-6 over the 3.4 to 3.6 GHz range.

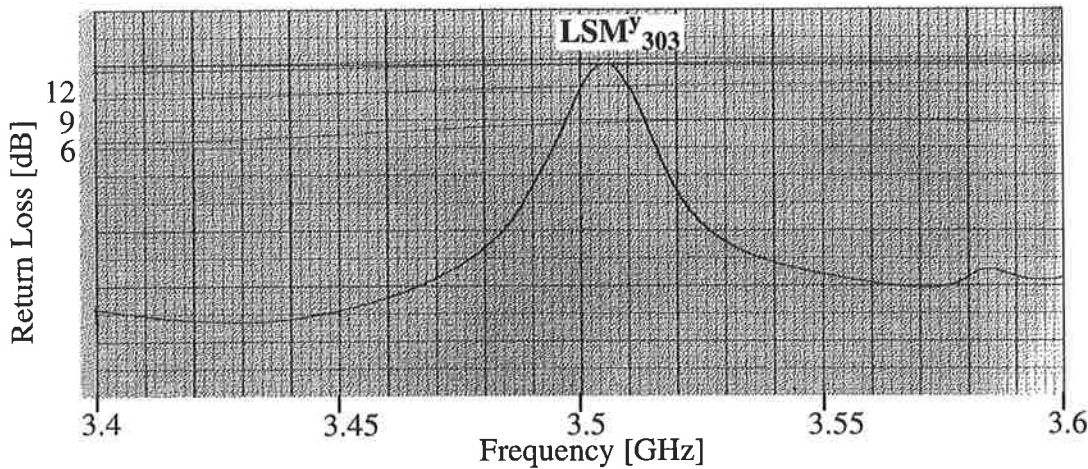


Figure 7-7. Frequency response of the dominant mode  $LSM^Y_{303}$

Accordingly, the loaded -Q of the assembly is easily obtained in this case as [56, pp. 136-143],

$$Q_L = \frac{f_0}{\Delta f} = \frac{3506}{10} = 350 \quad (7-5)$$

The external -Q is related to loaded -Q through the expression:

$$\frac{1}{Q_L} = \frac{1}{Q_{ext}} + \frac{1}{Q_u} \quad (7-6)$$

and the external -Q is related to the coupling factor  $\beta$  such that:

$$\beta = Q_u / Q_{ext} \quad (7-7)$$

By substituting  $Q_{ext}$  from (7-7) into (7-6) the unloaded Q is obtained as:

$$Q_u = Q_L \cdot (1 + \beta) \quad (7-8)$$

Using  $\beta = 1.67$  and  $Q_L = 350$  from Figures 7-6 and 7-7, the unloaded Q can be determined from (7-8) as  $Q_u = 936$  which is 9% higher than the value calculated from the

$\tan\delta$  of the dielectric filling (i.e.  $Q'_{LSM_{303}^y} = 852$ ) as given by (C-47). From this equation it may be concluded that the increase of  $Q_u$  is due to a decrease in conductor loss. As the cavity field is strongly concentrated inside the dielectric, it is suggested that the air gaps between the dielectric and the cavity walls may be responsible for a decrease in surface current and consequently conductor loss.

The output spectrum of the version 1 single transistor oscillator assembly with layout -1 is shown in Figure 7-8

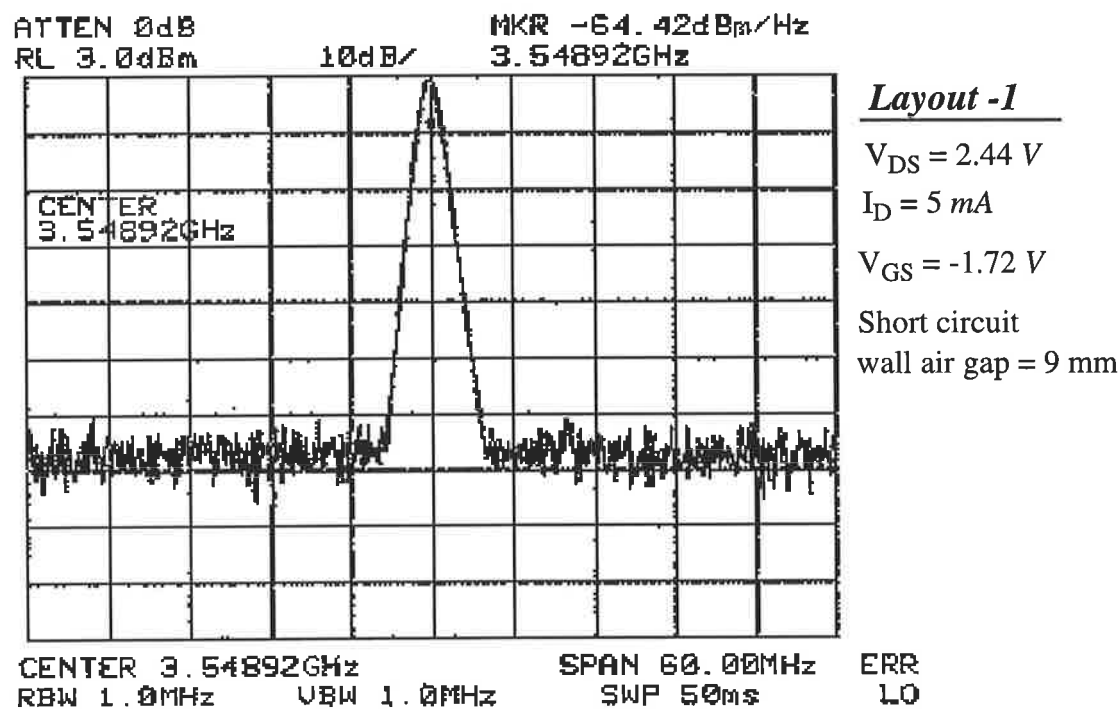


Figure 7-8. Output spectrum of the single transistor oscillator version 1

The oscillation was initially observed at about 3.5 GHz with an output power of -3 dBm and 12% efficiency. By gradually moving the short circuit wall back from the dielectric, the power output and drain current increased, so that at 9 mm air gap, +3 dBm RF power had been achieved as shown in Figure 7-8 with 16% DC to RF conversion efficiency. Adjusting the height of the transformer waveguide by replacing the metal blocks did not improve the efficiency beyond 16%.

### **7.3.1.3 Conclusion**

These initial test results clearly validate the combination of concepts that form the overall design as well as the analytical methods that have been developed for designing the cascade of components that form the assembly. In particular the oscillation frequency of 3.549 GHz compares favourably with the specification of 3.5 GHz and the passive structure resonance measurement of 3.505 GHz as read from Figure 7-7.

Power output and efficiency are comparable with results obtained with a similar transistor operating in a conventional microstrip circuit without a resonator coupled to the drain output port as detailed in Appendix G, Section 4.2 and Figure 10. The 1.67 value for coupling factor obtained from reflectometer measurement of the passive structure is comparable with but lower than the design value of 2.2 set out in step 7. Given the uncertainty with regard to losses in the actual test structure and also their theoretical modelling the agreement is better than might be expected.

In starting the oscillator the gate bias was initially set so that the MESFET channel was pinched off and the drain current was zero. The oscillation commenced as the gate bias was reduced but below a certain level of external bias setting a self bias level appeared due to the clamping action described in Section 2.6 and reported in reference [64]. However the MESFET does not appear to be operating under class C conditions because the efficiency as an indicator is too low. During the testing of this oscillator some difficulty was experienced in setting conditions that would cause the oscillations to start spontaneously. This coincides with the observation made in step 11 of the design that the negative resistance calculated is smaller than the empirical value normally required for small-signal based design to give good spontaneous oscillation build-up in practice.

## *7.3.2 Single Transistor Oscillator Version 2: Improved Efficiency*

### **7.3.2.1 Improving the Oscillator Performance**

In the version 1 design, some inconsistency in the start up of oscillation was found apparently due to the magnitude of the device negative resistance not being high enough relative to the level of load resistance. To clarify the problem, the driving point impedance of the coupling probe current strip,  $Z_{\text{strip}}$ , and its transformed value over the phasing line

to  $Z_L$  at the transistor drain are illustrated in Figure 7-9. The high level of the strip resistance results in low values for load resistance and poor coupling between the cavity and oscillator output for most lengths of strips.

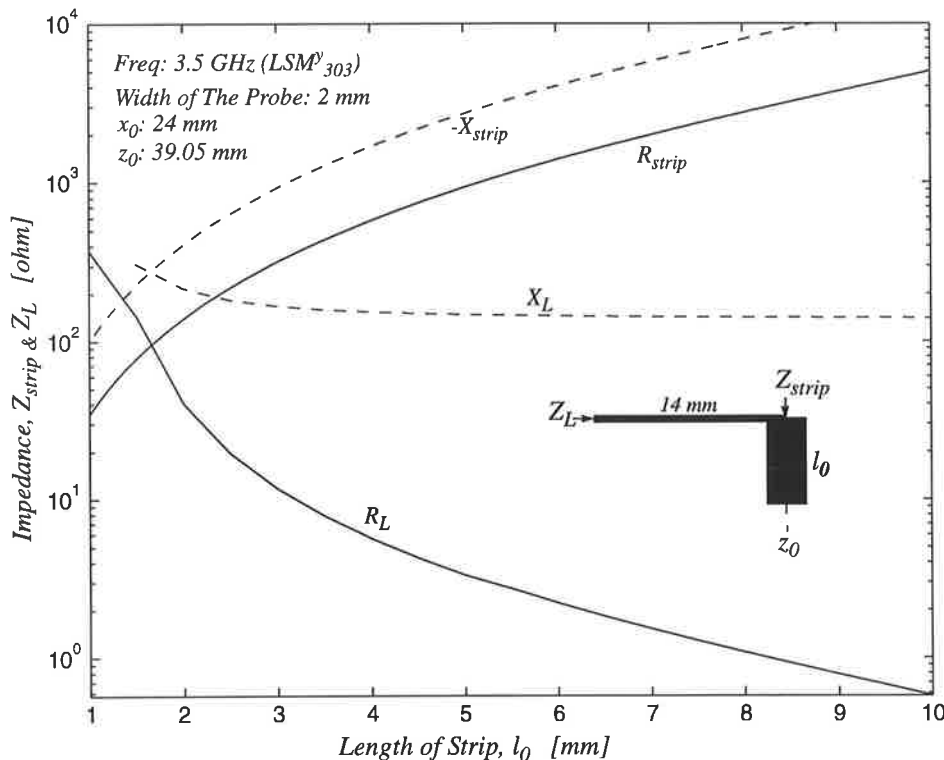


Figure 7-9. Load and driving point impedance of the coupling probe used in version 1 design

The highly capacitive reactance of the probe ( $-X_{\text{strip}}$ ) should be transformed by a relatively long phasing line to a moderate value of inductive reactance,  $X_L$ , because as previously explained, the device impedance is essentially capacitive (see Figure 4-15-C). The load resistance,  $R_L$ , is represented by the curve that rapidly drops below 10 ohms which is far lower than the normal 50 ohm load resistance. According to the variational equation (5-86) the probe driving point impedance depends on the intensity of the surface electric field at the strip and from calculations, the high impedance level of Figure 7-9 arises because the current strip of the version 1 design is located in a strong field area as shown in Figure 4-14. Therefore one approach to the question of how to improve the impedance and coupling level is to consider whether the probe strip can be located in an appropriate area

where the surface electric field intensity is reasonably low. This is shown in Figure 7-10.

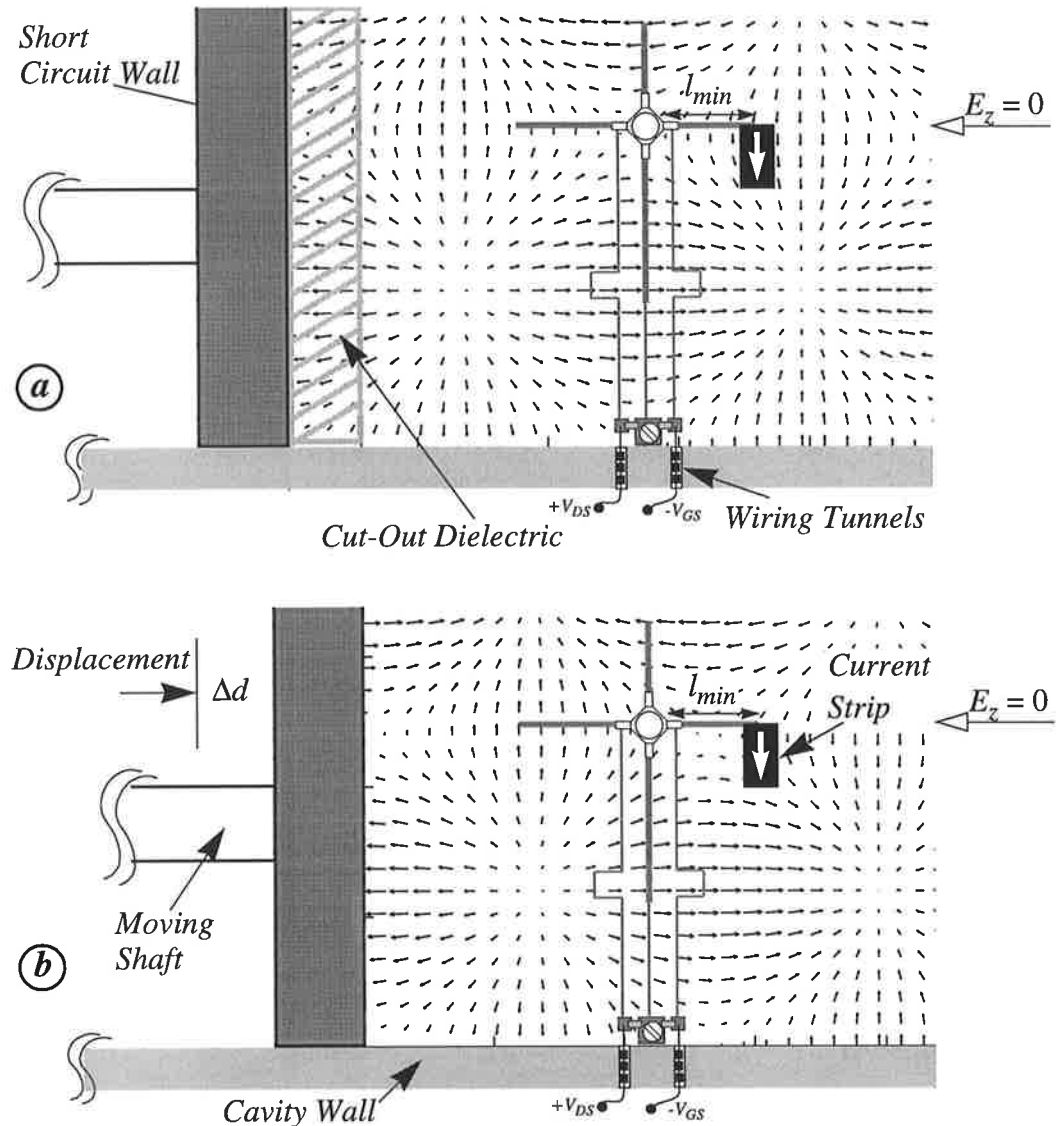


Figure 7-10. (a) Original position of the current strip with minimum length of phasing line (b) Displacement of the current strip into the lower-intensity electric fields

Figure 7-10 (a) illustrates the basic critical positioning layout where the transistor is located exactly at the null in surface electric field. The current strip should be at a minimum distance from the transistor, no more than  $\lambda_g/4$ , where  $\lambda_g$  is the wavelength in shielded-inverted microstrip. This minimum length phasing line is essential for transforming the capacitive probe (which is the effect of the capacitive iris) into an inductive reactance in order to cancel out the capacitive reactance at the transistor drain so fulfilling the oscillation condition. Figure 7-10 (b) shows a practical way of repositioning the current

strip relative to the surface E-field. Instead of displacing the circuit, the electric field is shifted with respect to the fixed position of the transistor and its connected strips. This is because the bias circuits should be connected to the permanent wiring tunnels that have been cut through the walls of the cavity. By reducing the length of the dielectric substrate and also reducing the length of the cavity by adjusting the short circuit wall, the field distribution will be consequently displaced with respect to the fixed circuit metallisations. This method is clearly shown in Figure 7-10 (b) where a portion of dielectric substrate with a length  $\Delta d$  has been cut off and the short circuit wall adjusted to reduce the cavity length by  $\Delta d$ . It is observed that the field distribution has shifted by the same length so that the current strip is located in a reasonably low field area.

This approach leads to the improved oscillator design that is presented in the following section.

### 7.3.2.2 Design

To improve the oscillator performance, a small portion of the dielectric substrate is removed and the length of the cavity is reduced as demonstrated in Figure 7-10. The new specifications are outlined in Table 7-3 where the cavity length is reduced about 11% compared with version 1, leading to a higher operating frequency that is determined by the  $LSM^y_{303}$  mode of interest.

**Table 7-3 Specifications for the single transistor oscillator -version 2**

Operating Frequency	Cavity Length	Height of the Transformer	Max. No. of Oscillators
3.6 GHz	71.2 mm	18.2 mm <sup>a</sup>	4

a. Two metal blocks are used as shown in Figure 6-2 with  $H = 7.9$  mm

**Steps 1 to 4:** As previously explained, this mode provides accommodation for as many as four transistor oscillators within the versatile test structure of Figure 7-2. Therefore design steps 1 to 4 are the same in this design as in version 1.

**Step 5.** Following the procedure of the design version 1, the resonant frequencies of the closed cavity are given in Figure 7-11 where the selected mode is highlighted.

Resonant Mode	Resonant Frequency [GHz]		
	Air Filled	Partially Filled	Dielectric Filled
LSM <sup>y</sup> <sub>301</sub>	6.591	2.982	2.023
LSM <sup>y</sup> <sub>302</sub>	7.533	3.259	2.312
<b>LSM<sup>y</sup><sub>303</sub></b>	<b>8.883</b>	<b>3.634</b>	<b>2.727</b>
LSM <sup>y</sup> <sub>304</sub>	10.485	4.066	3.218
LSM <sup>y</sup> <sub>305</sub>	11.240	4.536	3.757
LSM <sup>y</sup> <sub>306</sub>	14.092	5.038	4.325
LSM <sup>y</sup> <sub>307</sub>	16.006	5.563	4.913
.....	.....	.....	.....



Figure 7-11. Calculated resonant frequencies for the cavity with reduced length 71.2 mm

**Step 6.** The mode matching calculations of the coupling structure are then repeated for the new operating frequency to yield a new cavity wall aperture admittance:

$$\bar{Y}_{jun} = 0.446 + j0.522 \quad \text{at } 3.634 \text{ GHz} \quad (7-9)$$

which is not greatly different from (7-4).

**Step 7.** The exact resonant frequency and the output coupling factor are obtained from the numerical solution of (5-65) as outlined in Figure 7-12, with a coupling factor that is numerically higher than that of design version 1 (Figure 5-10). The slight increase of the resonant frequency of about 2 percent is due to the effect of the capacitive component of wall aperture admittance. The increased overcoupling should improve the DC to RF conversion efficiency.

**Step 8.** The field distribution for the new cavity length is determined as sketched in Figure 7-13. Note that while the field at the coupling probe has been reduced the transistor position is 54.32 mm distant from the iris wall as in design version 1 (Figure 7-5).

Closed Cavity Resonant Freq at  $\text{TM}_{303}^y$  = 3.634 GHz  
 Exact Resonant Freq at  $\text{TM}_{303}^y$  = 3.698 GHz  
 Output Coupling Factor = 3.062  
 Cavity Impedance at the Intersection is  $Z_{\text{cav}} = 12.58 + 155i \text{ ohm}$   
 Impedance of the Coupling Structure is  $Z_{\text{jun}} = 132.5 - 155i \text{ ohm}$   
 Normalised cavity Admittance is  $y_{\text{cav}} = 0.0728 - 0.897i$   
 Normalised Port Admittance is  $y_{\text{jun}} = 0.446 + 0.522i$   
 Normalised Input Admittance is  $y_{\text{in}} = 3.062 - 0.0i$   
 Minimum Error = 1.775e-026

Figure 7-12. Exact resonant frequency of the coupled cavity and output coupling factor

With a minimum phasing line length of 7mm, the current strip is located at a distance of 46.05 mm from the iris wall and is in a relatively low-intensity E-field area.

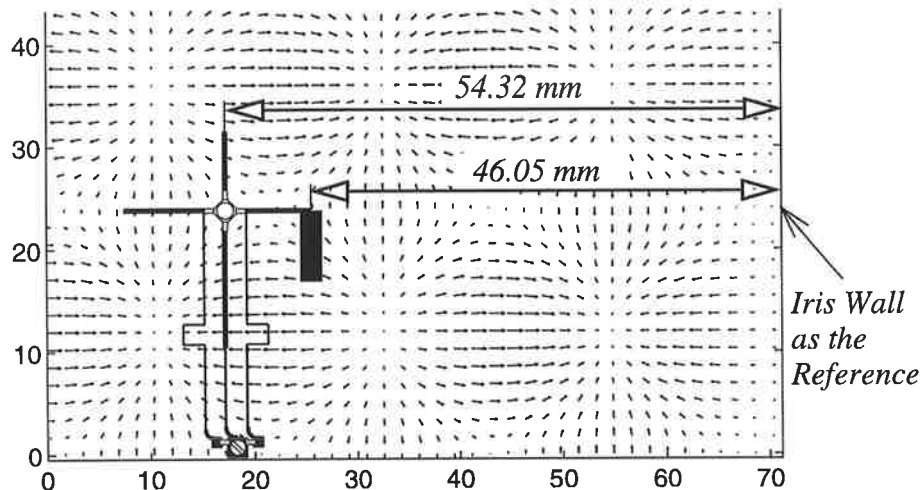


Figure 7-13. Positioning of the circuit on the E-field distribution for version 2 design

**Step 9.** The impedance of the probe strip is determined by the variational equation (5-86) for the transversal strip with the driving point as specified from Figure 7-13 ( $x_0 = 24 \text{ mm}$  and  $z' = 46.05 \text{ mm}$ , where  $z'$  is the distance from the iris wall). The driving point impedance of the current strip,  $Z_{\text{strip}}$ , and its transformed value,  $Z_L$ , is shown in Figure 7-14.

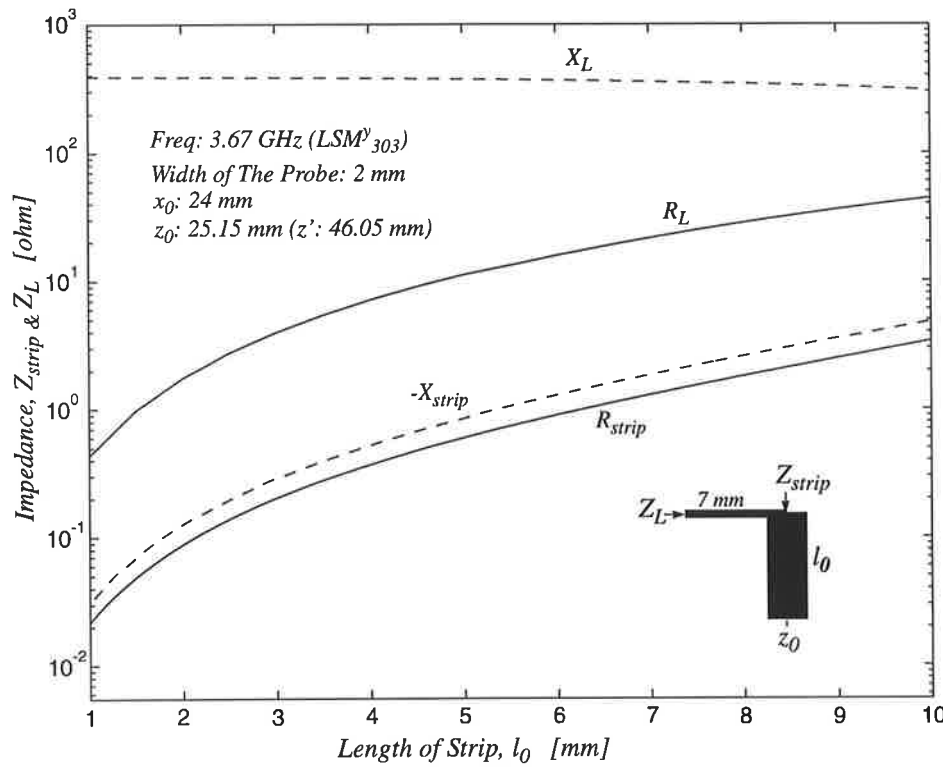


Figure 7-14. Impedance characteristics of the probe strip in the version 2 design

The probe exhibits a low level of impedance due to its location in a low-intensity E-field area. The transformed load resistance ( $R_L$ ) increases monotonically to around 50 ohm which is comparable with conventional 50 ohm microstrip. Also the transformed inductive reactance ( $X_L$ ) varies between 300 and 400  $\Omega$  which is well within the range of the capacitive reactance that the transistor drain presents.

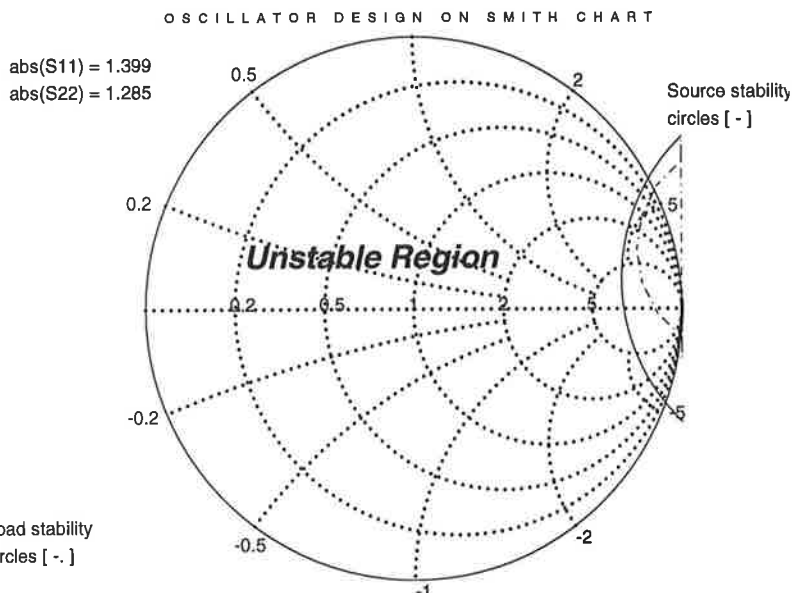
**Step 11.** The oscillator design program in shielded-inverted microstrip can be executed in a similar way to that described in Section 4.6 . The program messages relevant to this version 2 design are outlined in Figure 7-15. The oscillator frequency has been chosen to be 3.67 GHz which is slightly less than the exact resonant frequency of the cavity, 3.698 GHz, to allow some frequency adjustments using the cavity short circuit and the gate microstrip tuning screw.

DESIGN OF MICROWAVE MESFET OSCILLATOR  
ON  
SHIELDED INVERTED MICROSTRIP  
USING  
ATF -13036 FET TRANSISTOR

ENTER Oscillator frequency in GHz = 3.67  
SELECT common-source/ common-gate [cs/ cg] : cs  
-----<< Selection of series feedback >>-----  
If you want a short circuit stub choose : s  
If you want a open circuit stub choose : o  
If you do not need a feedback choose : n  
ENTER your choice: [ s, o, n ] o  
Graphical analysis of series feedback?? [y/n] n  
Length of the feedback strip in degree = 40  
Width of the feedback strip in millimetre = 0.5  
Graph - A is displayed  
-----<< Initialisation >>-----  
Starting from the last minimum point ? [y/ n]: n  
Graph - B and C are displayed  
ENTER the min. length of Gate strip [mm]: 5  
ENTER the max length of Gate strip [mm]: 10  
ENTER the width of Gate strip [mm]: 0.5  
ENTER min. length of Probe strip [mm]: 6  
ENTER max length of Probe strip [mm]: 10  
ENTER the width of Phasing strip [mm]: .5

Figure 7-15. Program messages for the version 2 design

The amount of series feedback is chosen from the required level of the device reactance,  $X_d$ , which should be cancelled out by the load reactance,  $X_L$ . For 45 degrees series feedback the device and load characteristics are illustrated in graphs A, B and C of Figure 7-16.



*Graph - A: A highly unstable device is obtained by using 40 degree series feedback*

*Graph - B is illustrated in Figure 7-14*

*Graph - C*

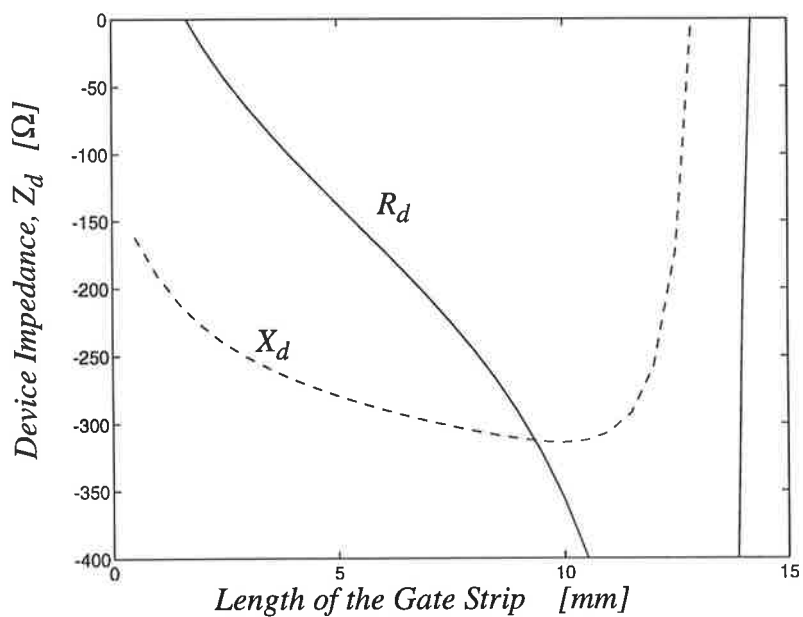


*Figure 7-16. Program graphics: Graph -A) stability circles, Graph-B)  $Z_L$  and Graph-C)  $Z_d$*

The program initialisations include the minimum and maximum lengths of the gate and probe strips. These are set from graphs B and C which appear on the computer display screen. The program results outlined in Figure 7-17 exhibit a high negative resistance that will give rise to strong start -up of oscillations.

```
<< THE Hooke & Jeeves Optimization Routine >>
```

```
Minimum error function is Fmin = 7.0421 e-006
```

```
Number of function evaluations: 409
```

```
Zdev = -6.6876 - 5.7131i Zload = 0.6950 + 5.7131i
```

```
<<< Optimization Result for The Shielded Inverted Oscillator Design >>>
```

```
transistor: ATF-13036 MESFET
```

```
oscillator frequency = 3.67 GHz
```

```
length of gate strip = 9.88 mm
```

```
width of gate strip = 0.5 mm
```

```
length of current strip = 9.2 mm
```

```
width of current strip = 2 mm
```

```
type of series feedback : open circuit stub
```

```
length of equivalent single source-strip = 40 degree
```

```
length of upper source-strip = 5.489 mm
```

```
length of lower source-strip = 13 mm
```

```
width of source-strips = 0.5 mm
```

```
length of DC-return strip = 8.202 mm
```

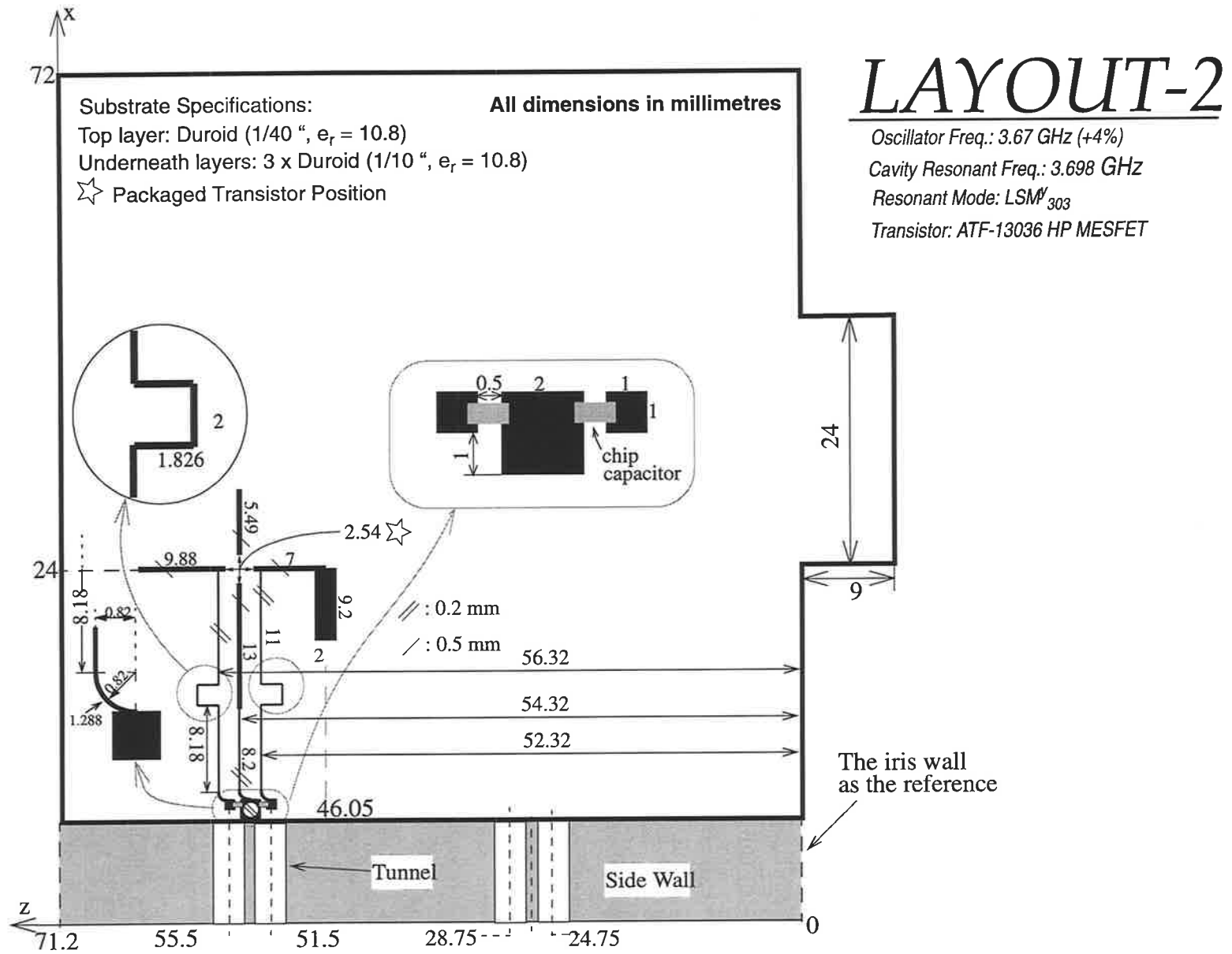
```
width of DC-return strip = 0.2 mm
```

```
length of phasing strip = 7 mm
```

Figure 7-17. Program result for oscillator version 2 design on shielded inverted microstrip

The complete layout of the version 2 design is drawn in Figure 7-18 where the cavity length has been reduced to 71.2 mm in comparison with the version 1 layout. However the transistor position has not been changed with respect to the iris wall as the reference plane.

Figure 7-18. Complete layout of the version 2 design



### 7.3.2.3 Test Results

The swept frequency measurement of the cavity for the version 2 design, reveals a higher resonant frequency for the  $LSM^y_{303}$  mode as was expected and is shown in Figure 7-19.

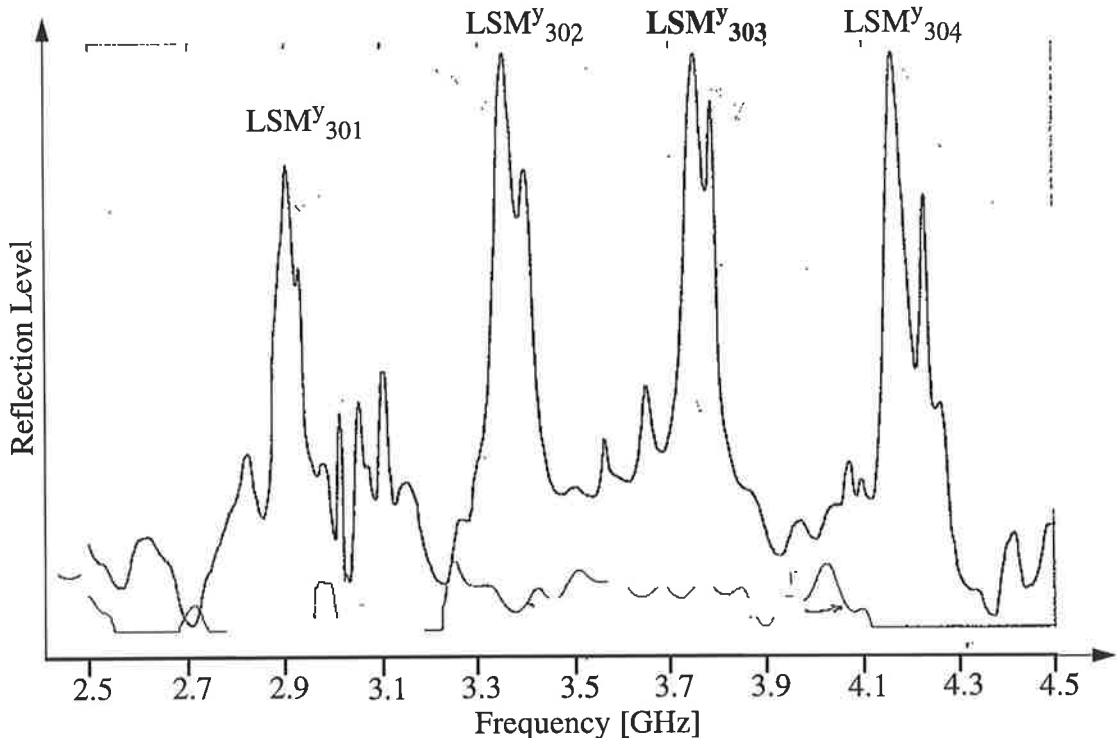
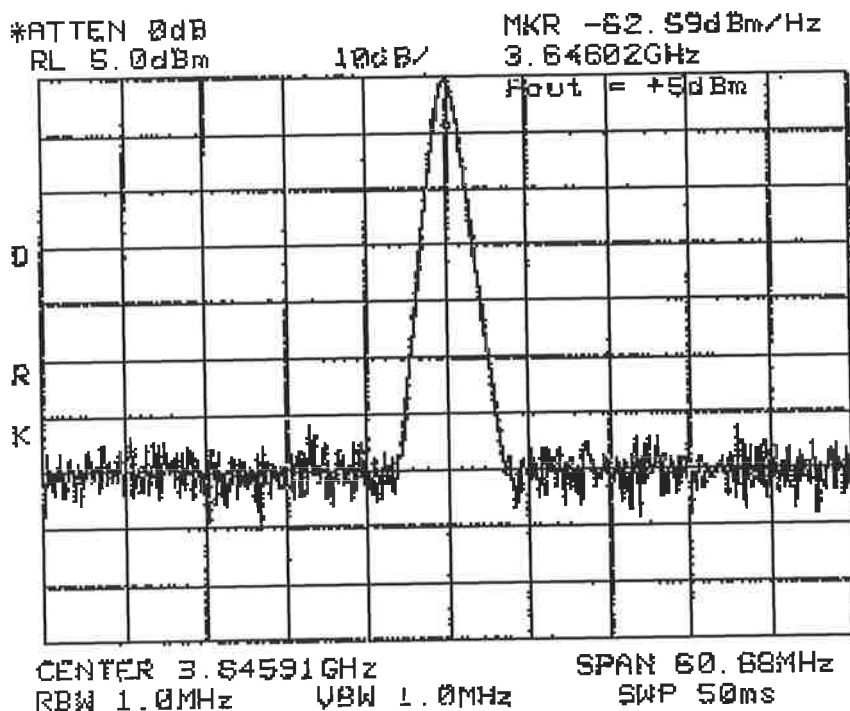


Figure 7-19. Swept frequency measurement of the version 2 design with reduced cavity length

The output spectrum of the version 2 design is shown in Figure 7-20 with +5 dBm power output and 26 percent DC to RF conversion efficiency. The oscillator frequency, 3.646 GHz, is slightly lower than the resonant frequency of the cavity  $LSM^y_{303}$  mode which is 3.75 GHz in Figure 7-19. This is expected due to the driving effect of the oscillator circuit on the cavity resonant frequency.

During the measurement, consistent start -up and strong oscillation has been observed with relatively high efficiency. This is evidence of the high level of negative resistance of the active device and the improved coupling of the oscillator output to the partially-filled cavity by locating the probe strip in a sufficiently low intensity E-field area on the dielectric interface as discussed earlier. The results are superior to those for the version 1 design

that demonstrated relatively poor oscillator behaviour with low efficiency. The strength of the build-up and oscillation level as the externally applied gate bias is reduced is such that it can be set to zero in which case a bias voltage still persists that is due to the function of the Schottky diode type gate with a relatively large amplitude RF voltage applied to it through feedback. This is the self biasing effect referred to in Section 2.6 and observed in the version 1 design in Section 7.3.1.3.



### Layout -2

$$V_{DS} = 2.44 \text{ V}$$

$$I_D = 5 \text{ mA}$$

$$\text{external } V_{GS} = 0$$

$$\text{Air Gap} = 9 \text{ mm}$$

Figure 7-20. Output spectrum of the version 2 design with 5 dBm power output in the  $LSM^V_{303}$  mode

The DC to RF efficiency can grow even higher than 26% by further adjustments of (1) the bias voltage,  $V_{DS}$ , (2) the short circuit end wall gap, and (3) the oscillator gate strip tuning screw on the cavity lid. It has been observed that adjustment of the short circuit gap has a primary effect on improving the output power level. For a fixed position of short circuit gap, the DC to RF conversion efficiency can be improved by reducing the externally applied gate bias voltage  $V_{GS}$  to zero. Also the tuning screws on the cavity lid may also improve the power output and efficiency. Finally, for a fixed setting of the short circuit gap

and the externally applied gate bias set to zero the output power will smoothly rise with increasing drain bias voltage. A typical characteristic for the measured output power for the version 2 design is shown in Figure 7-21, where the measured points are indicated by small circles. Also the DC to RF conversion efficiency which is calculated with the following relation is shown in the diagram below the first one.

$$\eta = \frac{P_{out}}{V_{DS} \times I_D} \% \quad (7-10)$$

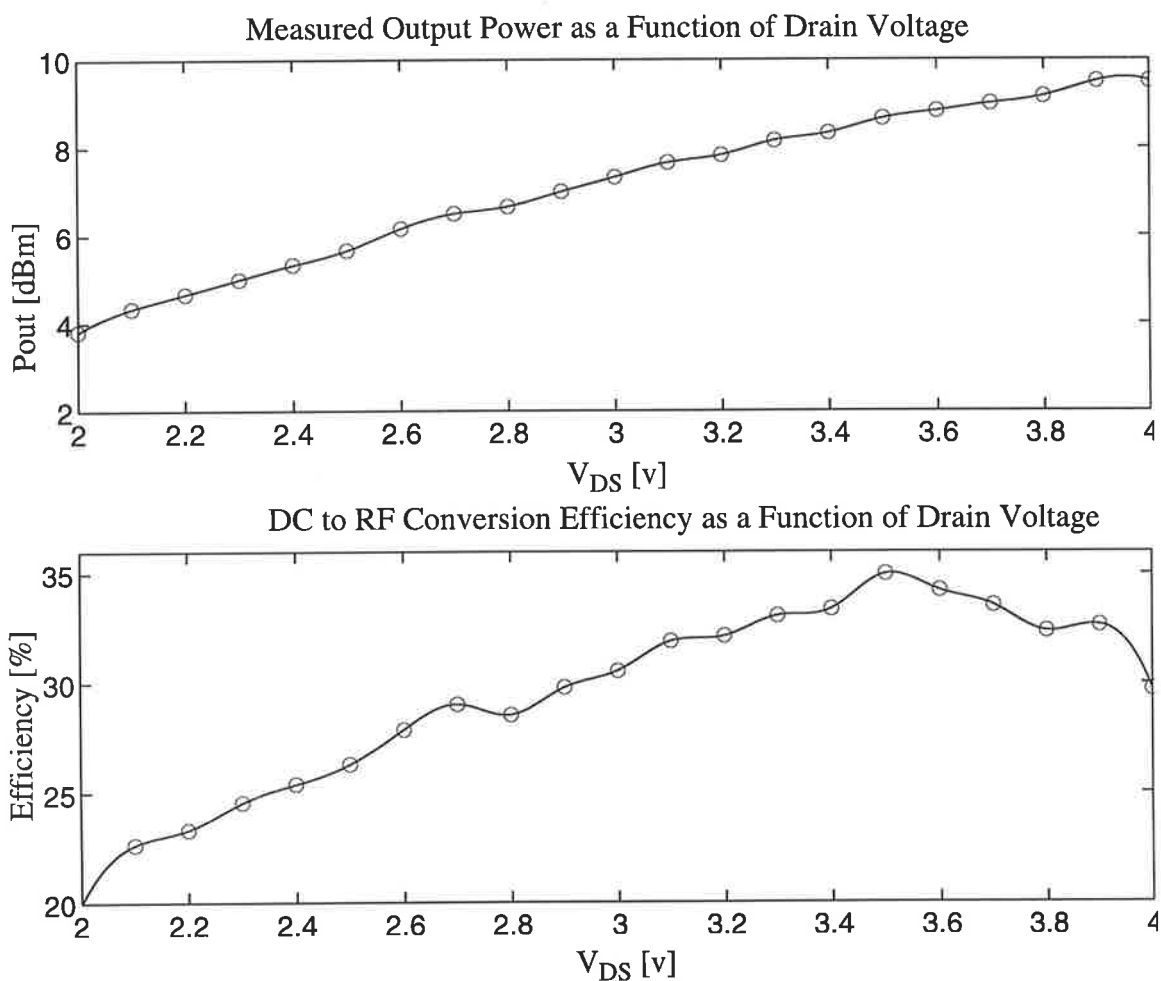
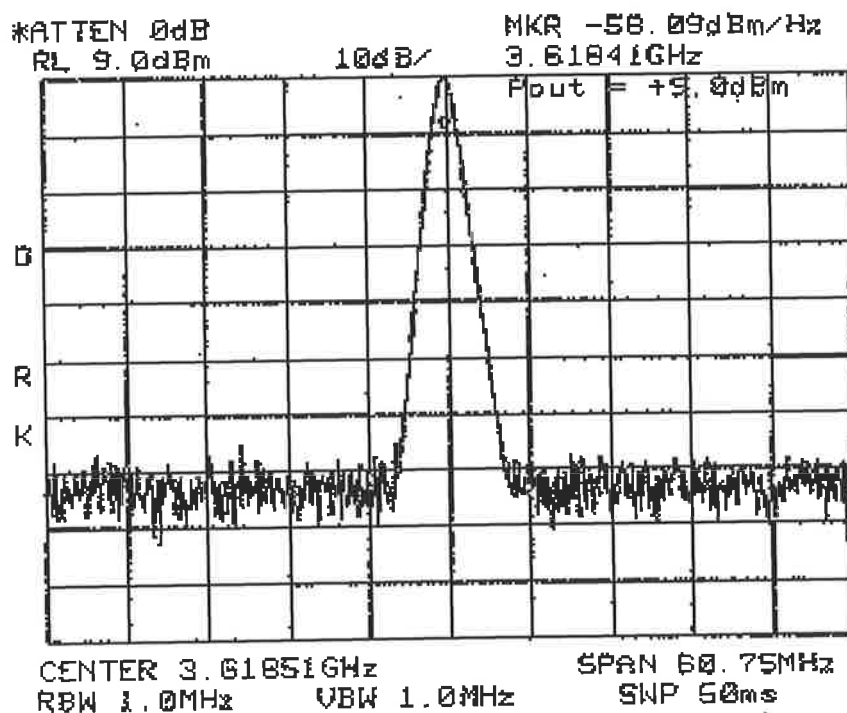


Figure 7-21. Measured output power and efficiency of the version 2 design versus drain voltage

For the particular settings of the short circuit gap, gate bias and the tuning screw, a

maximum efficiency of 35% is achieved with  $V_{DS} \approx 3.5$  volts. The measured output power in this case is about +8.5 dBm (7 mW). Also by increasing the drain voltage above this value, the output power will gradually increase as shown in Figure 7-21, but the efficiency will diminish due to the rapid increase in the drain current which will result in proportionately higher DC power input and lower efficiency. For a drain voltage of 3.72 volts, an output power of +9.0 dBm with a DC to RF conversion efficiency of 33% has been measured which is graphed from the spectrum analyser record shown in Figure 7-22. The oscillator frequency is 3.618 GHz which is slightly lower than that of the Figure 7-20 spectrum due mainly to the larger short circuit gap and other adjustments such as bias voltages and the tuning screw, made in order to optimise the oscillator power output and efficiency.



Layout -2  
 $V_{DS} = 3.72 V$   
 $I_D = 6.5 mA$   
self bias  $V_{GS} = -0.96 V$   
Air Gap = 18 mm

Figure 7-22. Spectrum of maximum output power for the version 2 design with 33% efficiency

#### 7.3.2.4 Conclusions

The results that have been obtained in tests on the version 2 single transistor oscillator are further validation of the design concepts and methods that have been presented. The measured oscillation frequency of 3.646 GHz differs from the frequency of 3.670 GHz

adopted in preparing the layout of the metal stripline components by 0.7 percent. Improvement in the design of the coupling probe and phasing line has yielded a large increase in output power and more than a doubling of the DC to RF conversion efficiency to a maximum of 35 percent.

Part of the improvement may have arisen for reasons apart from the design changes. Moving the transistor away from the surface electric field null position exposes the metal strips from the source electrodes to a small parallel component of electric field that will induce a voltage that will modify the feedback. Also the version 2 oscillator uses a different transistor although it is from the same batch as the one used in the version 1 oscillator.

The research is directed towards the passive mounting structure and not the active device which because of resource limitations is imperfectly known. In design the MESFET is simply represented in terms of the manufacturer's small signal scattering parameters and recommended operating conditions and limits reproduced in Appendix H for reference. However a vital function of the passive mounting structure is feedback. It affects the start-up behaviour as well as the steady state characteristics. In particular it determines the mode of operation of the active device. As explained in Sections 2.6 and 3.3.16 a resonant structure in cascade with the load is needed for class C operation with high efficiency low distortion output. 35 percent efficiency may be a fortuitous result but it is also a result that suggests that the partially-filled resonator can be used in this assembly to yield class C operation. The feedback function for class C operation of a MESFET oscillator involves highly non-linear operation of the transistor. Self-biasing through rectification and clamping action at the gate must be such that drain current flows for less than half of the RF cycle, and the loaded quality factor of the resonator connected to the drain together with the level of feedback must provide a large enough RF level at the gate for the necessary level of self biasing voltage. It is evident that the design of the passive mounting structure for class C oscillator operation involves an accurate knowledge of the operating characteristics under highly nonlinear conditions for the particular MESFET to be tested in that structure.

## 7.4 Design Validation Testing: Power Combining

### 7.4.1 *The Dielectric Resonator as a Power Combiner*

The measurements of frequency, power output and efficiency on the single transistor designs have shown very good agreement with results expected from design theory as given in detail in Section 7.3. The results so far, validate the concepts and the design methodology proposed in this thesis for planar oscillator circuits built on electrically thick dielectric wafers. They are clear evidence that the novel assembly that has been developed on the basis of monolithic fabrication constraints will work.

However in order to achieve an important goal towards the production of efficient and cost effective millimetre-wave sources, further experiments are needed to verify that the partially-filled cavity can act as a multiple -oscillator power combiner, so that a number of oscillators placed inside the partially filled cavity may be used to compensate for reduced single device power output at higher frequencies. In this case the individual oscillators will contribute to the overall output in a power combined manner, leading to a new class of resonant cavity power combiner in which the thick dielectric superstrate is exploited as the combining medium and the surface wave mode resonance as the synchronising and phasing mechanism for all of the oscillators. This phenomenon has been found in thick substrates in certain spatial power combining structures of the quasi-optical grid oscillator type. However the substrate mode effect has been neglected in the design methods used for these structures, and it is only the experiments at millimetre wave frequencies that have revealed invalid assumptions as the cause of erroneous design and significant errors.

In this assembly the thick superstrate is enclosed by the cavity resulting in more intimate coupling between the oscillator circuits which is enhanced by the resonant field distribution in what has become a partially-filled cavity. Such a coupling arrangement amongst a planar array of oscillators appears not to have been reported in the literature. The successful results for single transistor oscillators may not necessarily indicate the feasibility of this power combining theory. A design is necessary, that incorporates at least two oscillator circuits for testing, in order to verify the power combining function of the partially-filled resonator.

### 7.4.2 Power Combined Two Transistor Oscillator

#### 7.4.2.1 Design

The same cavity length as that used in the version 2 single transistor oscillator will accommodate two oscillators and is the basis of the specifications in Table 7-4.

**Table 7-4 Specifications for the design of the power combined two transistor oscillator**

Operating Frequency	Cavity Length	Resonant Mode	Transformer Height	No. of Oscillators
3.6 GHz	71.2 mm	LSM <sup>y</sup> <sub>303</sub>	18.2 mm <sup>a</sup>	2

a. Two metal blocks are used as shown in Figure 6-2 with  $H = 7.9$  mm

**Steps 1 to 8** are exactly the same as described in the version 2 single transistor oscillator design of Section 7.3.2.2 with the aim of achieving the high performance of the previous design. The driving points of the probe current strips are located in the same position relative to the iris and side wall as shown in the version 2 oscillator layout of Figure 7-18 and each is connected to its transistor drain with a 7 mm phasing line. The oscillators are transversally positioned with perfect mirror-symmetry as shown in Figure 7-23. For future reference, the oscillators are numbered as device 1 and 2 as specified in Figure 7-23.

**Step 9.** The variational calculation for the driving point impedance of each current strip is similar to that for the single oscillator design except that both current strips should be taken into account in the volume source integration of equation (5-83).

Due to the mirror symmetry of the current strips and the cavity relative orientation of the electric field distribution on the surface of the superstrate as shown in Figure 7-23, both current strips will exhibit the same driving point impedance that is sketched in Figure 7-24. Similar to the version 2 oscillator design result the current strip exhibits a capacitive impedance,  $Z_{strip}$ , which is transformed through the 7 mm phasing line to an inductive load,  $Z_L$ .

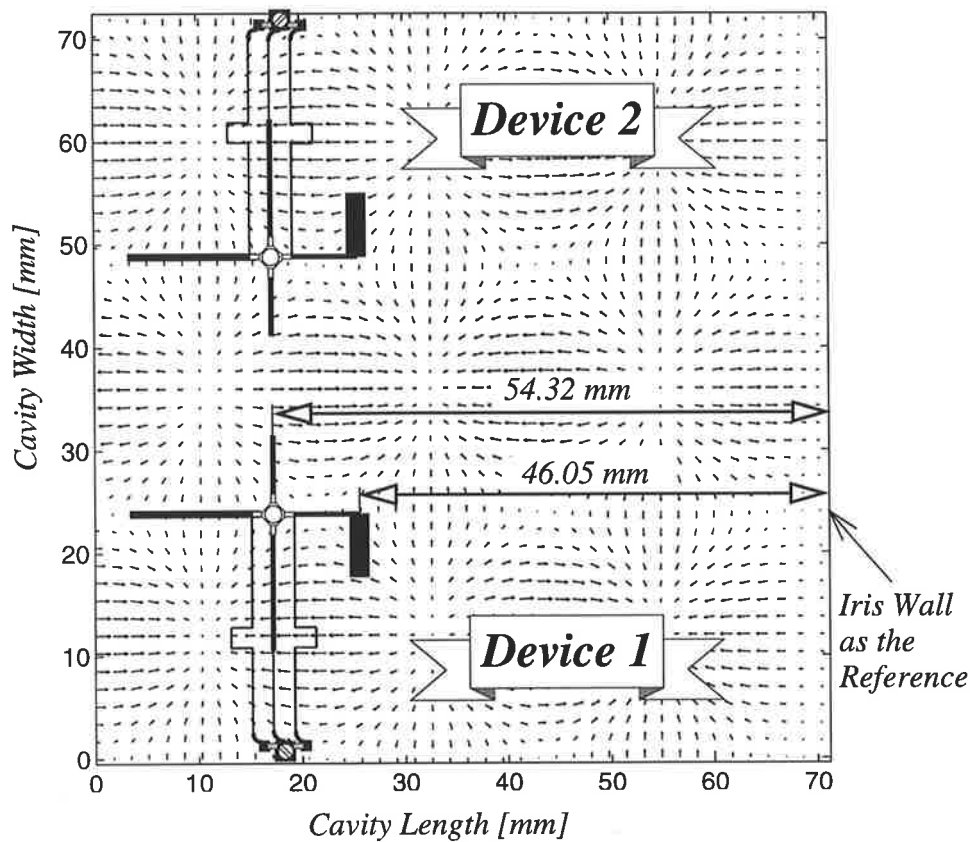


*Figure 7-23. Transversal position of two oscillators with perfect mirror-symmetry*

**Step 10** uses the data calculated in the design in Section 7.3.1.1.

**Step 11.** The oscillator design program is executed in a similar way to that described in the version 2 design. The oscillation frequency is chosen to be 3.65 GHz and the electrical length of the series feedback to be 50 degrees. The program messages are given in Figure 7-25, with the initialisation graphs as shown in Figure 7-26. The program results are subsequently shown in Figure 7-27.

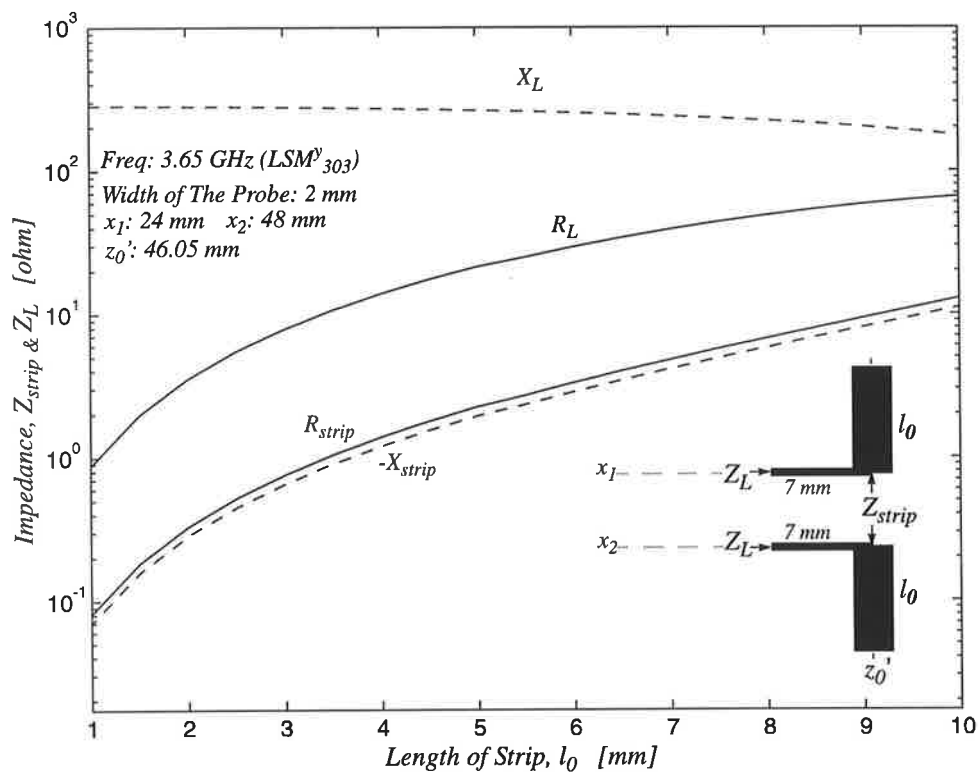


Figure 7-24. Impedance characteristics of the symmetrical current strips in the power combiner design

```

DESIGN OF MICROWAVE MESFET OSCILLATOR
ON
SHIELDED INVERTED MICROSTRIP

ENTER Oscillator frequency in GHz = 3.65
SELECT common-source/ common-gate [cs/ cg] : cs
-----<< Selection of series feedback >>-----
If you want a short circuit stub choose : s
If you want a open circuit stub choose : o
If you do not need a feedback choose : n
ENTER your choice: [ s, o, n ] o
Graphical analysis of series feedback?? [y/n]  n
Length of the feedback strip in degree =  50
Width of the feedback strip in millimetre =  0.5
Graph - A is displayed

```

Figure 7-25. Program messages for the power combiner design

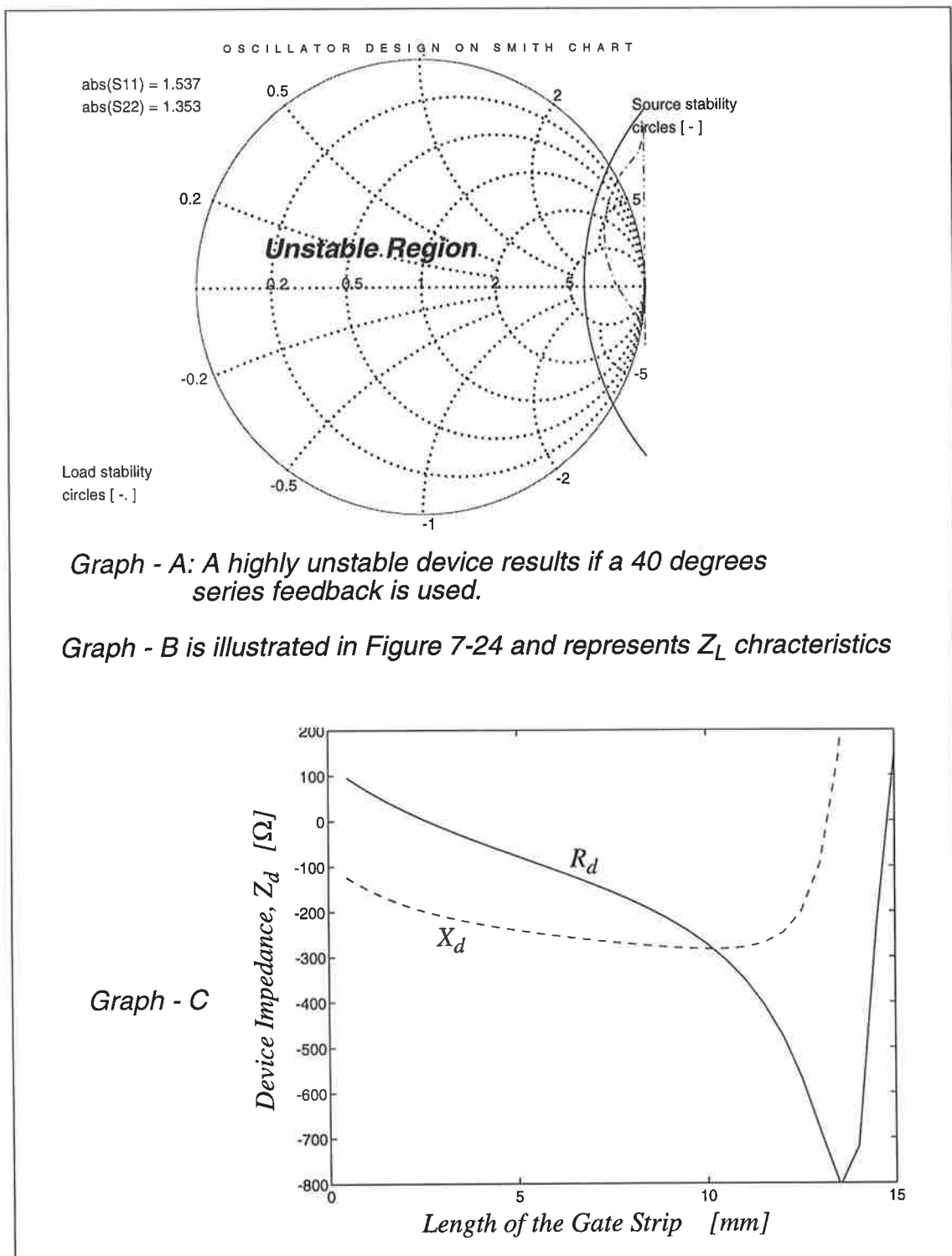


Figure 7-26. Program graphics for the power combiner design, including stability circles,  $Z_L$  and  $Z_d$

```
<< THE Hooke & Jeeves Optimization Routine >>
Minimum error function is Fmin = 2.1312 e-005
Number of function evaluations: 400
Zdev = -10.6133 - 4.4525i Zload = 0.9729 + 4.4525i
```

```
<<< Optimization Result for The Shielded Inverted Oscillator Design >>>
transistor: ATF-13036 MESFET
oscillator frequency = 3.65 GHz
length of gate strip = 12 mm
width of gate strip = 0.5 mm
length of current strip = 8.1 mm
width of current strip = 2 mm
type of series feedback : open circuit stub
length of equivalent single source-strip = 50 degree
length of upper source-strip = 5.818 mm
length of lower source-strip = 14.63 mm
width of source-strips = 0.5 mm
length of DC-return strip = 8.725 mm
width of DC-return strip = 0.2 mm
length of phasing strip = 7 mm
```

Figure 7-27. Program results for the power combiner design

The complete layout of the two transistor oscillator power combiner is given by Figure 7-28. The circuit was fabricated and tested and the experimental results are presented in the following section.

## Substrate Mode Power Combiner

# LAYOUT-3

Oscillator Freq.: 3.65 GHz  
 Cavity Resonant Freq.: 3.698 GHz  
 Resonant Mode:  $LSM_{303}^y$   
 Transistor: ATF-13036 HP MESFET

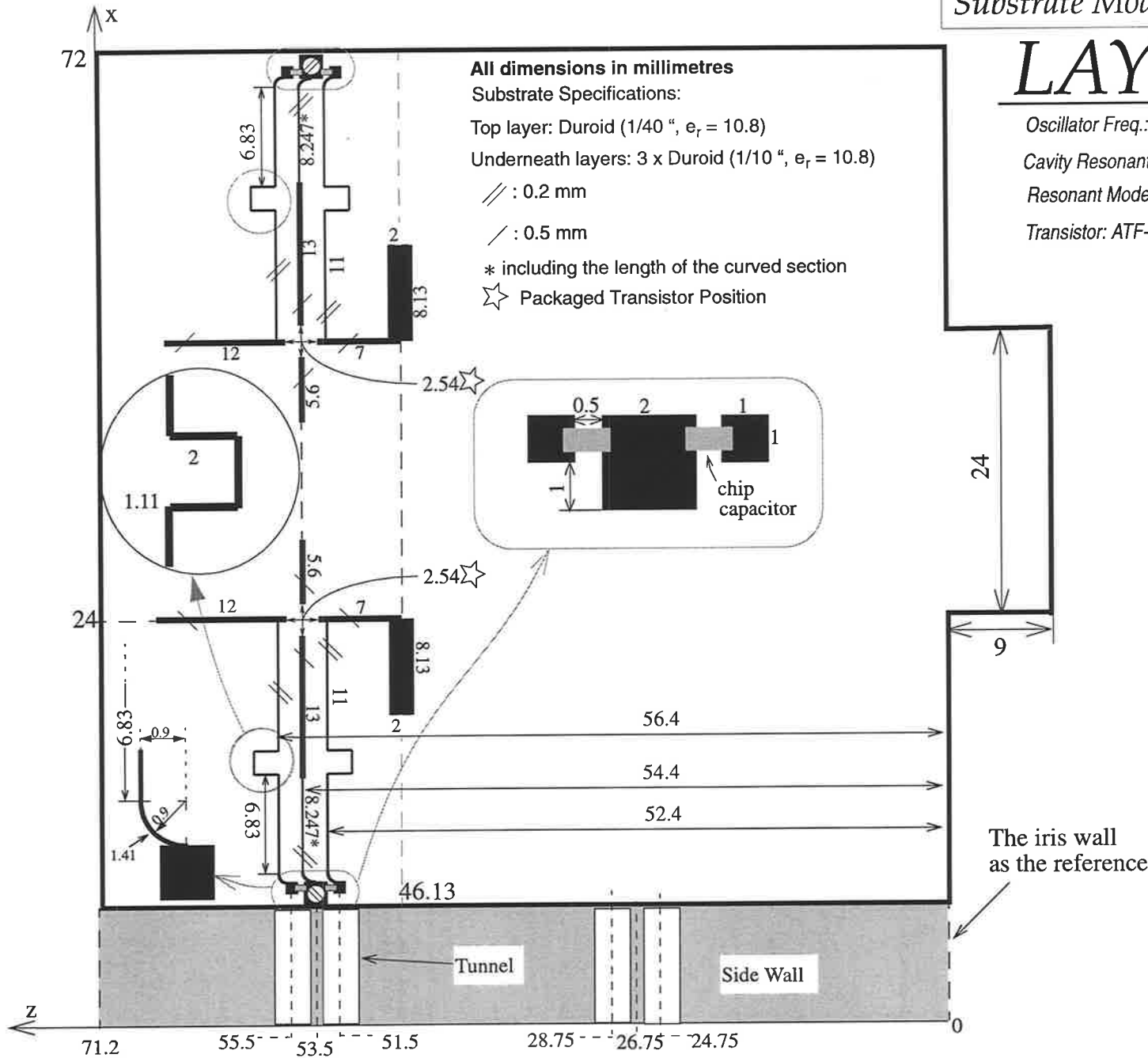
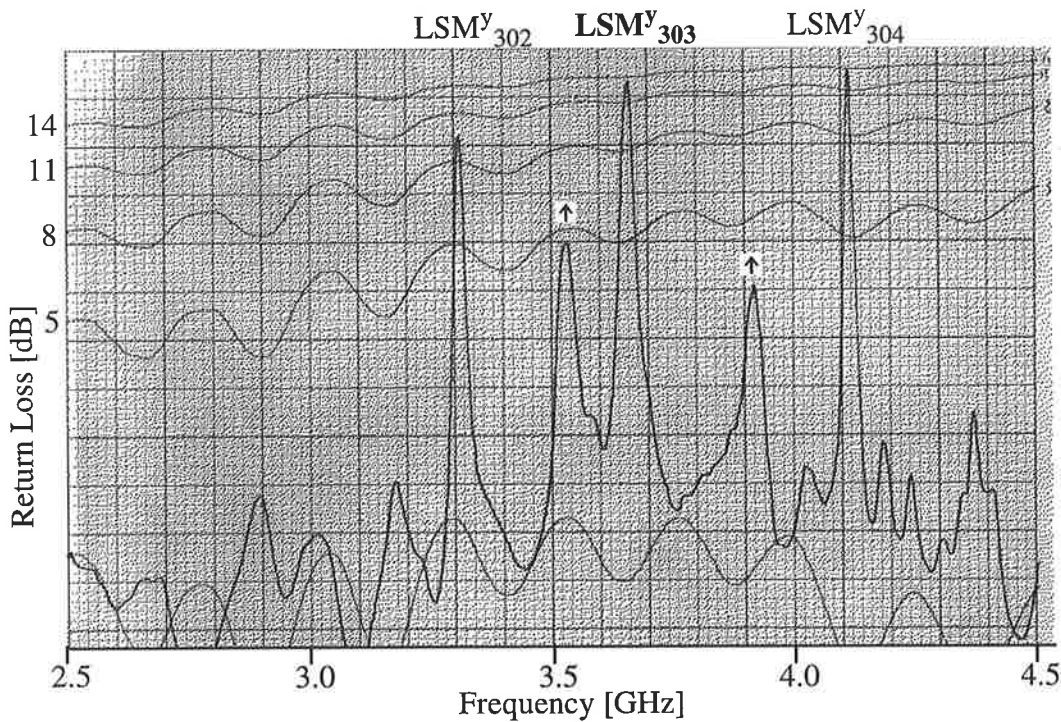


Figure 7-28. Complete layout of the two transistor power combiner design

#### 7.4.2.2 Results

A swept frequency measurement of the partially-filled cavity with the power combined two transistor oscillator in place but with no bias applied is shown in Figure 7-29, where the measured resonant frequency of the  $\text{LSM}^y_{303}$  mode of interest is 3.66 GHz. Also other resonant modes are clearly observed but they are either loosely coupled to the load or well separated in frequency from the oscillator design frequency.



*Figure 7-29. Swept frequency reflection characteristic of the passive two transistor oscillator power combiner*

In particular the loosely coupled resonances on either side of the  $\text{LSM}^y_{303}$  resonance, identified by small cursors, that have appeared for the first time may be produced by the metallisations and MESFET packages of the oscillator circuits introducing extra perturbation inside the partially-filled cavity.

Oscillation was found to occur with either one or both transistors biased. The output spectrum of the assembly, with device 1 turned on and device 2 turned off has been measured with the spectrum analyser and is printed in Figure 7-30, with -2.2 dBm output power at 3.6095 GHz oscillation frequency. The drain voltage was set at 2.0 volts, the gate bias reading was

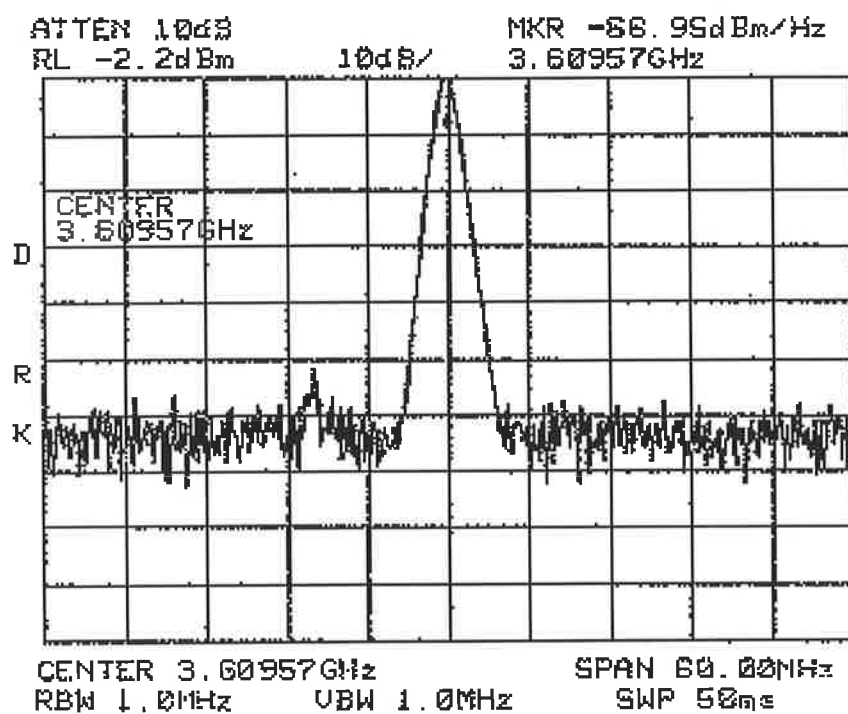
-1.16 volts, and 4.5 mA drain current was measured. In the second test, device 1 was turned off and device 2 turned on, giving the output spectrum as shown in Figure 7-31.

## 2 -Oscillator Power Combiner

### OUTPUT SPECTRUM -1

**Device -1: ON     $V_{DS} = 2.0 \text{ v}$ ,  $I_D = 4.5 \text{ mA}$ ,  $V_{GS} = -1.16 \text{ v}$**

Device -2: OFF



**Output Power = -2.2 dBm**

**Oscillation Frequency = 3.6095 GHz**

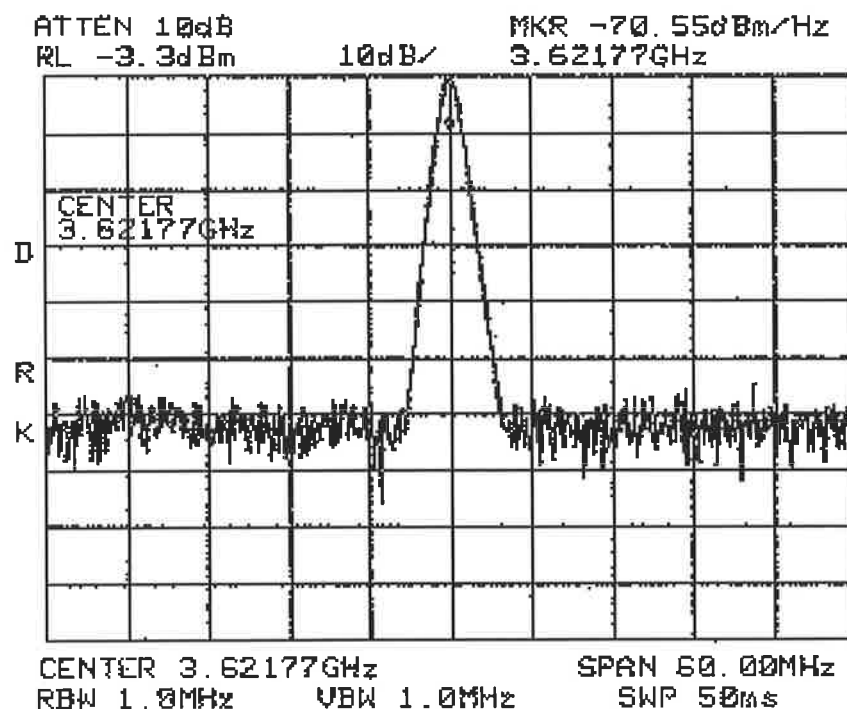
Figure 7-30. Output spectrum of the power combiner when device -1 only is turned on

2 -Oscillator Power Combiner

## OUTPUT SPECTRUM -2

Device -1: OFF

**Device -2: ON**     $V_{DS} = 2.0 \text{ v}$ ,  $I_D = 3.8 \text{ mA}$ ,  $V_{GS} = -1.34 \text{ v}$



Output Power = -3.3 dBm

Oscillation Frequency = 3.6218 GHz

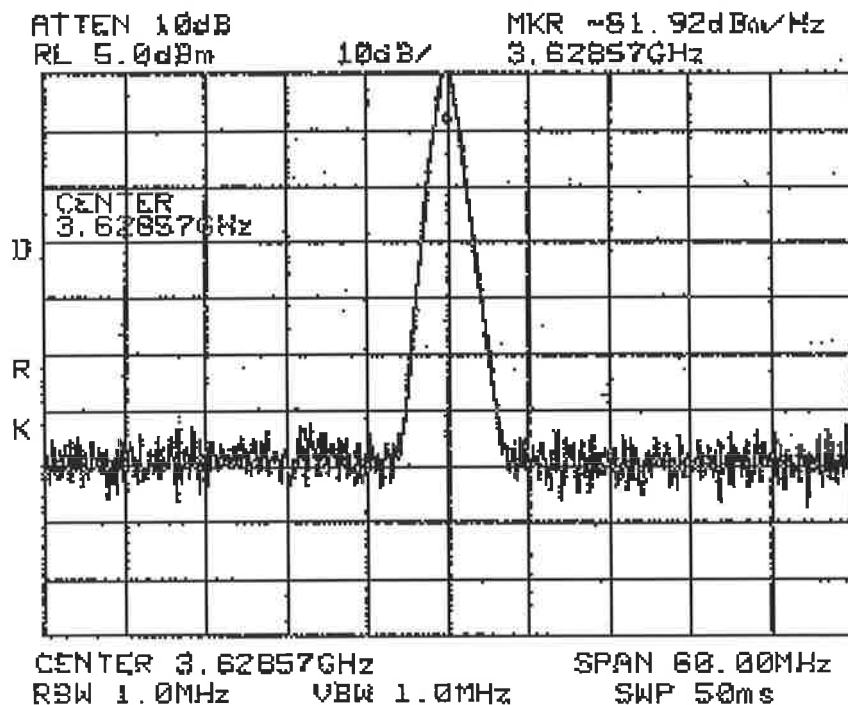
Figure 7-31. The output spectrum of the power combiner when device -2 only is turned on

**2 -Oscillator Power Combiner**

## OUTPUT SPECTRUM -3

**Device -1: ON**     $V_{DS} = 2.0 \text{ v}$ ,  $I_D = 4 \text{ mA}$ ,  $V_{GS} = -1.11 \text{ v}$

**Device -2: ON**     $V_{DS} = 2.0 \text{ v}$ ,  $I_D = 6 \text{ mA}$ ,  $V_{GS} = -1.34 \text{ v}$



**Output Power = +5 dBm**

**Oscillation Frequency = 3.6286 GHz**

*Figure 7-32. The output spectrum of the power combiner with both oscillators turned on*

The drain voltage was set to 2.0 volts, the gate bias reading was -1.34 volts and 3.8 mA of drain current was measured. An output power of -3.3 dBm at 3.6218 GHz was obtained which

is significantly different from the first test and is evidence, along with the different drain current, of differences between the two transistors in the assembly. Finally in the third test, both oscillators were turned on with the same 2.0 drain bias voltages applied as in tests 1 and 2. A power combined output of +5 dBm was achieved from the assembly as shown in the spectrum analyser record of Figure 7-32 at an operating frequency of 3.6286 GHz which is slightly different from the previous measurements. Note that the self-bias on the gate of device 1 has changed from -1.16 volts to -1.11 volts.

#### 7.4.2.3 Discussion and Conclusions

The drain bias voltages of the devices 1 and 2 are exactly the same as those that gave spectrum 1 and spectrum 2. However the drain currents measured when both oscillators are operating changed to 6 mA and 4 mA for devices 1 and 2 respectively which are different from the values in previous tests where only one device was operating. In addition the power combined output of +5 dBm is much higher than the simple addition of the single-device powers as previously measured or single device RF voltages derived from powers. This is because the oscillator circuits are not isolated devices but directly interconnected parts of the whole assembly. When both oscillators are operating their individual power outputs are greater and are combined leading to a superior output. Once one of the devices is turned off, not only does it fail to contribute power, but it also introduces a significant mismatch inside the partially-filled cavity leading to a reduction in the power and efficiency of the operating device. This phenomenon is specific to the novel resonant cavity power combiner and does not exist in the classical corporate power combiner where the oscillators are isolated from each other and their output powers are linearly added by hybrid connections, for example, to give the resulting power combined output.

Good start-up behaviour is found for power combining operation and also for single transistor operation. This appears to be in harmony with the empirical rule that the negative resistance produced by the active device at start-up should be equal to or greater than three times the load resistance. Switching off one transistor removes one of the two parallel negative resistances so that the effective negative resistance is doubled.

However power transfer appears to be affected because the optimum load for two os-

cillators operating in parallel is likely to be half the value suitable for a single oscillator. The DC to RF conversion efficiencies for the oscillators operated separately are 6.7 percent and 6.2 percent whereas for combined operation it is 15.8%. This is much less than the maximum efficiency achieved with the version 2 oscillator but the combiner was only tested with a conservative drain bias level of 2.0 volts. From Figure 7-21 the version 2 oscillator efficiency was 20 percent when its drain bias was 2.0 volts.

It is concluded that the partially filled resonant cavity functions effectively as a power combiner by synchronising and phasing oscillators that are coupled to it through the dielectric surface electric field distribution. The design methods that have been developed are accurate and appropriate for determining details for all of the passive components that form the electrically thick superstrate mounted array of oscillators.

---

## Chapter 8

# *Overall Conclusions & Recommendations*

The primary aim of the research has been to create an oscillator assembly that will conform to an assumed wafer thickness constraint that would make MMIC fabricated items electrically thick at millimetre wave frequencies. However the low loss nature of both shielded inverted microstrip line and partially-filled dielectric resonators raise the possibility that versions of this oscillator assembly fabricated with low loss, temperature stable materials and designed for low phase noise [65] may exhibit superior properties, at microwave frequencies. The thick substrate may be a standard thickness GaAs wafer on top of a thicker sapphire plate coupled so that the loaded Q of the oscillator is large enough to yield the desired low phase noise required. Indeed the details of construction will depend upon the intended operating frequency.

An important basic feature is that the oscillator is a packaged component with either a single port output, that may be one of the standard waveguides including coaxial transmission lines (Concepts 6 and 7) or a multiple port output of the radiating type (Concepts 12 and 13). The package acts as the resonator body and coupling structure for RF and incor-

porates the bias supply line connections for DC. The self-biasing effect at the gate can be exploited by omitting a separate gate bias supply or the DC connection can be used for applying pinch-off level pulses to digitally modulate the oscillator.

The partially-filled dielectric resonator-type cavity in cascade with the output from the drain of the MESFET oscillator offers the prospect of designing for high efficiency Class C mode operation in the oscillator. Detail knowledge of the nonlinear characteristics of the transistor at both the drain and the gate would be necessary and an alternative approach to the design of the oscillator circuit in shielded inverted substrate microstrip that takes account of the effect of the current pulse excited resonant cavity on the feedback within the oscillator would have to be developed. In the case of an array of oscillators the interaction that leads to synchronisation is a nonlinear effect that may somewhat compromise the design for Class C operation. At higher frequencies the transit time delay associated with carriers travelling across the channel in a MESFET or HEMT [66] may prevent effective Class C operation.

The development of double-heterojunction pseudomorphic HEMTs offers the prospect of significant efficiency improvement over MESFETs whether operated in Class A, AB or C mode [67]. The theoretical maximum efficiency of a Class A amplifier is 50 percent and in the case of Class B operation efficiencies as high as 65 percent are commonly achieved. It is likely that a more practical approach to the design of millimetre wave oscillators is to concentrate on Class A operation of transistors and use materials that will yield the higher efficiency. In that case the functions of the resonant cavity are (i) synchronisation of arrays of oscillators, (ii) stabilisation of frequency and (iii) phasing of the elements of an array by virtue of the position of each coupling probe in the resonator standing wave pattern.

The oscillators that have been successfully tested are an innovative cascade of components that appear to have been seldom, if at all, analysed, designed and used previously in practical systems. The component parts include,

- (v)the oscillator designed in shielded inverted microstrip line,

- (ii)the partially-filled dielectric resonator operating in the  $LSM^Y_{30N}$  mode,
- (iii)excitation of such a resonator by means of current carrying metal strips on the surface of the dielectric that partially fills the resonator, and,
- (iv)coupling between a partially-filled dielectric resonator and a standard air-filled rectangular waveguide by means of a thick iris in the form of a short length of partially-filled rectangular section waveguide that has the same dielectric thickness and air gap as the resonator.

These components have been conceived as an assembly that has the potential to solve a problem that arises due to surface wave excitation in electrically thick dielectric slabs. Demonstration of the accuracy of design methods that have been developed for each of these components leads to the possibility that other components and assemblies may be developed that extend the range of functions that can be performed using an electrically thick dielectric slab as the common structural component.

For example, it appears feasible to construct an amplifier by separating the partially-filled dielectric resonator that is used in the oscillator into two identical resonators by means of a metal wall across the cavity parallel to the strips connected to the source electrodes. The transistor would be in a region of zero or small electric field and could be in an aperture in the wall that would provide negligible coupling between the resonators, in contrast to the transistor that would take its input via the gate strip from the input resonator and feed its output via the drain strip to the output resonator. The amplifier proper would be designed and operated in shielded inverted microstrip line.

Electronic tuning of the oscillator by incorporating a varactor diode in series with the gate metal strip would be a useful alternative to the mechanical tuning explained in Concept 10. A series component controlled through an additional bias line would avoid the problems involved in mounting a component across the air gap and would satisfy the constraints of monolithic fabrication.

The maximum number of oscillators that can be combined as a synchronised array at

a specified operating frequency will depend upon the frequency and therefore the components that can be realistically incorporated when fabricating the assembly. Mechanically tuning individual oscillators, as explained in Concept 10, will not be feasible in the millimetre wave band but varactor tuning may be. Mechanically tuning the partially-filled cavity resonator, as explained in Concept 11, becomes increasingly difficult to build so that it is effective in small structures at very short operating wavelengths. Suppressing unwanted resonances and heat sinking by placing metal posts through the substrate, as explained in concept 14 and 15, may take the form of metal filling within etched holes and therefore may be practical for millimetre wave assemblies. The cavity resonant mode to be used for power combining must be separated from unwanted resonances by a frequency range that is large compared with the bandwidth of the negative resistance produced by the microstrip oscillators. It is evident that the larger the frequency range over which negative resistance may be generated the smaller the cavity and array that should be used. This is so that cavity resonances are more widely separated thus avoiding power being generated at an unwanted nearby cavity resonance. A further consideration that arises directly in the oscillator design is the smallest value of loaded Q of the resonator that may be used for efficient power transfer to the load. It will be a function of the size of the array and so the size may be limited by a minimum specified for the loaded Q.

The maximum size array that can function reliably may not generate sufficient output power. In that case it will be necessary to combine the output from more than one array. At millimetre wavelengths an assembly designed to radiate as an array antenna, as explained in Concept 13, is equivalent to an array of magnetic current elements on the surface of a near perfect conducting plane. If this type of active antenna is used to form an array, a flat mirror with an array of magnetic currents on its surface is created. When used as the flat active surface in an open resonator like that illustrated in Figure 2-19 synchronised in-phase oscillation throughout the assembly will occur. The ideal geometry of the region within the open resonator is not violated by a dielectric slab and the magnetic current sources may be distributed over the flat mirror in a way that optimises coupling to the open resonator mode. In such an assembly each oscillator is associated with three interconnected frequency selective structures. The first is the shielded inverted microstrip com-

ponents connected to the transistor, the second is the partially-filled dielectric cavity resonator that encloses an array of transistor oscillators and the third is the open cavity resonator that synchronises an array of dielectric cavity oscillators. In a free running sense all of the resonant frequencies should occur within a certain range for overall synchronisation to occur. Because of the direct interconnection throughout such an assembly the injection locking signal level is effectively the maximum that can be provided and as a consequence the spread of the resonances is the largest possible for acceptable synchronised performance. However, close tuning appears necessary for optimum performance.

The overall conclusion is that the concepts that have been introduced in this research and the validated design methods that have been developed are a starting point for numerous designs aimed at providing alternative solutions to systems problems that may occur at any frequency from the microwave range up to the millimetre wave limits where monolithic transistors have useful amplifier characteristics.

---

## Appendix A

# *Design of Shielded Inverted Microstrip Line Using Conformal Mapping*

### A.1 Design Procedure

In this Appendix a design procedure is developed base on the conformal mapping analysis of shielded inverted microstrip line [43, 44]. The structure is shown in Figure A-1. The substrate is assumed to be infinitely extended along the  $x$ -axis.

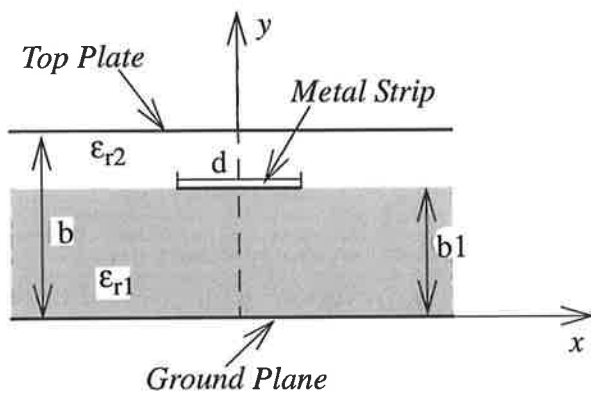


Figure A-1. Geometry of shielded inverted microstrip line

The aim is to determine the line capacitance per unit length. Also the line capacitance for the air-filled structure ( $\epsilon_{r1} = \epsilon_{r2} = 1$ ) is required. As in Figure A-1 due to the symmetry with respect to the  $y$ -axis, only the capacitance of one half of the cross section must be calculated. Once these capacitances are determined the effective dielectric constant will be easily calculated from the following relation:

$$\epsilon_{eff} = \sqrt{\frac{C}{C_0}} \quad (A-1)$$

where  $C$  is the capacitance of the line and  $C_0$  is that of an air-filled structure. The characteristic impedance  $Z_c$  is related to  $\epsilon_{eff}$  as below:

$$Z_c = \frac{Z_c^a}{\sqrt{\epsilon_{eff}}} \quad (A-2)$$

where  $Z_c^a$  is the characteristic impedance of the air-filled line. As from transmission line theory  $Z_c^a$  is a function of the line capacitance :

$$Z_c^a = \sqrt{\frac{\mu_0}{C_0}} \quad (A-3)$$

where  $\mu_0$  is the permeability of free space. Consequently a knowledge of the line capacitances  $C$  and  $C_0$  will suffice to design the transmission line. The rest of this Appendix is devoted to the mathematical calculation of the capacitances based on the conformal mapping method.

### List of symbols

$K(m_s), K'(m_s)$  = Complete elliptic integrals of the first kind

$F(\phi/m_s)$  = Incomplete elliptic integral of the first kind

$E(m_s)$  = Complete elliptic integral of the second kind

$E(\phi/m_s)$  = Incomplete elliptic integral of the second kind

$\Pi(n_s, \text{asin } \alpha | m_s)$  = Incomplete elliptic integral of the third kind

$m_s$  = elliptic modulus

$n_s$  = elliptic characteristic

## A.2 Calculation of $C$

We consider the microstrip structure as a conformal transformation from the complex t-plane (Figure A-2 (b)) to the z-plane (Figure A-2 (a)). A second transformation from the t-plane into the w-plane will lead to the diagram of potential versus flux in which the capacitance is directly proportional to the total area of the diagram (Figure A-2 (c)).

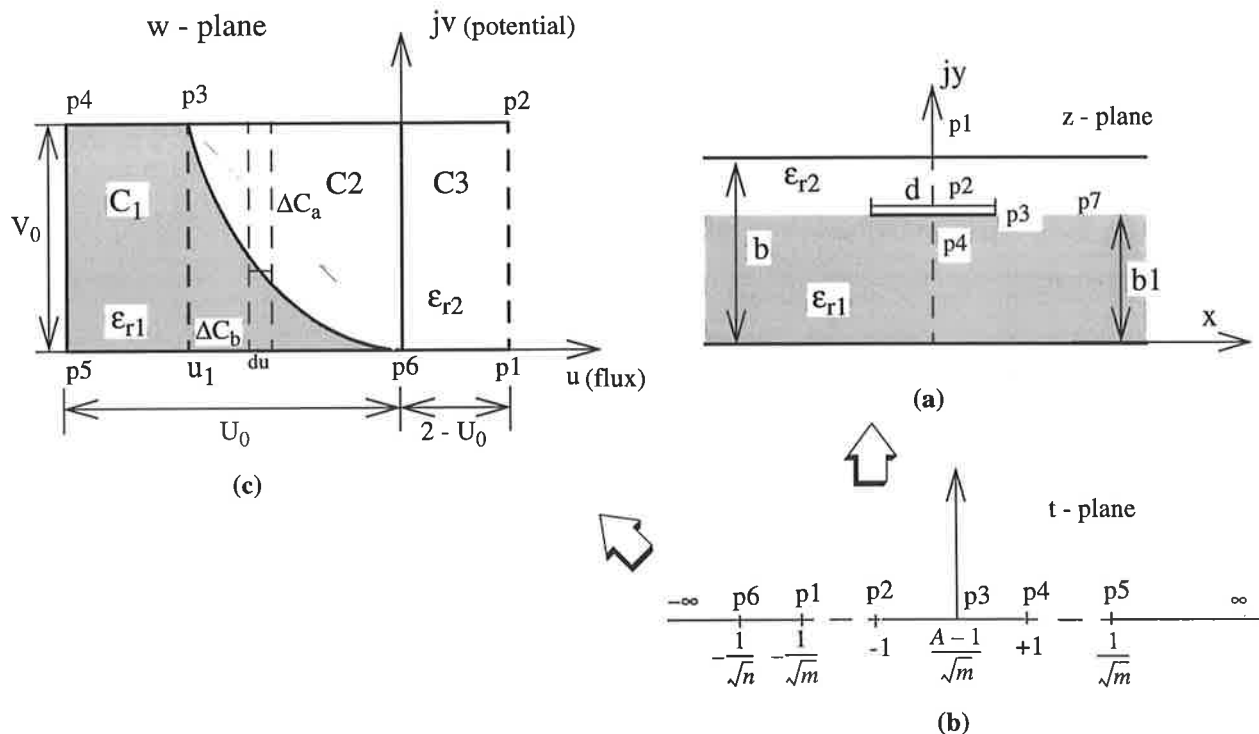


Figure A-2. (a) microstrip structure is transformed from complex t-plane, (b) t-plane, (c) alternative transformation from t-plane to w-plane results in the potential-flux diagram

The area of the potential-flux diagram is divided in three section as shown in Figure A-2 (c).  $C_1$  is the capacitance relevant to the dielectric filled section and is obtained from Figure A-2 (c)

$$C_1 = \frac{\epsilon_0 \cdot \epsilon_{r2} (U_0 - u_1)}{V_0} \quad (\text{A-4})$$

Also  $C_3$  is easily determined from the air filled region as,

$$C_3 = \frac{\epsilon_0 \cdot \epsilon_{r1} (2 - U_0)}{V_0} \quad (\text{A-5})$$

$C_2$  is the capacitance of the mixed area consisting of air-filled and dielectric regions.

For a flux increment  $du$ , the capacitance  $\Delta C_2$  is the series combination of  $\Delta C_a$  and  $\Delta C_b$  for a strip shown with dashed lines with,

$$\Delta C_a = \frac{\epsilon_0 \epsilon_{r2} \cdot du}{V_0 - v} \quad \Delta C_b = \frac{\epsilon_0 \epsilon_{r1} \cdot du}{v} \quad (\text{A-6})$$

Therefore  $C_2$  is obtained by integration of  $\Delta C = [\Delta C_a + \Delta C_b]^{-1}$  over  $u_1 \leq u \leq 0$  as follows:

$$C_2 = \int_0^{u_1} \frac{\epsilon_0 \epsilon_{r1} \epsilon_{r2} \cdot du}{V_0 \left[ \epsilon_{r1} + \frac{v}{V_0} (\epsilon_{r2} - \epsilon_{r1}) \right]} \quad (\text{A-7})$$

The diagram of Figure A-2 (c) is established for only the right hand half of the structure of Figure A-2 (a) and because of the symmetry with respect to the  $jy$  axis the overall capacitance would therefore be:

$$C = 2(C_1 + C_2 + C_3) \quad (\text{A-8})$$

Parameters  $U_0$ ,  $V_0$  and  $u_1$  are determined from a conformal transformation equation between the  $w$ -plane and complex  $t$ -plane as below:

$$w = u + jv = -\frac{F(\phi|m_s)}{K(m_s)} - \frac{F(\operatorname{asin} \sqrt{n_s/m_s}|m_s)}{K(m)} + \frac{jK'(m_s)}{K'(m_s)} \quad (\text{A-9})$$

where  $K(m_s)$  and  $F(\phi|m_s)$  are complete and incomplete elliptic integrals of the first kind respectively where  $m$  is the elliptic modulus and  $n$  is the elliptic characteristic. Also  $K'(m_s) = K'(m_s')$  where  $m_s' = 1 - m_s$ .  $\phi$  is related to  $t$  as below,

$$\phi = \operatorname{asin} t \quad (\text{A-10})$$

which is a variable on the complex  $t$ -plane.  $U_0$  and  $V_0$  are coordinates of the point  $P_4$  on the  $w$ -plane which is analogous to  $t = 1$  from Figure A-2 (b). From equation (A-9)  $\phi = \pi/2$ . Substituting  $\phi$  into (A-8) results in,

$$U_0 = 1 + \frac{F(\operatorname{asin} \sqrt{n_s/m_s}|m_s)}{K(m_s)} \quad (\text{A-11})$$

$$V_0 = \frac{K'(m_s)}{K(m_s)} \quad (\text{A-12})$$

Similarly  $u_1$  is determined by the coordinate of point  $P_3$  on the  $t$ -plane, that is,

$$t = \frac{A-1}{\sqrt{m_s}} \quad (\text{A-13})$$

Substituting (A-12) into (A-9) and (A-8) results in the parameter  $u_1$  being,

$$u_1 = \frac{F\left(\operatorname{asin}\left(\frac{A-1}{\sqrt{m_s}}\right)|m_s\right) + F(\operatorname{asin} \sqrt{n_s/m_s}|m_s)}{K(m_s)} \quad (\text{A-14})$$

where  $A$  is given by,

$$A = \frac{K(m_s)}{\Pi(n_s; K(m_s)|m_s)} \quad (\text{A-15})$$

where  $\Pi(n_s; K(m_s)|m_s)$  is an elliptic integral of the third kind and  $n_s$  is a characteristic.

### A.3 Structure Dimensions

The key dimensions of the shielded inverted microstrip line such as strip width  $d$  and dielectric thickness  $b_1$  are determined from the following expressions,

$$\frac{b_1}{2b} = 1 - \frac{F(\arcsin \sqrt{n_s/m_s} | m_s)}{K(m_s)} \quad (\text{A-16})$$

$$\frac{d}{2b} = \frac{\sqrt{(1-n_s)(m_s-n_s)}}{\pi A \sqrt{n_s}} [F(\arcsin \alpha | m_s) - A \Pi(n_s; \arcsin \alpha | m_s)] - D \quad (\text{A-17})$$

where  $\alpha = \frac{1-A}{\sqrt{n_s}}$  and  $D$  is given by:

$$D = \frac{1}{2\pi} \ln \left[ \frac{\sqrt{(1-n_s)(1-m_s\alpha^2)} - \sqrt{(m_s-n_s)(1-\alpha^2)}}{\sqrt{(1-n_s)(1-m_s\alpha^2)} + \sqrt{(m_s-n_s)(1-\alpha^2)}} \right] \quad (\text{A-18})$$

### A.4 Determination of $Z_0$ and $C_0$

The characteristic impedance of the air-filled structure is easily determined by assuming that the area of w-plane (Figure A-2) is homogeneous with  $\epsilon_{r1} = \epsilon_{r2} = 1$ . Therefore the overall capacitance  $C_0$  is determined by:

$$C_0 = 2\epsilon_0 \cdot \frac{\text{flux}}{\text{potential}} = \epsilon_0 \cdot \frac{4}{V_0} = 4\epsilon_0 \frac{K(m_s)}{K'(m_s)} \quad (\text{A-19})$$

Also the characteristic impedance for air-filled stripline is found from,

$$Z_c^a = \sqrt{\frac{\mu_0}{C_0}} = 30\pi \cdot \frac{K'(m_s)}{K(m_s)} \quad (\text{A-20})$$

## A.5 Numerical Result

The design procedure mentioned above has been implemented by computer programs on MATLAB. It should be noted that due to the mathematical complexity of the equations that involve elliptic integrals with unknown modulus and characteristic, none of the parameters could be found explicitly. Therefore a recursive approach using an optimisation method has been used to obtain the characteristic impedance and effective dielectric constant. A typical result of the program execution for the structure of Figure A-1. with  $b_1/b = 1/6$ ,  $\epsilon_{r1} = 9.9$  and  $\epsilon_{r2} = 1$  is compared with the published data [39] as shown in Figure A-3 and the agreement is found to be very satisfactory.

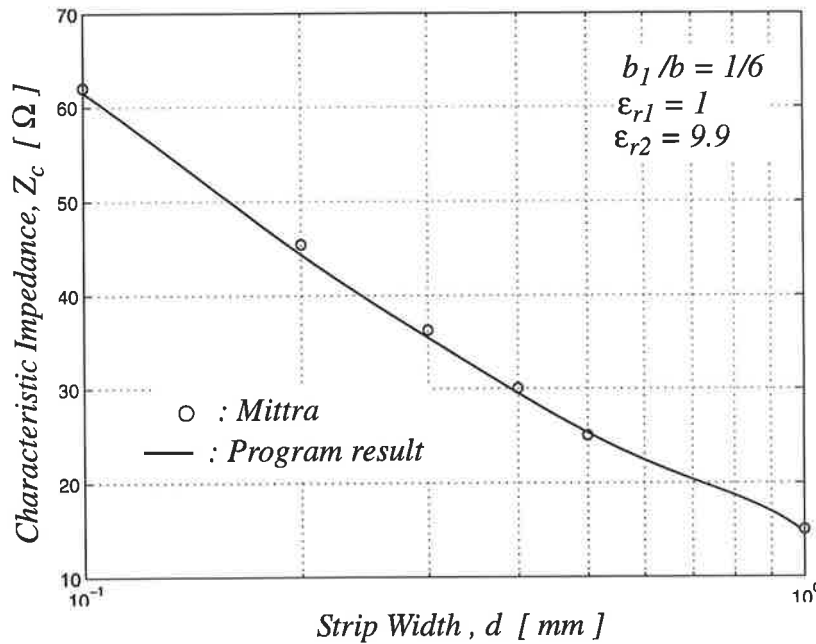


Figure A-3. The calculated characteristic impedance and the comparison with the result obtained by Mittra [39].

---

## Appendix B

# *Hybrid Modes in Partially-Filled Waveguides*

### B.1 Introduction

A partially-filled waveguide consists of a hollow rectangular waveguide with a dielectric slab filling part of the cross-section as shown in Figure B-1. The slab may be positioned along the broad wall or the narrow wall. Neither  $TE^z$  nor  $TM^z$  modes can satisfy the boundary condition of such a waveguide. Generally *hybrid* modes which are combinations of  $TE^z$  and  $TM^z$  modes are used as the normal modes of propagation. The hybrid modes have been classified as longitudinal section electric (LSE) and longitudinal section magnetic (LSM), or H and E modes [55]. For the partially-filled waveguide shown in Figure B-1, the hybrid modes that satisfy the boundary conditions are  $LSE^y$  designated by some as  $TE^y$  or  $H^y$  and /or  $LSM^y$  designated by some as  $TM^y$  or  $E^y$ . The purpose of this Appendix is to derive the eigenfunctions of the  $LSE^y$  and  $LSM^y$  modes for the waveguide of Figure B-1. These eigenfunctions will be needed for the partially-filled cavity and mode-matching analysis. Detailed solution of partially-filled waveguides are given in the literature [24], [49] and [55].

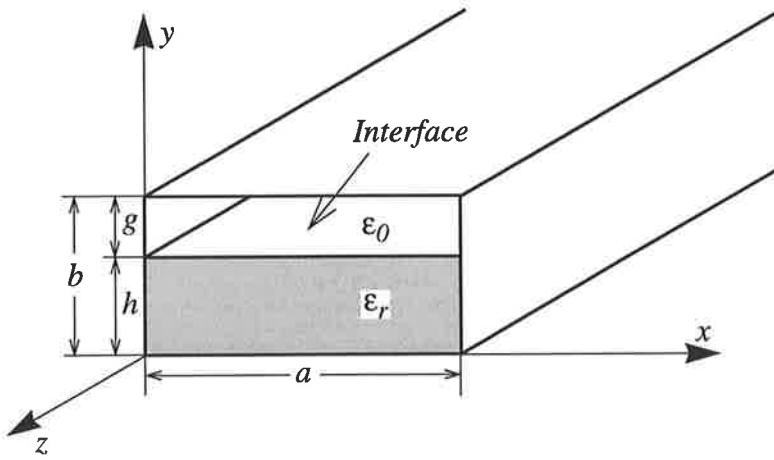


Figure B-1. Partially-filled waveguide

## B.2 LSE<sup>y</sup> Modes

The fields of LSE<sup>y</sup> modes are denoted as  $\bar{E}^h$  and  $\bar{H}^h$  and are obtained from the magnetic vector potential [49] as below:

$$\bar{E}^h = -j\omega\mu_0 \bar{\nabla} \times \bar{\Pi}_h \quad (\text{B-1})$$

$$\bar{H}^h = \kappa k_0^2 \bar{\Pi}_h + \bar{\nabla} \bar{\nabla} \cdot \bar{\Pi}_h \quad (\text{B-2})$$

where  $\kappa$  is the relative permittivity of the medium and  $\bar{\Pi}_h$  is the magnetic-type Hertzian potential which is expressed as:

$$\bar{\Pi}_h = \psi^h e^{-\gamma z} \hat{a}_z \quad (\text{B-3})$$

where  $\psi^h$  is a scalar mode function and is determined from the Helmholtz equation:

$$\nabla_t^2 \psi^h + (\gamma^2 + \kappa k_0^2) \psi^h = 0 \quad (\text{B-4})$$

For the structure of Figure B-1  $\kappa$  is defined as:

$$\kappa = \begin{cases} \epsilon_r & \text{for } 0 < y < h \\ 1 & \text{for } h < y < b \end{cases} \quad (\text{B-5})$$

Therefore equation (B-4) will have two solutions as follows:

$$\psi_{mn}^{d,h} = A^{d,h} \cos\left(\frac{m\pi}{a}x\right) \sin(k_n^d y) \quad (\text{B-6})$$

$$\psi_{mn}^{a,h} = A^{a,h} \cos\left(\frac{m\pi}{a}x\right) \sin(k_n^a(b-y)) \quad (\text{B-7})$$

where  $\psi_{mn}^{d,h}$  and  $\psi_{mn}^{a,h}$  are the mode functions for the dielectric and air-filled regions respectively. It should be noted that in all terms the superscript  $h$  indicates the LSE mode. Considerable simplification of equations (B-1) and (B-2) is obtained by decomposing  $\bar{\nabla}$  and the field vectors into transverse and axial components and separating out the  $z$  dependence. Thus let

$$\bar{\nabla} = \bar{\nabla}_t + \gamma \hat{a}_z \quad (\text{B-8})$$

$$\bar{E}^h(x, y, z) = \bar{E}_t^h(x, y, z) + \bar{E}_z^h(x, y, z) = \bar{e}_t^h(x, y) e^{-\gamma z} + \bar{e}_z^h(x, y) e^{-\gamma z} \quad (\text{B-9})$$

$$\bar{H}^h(x, y, z) = \bar{H}_t^h(x, y, z) + \bar{H}_z^h(x, y, z) = \bar{h}_t^h(x, y) e^{-\gamma z} + \bar{h}_z^h(x, y) e^{-\gamma z} \quad (\text{B-10})$$

where  $\bar{\nabla}_t$ ,  $\bar{E}_t^h$  and  $\bar{H}_t^h$  are the transverse, and  $\bar{E}_z^h$ ,  $\bar{H}_z^h$  are the axial components.

Also  $\bar{e}_t^h(x, y)$  and  $\bar{h}_t^h(x, y)$  are transverse vector functions of the transverse coordinates only, and  $\bar{e}_z^h(x, y)$ ,  $\bar{h}_z^h(x, y)$  are axial vector functions of the transverse coordinates. Substituting (B-3), (B-8) and (B-9) into the wave equation (B-1) will result in the electric vector functions as below:

$$\bar{e}_t^{i,h} = -j\omega\mu_0\gamma\psi_{mn}^{i,h}\hat{a}_x \quad (\text{B-11})$$

$$\bar{e}_z^{i,h} = -j\omega\mu_0\frac{\partial}{\partial x}\psi_{mn}^{i,h}\hat{a}_z \quad (\text{B-12})$$

where  $i$  is defined as the medium index, indicating a pair of equations that are obtained by replacing  $i$  by  $d$  and  $a$  for dielectric and air-filled regions respectively. Due to

the two distinct media involved in the guiding structure, such a definition is quite helpful to retain brevity. There is no  $y$ -component in the transverse vector as is expected for LSE $^y$  modes. Similarly by substitution of (B-3), (B-8) and (B-10) into the wave equation (B-2) we obtain the transverse and axial components of magnetic vector functions as below:

$$\bar{h}_t^{i,h} = \frac{\partial^2}{\partial x \partial y} \Psi_{mn}^{i,h} \hat{a}_x + \left( \kappa k_0^2 + \frac{\partial^2}{\partial y^2} \right) \Psi_{mn}^{i,h} \hat{a}_y \quad (\text{B-13})$$

$$\bar{h}_z^{i,h} = -\gamma \frac{\partial}{\partial y} \Psi_{mn}^{i,h} \hat{a}_z \quad (\text{B-14})$$

Substituting (B-6) and (B-7) into the equations (B-11), (B-12) and separating the equations for dielectric and air-filled regions we obtain electric eigenfunctions as below:

$$\bar{e}_t^{d,h} = \bar{e}_x^{d,h} = A_{mn}^{d,h} \cos\left(\frac{m\pi}{a}x\right) \sin(k_n^d y) \hat{a}_x \quad (\text{B-15})$$

$$\bar{e}_t^{a,h} = \bar{e}_x^{a,h} = A_{mn}^{a,h} \cos\left(\frac{m\pi}{a}x\right) \sin(k_n^a(b-y)) \hat{a}_x \quad (\text{B-16})$$

$$\bar{e}_z^{d,h} = -\frac{A_{mn}^{d,h}}{\gamma} \left( \frac{m\pi}{a} \right) \sin\left(\frac{m\pi}{a}x\right) \sin(k_n^d y) \hat{a}_z \quad (\text{B-17})$$

$$\bar{e}_z^{a,h} = -\frac{A_{mn}^{a,h}}{\gamma} \left( \frac{m\pi}{a} \right) \sin\left(\frac{m\pi}{a}x\right) \sin(k_n^a(b-y)) \hat{a}_z \quad (\text{B-18})$$

where  $A_{mn}^{i,h}$  is the amplitude of the transverse component which is related to the amplitude of the mode function as follows:

$$A_{mn}^{i,h} = -j\omega\mu_0\gamma A^{i,h} \quad (\text{B-19})$$

Also the magnetic eigenfunctions are obtained by substituting (B-6), (B-7) and (B-19) into the equations (B-13) and (B-14). Hence let

$$\bar{h}_x^{d,h} = -Y_{mn}^{d,h} A_{mn}^{d,h} \left( \frac{k_n^d \frac{m\pi}{a}}{\epsilon_r k_0^2 - k_n^{d2}} \right) \sin\left(\frac{m\pi}{a}x\right) \cos(k_n^d y) \hat{a}_x \quad (\text{B-20})$$

$$\bar{h}_x^{a,h} = -Y_{mn}^{a,h} A_{mn}^{a,h} \left( \frac{k_n^a \frac{m\pi}{a}}{k_0^2 - k_n^a} \right) \sin\left(\frac{m\pi}{a}x\right) \cos(k_n^a(b-y)) \hat{a}_x \quad (\text{B-21})$$

$$\bar{h}_y^{d,h} = Y_{mn}^{d,h} A_{mn}^{d,h} \cos\left(\frac{m\pi}{a}x\right) \sin(k_n^d y) \hat{a}_y \quad (\text{B-22})$$

$$\bar{h}_y^{a,h} = Y_{mn}^{a,h} A_{mn}^{a,h} \cos\left(\frac{m\pi}{a}x\right) \sin(k_n^a(b-y)) \hat{a}_y \quad (\text{B-23})$$

$$\bar{h}_z^{d,h} = -\left(\frac{k_n^d}{j\omega\mu_0}\right) A_{mn}^{d,h} \cos\left(\frac{m\pi}{a}x\right) \cos(k_n^d y) \hat{a}_z \quad (\text{B-24})$$

$$\bar{h}_z^{a,h} = -\left(\frac{k_n^a}{j\omega\mu_0}\right) A_{mn}^{a,h} \cos\left(\frac{m\pi}{a}x\right) \cos(k_n^a(b-y)) \hat{a}_z \quad (\text{B-25})$$

where  $Y_{mn}^{i,h}$  is the wave admittance of the LSE<sup>y</sup> mode and is given by:

$$Y_{mn}^{d,h} = Y_0 \frac{\epsilon_r k_0^2 - k_n^d}{-jk_0\gamma} \quad (\text{B-26})$$

$$Y_{mn}^{a,h} = Y_0 \frac{k_0^2 - k_n^a}{-jk_0\gamma} \quad (\text{B-27})$$

where,  $Y_0 = (\epsilon_0/\mu_0)^{1/2}$  and  $\gamma = j\beta_z$  is the propagation constant.

### B.2.1 Continuity Equation for LSE<sup>y</sup> Modes

Referring to Figure B-1 the boundary condition at the air-dielectric interface is as below:

$$\bar{e}_x^{d,h} \Big|_{y=h} = \bar{e}_x^{a,h} \Big|_{y=h} \quad (\text{B-28})$$

$$\bar{h}_x^{d,h} \Big|_{y=h} = \bar{h}_x^{a,h} \Big|_{y=h} \quad (\text{B-29})$$

Equations (B-28) and(B-29) are simplified to the following relations respectively:

$$A_{mn}^{d,h} \sin(k_n^d h) = A_{mn}^{a,h} \sin(k_n^a g) \quad (\text{B-30})$$

$$A_{mn}^{d,h}(k_n^d) \cos(k_n^d h) = -A_{mn}^{a,h}(k_n^a) \cos(k_n^a g) \quad (\text{B-31})$$

where  $g = b - h$ . The boundary relations of the z-components will give the same results. The continuity equations (B-30) and (B-31) are combined to give the following transcendental equation

$$k_n^d \cot(k_n^d h) = -k_n^a \cot(k_n^a g) \quad (\text{B-32})$$

### B.2.2 Normalisation of LSE<sup>y</sup> Modes

The orthogonality relation between the electromagnetic fields in the waveguide of Figure B-1 is expressed in terms of transverse field components. Let

$$Q_{mn}^{i,h} = \int_{S_i} \bar{e}_t^{i,h} \times \bar{h}_t^{i,h} \cdot \hat{a}_z ds \quad (\text{B-33})$$

Substituting  $\bar{e}_t^{i,h}$  from (B-15), (B-16), and  $\bar{h}_t^{i,h}$  from (B-22) and (B-23) will yield

$$Q_{mn}^{i,h} = (A_{mn}^{i,h})^2 Y_{mn}^{i,h} \left( \frac{ah^i}{2\epsilon_{0m}} \right) [1 - \text{sinc}(2k_n^i h^i / \pi)] \quad (\text{B-34})$$

where  $h^i = \begin{cases} h & \text{for } i \rightarrow d \\ g & \text{for } i \rightarrow a \end{cases}$ ,  $Q_{mn}^{i,h}$  is the normalisation constant and  $\text{sinc}(x) = (\sin \pi x) / (\pi x)$ . Also  $\epsilon_{0m} = \begin{cases} 1 & \text{for } m = 0 \\ 2 & \text{for } m \neq 0 \end{cases}$  is Neumann's factor.

The normalised wave amplitude for a selected constant is easily obtained from (B-34) as below:

$$A_{mn}^{i,h} = \left( \frac{2\epsilon_{0m}}{ah^i} \right)^{\frac{1}{2}} [1 - \text{sinc}(2k_n^i / \pi)]^{-\frac{1}{2}} \sqrt{\frac{Q_{mn}^{i,h}}{Y_{mn}^{i,h}}} \quad (\text{B-35})$$

### B.3 LSM<sup>y</sup> Modes

The fields of LSM<sup>y</sup> modes are denoted as  $\bar{H}^e$  and  $\bar{E}^e$  and are obtained from the electric-type Hertzian potential [49] as below:

$$\bar{H}^e = j\omega\epsilon\bar{\nabla} \times \bar{\Pi}_e \quad (\text{B-36})$$

$$\bar{E}^e = k\bar{\Pi}_e + \bar{\nabla}\bar{\nabla} \cdot \bar{\Pi}_e \quad (\text{B-37})$$

where  $k$  is the medium phase constant and  $\bar{\Pi}_e$  is the electric Hertzian potential which is expressed as:

$$\bar{\Pi}_e = \psi^e e^{-\gamma z} \hat{a}_z \quad (\text{B-38})$$

where  $\psi^e$  is the mode function similar to  $\psi^h$  and is the solution of the Helmholtz equation (B-4). For the structure of Figure B-1 it follows that:

$$\psi_{mn}^{d,e} = A^{d,e} \sin\left(\frac{m\pi}{a}x\right) \cos(k_n^d y) \quad (\text{B-39})$$

$$\psi_{mn}^{a,e} = A^{a,e} \sin\left(\frac{m\pi}{a}x\right) \cos(k_n^a(b-y)) \quad (\text{B-40})$$

The superscript  $e$  indicates the LSM mode. Using the same decomposition as expressed by (B-8) to (B-10) and substituting (B-38) into the wave equations (B-36) and (B-37) will give the LSM<sup>y</sup> vector functions as follows:

$$\bar{e}_t^{i,e} = \frac{\partial^2}{\partial y \partial x} \psi_{mn}^{i,e} \hat{a}_x + \left( \kappa k_0^2 + \frac{\partial^2}{\partial y^2} \right) \psi_{mn}^{i,e} \hat{a}_y \quad (\text{B-41})$$

$$\bar{e}_z^{i,e} = -\gamma \frac{\partial}{\partial y} \psi_{mn}^{i,e} \hat{a}_z \quad (\text{B-42})$$

$$\bar{h}_t^{i,e} = \bar{h}_x^{i,e} = j\omega\kappa\epsilon_0\gamma\psi_{mn}^{i,e} \hat{a}_x \quad (\text{B-43})$$

$$\bar{h}_z^{i,e} = j\omega\kappa\epsilon_0 \frac{\partial}{\partial x} \psi_{mn}^{i,e} \hat{a}_z \quad (\text{B-44})$$

where  $\kappa$  is the permittivity factor as defined in (B-5). Substituting the mode function from (B-40), (B-41) into the eigenfunction equations (B-41) to (B-44) and normalising

the vectors with respect to the amplitude of the  $y$ -component electric field we obtain the LSM $^y$  eigenfunctions as below:

$$\bar{e}_y^{d, e} = A_{mn}^{d, e} \sin\left(\frac{m\pi}{a}x\right) \cos(k_n^d y) \hat{a}_y \quad (\text{B-45})$$

$$\bar{e}_y^{a, e} = A_{mn}^{a, e} \sin\left(\frac{m\pi}{a}x\right) \cos(k_n^a(b-y)) \hat{a}_y \quad (\text{B-46})$$

$$\bar{e}_x^{d, e} = -A_{mn}^{d, e} \left( \frac{k_n^d \frac{m\pi}{a}}{\epsilon_r k_0^2 - k_n^{d2}} \right) \cos\left(\frac{m\pi}{a}x\right) \sin(k_n^d y) \hat{a}_x \quad (\text{B-47})$$

$$\bar{e}_x^{a, e} = -A_{mn}^{a, e} \left( \frac{k_n^a \frac{m\pi}{a}}{k_0^2 - k_n^{a2}} \right) \cos\left(\frac{m\pi}{a}x\right) \sin(k_n^a(b-y)) \hat{a}_x \quad (\text{B-48})$$

$$\bar{e}_z^{d, e} = \left( \frac{\gamma k_n^d}{\epsilon_r k_0^2 - k_n^{d2}} \right) A_{mn}^{d, e} \sin\left(\frac{m\pi}{a}x\right) \sin(k_n^d y) \hat{a}_z \quad (\text{B-49})$$

$$\bar{e}_z^{a, e} = \left( \frac{\gamma k_n^a}{\epsilon_r k_0^2 - k_n^{a2}} \right) A_{mn}^{a, e} \sin\left(\frac{m\pi}{a}x\right) \sin(k_n^a(b-y)) \hat{a}_z \quad (\text{B-50})$$

$$\bar{h}_x^{d, e} = -Y_{mn}^{d, e} A_{mn}^{d, e} \sin\left(\frac{m\pi}{a}x\right) \cos(k_n^d y) \hat{a}_x \quad (\text{B-51})$$

$$\bar{h}_x^{a, e} = -Y_{mn}^{a, e} A_{mn}^{a, e} \sin\left(\frac{m\pi}{a}x\right) \cos(k_n^a(b-y)) \hat{a}_x \quad (\text{B-52})$$

$$\bar{h}_z^{d, e} = -Y_{mn}^{d, e} A_{mn}^{d, e} \left( \frac{m\pi}{a} \right) \cos\left(\frac{m\pi}{a}x\right) \cos(k_n^d y) \hat{a}_z \quad (\text{B-53})$$

$$\bar{h}_z^{a, e} = -Y_{mn}^{a, e} A_{mn}^{a, e} \left( \frac{m\pi}{a} \right) \cos\left(\frac{m\pi}{a}x\right) \cos(k_n^a(b-y)) \hat{a}_z \quad (\text{B-54})$$

where  $Y_{mn}^{i, e}$  is the wave admittance of LSM $^y$  mode and is given by:

$$Y_{mn}^{d, e} = Y_0 \frac{-jk_0\gamma}{\epsilon_r k_0^2 - k_n^{d2}} \quad (\text{B-55})$$

$$Y_{mn}^{a, e} = Y_0 \frac{-jk_0\gamma}{k_0^2 - k_n^{a2}} \quad (\text{B-56})$$

### B.3.1 Continuity Equation for LSM<sup>y</sup> Modes

Referring to Figure B-1 the boundary condition at the air-dielectric interface is as below:

$$\bar{e}_x^{d,e} \Big|_{y=h} = \bar{e}_x^{a,e} \Big|_{y=h} \quad (\text{B-57})$$

$$\bar{h}_x^{d,e} \Big|_{y=h} = \bar{h}_x^{a,e} \Big|_{y=h} \quad (\text{B-58})$$

and the continuity equations are obtained as:

$$A_{mn}^{d,e}(k_n^d) \sin(k_n^d h) = -A_{mn}^{a,e}(k_n^a) \sin(k_n^a g) \quad (\text{B-59})$$

$$A_{mn}^{d,e} \epsilon_r \cos(k_n^d h) = A_{mn}^{a,e} \cos(k_n^a g) \quad (\text{B-60})$$

By combining the above equations, the transcendental equation is obtained as below:

$$k_n^d \tan(k_n^d h) = -\epsilon_r k_n^a \tan(k_n^a g) \quad (\text{B-61})$$

### B.3.2 Normalisation of LSM<sup>y</sup> Modes

The orthogonality relation similar to (B-33) is defined below:

$$Q_{mn}^{i,e} = \int_{S_i} \bar{e}_t^{i,e} \times \bar{h}_t^{i,e} \cdot \hat{a}_z ds \quad (\text{B-62})$$

Substituting  $\bar{e}_t^{i,e}$  from (B-45) to (B-48) and  $\bar{h}_t^{i,e}$  from (B-51) to (B-52) will give

$$Q_{mn}^{i,e} = (A_{mn}^{i,e})^2 Y_{mn}^{i,e} \left( \frac{ah^i}{4} \right) [1 + \text{sinc}(2k_n^i h^i / \pi)] \quad (\text{B-63})$$

where  $h^i = \begin{cases} h & \text{for } i \rightarrow d \\ g & \text{for } i \rightarrow a \end{cases}$ ,  $Q_{mn}^{i,e}$  is the normalisation constant. The nor-

malised wave amplitude for LSM<sup>y</sup> mode is easily obtained from (B-63) as below:

$$A_{mn}^{i,e} = \left( \frac{4}{ah^i} \right)^{\frac{1}{2}} [1 + \text{sinc}(2k_n^i h^i / \pi)]^{-\frac{1}{2}} \sqrt{\frac{Q_{mn}^{i,e}}{Y_{mn}^{i,e}}} \quad (\text{B-64})$$

---

## Appendix C

# *Mode Expansion of Maxwell's Equations in Partially-Filled Cavities*

The expansion of Maxwell's equations for hollow cavities was presented by Collin [49] and Kurokawa [50]. Using similar methods we can expand the fields inside a partially-filled cavity in terms of LSE and LSM modes. However due to the air-dielectric nature of the medium, care should be taken in handling the volume and surface integrals involved in the analysis. We consider the cavity of Figure C-1 in which an electric current source exists. Maxwell's equations are:

$$\bar{\nabla} \times \bar{E} = -j\omega\mu_0 \bar{H} \quad (\text{C-1})$$

$$\bar{\nabla} \times \bar{H} = -j\omega\kappa\epsilon_0 \bar{E} + \bar{J} \quad (\text{C-2})$$

where  $\kappa$  is the relative permittivity and is defined as:

$$\kappa = \begin{cases} \epsilon_r & \text{for } 0 < y < h \\ 1 & \text{for } h < y < b \end{cases} \quad (\text{C-3})$$

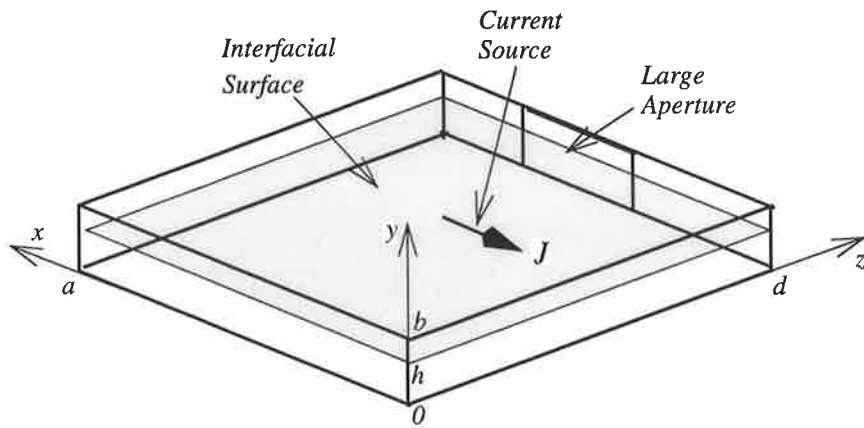


Figure C-1. Partially-filled cavity with current source and aperture.

Substitution of  $\kappa$  into the Maxwell's equations will result in separate solutions for dielectric and air-filled regions namely:

$$\bar{E} = \begin{cases} \bar{E}^d & \text{for } 0 < y < h \\ \bar{E}^a & \text{for } h < y < b \end{cases} \quad \bar{H} = \begin{cases} \bar{H}^d & \text{for } 0 < y < h \\ \bar{H}^a & \text{for } h < y < b \end{cases} \quad (\text{C-4})$$

where superscripts 'd' and 'a' indicate dielectric and air-filled regions respectively. Regarding the equations (C-1) and (C-2),  $\bar{E}$  and  $\bar{H}$  can be expressed in terms of the eigenfunctions of the totally enclosed cavity. Thus let

$$\bar{E} = \sum_n (e_n \bar{E}_n + f_n \bar{F}_n) \quad (\text{C-5})$$

$$\bar{H} = \sum_n (h_n \bar{H}_n + g_n \bar{G}_n) \quad (\text{C-6})$$

where  $\bar{E}_n$  and  $\bar{H}_n$  are the solenoidal fields corresponding to the  $n$ th resonant eigenmode. They are the global fields throughout the structure.  $\bar{F}_n$  and  $\bar{G}_n$  are the irrotational fields and are produced by electric and magnetic currents respectively.  $\bar{F}_n$  is formed around the metal strip carrying the electric current and  $\bar{G}_n$  is produced near the cavity aperture supporting a magnetic current. Therefore irrotational eigenfunctions are physi-

cally local fields.  $\bar{E}_n$  and  $\bar{H}_n$  should satisfy Maxwell's equations for a source-free cavity. Thus let

$$\bar{\nabla} \times \bar{E}_n = k_n \bar{H}_n \quad (\text{C-7})$$

$$\bar{\nabla} \times \bar{H}_n = k_n \bar{E}_n \quad (\text{C-8})$$

where  $k_n$  is the eigenvalue for  $n$ th resonant mode inside a totally enclosed cavity.

The amplitudes  $e_n$ ,  $h_n$ ,  $g_n$ , and  $f_n$  are defined as below:

$$e_n = \iiint_V (\bar{E} \cdot \bar{E}_n) dV \quad (\text{C-9})$$

$$h_n = \iiint_V (\bar{H} \cdot \bar{H}_n) dV \quad (\text{C-10})$$

$$g_n = \iiint_V (\bar{G} \cdot \bar{G}_n) dV \quad (\text{C-11})$$

$$f_n = \iiint_V (\bar{F} \cdot \bar{F}_n) dV \quad (\text{C-12})$$

where  $V$  is the total volume of the cavity. Once these amplitudes are generally determined then the fields inside the cavity are completely specified from (C-5) and (C-6).

Now using (C-8) and a well known vector identity<sup>1</sup>, with some manipulation we obtain:

$$\iiint_V (\bar{\nabla} \times \bar{E} \cdot \bar{H}_n) dV = \iiint_V k_n \bar{E} \cdot \bar{E}_n dV + \iiint_V (\bar{\nabla} \cdot \bar{E} \times \bar{H}_n) dV \quad (\text{C-13})$$

Using (C-9), the first integral in the right hand side of (C-13) is simplified to  $k_n e_n$ .

---

1.  $(\bar{\nabla} \times \bar{A}) \cdot \bar{B} = (\bar{\nabla} \times \bar{B}) \cdot \bar{A} + \bar{\nabla} \cdot (\bar{A} \times \bar{B})$

The second one will be reduced to a surface integral by applying the divergence theorem<sup>1</sup>. Hence:

$$\iiint_V (\bar{\nabla} \cdot \bar{E} \times \bar{H}_n) dV = - \iint_S (\bar{E} \times \bar{H}_n \cdot \hat{n}) dS \quad (C-14)$$

The surface  $S$  incorporates the cavity walls and the aperture that surrounds the dielectric and air-filled regions as shown in Figure C-2. As is illustrated,  $S'$  is the total surface of the conducting walls,  $S_0$  is the surface of the aperture, including  $S_0^d$  and  $S_0^a$  facing the dielectric and air-filled regions respectively. The minus sign in (C-14) stems from the direction of the inward normal vector  $\hat{n}$  that is opposite to the direction of the Poynting vector. Further modification of (C-14) using another vector identity<sup>2</sup> and substitution of (C-14) and (C-9) into (C-13) yields the following expression:

$$\iiint_V (\bar{\nabla} \times \bar{E} \cdot \bar{H}_n) dV = k_n e_n - \iint_S \hat{n} \times \bar{E} \cdot \bar{H}_n dS \quad (C-15)$$

Using the above procedure the integral  $\iiint_V (\bar{\nabla} \times \bar{E} \cdot \bar{G}_n) dV$  will be derived as below:

$$\iiint_V (\bar{\nabla} \times \bar{E} \cdot \bar{G}_n) dV = \iiint_V \bar{E} \cdot \bar{\nabla} \times \bar{G}_n dV - \iint_S \hat{n} \times \bar{E} \cdot \bar{H}_n dS \quad (C-16)$$

---

1.  $\int_{V_{total}} (\bar{\nabla} \cdot \bar{E} \times \bar{H}_n) dV = \oint_{S_{total}} (\bar{E} \times \bar{H}_n \cdot \hat{n}) dS$

2.  $\bar{A} \cdot \bar{B} \times \bar{C} = \bar{A} \times \bar{B} \cdot \bar{C} = \bar{C} \times \bar{A} \cdot \bar{B}$

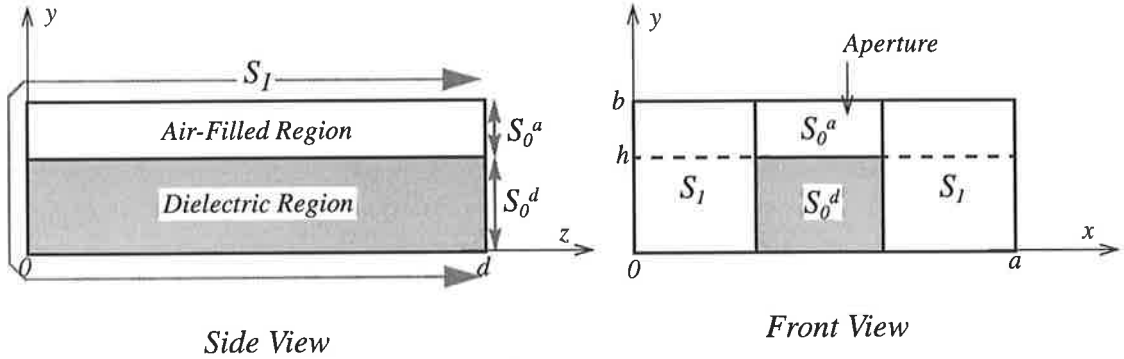


Figure C-2. Sections of the cavity walls and the aperture surrounding the regions.

As  $\bar{G}_n$  is an irrotational field, the first term on the right-hand side is zero and equation (C-16) will be simplified as below:

$$\iiint_{V^i} (\bar{\nabla} \times \bar{E} \cdot \bar{G}_n) dV = - \iint_{S^i} \hat{n} \times \bar{E} \cdot \bar{H}_n dS \quad (C-17)$$

Similarly using the above procedure and the divergence theorem we can obtain:

$$\iiint_V (\bar{\nabla} \times \bar{H} \cdot \bar{E}_n) dV = k_n h_n - \iint_S \bar{E}_n \times \hat{n} \cdot \bar{H} dS \quad (C-18)$$

As  $\bar{E}_n$  is divergence-free, thus  $\bar{E}_n \times \hat{n} = 0$  and (C-18) is simplified to give:

$$\iiint_{V^i} (\bar{\nabla} \times \bar{H} \cdot \bar{E}_n) dV = k_n h_n \quad (C-19)$$

Using the identity of Footnote 1 on page C-206, we can expand  $\bar{\nabla} \times \bar{H} \cdot \bar{F}_n$  and take a volume integral of the relation. Noting that  $\bar{F}_n$  is irrotational (curl-free) we obtain:

$$\iiint_V (\bar{\nabla} \times \bar{H} \cdot \bar{F}_n) dV = \iint_S (\bar{F}_n \times \hat{n} \cdot \bar{H}) dS \quad (C-20)$$

The right hand side vanishes as  $\bar{F}_n \times \hat{n} = 0$ , thus resulting the final relation:

$$\iiint_V (\bar{\nabla} \times \bar{H} \cdot \bar{F}_n) dV = 0 \quad (C-21)$$

Substitution of (C-1) into (C-9) and (C-10) yields:

$$h_n = -\frac{1}{j\omega\mu_0} \iiint_V (\bar{\nabla} \times \bar{E} \cdot \bar{H}_n) dV \quad (C-22)$$

$$g_n = -\frac{1}{j\omega\mu_0} \iiint_{V'} (\bar{\nabla} \times \bar{E} \cdot \bar{G}_n) dV \quad (C-23)$$

Substituting these expression into (C-6), the expansion of  $\bar{\nabla} \times \bar{E}$  becomes:

$$\bar{\nabla} \times \bar{E} = \sum_n \bar{H}_n \iiint_V (\bar{\nabla} \times \bar{E} \cdot \bar{H}_n) dV + \sum_n \bar{G}_n \iiint_V (\bar{\nabla} \times \bar{E} \cdot \bar{G}_n) dV \quad (C-24)$$

This equation will be referred to later on.

By substituting (C-15) and (C-17) into (C-24) we obtain:

$$\bar{\nabla} \times \bar{E} = \sum_n \bar{H}_n \left[ k_n e_n - \iint_S \hat{n} \times \bar{E} \cdot \bar{H}_n dS \right] + \sum_n \bar{G}_n \left[ - \iint_S \hat{n} \times \bar{E} \cdot \bar{H}_n dS \right] \quad (C-25)$$

By substituting (C-2) into (C-9) and (C-12) and the resulting expressions into (C-5), the electric field is obtained as below:

$$\begin{aligned} \bar{E} = & \frac{1}{j\omega\kappa\epsilon_0} \sum_n \bar{E}_n \left[ \iiint_V \bar{\nabla} \times \bar{H} \cdot \bar{E}_n dV - \iiint_V \bar{J} \cdot \bar{E}_n dV \right] \\ & + \frac{1}{j\omega\kappa\epsilon_0} \sum_n \bar{F}_n \left[ \iiint_V \bar{\nabla} \times \bar{H} \cdot \bar{F}_n dV - \iiint_V \bar{J} \cdot \bar{F}_n dV \right] \end{aligned} \quad (C-26)$$

By substituting (C-19) and (C-21) into (C-26) and also by substituting (C-26) into Maxwell's equation (C-2) the following equation is obtained:

$$\bar{\nabla} \times \bar{H} = \sum_n \bar{E}_n \left[ k_n h_n - \iint_V \bar{J} \cdot \bar{E}_n dV \right] - \sum_n \bar{F}_n \iint_V \bar{J} \cdot \bar{F}_n dV + \bar{J} \quad (C-27)$$

Now by substituting (C-5), (C-6), (C-25), and (C-27) into Maxwell's equations (C-1) and (C-2) and simplifying we obtain:

$$\sum_n \bar{H}_n \left[ k_n e_n - \iint_S \hat{n} \times \bar{E} \cdot \bar{H}_n dV \right] - \sum_n \bar{G}_n \left[ -\iint_S \hat{n} \times \bar{E} \cdot \bar{G}_n dV \right] = -j\omega\mu_0 \bar{H} \quad (\text{C-28})$$

$$\sum_n \bar{E}_n \left[ k_n h_n - \iiint_V \bar{J} \cdot \bar{E}_n dV \right] - \sum_n \bar{F}_n \iiint_V \bar{J} \cdot \bar{F}_n dV = j\omega\kappa\epsilon_0 \bar{E} \quad (\text{C-29})$$

By substituting  $\bar{H}_n$  and  $\bar{E}_n$  from (C-6) and (C-5) into (C-28) and (C-29) respectively and equating the coefficients of each eigenfunction on both sides of the above equations we finally obtain:

$$k_n e_n - \iint_S \hat{n} \times \bar{E} \cdot \bar{H}_n dV = -j\omega\mu_0 h_n \quad (\text{C-30})$$

$$\iint_S \hat{n} \times \bar{E} \cdot \bar{G}_n dV = j\omega\mu_0 g_n \quad (\text{C-31})$$

$$k_n h_n - \iiint_V \bar{J} \cdot \bar{E}_n dV = j\omega\kappa\epsilon_0 e_n \quad (\text{C-32})$$

$$-\iiint_V \bar{J} \cdot \bar{F}_n dV = j\omega\kappa\epsilon_0 f_n \quad (\text{C-33})$$

The above expressions constitute the fundamental wave amplitude equations of partially-filled cavities.

The surface integrals in (C-30) and (C-31) involving the unknown electric field  $\bar{E}$  may be decomposed to the following:

$$\iint_S \hat{n} \times \bar{E} \cdot \bar{H}_n dV = \iint_{S_1} \hat{n} \times \bar{E} \cdot \bar{H}_n dV + \iint_{S_0} \hat{n} \times \bar{E} \cdot \bar{H}_n dV \quad (\text{C-34})$$

$$\iint_S \hat{n} \times \bar{E} \cdot \bar{G}_n dV = \iint_{S_1} \hat{n} \times \bar{E} \cdot \bar{G}_n dV + \iint_{S_0} \hat{n} \times \bar{E} \cdot \bar{G}_n dV \quad (\text{C-35})$$

Assuming a finite conductivity for the cavity walls we can define the surface impedance  $Z_w$  as below:

$$\hat{n} \times \bar{E} = Z_w \bar{H} \quad (\text{C-36})$$

Equation (C-36) may be further simplified by assuming the operating frequency is close to resonant mode of the totally enclosed cavity (this is valid in practice), i.e.  $\omega \approx \omega_n$ . Thus let

$$\bar{H} \approx h_n \bar{H} \quad \text{at } \omega \approx \omega_n \quad (\text{C-37})$$

Using (C-36) and (C-37) we obtain:

$$\iint_{S_1} \hat{n} \times \bar{E} \cdot \bar{H}_n dS = -Z_w h_n \iint_{S_1} H_n^2 dS \quad (\text{C-38})$$

The right-hand of (C-38) accounts for the conductivity loss of the cavity and may be expressed by the appropriate Q-factor as below:

$$Z_w \iint_{S_1} H_n^2 dS = (1+j)\omega_n \mu_0 Q_{sn}^{-1} \quad (\text{C-39})$$

where  $Q_{sn}$  is the Q-factor due to conductivity loss of the surface  $S$  evaluated at the  $n$ th resonant mode. Substituting (C-39) into (C-38) yields:

$$\iint_{S_1} \hat{n} \times \bar{E} \cdot \bar{H}_n dS = -(1+j)\omega_n \mu_0 Q_{sn}^{-1} \quad (\text{C-40})$$

Using a similar procedure we can show that:

$$\iint_{S_1} \hat{n} \times \bar{E} \cdot \bar{G}_n dS = -Z_w \iint_{S_1} \bar{H} \cdot \bar{G}_n dS \quad (\text{C-41})$$

Substituting (C-40) and (C-41) into (C-34) and (C-35) and then substituting (C-34) and (C-35) into (C-30) and (C-31) yields the following equations:

$$k_n e_n + j\omega \mu_0 h_n + (1+j)\mu_0 \omega_n h_n Q_{sn}^{-1} = \iint_{S_0} \hat{n} \times \bar{E} \cdot \bar{H}_n dS \quad (C-42)$$

$$j\omega \mu_0 g_n - Z_w \iint_{S_1} \bar{H} \cdot \bar{G}_n dS = \iint_{S_0} \hat{n} \times \bar{E} \cdot \bar{G}_n dS \quad (C-43)$$

The surface integral on the left-hand side of relation (C-43) is the conductor loss which is negligible with respect to the term  $j\omega \mu_0 g_n$  and can be omitted without significant error. Also  $e_n$  in equation (C-42) can be substituted from (C-30). Thus let

$$\Delta_n h_n = \frac{k_n}{j\omega \kappa \epsilon_0} \iint_V \bar{J} \cdot \bar{E}_n dV + \iint_{S_0} \hat{n} \times \bar{E} \cdot \bar{H}_n dS \quad (C-44)$$

$$j\omega \mu_0 g_n = \iint_{S_0} \hat{n} \times \bar{E} \cdot \bar{G}_n dS \quad (C-45)$$

where

$$\Delta_n = \frac{k_n^2}{j\omega \kappa \epsilon_0} + j\omega \mu_0 + (1+j)\mu_0 \omega_n Q_{sn}^{-1} \equiv \mu_0 \omega_n \left[ \left\{ \frac{\omega}{\omega'_n} - \frac{\omega'_n}{\omega} \right\} j + \frac{1}{Q'_n} \right] \quad (C-46)$$

where  $\omega'_n = \omega_n \left( 1 - \frac{1}{2Q_{sn}} \right)$  is the modified resonant frequency due to the conductor losses and  $Q'_n$  is the unloaded-Q factor of the cavity for  $n$ th resonant mode. Thus:

$$Q'_n = (Q_{sn}^{-1} + Q_d^{-1})^{-1} \quad (C-47)$$

with  $Q_d = \tan \delta^{-1}$ , where  $\tan \delta$  is the loss tangent of the dielectric material. By substituting  $h_n$  from (C-44) into (C-32) the result is:

$$\Delta_n e_n + Z_0^2 \iint_V \bar{J} \cdot \bar{E}_n dV = \frac{k_n}{j\omega \kappa \epsilon_0} \iint_{S_0} \hat{n} \times \bar{E} \cdot \bar{H}_n dS \quad (C-48)$$

where  $Z_0 = \sqrt{\mu_0/\kappa\epsilon_0}$ . The equations (C-44), (C-45), (C-48), and (C-33) constitute the basic cavity expressions. The surface integrals in these equations represent the effect of the aperture fields on the cavity field distributions. They are critically important and can be expanded in terms of the waveguide and cavity eigenfunctions. Details are given in Chapter 5.

---

## Appendix D

# *Eigenfunctions of Partially-Filled Cavities*

### D.1 Introduction

Among several references, the most complete analysis for a fully enclosed hollow rectangular box cavity is given by Collin [49]. It includes the derivation of a dyadic Green's function from which the cavity eigenfunctions are obtained. The same procedure may be applied to a partially-filled rectangular box shown in Figure D-1 using hybrid mode expansions. However in this case, no specific results have been found in the literature. In this Appendix the eigenfunctions of a partially-filled rectangular box are derived based on the above procedure. There will be two sets of eigenfunctions for a partially-filled box cavity depending on LSE<sup>y</sup> and LSM<sup>y</sup> modes as explained below.

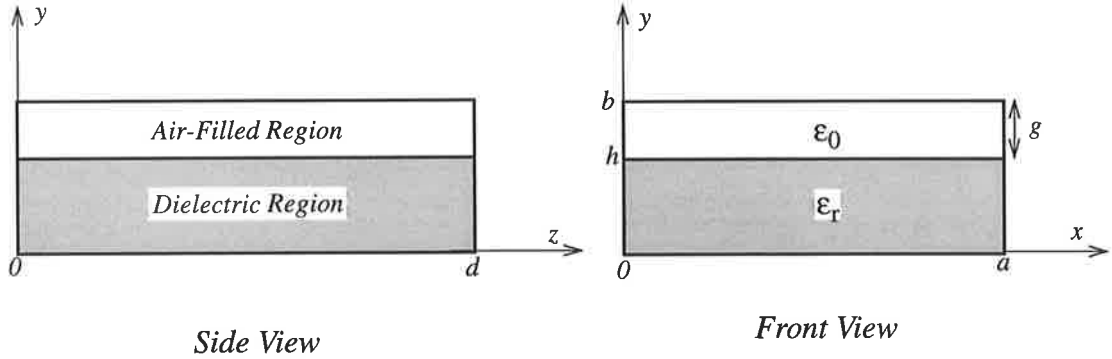


Figure D-1. Partially-filled rectangular box cavity

## D.2 LSE<sup>y</sup><sub>mnl</sub> Modes

The cavity fields are classified into solenoidal and irrotational groups. The solenoidal electric field for the partially-filled box of Figure D-1 is obtained from the following:

$$\bar{E}_{mnl}^{i,h} = \bar{\nabla} \times \hat{a}_y \Psi_{mnl}^{i,h} \quad (\text{D-1})$$

where  $\bar{E}_{mnl}^{i,h}$  is the electric field of the  $mnl$ -mode and  $\Psi_{mnl}^{i,h}$  is the scalar mode function which satisfies the boundary conditions for the LSE<sup>y</sup><sub>mnl</sub> mode. From equation (D-1) and the boundary conditions we obtain:

$$\Psi_{mnl}^{i,h} = A_{mnl}^{i,h} \cos\left(\frac{m\pi}{a}x\right) \sin(\beta_n^i y^i) \cos\left(\frac{l\pi}{d}z\right) \quad (\text{D-2})$$

where  $m$  and  $l$  are eigennumbers and  $\beta_n^i$  is the eigenvalue in the  $y$ -direction which is specified from the transcendental equation (B-30) in Appendix B.

$$y^i = \begin{cases} y & \text{for } i \rightarrow d \\ b - y & \text{for } i \rightarrow a \end{cases} \quad (\text{D-3})$$

Similar to expressions in Appendix B equation (D-2) provides the mode function for the dielectric and air-filled media upon substituting the superscripts ' $i$ ' with either ' $d$ ' or ' $a$ ' respectively. By substituting (D-2) into (D-1) we obtain the electric eigenfunctions as below:

$$\bar{E}_{mnl}^{i,h}|_x = A_{mnl}^{i,h} \left(\frac{l\pi}{d}\right) \cos\left(\frac{m\pi}{a}x\right) \sin(\beta_n^i y^i) \sin\left(\frac{l\pi}{d}z\right) \hat{a}_x \quad (\text{D-4})$$

$$\bar{E}_{mnl}^{i,h}|_z = -A_{mnl}^{i,h} \left(\frac{m\pi}{a}\right) \sin\left(\frac{m\pi}{a}x\right) \sin(\beta_n^i y^i) \cos\left(\frac{l\pi}{d}z\right) \hat{a}_z \quad (\text{D-5})$$

The normalisation condition for the cavity is given below:

$$N = \iiint_{V^i} \bar{E}_{mnl}^{i,h} \cdot \bar{E}_{mnl}^{i,h} dV = 1 \quad (\text{D-6})$$

By substituting electric field components from (D-4) and (D-5) into (D-6) and integrating throughout the volume  $V^i$  of the medium, we obtain the normalised amplitude as follows:

$$A_{mnl}^{i,h} = \left( \frac{\epsilon_{0m} \epsilon_{0n} \epsilon_{0l}}{ah^i d} \right)^{\frac{1}{2}} [1 - \text{sinc}(2\beta_n^i h^i / \pi)]^{-\frac{1}{2}} \left[ \left( \frac{m\pi}{a} \right)^2 + \left( \frac{l\pi}{d} \right)^2 \right]^{-\frac{1}{2}} \quad (\text{D-7})$$

where  $\text{sinc}(x) = (\sin \pi x) / (\pi x)$ ,  $\epsilon_{0k}$  is the Neumann constant and defined by:

$$\epsilon_{0k} = \begin{cases} 1 & \text{for } k = 0 \\ 2 & \text{for } k \neq 0 \end{cases}, \text{ and } h^i \text{ is the height of the medium given as:}$$

$$h^i = \begin{cases} h & \text{for } i \rightarrow d \\ g & \text{for } i \rightarrow a \end{cases}$$

The magnetic field is determined from the source-free Maxwell's equation as below:

$$\bar{H}_{mnl}^{i,h} = \frac{1}{k_{mnl}} \bar{\nabla} \times \bar{E}_{mnl} = \frac{1}{k_{mnl}} \bar{\nabla} \times \bar{\nabla} \times \hat{a}_y \Psi_{mnl}^{i,h} \quad (\text{D-8})$$

By substituting (D-4) into (D-8) we obtain the magnetic eigenfunctions for LSE<sup>y</sup><sub>mnl</sub> as below:

$$\bar{H}_{mnl}^{i,h}|_x = \mp A_{mnl}^{i,h} (k_{mnl})^{-1} \left( \frac{m\pi}{a} \right) (\beta_n^i) \sin\left(\frac{m\pi}{a}x\right) \cos(\beta_n^i y^i) \cos\left(\frac{l\pi}{d}z\right) \hat{a}_x \quad (\text{D-9})$$

$$\bar{H}_{mnl}^{i,h}|_y = A_{mnl}^{i,h} (k_{mnl})^{-1} \left[ \left( \frac{m\pi}{a} \right)^2 + \left( \frac{l\pi}{d} \right)^2 \right] \cos\left(\frac{m\pi}{a}x\right) \sin(\beta_n^i y^i) \cos\left(\frac{l\pi}{d}z\right) \hat{a}_y \quad (\text{D-10})$$

$$\bar{H}_{mn}^{i,h}|_z = \mp A_{mn}^{i,h} (k_{mn})^{-1} \left( \frac{l\pi}{a} \right) (\beta_n^i) \cos \left( \frac{m\pi}{a} x \right) \sin(\beta_n^i y^i) \sin \left( \frac{l\pi}{d} z \right) \hat{a}_z \quad (D-11)$$

where minus sign and plus sign in the  $x$  and  $z$  components account for dielectric and air-filled regions respectively.

### D.3 LSM<sup>y</sup><sub>mn</sub> Modes

Similar to Section D.2 the magnetic field is expressed in terms of a scalar mode function as below:

$$\bar{H}_{mn}^{i,e} = \bar{\nabla} \times \hat{a}_y \Psi_{mn}^{i,e} \quad (D-12)$$

where  $\Psi_{mn}^{i,e}$  is derived from (D-12) and the cavity boundary conditions to yield:

$$\Psi_{mn}^{i,e} = A_{mn}^{i,e} \sin \left( \frac{m\pi}{a} x \right) \cos(\beta_n^i y^i) \sin \left( \frac{l\pi}{d} z \right) \quad (D-13)$$

By substituting  $\Psi_{mn}^{i,e}$  from (D-13) into (D-12) we obtain the magnetic eigenfunctions for the LSM<sup>y</sup><sub>mn</sub> mode as below:

$$\bar{H}_{mn}^{i,e}|_x = -A_{mn}^{i,e} \left( \frac{l\pi}{d} \right) \sin \left( \frac{m\pi}{a} x \right) \cos(\beta_n^i y^i) \cos \left( \frac{l\pi}{d} z \right) \hat{a}_x \quad (D-14)$$

$$\bar{H}_{mn}^{i,e}|_z = A_{mn}^{i,e} \left( \frac{m\pi}{a} \right) \cos \left( \frac{m\pi}{a} x \right) \cos(\beta_n^i y^i) \sin \left( \frac{l\pi}{d} z \right) \hat{a}_z \quad (D-15)$$

To derive the normalised amplitude we can use the following orthogonality condition:

$$N = \iiint_{V^i} \bar{H}_{mn}^{i,e} \cdot \bar{H}_{mn}^{i,e} dV = 1 \quad (D-16)$$

By substituting  $\bar{H}_{mn}^{i,e}$  components from (D-14) and (D-15) into (D-16) and integrating over the volume of each medium  $V^i$  the amplitude  $A_{mn}^{i,e}$  is obtained as

$$A_{mnl}^{i,h} = \left( \frac{\epsilon_{0m}\epsilon_{0n}\epsilon_{0l}}{ah^id} \right)^{\frac{1}{2}} [1 + \text{sinc}(2\beta_n^i h^i/\pi)]^{-\frac{1}{2}} \left[ \left( \frac{m\pi}{a} \right)^2 + \left( \frac{l\pi}{d} \right)^2 \right]^{-\frac{1}{2}} \quad (\text{D-17})$$

with the parameters the same as for expression (D-7). Using a wave equation similar to (D-8) the electric field eigenfunctions are obtained as follows:

$$\bar{E}_{mnl}^{i,e}|_x = \mp A_{mnl}^{i,e} (k_{mnl})^{-1} \left( \frac{m\pi}{a} \right) (\beta_n^i) \cos \left( \frac{m\pi}{a} x \right) \sin(\beta_n^i y^i) \sin \left( \frac{l\pi}{d} z \right) \hat{a}_x \quad (\text{D-18})$$

$$\bar{E}_{mnl}^{i,e}|_y = A_{mnl}^{i,e} (k_{mnl})^{-1} \left[ \left( \frac{m\pi}{a} \right)^2 + \left( \frac{l\pi}{d} \right)^2 \right] \sin \left( \frac{m\pi}{a} x \right) \cos(\beta_n^i y^i) \sin \left( \frac{l\pi}{d} z \right) \hat{a}_y \quad (\text{D-19})$$

$$\bar{E}_{mnl}^{i,e}|_z = \mp A_{mnl}^{i,e} (k_{mnl})^{-1} \left( \frac{l\pi}{d} \right) (\beta_n^i) \sin \left( \frac{m\pi}{a} x \right) \sin(\beta_n^i y^i) \cos \left( \frac{l\pi}{d} z \right) \hat{a}_z \quad (\text{D-20})$$

where the minus sign is for the dielectric and plus sign for the air-filled region.

## D.4 Irrotational Fields

So far the solenoidal fields have been considered. They are the global fields in a cavity and are adequate to explain the results of applying Maxwell's equations to a fully enclosed cavity. However the presence of apertures or current strips in the cavity, will excite irrotational fields such as  $\bar{G}$ , and  $\bar{F}$  which should be added to the field expansion. These are local fields that are established around the currents that are equivalent to the apertures or the metal strips. It should be noted that small<sup>1</sup> apertures or probes do not excite such fields to any significant extent.

### D.4.1 Local Electric Fields

The irrotational nature of the field imply the following relations:

$$[\nabla^2 + k_{mnl}] \bar{F}_{mnl}^i = 0 \quad (\text{D-21})$$

$$\bar{\nabla} \times \bar{F}_{mnl}^i = 0 \quad (\text{D-22})$$

---

1. 'small' indicates that the dimension of the aperture or probe is less than 10% of the medium wavelength

Obviously  $\bar{F}_{mn}^i$  will be the gradient of a scalar electric potential  $\Psi^{i,f}$ . Thus let

$$\bar{F}_{mn}^i = \frac{1}{k_{mn}^i} \bar{\nabla} \Psi_{mn}^{i,f} \quad (\text{D-23})$$

where  $m$ ,  $n$ , and  $l$  are the eigennumbers in the  $x$ ,  $y$ , and  $z$  direction, and the superscripts ‘ $i$ ’ and ‘ $f$ ’ indicate the medium such as dielectric or air-filled region and  $\bar{F}$  denotes the electric field. As  $\bar{F}_{mn}^i$  has no tangential component on the conductor surface the boundary condition is:

$$\hat{n} \times \bar{F}_{mn}^i = 0 \quad \text{on } S^i \quad (\text{D-24})$$

Using (D-23) and (D-24) the scalar function is obtained as below:

$$\Psi_{mn}^{i,f} = A_{mn}^{i,f} \sin\left(\frac{m\pi}{a}x\right) \sin(\beta_n^i y^i) \sin\left(\frac{l\pi}{d}z\right) \quad (\text{D-25})$$

where  $y^i$  is given by (D-3). By substituting (D-25) into (D-23) the eigenfunctions of the  $\bar{F}_{mn}^i$  field are obtained as below:

$$\bar{F}_{mn}^i|_x = A_{mn}^{i,f} (k_{mn}^i)^{-1} \left(\frac{m\pi}{a}\right) \cos\left(\frac{m\pi}{a}x\right) \sin(\beta_n^i y^i) \sin\left(\frac{l\pi}{d}z\right) \hat{a}_x \quad (\text{D-26})$$

$$\bar{F}_{mn}^i|_y = \pm A_{mn}^{i,f} (k_{mn}^i)^{-1} (\beta_n^i) \sin\left(\frac{m\pi}{a}x\right) \cos(\beta_n^i y^i) \sin\left(\frac{l\pi}{d}z\right) \hat{a}_y \quad (\text{D-27})$$

$$\bar{F}_{mn}^i|_z = A_{mn}^{i,f} (k_{mn}^i)^{-1} \left(\frac{l\pi}{d}\right) \sin\left(\frac{m\pi}{a}x\right) \sin(\beta_n^i y^i) \cos\left(\frac{l\pi}{d}z\right) \hat{a}_z \quad (\text{D-28})$$

where the plus sign in (D-27) applies to the dielectric and the minus sign to the air-filled region. A normalisation condition similar to (D-6) and (D-16) can be defined as:

$$N = \iiint_{V^i} \bar{F}_{mn}^i \cdot \bar{F}_{mn}^i dV = 1 \quad (\text{D-29})$$

Now substituting the field components from (D-26) to (D-28) into (D-29) and integrating over the volume of each medium we obtain the normalised amplitude as below:

$$A_{mnl}^{i,f} = \left( \frac{\epsilon_{0m}\epsilon_{0n}\epsilon_{0l}}{ah^id} \right)^{\frac{1}{2}} [1 - \text{sinc}(2\beta_n^i h^i/\pi)]^{-\frac{1}{2}} [1 + T_f]^{-\frac{1}{2}} \quad (\text{D-30})$$

where

$$T_f = \left[ \frac{2(\beta_n^i)^2}{k_{mnl}^2} \right] \frac{\text{sinc}(2\beta_n^i h^i/\pi)}{1 - \text{sinc}(2\beta_n^i h^i/\pi)} \quad (\text{D-31})$$

#### D.4.2 Local Magnetic Fields

Using the irrotational equations (D-21) and (D-22) it can be shown that the local magnetic field  $\bar{G}_{mnl}$  is derived from a scalar function as below:

$$\bar{G}_{mnl}^i = \frac{1}{k_{mnl}} \bar{\nabla} \Psi_{mnl}^{i,g} \quad (\text{D-32})$$

where superscript ‘g’ indicates the  $\bar{G}_{mnl}$  fields. However the boundary condition is different and is:

$$\hat{n} \cdot \bar{G}_{mnl} = \frac{\partial}{\partial n} \Psi_{mnl}^{i,g} = 0 \quad \text{on } S^i \quad (\text{D-33})$$

From (D-32) and (D-33),  $\Psi_{mnl}^{i,g}$  is obtained as below:

$$\Psi_{mnl}^{i,g} = A_{mnl}^{i,g} \cos\left(\frac{m\pi}{a}x\right) \cos(\beta_n^i y^i) \cos\left(\frac{l\pi}{d}z\right) \quad (\text{D-34})$$

Now substituting (D-34) into (D-32) will finally give the eigenfunctions of the  $\bar{G}_{mnl}$  as follows:

$$\bar{G}_{mnl}^i \Big|_x = -A_{mnl}^{i,g} (k_{mnl})^{-1} \left( \frac{m\pi}{a} \right) \sin\left(\frac{m\pi}{a}x\right) \cos(\beta_n^i y^i) \cos\left(\frac{l\pi}{d}z\right) \hat{a}_x \quad (\text{D-35})$$

$$\bar{G}_{mnl}^i \Big|_y = \mp A_{mnl}^{i,g} (k_{mnl})^{-1} (\beta_n^i) \cos\left(\frac{m\pi}{a}x\right) \sin(\beta_n^i y^i) \cos\left(\frac{l\pi}{d}z\right) \hat{a}_y \quad (\text{D-36})$$

$$\bar{G}_{mnl}^i \Big|_z = -A_{mnl}^{i,g} (k_{mnl})^{-1} \left( \frac{l\pi}{d} \right) \cos\left(\frac{m\pi}{a}x\right) \cos(\beta_n^i y^i) \sin\left(\frac{l\pi}{d}z\right) \hat{a}_z \quad (\text{D-37})$$

where the minus sign in (D-36) is for the dielectric region. Using the following normalisation:

$$N = \iiint_{V^i} \bar{G}_{mnl}^i \cdot \bar{G}_{mnl}^i dV = 1 \quad (\text{D-38})$$

and substituting the  $\bar{G}_{mnl}^i$  components from (D-35) to (D-37) into (D-38) the normalised amplitude is obtained as below:

$$A_{mnl}^{i,g} = \left( \frac{4\epsilon_0 l}{a h^i d} \right)^{\frac{1}{2}} [1 + \operatorname{sinc}(2\beta_n^i h^i / \pi)]^{-\frac{1}{2}} [1 + T_g]^{-\frac{1}{2}} \quad (\text{D-39})$$

where

$$T_g = \left[ \frac{2(\beta_n^i)^2}{k_{mnl}^2} \right] \frac{\operatorname{sinc}(2\beta_n^i h^i / \pi)}{1 + \operatorname{sinc}(2\beta_n^i h^i / \pi)} \quad (\text{D-40})$$

---

## Appendix E

# *Coefficients of Surface Integral Expansion*

These coefficients are defined in Chapter 5 and are determined from the reaction integrals between the cavity and waveguide eigenfunctions as below:

$$B_{nk}^e = \iint_{S_0} (\bar{e}_k^e \times \bar{H}_n) \cdot \hat{a}_z dS \quad (E-1)$$

$$B_{nk}^h = \iint_{S_0} (\bar{e}_k^h \times \bar{H}_n) \cdot \hat{a}_z dS \quad (E-2)$$

$$C_{nk}^e = \iint_{S_0} (\bar{e}_k^e \times \bar{G}_n) \cdot \hat{a}_z dS \quad (E-3)$$

$$C_{nk}^h = \iint_{S_0} (\bar{e}_k^h \times \bar{G}_n) \cdot \hat{a}_z dS \quad (E-4)$$

where  $\bar{e}_k^e$  and  $\bar{e}_k^h$  are the waveguide eigenvectors as obtained from Appendix B. The cavity eigenfunctions  $\bar{H}_n$  and  $\bar{G}_n$  are given in Appendix D.

The integrals are determined using the same procedure. Starting with (E-2) we can reduce the eigenvectors to transverse components. Also it can be proved that the integral generally vanishes due to the orthogonality condition except that  $\bar{e}_k^{mode}$  and  $\bar{H}_n$  are proportional, *i.e.* their eigenvalues in the  $x$  and  $y$  directions are the same. Thus let:

$$B_{mn}^e = \iint_{S_0} (\bar{e}_{mn}^e \times \bar{H}_{mn}^e) \cdot \hat{a}_z dS \quad (E-5)$$

where  $\bar{e}_{mn}^e$  and  $\bar{H}_{mn}^e$  are the transverse components of waveguide and cavity eigenvectors respectively.  $\bar{H}_{mn}^e$  is given by (D-14) and  $\bar{e}_{mn}^e$  is obtained from (B-45) to (B-48). The integral is decomposed into the corresponding terms for dielectric and air-filled media resulting in a lengthy calculation. However due to the above proportionality, a short-cut method can be applied in which  $\bar{H}_{mn}^e$  is interpreted in terms of the corresponding waveguide field  $\bar{h}_{mn}^e$ . Therefore using (B-51), (B-52) and (D-14) we obtain:

$$\bar{H}_{mn}^e = \left(\frac{l\pi}{d}\right) \left[ \left(\frac{m\pi}{a}\right)^2 + \left(\frac{l\pi}{d}\right)^2 \right] \left(\frac{2}{d}\right)^{\frac{1}{2}} (Y_{mn}^e)^{-1} \cos\left(\frac{l\pi}{d}z\right) \bar{h}_{mn}^e \quad (E-6)$$

where  $Y_{mn}^e$  is the wave admittance for the  $LSM^y_{mn}$  propagating mode. Substituting  $\bar{H}_{mn}^e$  from (E-6) into (E-5) and noting that  $z = d$  results in:

$$B_{mn}^e = \left(\frac{l\pi}{d}\right) \left[ \left(\frac{m\pi}{a}\right)^2 + \left(\frac{l\pi}{d}\right)^2 \right] \left(\frac{2}{d}\right)^{\frac{1}{2}} (Y_{mn}^e)^{-1} \cos(l\pi) \iint_{S_0} \bar{e}_{mn}^e \times \bar{h}_{mn}^e \cdot \hat{a}_z dS \quad (E-7)$$

where the surface integral in (E-7) is equal to the wave admittance according to equations (5-18) to (5-20) in Chapter 5. Thus let:

$$B_{mn}^e = \left(\frac{l\pi}{d}\right) \left[ \left(\frac{m\pi}{a}\right)^2 + \left(\frac{l\pi}{d}\right)^2 \right] \left(\frac{2}{d}\right)^{\frac{1}{2}} \cos(l\pi) \quad (E-8)$$

Using (D-9) to (D-10) and (B-20) to (B-23)  $\bar{H}_{mn}^h$  is expressed in terms of  $\bar{h}_{mn}^h$  as below:

$$\bar{H}_{mn}^h = (k_{mn})^{-1} \left[ \left( \frac{m\pi}{a} \right)^2 + \left( \frac{l\pi}{d} \right)^2 \right] \left( \frac{2}{d} \right)^{\frac{1}{2}} (Y_{mn}^h)^{-1} \cos \left( \frac{l\pi}{d} z \right) \bar{h}_{mn}^h \quad (\text{E-9})$$

Substituting (E-9) into (E-2) and using the same orthogonality conditions we obtain:

$$B_{mn}^h = (k_{mn})^{-1} \left[ \left( \frac{m\pi}{a} \right)^2 + \left( \frac{l\pi}{d} \right)^2 \right] \left( \frac{2}{d} \right)^{\frac{1}{2}} \cos(l\pi) \quad (\text{E-10})$$

Similarly  $C_{nk}^e$  and  $C_{nk}^h$  can be derived using the above procedure. The transverse eigenvector  $\bar{G}_{mn}$  comprises  $x$ - and  $y$ - components as given by (D-35) and (D-36). Substituting these and (B-45) to (B-48) into (E-3) results in the following:

$$C_{mn}^{i,e} = (k_{mn})^{-1} \left( \frac{m\pi}{a} \right) \cos(l\pi) \left( \frac{\epsilon_{0l}}{d} \right)^{1/2} (1 - T_g)^{-1/2} \left\{ 1 - \frac{\beta_n^i{}^2}{\kappa k_0^2 - \beta_n^i{}^2} \right\} \quad (\text{E-11})$$

$$\text{where } T_g = \left[ \frac{2(\beta_n^i)^2}{k_{mn}^2} \right] \frac{\text{sinc}(2\beta_n^i h^i / \pi)}{1 + \text{sinc}(2\beta_n^i h^i / \pi)}$$

The superscript ' $i$ ' accounts for the medium and is defined where  $i$  becomes  $d$  for dielectric and  $i$  becomes  $a$  for air-filled regions respectively.

Similarly, substituting (D-36) and (B-15) to (B-16) into (E-4) will yield:

$$C_{mn}^{i,h} = -(k_{mn})^{-1} A_{mn}^{i,g_l} A_{mn}^{i,h} \left( \frac{m\pi}{a} \right) \left( \frac{a}{2} \right)^{\frac{h'}{2}} \cos(l\pi) \quad (\text{E-12})$$

where  $A_{mn}^{i,h}$  is determined from (B-35) and  $h'$  is given by

$$h' = 1 - \text{sinc}(2\beta_n^i h^i / \pi) \quad (\text{E-13})$$

---

## Appendix F

# *Theory of Mode-Matching Technique*

### F.1 Introduction

Mode-matching is currently recognised as a powerful method for treating waveguide discontinuities. In the case of rectangular waveguides, this technique has been successfully applied to single- and double-step junctions [58], [59]. The feature that ranks the mode-matching method superior to the classical transmission-line method is its multi-mode nature, i.e., the inclusion of higher-order modes of excitation in the numerical calculations. These higher-order modes are inevitably activated in the vicinity of every waveguide discontinuity, such as aperture, or step, and affect the propagation of electromagnetic power across the junction.

Therefore the junction parameters, such as transmission and reflection coefficients cannot be solely determined from the dominant mode propagation and the application of classical single-mode transmission-line techniques [28] has always led to significant errors between theoretical and experimental results. In the case of double-step discontinuities, due to the significant influence of the higher-order modes, in the past only empirical

designs were developed from individual measurements [63]. Mode-matching analysis of double-step planar junctions for hollow waveguides has been given by Patzelt [59], and a more comprehensive form has been applied to dielectric-filled junctions [60], [61]. However the coupling structure of Figure F-1 can be separated into junctions involving partially filled guides that are well described by longitudinal section modes or hybrid modes. Therefore in this appendix a mode-matching theory is developed with special focus on the hybrid mode expansion. The theory is given for a generalised double-step plane junction between rectangular waveguides and the fields are expanded in terms of LSE<sup>y</sup> and LSM<sup>y</sup> modes.

## F.2 Basic Terminology

A double-step planar discontinuity is shown in Figure F-1, where  $S_1$  and  $S_2$  are the cross-sectional areas of guides #1 and #2 respectively.

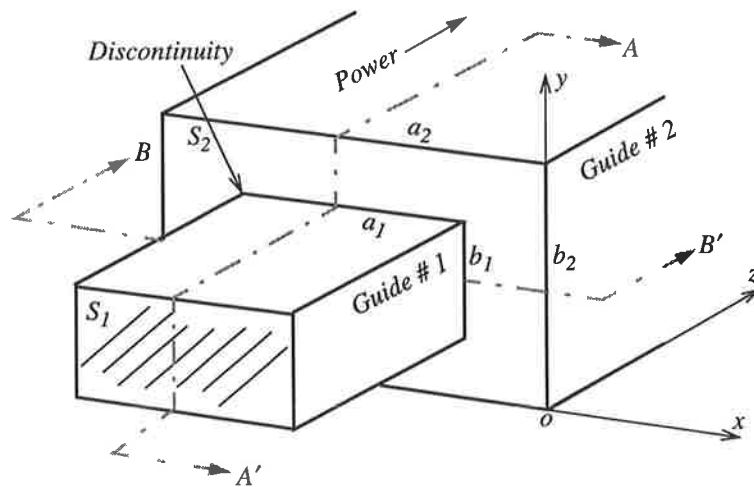


Figure F-1. Typical double-step planar discontinuity. Cross-sections A – A' and B – B' are shown in Figure F-2

Also  $a_1$ ,  $a_2$  and  $b_1$ ,  $b_2$  are the widths and heights of the waveguides respectively. The width and height offsets or steps are defined as:

$$a_0 = \frac{a_2 - a_1}{2} \quad (\text{F-1})$$

$$b_0 = \frac{b_2 - b_1}{2} \quad (\text{F-2})$$

with the offsets or steps clearly shown in Figure F-2 where the views of longitudinal and transversal cross-sections are given. The axial centre-lines of the two metal pipes coincide.

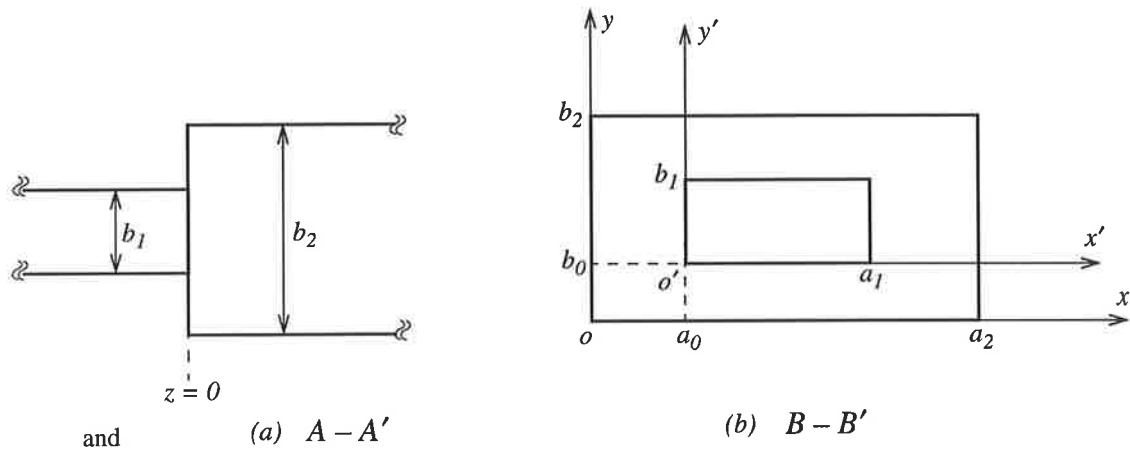


Figure F-2. Views of (a) longitudinal and (b) transversal cross-sections of the waveguide junction

The cross-section of guide #1 is defined in the plane  $z' = 0$  of the  $x'y'z'$  cartesian system and that of guide #2 in the plane  $z = 0$  of the  $xyz$  cartesian system. From Figure F-2 the two coordinates are related to each other by:

$$x = x' + a_0 \quad (\text{F-3})$$

$$y = y' + b_0 \quad (\text{F-4})$$

### F.2.1 Fields of Guide #1

The tangential electric field of the guide #1 i.e.  $\bar{E}_t^{(1)}$  on the cross-section  $(B - B')$  can be expanded in terms of the LSE<sup>y</sup> and LSM<sup>y</sup> eigenfunctions:

$$\bar{E}_t^{(1)} = \sum_{k,l}^N V_{kl}^{1,e} e^{-\gamma_{kl}^{1,e} z} + \sum_{k,l}^N V_{kl}^{1,h} e^{-\gamma_{kl}^{1,h} z} \quad (\text{F-5})$$

where  $V_{kl}^{1,e}$  and  $V_{kl}^{1,h}$  are the normalised voltages corresponding to the equivalent transmission-line models of  $\text{LSM}^y_{kl}$  and  $\text{LSE}^y_{kl}$  eigenmodes respectively. k and l are the eigennumbers in the x and y directions. Superscript “1” indicates the guide #1 and “e” or “h” indicates the e-mode or  $\text{LSM}^y$  and h-mode or  $\text{LSE}^y$  respectively. It can be shown that the transmission-line voltages  $V_{kl}^{1,e}$  and  $V_{kl}^{1,h}$  are related to the normalised wave-amplitudes as follows:

$$V_{kl}^{1,\text{mode}} = \frac{a_{kl}^{1,\text{mode}}}{\sqrt{Y_{kl}^{1,\text{mode}}}} e^{-\gamma_{kl}^{1,\text{mode}} z} + \frac{b_{kl}^{1,\text{mode}}}{\sqrt{Y_{kl}^{1,\text{mode}}}} e^{\gamma_{kl}^{1,\text{mode}} z} \quad (\text{F-6})$$

where  $Y_{kl}^{1,\text{mode}}$  is the wave admittance, and  $a_{kl}^{1,\text{mode}}$  and  $b_{kl}^{1,\text{mode}}$  are the normalised wave-amplitudes in the forward and backward directions respectively.  $\gamma_{kl}^{1,\text{mode}}$  is the complex propagation constant incorporating both propagating and evanescent modes. The superscript “mode” stands for “e” ( $\text{LSM}^y_{kl}$ ) or “h” ( $\text{LSE}^y_{kl}$ ).

Similarly the tangential magnetic field of guide #1 is given by:

$$\bar{H}_t^{(1)} = \sum_{k,l}^N I_{kl}^{1,e} \bar{h}_{kl}^{1,e} + \sum_{k,l}^N I_{kl}^{1,h} \bar{h}_{kl}^{1,h} \quad (\text{F-7})$$

where  $I_{kl}^{1,\text{mode}}$  is the normalised equivalent current corresponding to eigenmode  $\text{LSM}^y_{kl}$  or  $\text{LSE}^y_{kl}$ . Also  $I_{kl}^{1,\text{mode}}$  is related to the normalised wave-amplitudes:

$$I_{kl}^{1,\text{mode}} = \frac{a_{kl}^{1,\text{mode}}}{\sqrt{Y_{kl}^{1,\text{mode}}}} e^{-\gamma_{kl}^{1,\text{mode}} z} - \frac{b_{kl}^{1,\text{mode}}}{\sqrt{Y_{kl}^{1,\text{mode}}}} e^{\gamma_{kl}^{1,\text{mode}} z} \quad (\text{F-8})$$

### F.2.2 Fields of Guide #2

The tangential electric and magnetic fields of guide #2 on the cross-section ( $B - B'$ ) can be expanded in terms of the LSM<sup>y</sup> and LSE<sup>y</sup> eigenfunctions:

$$\begin{aligned}\bar{E}_t^{(2)} &= \sum_{m,n}^M V_{mn}^{2,e} \bar{e}_{mn}^{-2,e} + \sum_{m,n}^M V_{kmn}^{2,h} \bar{e}_{mn}^{-2,h} \\ \bar{H}_t^{(2)} &= \sum_{m,n} I_{mn}^{2,e} \bar{h}_{mn}^{-2,e} + \sum_{m,n} I_{kmn}^{2,h} \bar{h}_{mn}^{-2,h}\end{aligned}\quad (\text{F-9}) \quad (\text{F-10})$$

where similar to equations (F-6) and (F-8) we can define mode voltages and mode currents in terms of the normalised wave-amplitudes:

$$V_{mn}^{2, mode} = \frac{a_{mn}^{2, mode}}{\sqrt{Y_{mn}^{2, mode}}} e^{-\gamma_{mn}^{2, mode} z} + \frac{b_{mn}^{2, mode}}{\sqrt{Y_{mn}^{2, mode}}} e^{\gamma_{mn}^{2, mode} z} \quad (\text{F-11})$$

$$I_{mn}^{2, mode} = -\frac{a_{mn}^{2, mode}}{\sqrt{Y_{mn}^{2, mode}}} e^{-\gamma_{mn}^{2, mode} z} + \frac{b_{mn}^{2, mode}}{\sqrt{Y_{mn}^{2, mode}}} e^{\gamma_{mn}^{2, mode} z} \quad (\text{F-12})$$

where *mode* stands for “e” or “h”. The sign difference between equation (F-12) and (F-8) stems from the fact that the direction of the Poynting vector in guide #1 is inward to the junction whereas in guide #2 it is outward from the discontinuity.

## F.3 Normalised Mode-Vectors

The vectors  $\bar{e}^{v, mode}$  and  $\bar{h}^{v, mode}$  in equations (F-5), (F-7), (F-9) and (F-10) are eigenvectors or normalised mode-vectors and they are defined for each hybrid mode inside the guide #v. For partially-filled waveguides in particular, these vectors are directly obtained from Appendix B. Also dielectric-filled waveguides (including hollow waveguide) are special cases of partially-filled waveguides in which the dielectric constants of the media are the same, hence the same eigenfunctions can be used. Generally

the orthogonality of the eigenvectors in each waveguide is expressed by the following relation:

$$\int_{S_v} (\bar{e}_{mn}^{v, mode1} \times \bar{h}_{m'n'}^{v, mode2}) \cdot \hat{a}_z dS = \begin{cases} Q_{mn}^{v, mode} & mode1=mode2, m=m', n=n' \\ 0 & mode1 \neq mode2, m \neq m', n \neq n' \end{cases} \quad (F-13)$$

where  $v$  is the number of the waveguide, *i.e.* 1 or 2. For instance the orthogonality relation for the  $LSM^y_{mn}$  mode in guide #2 is given from (F-13) as:

$$\int_{S_2} (\bar{e}_{mn}^{2, e} \times \bar{h}_{mn}^{2, e}) \cdot \hat{a}_z dS = Q_{mn}^{2, e} \quad (F-14)$$

where the surface integral is calculated over the cross-section of guide #2.  $Q_{mn}^{2, e}$  is the normalisation constant and can be arbitrarily defined. It is common practice to set this constant equal to the wave admittance:

$$Q_{mn}^{v, mode} = Y_{mn}^{v, mode} \quad (F-15)$$

This assumption will simplify mode-matching equations.

## F.4 Mode-Matching Equations

The continuity of tangential electric and magnetic field at the junction cross-section ( $B - B'$ ) of Figure F-2 calls for the following field relations:

$$\bar{E}_t^{(2)} = \begin{cases} \bar{E}_t^{(1)} & \text{on } S_1 \\ 0 & \text{on } (S_2 - S_1) \end{cases} \quad (F-16)$$

$$\bar{H}_t^{(2)} = \bar{H}_t^{(1)} \quad \text{on } S_1 \quad (F-17)$$

where  $S_1$  and  $S_2$  are cross-section areas of guides #1 and #2 respectively. Substituting (F-5) and (F-9) into Equation (F-17) will result in:

$$\sum_{k,l}^N V_{kl}^{1,e} \bar{e}_{kl}^{1,e} + \sum_{k,l}^N V_{kl}^{1,h} \bar{e}_{kl}^{1,h} = \sum_{m,n}^M V_{mn}^{2,e} \bar{e}_{mn}^{2,e} + \sum_{m,n}^M V_{kmn}^{2,h} \bar{e}_{mn}^{2,h} \quad \text{on } S_1 \quad (\text{F-18})$$

By multiplying the eigenvector  $\bar{h}_{pq}^{2, mode}$  with both sides of (F-18) and integrating the terms over cross-section  $S_2$  we obtain:

$$\sum_{k,l}^N V_{kl}^{1,e} \mathfrak{R}_{pqkl}^{e, mode} + \sum_{k,l}^N V_{kl}^{1,h} \mathfrak{R}_{pqkl}^{h, mode} = V_{pq}^{2, mode} Q_{pq}^{2, mode} \quad (\text{F-19})$$

where the right-hand side has shrunk to one term because of the orthogonality condition (F-13).  $\mathfrak{R}_{pqkl}^{e, mode}$  and  $\mathfrak{R}_{pqkl}^{h, mode}$  are the integrals of cross-products between the eigenvectors of guides #1 and #2 as follows:

$$\mathfrak{R}_{pqkl}^{e, mode} = \int_{S_1} (\bar{e}_{kl}^{1,e} \times \bar{h}_{pq}^{2, mode}) \cdot \hat{a}_z dS \quad (\text{F-20})$$

$$\mathfrak{R}_{pqkl}^{h, mode} = \int_{S_1} (\bar{e}_{kl}^{1,h} \times \bar{h}_{pq}^{2, mode}) \cdot \hat{a}_z dS \quad (\text{F-21})$$

It should be noted that the above integrals are reduced over the cross-section  $S_1$  as  $\bar{e}_{kl}^{1, mode}$  generally vanishes on the ( $S_2 - S_1$ ) area. This is also clear from the continuity equation (F-16). The terms  $\mathfrak{R}_{pqkl}^{e, mode}$  and  $\mathfrak{R}_{pqkl}^{h, mode}$  are called the *reaction elements* of guide #1 versus guide #2 and are readily determined from (F-20) and (F-21). The superscript *mode* denotes the e- or h-mode of guide #2. For instance the term  $\mathfrak{R}_{pqkl}^{e,h}$  is the reaction element between  $\text{LSM}^y_{kl}$  mode of guide #1 and  $\text{LSE}^y_{pq}$  of guide #2. Using assumption (F-15) the normalised constant in equation (F-19) can be replaced by the wave admittance  $Y_{pq}^{2, mode}$ . This assumption would be necessary in order to facilitate the mode-matching equations. Thus substituting from (F-15) into (F-19) results in:

$$\sum_{k,l}^N V_{kl}^{1,e} \mathfrak{R}_{pqkl}^{e, mode} + \sum_{k,l}^N V_{kl}^{1,h} \mathfrak{R}_{pqkl}^{h, mode} = V_{pq}^{2, mode} Y_{pq}^{2, mode} \quad (\text{F-22})$$

#### F.4.1 First Equation

Equation (F-22) corresponds to one particular mode of guide #2. Therefore by repeating this equation for M possible modes, one can obtain the following matrix equation:

$$[\mathfrak{R}] \cdot [V^{(1)}] = [Y^{(2)}] \cdot [V^{(2)}] \quad (\text{F-23})$$

where

$$[V^{(1)}] = \begin{bmatrix} V_1^{1,e} \\ \vdots \\ V_{N_e}^{1,e} \\ V_{N_e+1}^{1,h} \\ \vdots \\ V_N^{1,h} \end{bmatrix}_{(N \times 1)} = \begin{bmatrix} [V^{(1),e}] \\ [V^{(1),h}] \end{bmatrix} \quad [V^{(2)}] = \begin{bmatrix} V_1^{2,e} \\ \vdots \\ V_{M_e}^{2,e} \\ V_{M_e+1}^{2,h} \\ \vdots \\ V_M^{2,h} \end{bmatrix}_{(M \times 1)} = \begin{bmatrix} [V^{(2),e}] \\ [V^{(2),h}] \end{bmatrix} \quad (\text{F-24})$$

$$[\mathfrak{R}] = \begin{bmatrix} [\mathfrak{R}^{e,e}] & [\mathfrak{R}^{h,e}] \\ [\mathfrak{R}^{e,h}] & [\mathfrak{R}^{h,h}] \end{bmatrix}_{(M \times N)} \quad [Y^{(2)}] = \begin{bmatrix} Y_1^{2,e} & 0 & 0 & 0 & 0 & 0 \\ 0 & \ddots & 0 & 0 & 0 & 0 \\ 0 & 0 & Y_{M_e}^{2,e} & 0 & 0 & 0 \\ 0 & 0 & 0 & Y_{M_e+1}^{2,h} & 0 & 0 \\ 0 & 0 & 0 & 0 & \ddots & 0 \\ 0 & 0 & 0 & 0 & 0 & Y_M^{2,h} \end{bmatrix}_{(M \times M)} \quad (\text{F-25})$$

$N_e$  or  $M_e$  and  $N_h$  or  $M_h$  are the number of LSM and LSE modes in guides #1 and #2 respectively. Hence the total number of modes are given by:

$$N = N_e + N_h \quad M = M_e + M_h \quad (\text{F-26})$$

### F.4.2 Second Equation

Similarly substituting (F-7) and (F-10) into continuity equation (F-17) will result in:

$$\sum_{k,l}^{N,N} I_{kl}^{1,e} \bar{h}_{kl}^{1,e} + \sum_{k,l}^{N,N} I_{kl}^{1,h} \bar{h}_{kl}^{1,h} = \sum_{m,n}^{M,M} I_{mn}^{2,e} \bar{h}_{mn}^{2,e} + \sum_{m,n}^{M,M} I_{kmn}^{2,h} \bar{h}_{mn}^{2,h} \quad \text{on } S_1 \quad (\text{F-27})$$

By multiplying both sides of (F-27) with the eigenvector  $\bar{e}_{pq}^{-1, mode}$  and integrating over the surface  $S_1$  we obtain:

$$\sum_{m,n}^{M,M} I_{mn}^{2,e} \mathfrak{R}_{mnpq}^{e, mode} + \sum_{m,n}^{M,M} I_{mn}^{2,h} \mathfrak{R}_{mnpq}^{h, mode} = I_{pq}^{1, mode} Q_{pq}^{1, mode} \quad (\text{F-28})$$

where the reaction elements  $\mathfrak{R}_{mnpq}^{e, mode}$  and  $\mathfrak{R}_{mnpq}^{h, mode}$  are determined from (F-20) and (F-21) respectively. Also using the assumption of (F-15) we can set the normalisation constant equal to the wave admittance as:

$$\sum_{m,n}^{M,M} I_{mn}^{2,e} \mathfrak{R}_{mnpq}^{e, mode} + \sum_{m,n}^{M,M} I_{mn}^{2,h} \mathfrak{R}_{mnpq}^{h, mode} = I_{pq}^{1, mode} Y_{pq}^{1, mode} \quad (\text{F-29})$$

Similar to (F-22), the above equation corresponds to one particular mode of guide #1. With some manipulation the generalised matrix equation can be obtained as:

$$[\mathfrak{R}]^T \cdot [I^{(2)}] = [Y^{(1)}] \cdot [I^{(1)}] \quad (\text{F-30})$$

where

$$[\mathfrak{R}]^T = \begin{bmatrix} [\mathfrak{R}^{e,e}] & [\mathfrak{R}^{e,h}] \\ [\mathfrak{R}^{h,e}] & [\mathfrak{R}^{h,h}] \end{bmatrix}_{(N \times M)} \quad [Y^{(1)}] = \begin{bmatrix} Y_1^{1,e} & 0 & 0 & 0 & 0 & 0 \\ 0 & 0 & 0 & 0 & 0 & 0 \\ 0 & 0 & Y_{N_e}^{1,e} & 0 & 0 & 0 \\ 0 & 0 & 0 & Y_{N_e+1}^{1,h} & 0 & 0 \\ 0 & 0 & 0 & 0 & 0 & 0 \\ 0 & 0 & 0 & 0 & 0 & Y_N^{1,h} \end{bmatrix}_{(N \times N)} \quad (\text{F-31})$$

$$[I^{(1)}] = \begin{bmatrix} I_1^{1,e} \\ I_{N_e}^{1,e} \\ I_{N_e}^{1,h} \\ \vdots \\ I_N^{1,h} \end{bmatrix}_{(N \times 1)} = \begin{bmatrix} [I^{(1),e}] \\ [I^{(1),h}] \end{bmatrix} \quad [I^{(2)}] = \begin{bmatrix} I_1^{2,e} \\ I_{M_e}^{2,e} \\ I_{M_e+1}^{2,h} \\ \vdots \\ I_M^{2,h} \end{bmatrix}_{(M \times 1)} = \begin{bmatrix} [I^{(2),e}] \\ [I^{(2),h}] \end{bmatrix} \quad (\text{F-32})$$

$[\mathfrak{R}]^T$  is the transpose of  $[\mathfrak{R}]$  and  $[Y^{(1)}]$  is a diagonal matrix of wave admittances of guide #1. The generalised expression (F-30) is the second mode-matching equation.

The reaction matrix  $[\mathfrak{R}]$  and its transpose  $[\mathfrak{R}]^T$  that are present in fundamental equations (F-23) and (F-30) consist of reaction elements that are defined for every pair of eigenvectors  $\bar{e}_{kl}^{1, mode 1}$  and  $\bar{h}_{mn}^{2, mode 2}$  from guides #1 and #2 respectively. From (F-20) and (F-21) one can generally obtain:

$$\mathfrak{R}_{pqkl}^{mode 1, mode 2} = \int_{S_1} (\bar{e}_{kl}^{1, mode 1} \times \bar{h}_{mn}^{2, mode 2}) \cdot \hat{a}_z dS \quad (\text{F-33})$$

where the integration is taken over the cross-section of the smaller waveguide *i.e.*  $S_1$ . From (F-33) four types of reaction elements are defined as set out below:

$$\mathfrak{R}_{mnkl}^{e,e} = \int_{S_1} (\bar{e}_{kl}^{1,e} \times \bar{h}_{mn}^{2,e}) \cdot \hat{a}_z dS \quad (\text{F-34})$$

$$\mathfrak{R}_{mnkl}^{h,e} = \int_{S_1} (\bar{e}_{kl}^{1,e} \times \bar{h}_{mn}^{2,h}) \cdot \hat{a}_z dS \quad (F-35)$$

$$\mathfrak{R}_{mnkl}^{e,h} = \int_{S_1} (\bar{e}_{kl}^{1,h} \times \bar{h}_{mn}^{2,e}) \cdot \hat{a}_z dS \quad (F-36)$$

$$\mathfrak{R}_{mnkl}^{h,h} = \int_{S_1} (\bar{e}_{kl}^{1,h} \times \bar{h}_{mn}^{2,h}) \cdot \hat{a}_z dS \quad (F-37)$$

where the reactions integrals are over the surface  $S_1$  shown in Figure F-1. The reaction elements are calculated once the waveguides and their junctions are specified and the necessary eigenvectors are analytically determined.

## F.5 Generalised Junction Scattering Matrix

The fundamental mode-matching equations (F-23) and (F-30) are not directly related to the transmission and reflection parameters of the junction. Thus further elaboration is needed to restyle these equations into a sensible scattering matrix form. To begin with, we assume that the junction is located at the origin of the z-axis as shown in the ( $A - A'$ ) cross-section of Figure F-2 (b). This will simplify the relations (F-6), (F-8), (F-11) and (F-12) by dropping the exponential terms. Therefore the equivalent mode voltages and currents at the junction are defined by:

$$V_{kl}^{1,mode} = \frac{a_{kl}^{1,mode}}{\sqrt{Y_{kl}^{1,mode}}} + \frac{b_{kl}^{1,mode}}{\sqrt{Y_{kl}^{1,mode}}} \quad (F-38)$$

$$I_{kl}^{1,mode} = \frac{a_{kl}^{1,mode}}{\sqrt{Y_{kl}^{1,mode}}} - \frac{b_{kl}^{1,mode}}{\sqrt{Y_{kl}^{1,mode}}} \quad (F-39)$$

$$V_{mn}^{2,mode} = \frac{a_{mn}^{2,mode}}{\sqrt{Y_{mn}^{2,mode}}} + \frac{b_{mn}^{2,mode}}{\sqrt{Y_{mn}^{2,mode}}} \quad (F-40)$$

$$I_{mn}^{2, mode} = -\frac{a_{mn}^{2, mode}}{\sqrt{Y_{mn}^{2, mode}}} + \frac{b_{mn}^{2, mode}}{\sqrt{Y_{mn}^{2, mode}}} \quad (\text{F-41})$$

Equations (F-38), (F-39), (F-40) and (F-41) may be generalised into matrix form to include all possible modes:

$$[V^{(1)}] = [Y^{(1)}]^{-1/2} \{ [a^{(1)}] + [b^{(1)}] \} \quad (\text{F-42})$$

$$[I^{(1)}] = [Y^{(1)}]^{-1/2} \{ [a^{(1)}] - [b^{(1)}] \} \quad (\text{F-43})$$

$$[V^{(2)}] = [Y^{(2)}]^{-1/2} \{ [a^{(2)}] + [b^{(2)}] \} \quad (\text{F-44})$$

$$[I^{(2)}] = [Y^{(2)}]^{-1/2} \{ [b^{(2)}] - [a^{(2)}] \} \quad (\text{F-45})$$

As  $[Y^{(1)}]$  and  $[Y^{(2)}]$  are diagonal matrices the inverse square root of each is easily obtained by simply replacing each diagonal element with its inverse square root.

Now substituting the voltages and currents from (F-42) to (F-45) into the mode-matching equations (F-23) and (F-30) and noting that<sup>1</sup>:

$$[Y^{(\nu)}][Y^{(\nu)}]^{-1/2} = [Y^{(\nu)}]^{1/2} \quad (\text{F-46})$$

we obtain:

$$[\Re] \cdot [Y^{(1)}]^{-1/2} \{ [a^{(1)}] + [b^{(1)}] \} = [Y^{(2)}]^{1/2} \{ [a^{(2)}] + [b^{(2)}] \} \quad (\text{F-47})$$

$$[\Re]^T \cdot [Y^{(2)}]^{-1/2} \{ [b^{(2)}] - [a^{(2)}] \} = [Y^{(1)}]^{1/2} \{ [a^{(1)}] - [b^{(1)}] \} \quad (\text{F-48})$$

and with minor modification of the above equations we get:

$$[Y^{(2)}]^{-1/2} \cdot [\Re] \cdot [Y^{(1)}]^{-1/2} \{ [a^{(1)}] + [b^{(1)}] \} = \{ [a^{(2)}] + [b^{(2)}] \} \quad (\text{F-49})$$

1. This is valid for diagonal matrices

$$[Y^{(1)}]^{1/2} \cdot [\mathfrak{R}]^T \cdot [Y^{(2)}]^{-1/2} \{[b^{(2)}] - [a^{(2)}]\} = \{[a^{(1)}] - [b^{(1)}]\} \quad (\text{F-50})$$

To simplify the above we can introduce a *normalised wave-amplitude matrix*  $\Psi$  such that:

$$\Psi = [Y^{(2)}]^{-1/2} \cdot [\mathfrak{R}] \cdot [Y^{(1)}]^{-1/2} \quad (M \times N) \quad (\text{F-51})$$

$$\Psi^T = [Y^{(1)}]^{1/2} \cdot [\mathfrak{R}]^T \cdot [Y^{(2)}]^{-1/2} \quad (N \times M) \quad (\text{F-52})$$

Substituting  $\Psi$  and  $\Psi^T$  from (F-51) and (F-52) into (F-49) and (F-50) respectively, with some re-arrangements we finally obtain:

$$[a^{(1)}] + \Psi^T \cdot [a^{(2)}] = [b^{(1)}] + \Psi^T \cdot [b^{(2)}] \quad (\text{F-53})$$

$$\Psi \cdot [a^{(1)}] - [a^{(2)}] = -\Psi \cdot [b^{(1)}] + [b^{(2)}] \quad (\text{F-54})$$

The set of equations (F-53) and (F-54) may be combined into a more sensible matrix form:

$$\begin{bmatrix} U^T & \Psi^T \\ \dots & \dots \\ \Psi & -U \end{bmatrix} \begin{bmatrix} a^{(1)} \\ a^{(2)} \end{bmatrix} = \begin{bmatrix} U^T & \Psi^T \\ \dots & \dots \\ -\Psi & U \end{bmatrix} \begin{bmatrix} b^{(1)} \\ b^{(2)} \end{bmatrix}$$

$(M+N) \times (M+N)$     $(M+N) \times 1$     $(M+N) \times (M+N)$     $(M+N) \times 1$

(F-55)

where  $U$  is a unit matrix with dimension  $(N \times M)$ . Consequently  $U^T$  will be an  $(M \times N)$  matrix. The generalised scattering matrix of the junction is defined as:

$$\begin{bmatrix} b^{(1)} \\ \dots \\ b^{(2)} \end{bmatrix} = \begin{bmatrix} S_{11} & S_{12} \\ \dots & \dots \\ S_{21} & S_{22} \end{bmatrix} \cdot \begin{bmatrix} a^{(1)} \\ a^{(2)} \end{bmatrix}$$

$(M+N) \times 1$     $(M+N) \times (M+N)$     $(M+N) \times 1$

(F-56)

By comparing the equations (F-55) and (F-56) the generalised S-matrix is obtained as:

$$[S] = \begin{bmatrix} S_{11} & S_{12} \\ \cdots & \cdots \\ S_{21} & S_{22} \end{bmatrix}_{(M+N) \times (M+N)} = \begin{bmatrix} U^T & \Psi^T \\ \cdots & \cdots \\ -\Psi & U \end{bmatrix}^{-1} \cdot \begin{bmatrix} U^T & \Psi^T \\ \cdots & \cdots \\ \Psi & -U \end{bmatrix}$$

(F-57)

$S_{11}$  and  $S_{22}$  are  $(N \times N)$  and  $(M \times M)$  matrices that include reflection coefficients of guides #1 and #2 respectively. Similarly  $S_{12}$  and  $S_{21}$  are  $(N \times M)$  and  $(M \times N)$  matrices containing the transmission parameters of the waveguide discontinuity. The formulae and terminology that have been developed in this appendix will be used in Chapter 6 for the mode-matching calculation of the coupling structure. Calculation of the S-matrix for a specified structure from the final matrix equation (F-57) is rigorous but straightforward. Prior to that, the sub-matrices  $\Psi$  and  $\Psi^T$  should be calculated from the reaction and admittance matrices as in (F-51) to (F-52).  $[\Re]$  is attributed to the particular structure and the reaction elements may be determined by analytical or numerical solution of (F-34) to (F-37). With the exception of irregular geometries, analytical integration for simpler structures would be advantageous due to the gross reduction in computation time. Typical calculation for the junction of Figure F-2 is given in the following section. Although it is not the same as the junctions used in the coupling structure, the method of calculation is the same and the expressions will be addressed in Chapter 6.

## F.6 Derivation of Reaction Elements

Consider the junction of Figure F-1 for which the reaction elements have been derived from equations (F-34) to (F-37). The eigenvectors  $\bar{e}_{kl}^{1,e}$ ,  $\bar{e}_{kl}^{1,h}$  and  $\bar{h}_{mn}^{2,e}$ ,  $\bar{h}_{mn}^{2,h}$  are obtained from Appendix B as follows:

$$\bar{e}_{kl}^{1,e} = A_{kl}^{1,e} [-e_x^{1,e} \hat{a}_x + e_y^{1,e} \hat{a}_y] \quad (F-58)$$

$$\bar{e}_{kl}^{1,h} = A_{kl}^{1,h} e_x^{1,h} \hat{a}_x \quad (F-59)$$

$$\bar{h}_{mn}^{2,e} = A_{mn}^{2,e} Y_{mn}^{2,e} h_x^{2,e} \hat{a}_x \quad (\text{F-60})$$

$$\bar{h}_{mn}^{2,h} = A_{mn}^{2,h} Y_{mn}^{2,h} [-h_x^{2,h} \hat{a}_x + h_y^{2,h} \hat{a}_y] \quad (\text{F-61})$$

where  $A_{kl}^{1, mode}$  and  $A_{mn}^{2, mode}$  are normalised amplitudes and are obtained by minor modification of (B-35) and (B-64) to become:

$$A_{kl}^{1, mode} = \left( \frac{2\epsilon_{0k}}{a_1 b_1} \right)^{1/2} \quad (\text{F-62})$$

$$A_{mn}^{2, mode} = \left( \frac{2\epsilon_{0m}}{a_2 b_2} \right)^{1/2} \quad (\text{F-63})$$

The eigenfunctions are defined by:

$$e_x^{1,e} = \frac{\beta_l \alpha_k}{k_0^2 - \beta_l^2} \cos(\alpha_k x) \sin \beta_l y \quad (\text{F-64})$$

$$e_y^{1,e} = \sin(\alpha_k x) \cos \beta_l y \quad (\text{F-65})$$

$$e_x^{1,h} = \cos(\alpha_k x) \sin \beta_l y \quad (\text{F-66})$$

$$h_x^{2,e} = \sin(\alpha_m x) \cos \beta_n y \quad (\text{F-67})$$

$$h_x^{2,h} = \frac{\beta_n \alpha_m}{k_0^2 - \beta_n^2} \sin(\alpha_m x) \cos \beta_n y \quad (\text{F-68})$$

$$h_y^{2,h} = \cos(\alpha_m x) \sin \beta_n y \quad (\text{F-69})$$

where the eigenvalues for the dielectric-filled waveguide are simply given as:

$$\alpha_k = \frac{k\pi}{a_1}, \quad \alpha_m = \frac{m\pi}{a_2} \quad (\text{F-70})$$

$$\beta_l = \frac{l\pi}{b_1}, \quad \beta_n = \frac{n\pi}{b_2} \quad (\text{F-71})$$

Substituting (F-58) to (F-61) into the integral relations (F-34) to (F-37) results in:

$$\Re_{mnkl}^{e,e} = A_{kl}^{1,e} A_{mn}^{2,e} Y_{mn}^{2,e} \int_{S_1} (e_y^{1,e} h_x^{2,e}) dS = A_{kl}^{1,e} A_{mn}^{2,e} Y_{mn}^{2,e} J_x J_y \quad (\text{F-72})$$

$$\begin{aligned} \Re_{mnkl}^{h,e} &= A_{kl}^{1,e} A_{mn}^{2,h} Y_{mn}^{2,h} \int_{S_1} (-e_x^{1,e} h_y^{2,h} + e_y^{1,e} h_x^{2,h}) dS \\ &= A_{kl}^{1,e} A_{mn}^{2,h} Y_{mn}^{2,h} \left[ \frac{-\alpha_k \beta_l}{k_0^2 - \beta_l^2} I_x I_y + \frac{\alpha_m \beta_n}{k_0^2 - \beta_n^2} J_x J_y \right] \end{aligned} \quad (\text{F-73})$$

$$\Re_{mnkl}^{e,h} = \int_{S_1} (\bar{e}_{kl}^{1,h} \times \bar{h}_{mn}^{2,e}) dS = 0 \quad (\text{F-74})$$

$$\Re_{mnkl}^{h,h} = A_{kl}^{1,h} A_{mn}^{2,h} Y_{mn}^{2,h} \int_{S_1} (e_x^{1,h} h_y^{2,h}) dS = A_{kl}^{1,h} A_{mn}^{2,h} Y_{mn}^{2,h} I_x I_y \quad (\text{F-75})$$

where  $I_x$ ,  $I_y$ ,  $J_x$  and  $J_y$  are linear integrals over the double-step junction shown on cross-section ( $B - B'$ ) in Figure F-2 (b) and are given by the following:

$$I_x = \int_0^{a_1} \cos(\alpha_k x') \cdot \cos(\alpha_m x) dx' = \int_0^{a_1} \cos(\alpha_k x') \cdot \cos \alpha_m(x' + a_0) dx' \quad (\text{F-76})$$

$$I_y = \int_0^{b_1} \sin(\beta_l y') \cdot \cos(\beta_n y) dy' = \int_0^{b_1} \sin(\beta_l y') \cdot \cos \beta_n(y' + b_0) dy' \quad (\text{F-77})$$

$$J_x = \int_0^{a_1} \sin(\alpha_k x') \cdot \sin(\alpha_m x) dx' = \int_0^{a_1} \sin(\alpha_k x') \cdot \sin \alpha_m(x' + a_0) dx' \quad (\text{F-78})$$

$$J_y = \int_0^{b_1} \cos(\beta_l y') \cdot \cos(\beta_n y) dy' = \int_0^{b_1} \cos(\beta_l y') \cdot \cos \beta_n(y' + b_0) dy' \quad (\text{F-79})$$

These integrals may be determined either numerically or analytically. Due to their simplicity it is much easier to derive their analytic solution that offers the advantage of expediting calculations and considerably reducing computation time.

---

## Appendix G

# A Graphically Oriented Automation of Microstrip FET Amplifier and Oscillator Design

ALI A. SAYYAH AND DONALD W. GRIFFIN

*Indexing terms: Amplifiers, Oscillators, Field-effect transistors*

### Abstract

The clarity and reliability of classical microwave s-parameter design procedures have been exploited in a new simulation program which has been developed for the design of microstrip amplifier and oscillator circuits. This mini software is equipped with graphical tools that enable the designer to, (a) visualise the device stability criteria and the design constraints on an automated Smith chart, (b) extract the load and source impedances of his own choice from the Smith chart as the best starting point for the optimisation routine and, (c) check the result by monitoring the optimisation trace. The program is interactive, microstrip-oriented and well suited for educational purposes. Typical amplifier and oscillator circuits have been built based on this program using NE-72084 NEC and ATF-13036 Hewlett-Packard GaAs FET transistors. Test results have shown excellent agreement with this theoretical design procedure.

## 1 Introduction

Computer aided design (CAD) programs for hybrid and monolithic microwave integrated circuits need to be precise design tools because it is not possible to alter or adjust such circuits once they have been fabricated [1,2]. Precision in design is dependent primarily on the accuracy with which the microwave passive and active components are represented by analytical models that are the basis of the CAD programs. Many such programs have been developed extending from low-cost compact routines [3,4] to expensive, complex multi-purpose microwave circuit analysis software packages [5,6].

The structure of a CAD program for microwave design should include models for all components, analytical procedures and optimisation routines [7]. A diagram illustrating the basic functions of a CAD program for microwave integrated circuits is depicted in Figure 1. Modelling involves the characterisation of active and passive circuit components so that each part of the circuit can be represented in numerical or computer recognisable terms. Passive components such as transmission lines, couplers, attenuators, etc. may be represented adequately by open circuit impedance ( $Z$ ), short circuit admittance ( $Y$ ), scattering ( $S$ ) or ABCD parameters [8,9]. Active devices such as transistors may be represented by scattering matrix elements measured at frequencies within the design range or by an equivalent circuit extracted from those measurements [10]. Because they are nonlinear devices that have a critical effect on performance, different models have to be used depending on whether small or large-signal design is involved. Once the model for the assembly has been determined, the initial values of all of the parameters must be specified either by choice or estimation based on experience. Analysis is the next important stage and provides computed response to initial inputs. Optimisation is the dynamic stage of the program and involves the processes of checking the result and iteratively modifying the circuit parameters until the required design specification is satisfied.

Usually, there is no unique solution to a given design problem, particularly in amplifier or oscillator cases. The CAD result is always affected by three factors: design complexity, the optimisation algorithm selected and initial choices. Design complexity arises from the nature of the CAD program. Some programs are  $Z$ -oriented, that is, the result is simply expressed in terms of input and output impedances. There are more complex programs which are stripline or microstrip-oriented. These programs directly determine the optimised microstrip circuit dimensions. The optimisation program generally determines the design trajectory and should be chosen carefully, in accordance with the design complexity and the particular application. A number of optimisation routines are available in

the literature [11,12]. Finally, the initial choice of the circuit parameters which determines the CAD starting point, should be considered. In simple programs, the initial choices may be easily defined by the designer. However, in a microstrip-oriented amplifier and oscillator design program, where the circuit parameters are mainly physical dimensions, initial choices are often guesses based on experience. In this article, an automation program for the design of FET amplifiers and oscillators is described and the matter of initial choices has been solved by providing a graphical representation of the design constraints, superimposed on a Smith chart [13]. Therefore the designer can visually extract the proper source and load impedances directly from the Smith chart. From these values the CAD program automatically derives appropriate dimensions for microstrip matching sections which in turn are treated as the initial optimisation variables.

## 2 Program Structure

The design automation has been developed on a UNIX<sup>1</sup> workstation, using the MATLAB<sup>2</sup> mathematical software [14]. The primary aim has been to develop an interactive and user-friendly program for the design of MESFET amplifiers and oscillators. Figure 2 shows the block diagram of this program. The major functions that it performs in producing an optimised design are as follows

### 2.1 Design Information

At the beginning of the execution, the design information is entered by the designer. It consists of: (i) the circuit type,i.e., amplifier or oscillator, (ii) design specifications such as frequency, bandwidth, gain, noise figure etc., (iii) the MESFET configuration such as common-source, common-gate, etc. A subprogram will convert the common-source S-parameters to other configurations [15]. Then the topology of the matching sections is selected by the designer. Also the program provides an optional series feedback in the circuit. The feedback element is a length of microstrip-line connected in series with the common electrode of the MESFET. In this option, the designer is required to choose the length and the characteristic impedance of the feedback microstrip-line. This series feedback is then combined with the S-parameters of the MESFET to produce modified S-parameters. Series feedback if applied appropriately [16], can yield an equivalent transistor that in turn yields desirable overall circuit characteristics. In amplifier design, for example, an expansion of the stability areas may occur, and in oscillators, an increase in the device negative resistance may result.

---

1. UNIX is a trademark of Bell Laboratories and denotes a standard operating system for use on computer networks.

2. MATLAB is a trademark of Math Work, Inc.

## *2.2 Initialization*

After the circuit topology and the design objectives have been clarified there comes the choice of the initial values for starting the optimisation process. At this stage, the design constraints such as gain and noise figure circles as well as the device stability circles are depicted on an automated Smith chart. The analytical formulae are available in the literature [9,15 & 17]. The designer can now specify suitable source( $Z_S$ ) and load ( $Z_L$ ) impedance values, directly from the Smith chart. These are the  $Z_S$  and  $Z_L$  values that are to appear at the device ports. The program offers three options, namely, 1) starting from the centre of the Smith chart, i.e.  $Z_S = Z_L = 1$ . 2) starting from the last minimum point of the previous design iteration, or (3) as follows. In this last option the designer should extract the initial source and load impedances from the Smith chart. Once the initial  $Z_S$  and  $Z_L$  are determined, they are used in a specific program to synthesise appropriate matching sections. For this purpose the actual initial values for the length and characteristic impedance  $Z_C$  of each synthesised matching section would be used as initial values for optimisation.

## *2.3 Optimisation*

Various optimisation routines may be used in the program such as: direct search, gradient-descent and random techniques. Both direct search<sup>1</sup> and gradient-descent<sup>2</sup> routines have been used in this software [11,12]. Each technique has its own advantage. The gradient techniques appear to be better for finding the global minimum, however they appear to be much slower than direct search techniques, particularly in the case of microstrip oriented design with non-trivial objective functions. As mentioned above, the optimisation variables are the transmission-line parameters of the circuit matching sections, namely: length and  $Z_C$ . Therefore the total number of variables depends on the topological complexity of the matching sections. When the optimisation process comes to an end, the final impedances appear on the Smith chart and the physical dimensions of microstrip sections are also displayed on the screen. In amplifier design, the program may be executed to achieve maximum available gain. In this case the final  $Z_S$  and  $Z_L$  would be close to conjugate match values at the device ports and it is a matter of visual checking to determine whether they are within their stability regions or not, and optimisation may be restarted if needed. Thus, further graphical manipulations

---

1. Hooke and Jeeves optimisation algorithm.

2. Fletcher and Powell optimisation technique.

such as matching circles for seeking unconditional stability of conjugate-matched amplifiers would be unnecessary [20]. Such a conjugate-matched condition is not feasible if noise figure is to be optimised too [9].

### 3 Design Examples

#### 3.1 Amplifier Design

A low noise amplifier has been designed based on this novel program, using the NE-72084 NEC MESFET transistor and the layout shown in Figure 3. The program messages and the design specifications are shown below:

<p>DESIGN SPECIFICATIONS</p> <p>ENTER THE FREQUENCY RANGE AS FOLLOWS:</p> <p>MAXIMUM FREQUENCY (GHZ) = 3.15 MINIMUM FREQUENCY (GHZ) = 2.85 REQUIRED GAIN (dB) : 10 REQUIRED NOISE FIGURE (dB) : 1.5</p>	<p>MATCHING NETWORK SPECIFICATIONS</p> <table><tr><td>kind of matching section</td><td>code</td></tr><tr><td>transmission line section</td><td>TL</td></tr><tr><td>short circuited shunt stub</td><td>SS</td></tr><tr><td>open circuited shunt stub</td><td>OS</td></tr></table> <p>ENTER INPUT MATCHING SECTIONS (2 SEC.) :</p> <p>INPUT SECTION 1 :os INPUT SECTION 2 :tl</p> <p>ENTER OUTPUT MATCHING SECTIONS (2 SEC.) :</p> <p>OUTPUT SECTION 1 :tl OUTPUT SECTION 2 :os</p>	kind of matching section	code	transmission line section	TL	short circuited shunt stub	SS	open circuited shunt stub	OS
kind of matching section	code								
transmission line section	TL								
short circuited shunt stub	SS								
open circuited shunt stub	OS								

The initial values are selected on the graphical display shown in Figure 4. The selected  $Z_S$  and  $Z_L$  values are inserted following the relevant messages

```

Do you want to initialize from origin ? Y/N n
Starting from the last minimum point ? Y/N n
ENTER INITIAL SOURCE IMPEDANCE FROM SMITH CHART:
[ R + J * X ] 0,7+j*2.0
ENTER INITIAL LOAD IMPEDANCE FROM SMITH CHART:
[ R + J * X ] 0,1+j*0.1

```

From Figure 4. the stability circles are drawn for 2, 3 and 4 GHz.  $Z_S$  is chosen close to the noise circle (shown by [\*\*]), whereas  $Z_L$  may be chosen anywhere within the gain circle (marked++) but outside of the load stability circles (marked —•—•). Optimisation yields the following matching section dimensions and amplifier gain and noise figure performance predictions.

Final variables are			
$L_{s1}$ =	21.037 mm	$L_{o1}$ =	9.954 mm
$Z_{s1}$ =	56.445 ohm	$Z_{o1}$ =	79.2383 ohm
$L_{s2}$ =	4.605 mm	$L_{o2}$ =	30.665 mm
$Z_{s2}$ =	137.6367 ohm	$Z_{o2}$ =	120.2148 ohm

Frequency (GHz)	Gain (dB)	Noise fig. (dB)
2.85	9.98	1.38
3.00	9.98	1.38
3.15	10.05	1.98

### 3.2 Oscillator Design

A 3 GHz microstrip MESFET oscillator using the same NEC transistor has been designed using the same program in the following way. From the stability circles shown in Figure 4 it is clear that at 3 GHz, a large portion of the Smith chart lies in the region where stable amplifier operation may result. By applying suitable series feedback, it should be possible to change the stability region. Figure 5 shows the design messages plus the new stability criterion which can be monitored by the designer, when series feedback is introduced. The new stability circles at 3 GHz are shown in Figure 5. Although the circles have shrunk, note that  $|S_{11}|$  and  $|S_{22}|$  are both greater than one. Thus the whole of the Smith chart outside the stability circles forms an unstable region. Therefore the easiest initial

choice would be the centre of the chart, namely:  $Z_S = Z_L = 1$ . The physical effect of the series feedback that has been introduced is the creation of significant negative resistance at both ports of the combined MESFET and series feedback stub. Oscillations will occur and build up in amplitude until saturation effects in the MESFET make the negative resistance associated with the active part of the circuit equal to the passive resistance presented by the load at the drain port. The matching sections have been chosen intentionally as simple microstrip-lines with fixed width, say, 1.0 mm. Therefore, only the lengths of the lines are optimisation variables. The final result is shown below:

```

Final variables are:
Ls1 = 137.5898  degree   Lo1 = 82.1947  degree
Zs1 = 91.3822  ohm       Zo1 = 91.3822  ohm

Minimum error function:
Fmin = 0.2922

          Zdevice           ZLoad
      -8.7534 - 0.5506i    3.1993 + 0.5507i
  
```

$L_{s1}$  and  $L_{o1}$  are the optimised electrical lengths of the input and output microstrip-lines. The characteristic impedances of the input and output lines,  $Z_{s1}$  and  $Z_{o1}$  respectively, were assumed equal in this particular design. The optimised negative resistance at the output of the device is 8.7534 ohm which is more than twice the resistance of the terminated output matching section. Figure 6 shows optimisation iterations that are monitored on the Smith chart.

$Z_S$  traces along the perimeter of the chart because it is the input impedance of an open circuit terminated length of microstrip line. The trace of  $Z_d$ , the device output impedance extends to the negative resistance region outside the perimeter shown. The circuit layout shown in Figure 7, has been fabricated on a fiber-glass substrate with  $\epsilon_r = 4.0$  and thickness,  $h = 1.59\text{mm}$ . The input matching section is also open circuit terminated and the output is terminated as specified above.

Most of the calculations occur during the execution of the objective function which is a linear analysis subroutine and its algorithm for oscillator design is based on a negative resistance approach using small-signal s-parameters of the device as mentioned above. This technique usually gives the oscillation

tor frequency with good accuracy (< 5%). However the exact value of the oscillator frequency is determined by the large-signal behaviour of the transistor which is dependent, in turn, on the nonlinear characteristics of the device and the biasing conditions [18]. The program is composed of various subprograms which run in MATLAB and it can accommodate a large-signal design function. Such a function which is based on the MESFET large-signal equivalent circuit and can be included in the main program is currently under development.

## 4 Experimental Results

### 4.1 Amplifier Measurement

Figure 3 shows the layout of a low noise amplifier (LNA) designed using the automated procedure described above. The MESFET is a type NE - 72084 and the circuit has been fabricated on a fibre-glass substrate as used for oscillator layout shown in Figure 7. The size of the matching sections are derived as described in section III-A. A swept frequency measurement has indicated a nearly constant amplifier gain of 10.4 dB over the frequency range 2.7 - 3.4 GHz. Further measurements have been carried out that include and extend beyond the LNA specifications. Figure 8 shows a plot of amplifier gain and power added efficiency versus input power. The maximum amplifier output power is 14.5 dBm as shown on the diagram. This figure of merit will be referred to again later, when analysing the oscillator output. When the input level reaches 9.5 dBm, the amplifier gain begins to decline rapidly. The MESFET is thus, already at the onset of breakdown. At the 9.8 dBm input level, the breakdown is complete and both the output power and gain fall to low values as shown clearly in Figure 8.

### 4.2 Oscillator Measurement

For the MESFET oscillator designed on the basis of the procedure described in section III-B, and built-up as shown in Figure 7 an output spectral measurement is shown in Figure 9. This spectrum is for the same bias point as that used in measurement of the small-signal s-parameters. The measured oscillator frequency (2.92 GHz) is 2.6 percent lower than the design value (3.00 GHz) which is an excellent result for the automated design procedure based as it is on small signal assumptions. An output power of about 10 mW is obtained at 2.92 GHz. The second and third harmonic frequencies are also present in the output. However in this simple circuit, being about 20 dB below the fundamental power level, they will be insufficient to cause distortion in the output waveform.

It should be noted that the exact steady-state oscillator frequency is dominated by the large-signal components of the MESFET equivalent circuit which are nonlinear and bias-dependent. Therefore the oscillation frequency is not predicted by the small-signal s-parameters in the current negative resistance objective function. This can be remedied by replacing the currently installed small-signal function with a large-signal objective function which is able to handle the device large-signal equivalent circuit. The algorithm of such a large signal objective function is currently under development and the device large-signal equivalent circuit has been developed using specialised software [19].

Recalling from Figure 8 the maximum power capability of the NE-72084 MESFET is determined from the measurement of power added efficiency of the amplifier with the same device. From Figure 9, the measured oscillator power is 10 dBm some 4.5 dB less than the maximum output power as an amplifier as shown in Figure 8.

However maximum power output can be obtained from the MESFET oscillator by changing the bias point. Figure 10 shows the oscillator output spectrum when operated for maximum fundamental power output. The oscillator output is 13.8 dBm which is only 0.7 dB less than the maximum power output of Figure 8. The oscillation frequency has changed slightly at the new bias point to 2.9012 GHz. This shift in oscillation frequency is not unexpected, because there exists no high quality factor tuned-circuit at either the input or the output of the MESFET, in the design of Figure 7.

The increased level of the harmonic components in Figure 10 stems from the nonlinear behaviour of the MESFET at the new bias point. The peaks of the large-signal output bring the device into strong saturation, which causes the output waveform to be distorted. Such a distortion may be easily deduced from the spectrum of Figure 10.

## 5 Conclusion

A design automation for microstrip MESFET amplifier and oscillator circuits has been presented with special focus on the new graphical tool for guiding the designer to accurately determine the optimisation starting points and monitor the final result on the automated Smith chart. Representative amplifier and oscillator designs have been devised, fabricated and tested. The experimental results are in excellent agreement with theory.

## 6 References

- 1 Perlman B.S. and Gelnovatch V.G.: 'Computer Aided Design, Simulation and optimisation', in *Advances in Microwaves*, Young L. and Sobol H., Eds., vol. 8, New York: Academic Press, 1974.
- 2 White J.F.: Semiconductor Control, Dedham, Mass.: Artech House, 1977, see Ch. 6 on 'Mathematical Techniques and Computer Aided Design', pp. 177-243.
- 3 Staloff M.: 'Computer-Aided Design and Analysis of Microwave Transistor Amplifiers', *Microwave Journal*, May 1987, pp. 253-268.
- 4 Maas S.A. and Nichols A.: 'C/NL 2.0 for Windows, Linear and Nonlinear Microwave Circuit Analysis and Optimisation', Artech House Inc., Mass., 1994.
- 5 Super-Compact & CADEC, Communications Consulting Corp., 483 McLean Blvd., Paterson, NJ 07540.
- 6 Touchstone, EEsوف, 31194 La Baya Drive, Westlake Village, CA 91362.
- 7 Gupta K.C., Garg R. and Chadha R.: 'Computer Aided Design of Microwave Circuits', ch. 1, Artech House Inc., Mass., 1981.
- 8 Collin R.E.: "Foundations for Microwave Engineering", ch. 3, McGraw-Hill, N.Y., 1992.
- 9 Gonzales G.: 'Microwave Transistor Amplifiers Analysis and Design', Prentice-Hall, Inc., Englewood Cliffs, NJ, 1984.
- 10 Golio J.M.: 'Microwave MESFETs and HEMTs', ch. 4., Artech House Inc., Mass., 1991.
- 11 Kuester J.L. and Mize J.H., 'Optimization Techniques with Fortran', McGraw-hill, N.Y., 1973.
- 12 Gupta K.C., Garg R. and Chadha R.: 'Computer Aided Design of Microwave Circuits', ch. 16-18, Artech House Inc., Mass., 1981.
- 13 LaPlante P. and Borja J.: 'An Automated Smith Charting Tool', *Microwave Journal*, May 1987, pp. 373-378.
- 14 The Math Works, Inc., Cochichuate Place, 24 Prime Way, Natick, Mass. 01760.
- 15 Collin R.E.: 'Foundations for Microwave Engineering', ch. 12, pp. 843-849, McGraw-Hill, N.Y., 1992.
- 16 Palladino G.J.: 'Two-Port Parameter Analysis Produces Negative Resistance', *Microwave Journal*, April 1991, pp.106-113.
- 17 Vendelin G.D.: 'Microwave Circuit Design using Linear and Nonlinear Techniques', John Wiley, N.Y., 1990.
- 18 Maas S.A.: 'Nonlinear Microwave Circuits', ch. 12, Artech House Inc., Mass., 1988.

- 19 Golio J.M.: 'GASMAP, Gallium Arsenide Model Analysis Software', Artech House Inc., Mass., 1991.
- 20 Liu J.-C., Bor S.-S., Chang C.-C. and Lu P.-C.: 'Modified Determinations of Stability Criteria for Accurate Designing the Linear Two-Port Amplifiers', *IEE Proc.-Microw. Antenna Propag.*, vol. 141, no. 3, June 1994, pp. 238-240.

## List of Figures

- Figure 1. Simplified block diagram of a CAD program showing the fundamental stages.
- Figure 2. Block diagram of the design automation. The interactive sections are shown in the dashed-line.
- Figure 3. Layout of the 3 GHz low noise MESFET amplifier based on the design procedure of section III-A.
- Figure 4. Visual extraction of initial values from the automated Smith chart.
- Figure 5. The effect of series feedback on the NE-72084 MESFET stability criterion.
- Figure 6. Graphical display of the trajectory of the source, load and device impedance during the optimisation.
- Figure 7. The design layout of the 3 GHz MESFET oscillator with series feedback on fiber-glass substrate.
- Figure 8. The plot of amplifier gain and power added efficiency vs. the input signal power.
- Figure 9. Output spectrum of the MESFET oscillator. The same values of drain and gate bias as those used in measuring the S-parameters apply to these results.
- Figure 10. Output spectrum of the MESFET oscillator at maximum power output.

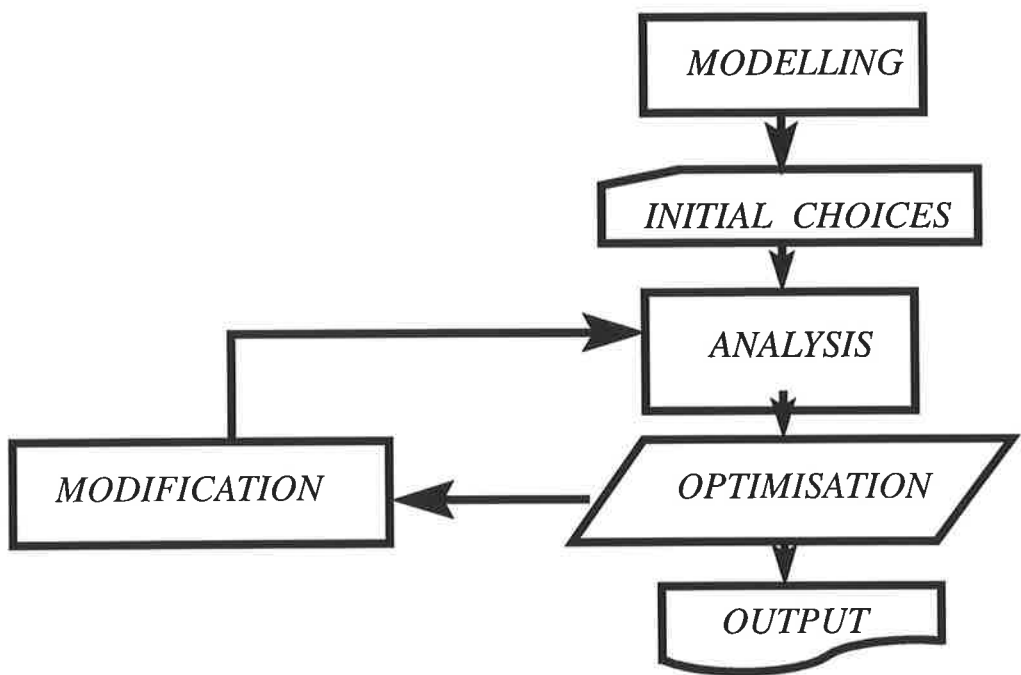


Figure (1)

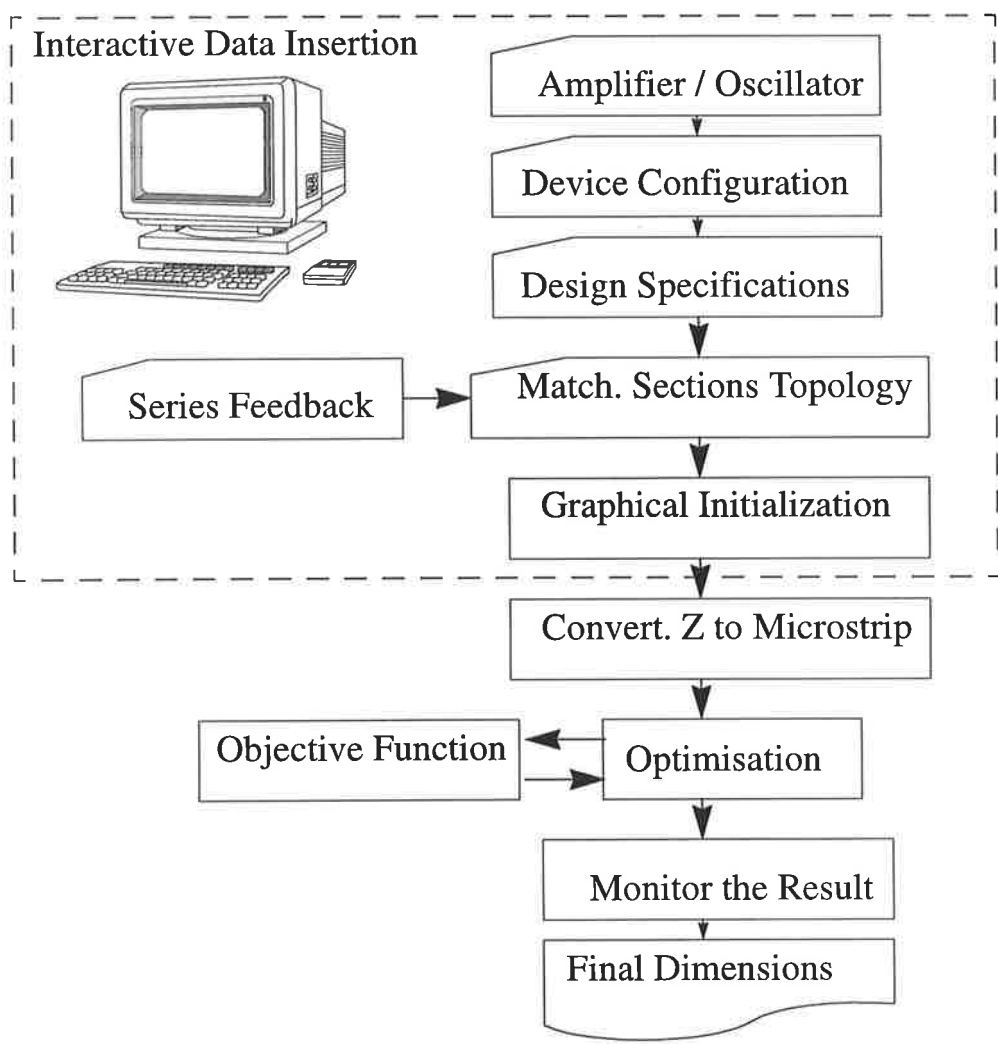


Figure (2)

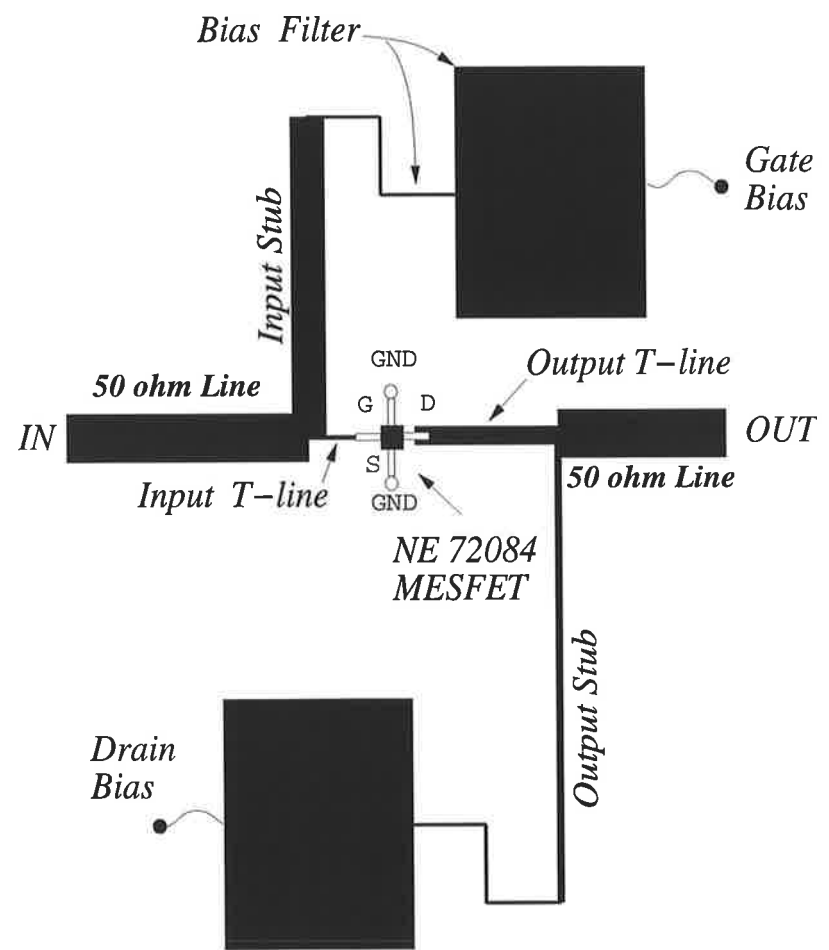


Figure (3)

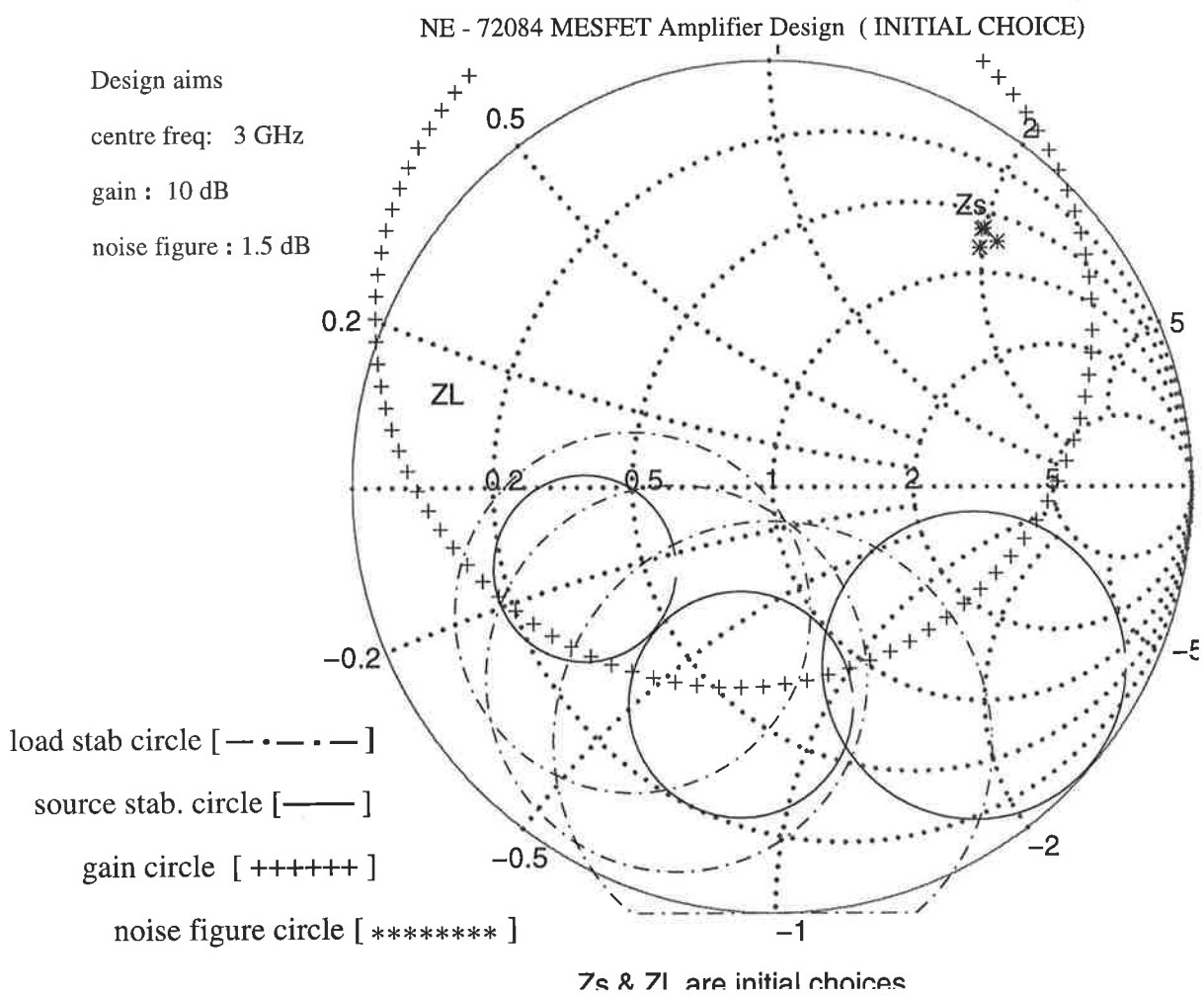


Figure (4)

NE-72084 MESFET Oscillator with Series Feedback (INITIAL CHOICE)

Design aim

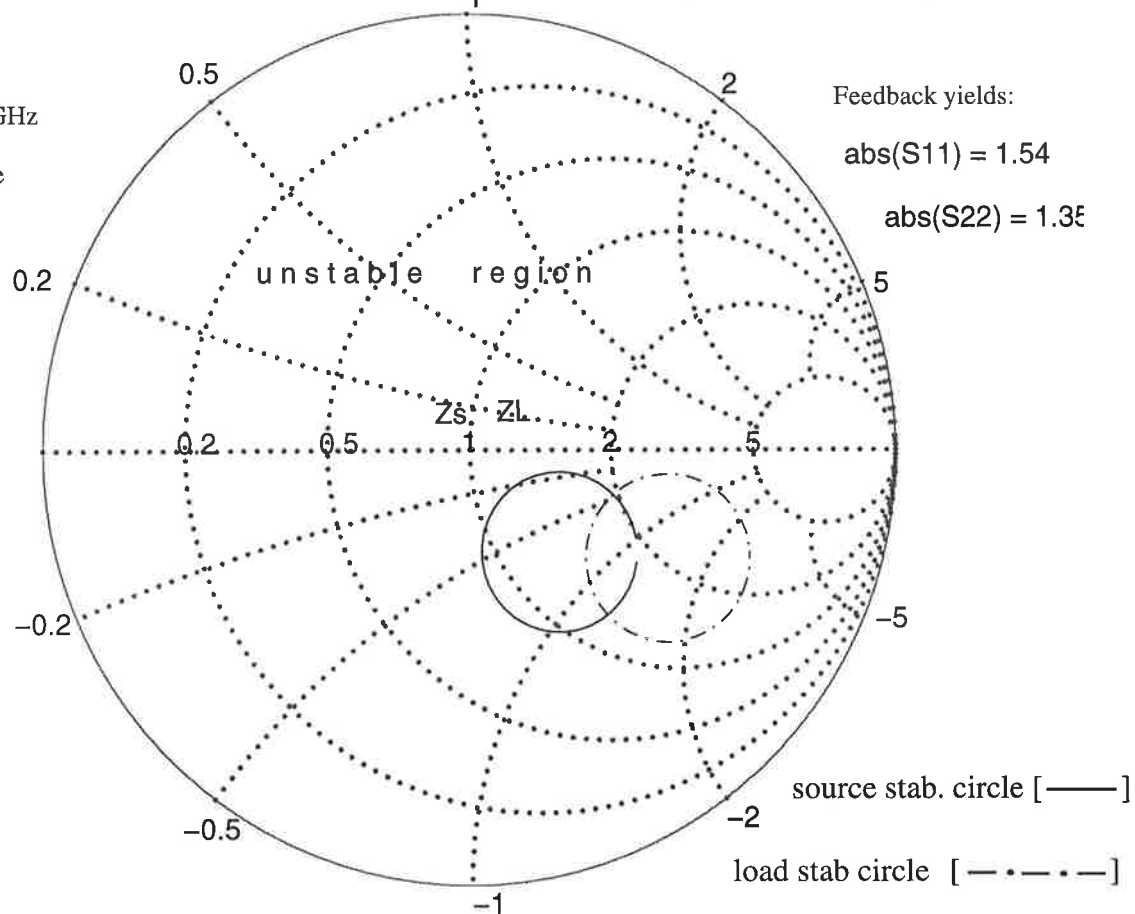
osc. freq = 3 GHz

50 ohm source

Feedback yields:

$$\text{abs}(S_{11}) = 1.54$$

$$\text{abs}(S_{22}) = 1.35$$



$Z_s$  &  $Z_L$  are initial choices

Do you want to initialize from origin ? Y/N      y

Figure (5)

Optimisation Iterations (RESULT MONITOR)

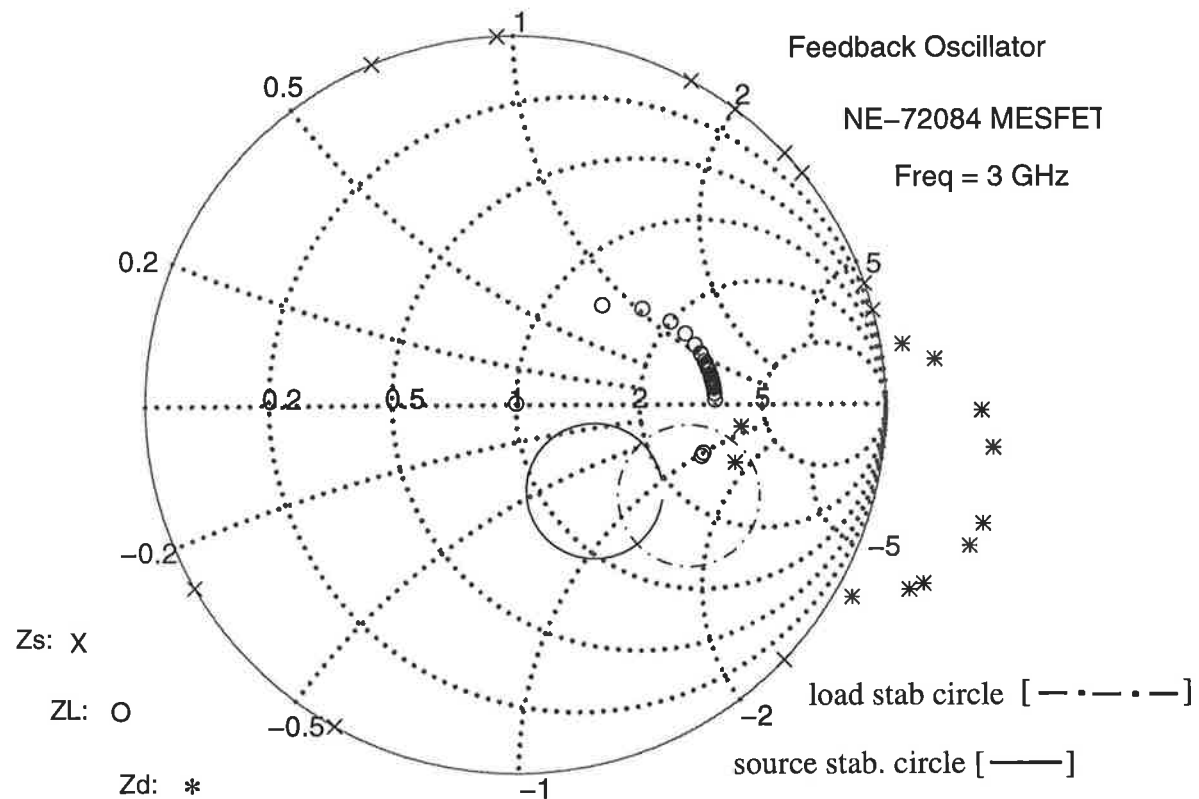


Figure (6)

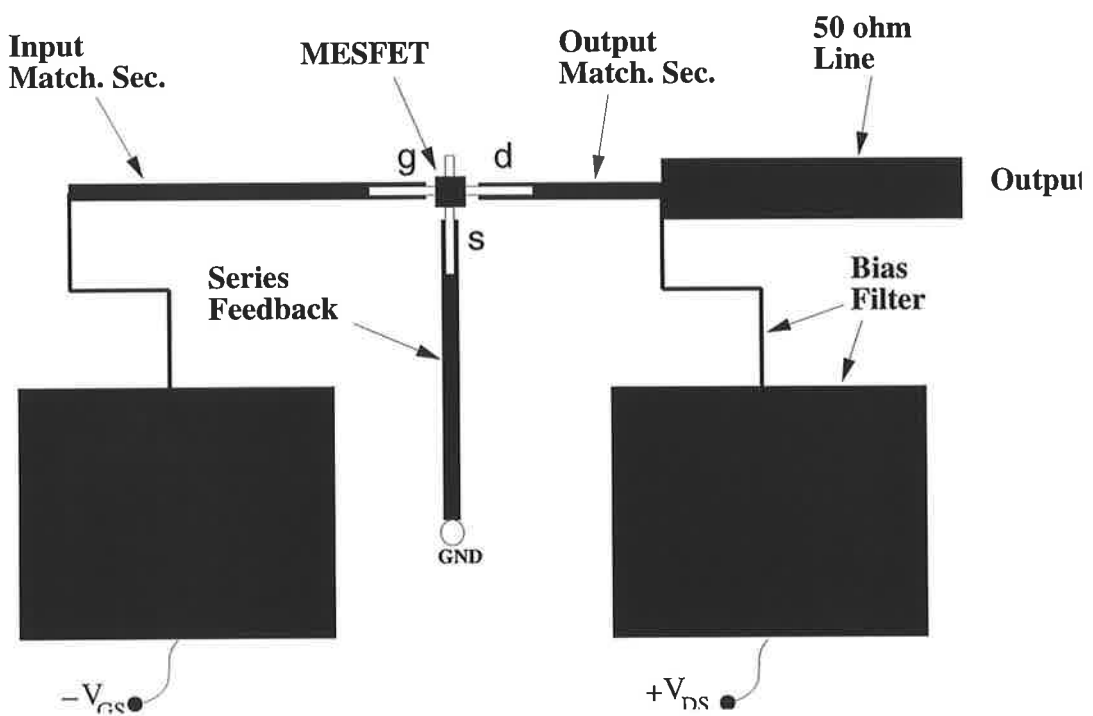


Figure (7)

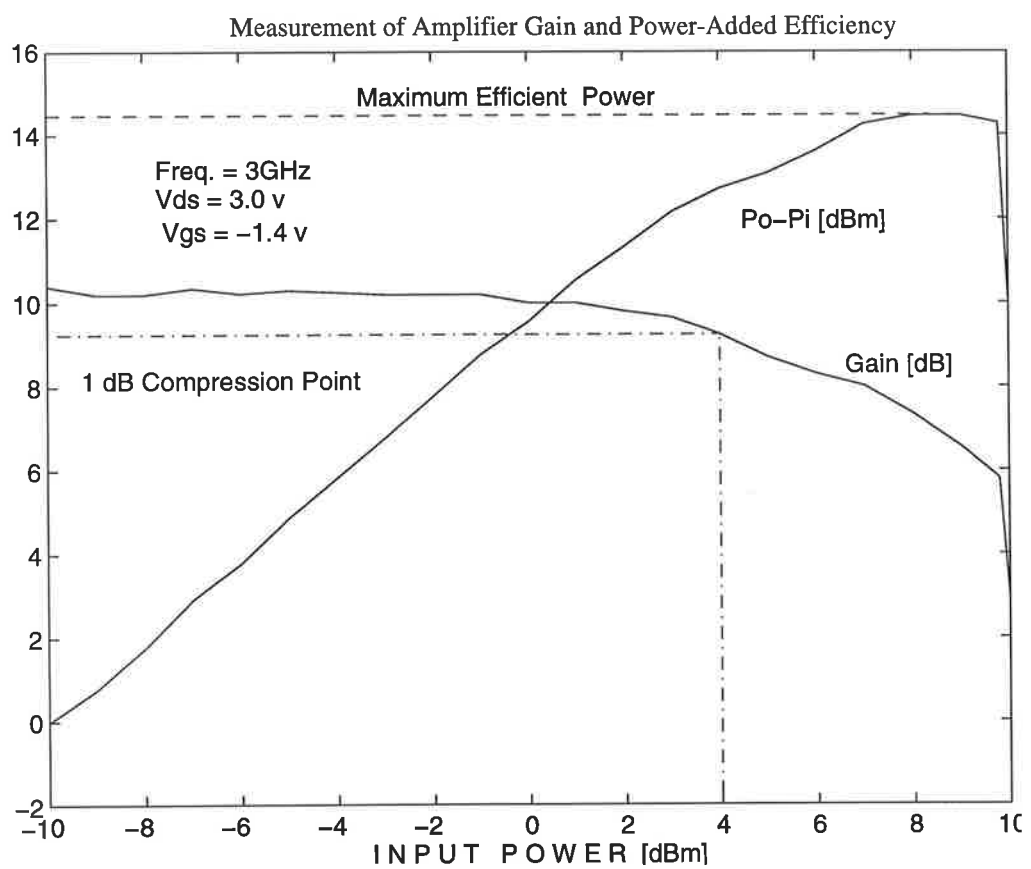


Figure (8)

Spectral Measurement of MESFET Oscillator with Series Feedback

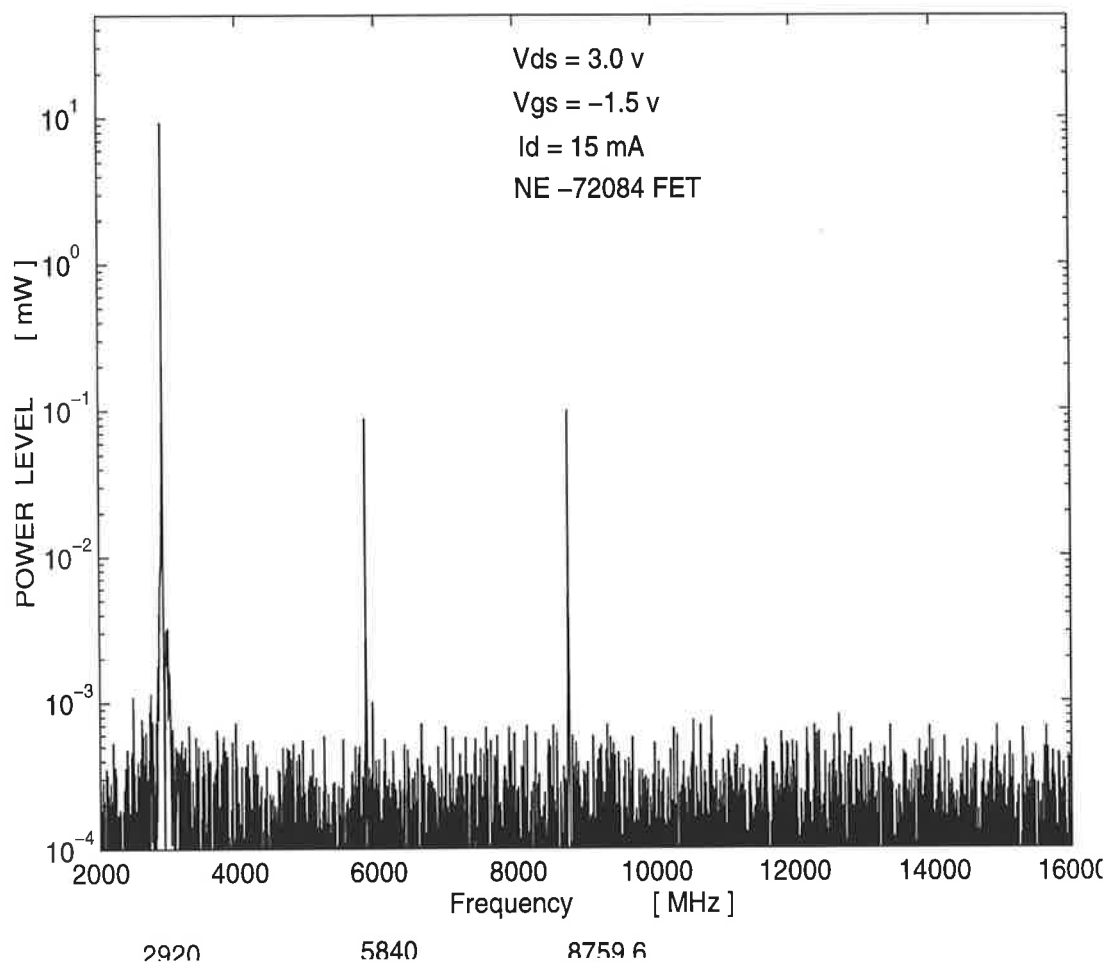


Figure (9)

Spectral Measurement of MESFET Oscillator with Series Feedback

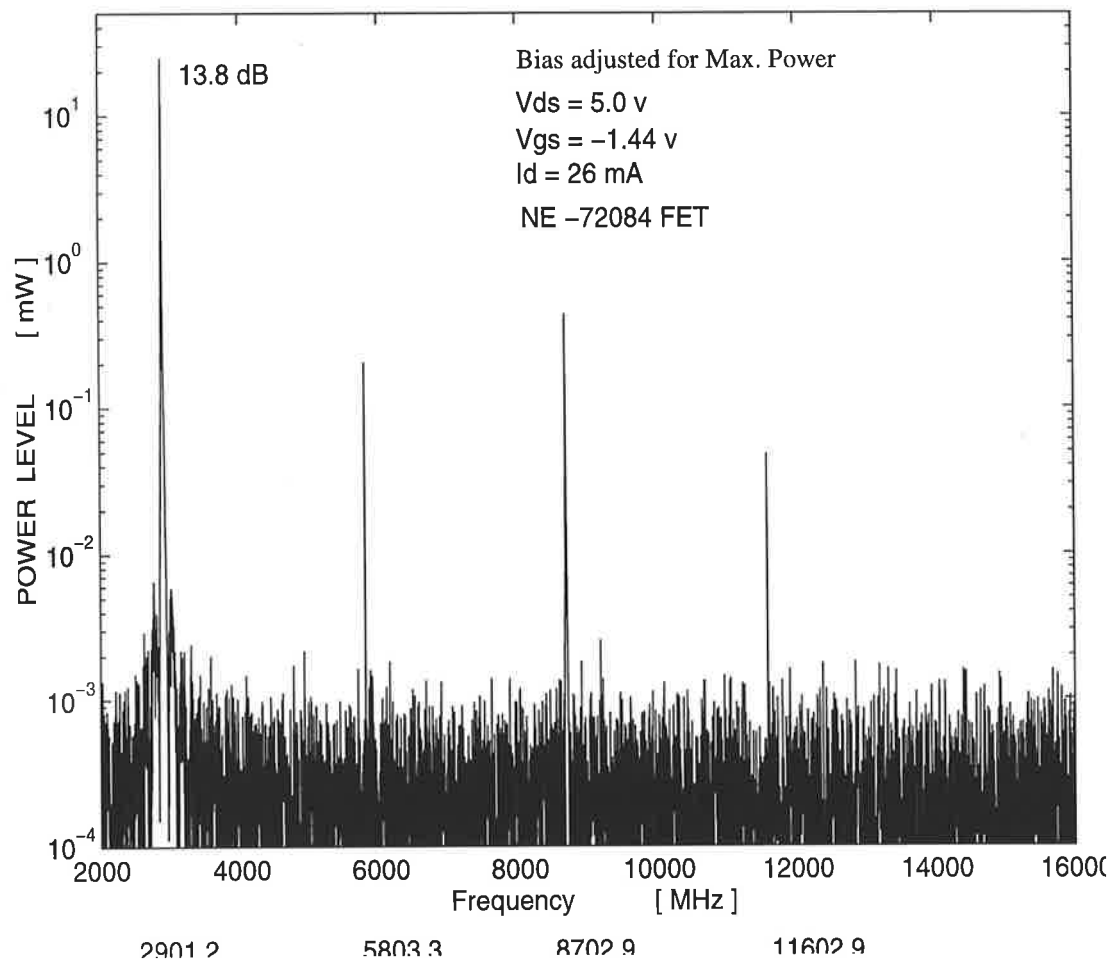


Figure (10)

---

## Appendix H

# *Transistor Data Sheets*

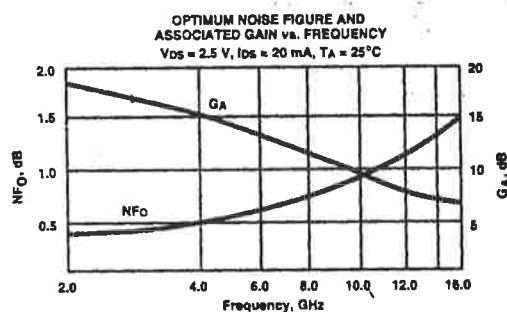
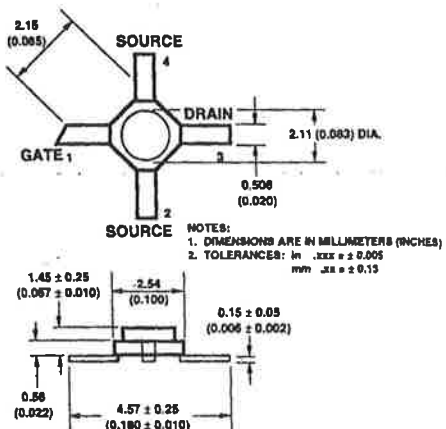
**ATF-13036**  
**2-16 GHz Low Noise**  
**Gallium Arsenide FET**
**Features**

- **Low Noise Figure:** 1.1 dB typical at 12 GHz
- **High Associated Gain:** 9.5 dB typical at 12 GHz
- **High Output Power:** 17.5 dBm typical P<sub>1 dB</sub> at 12 GHz
- **Cost Effective Ceramic Microstrip Package**
- **Tape-and-Reel Packaging Option Available<sup>2</sup>**

**Description**

The ATF-13036 is a high performance gallium arsenide Schottky-barrier-gate field effect transistor housed in a cost effective microstrip package. Its premium noise figure makes this device appropriate for use in the first stage of low noise amplifiers operating in the 2-16 GHz frequency range.

This GaAs FET device has a nominal 0.3 micron gate length with a total gate periphery is 250 microns. Proven gold based metallization systems and nitride passivation assure a rugged, reliable device.

**36 micro-X Package<sup>1</sup>**

**Noise Parameters: V<sub>DS</sub> = 2.5 V, I<sub>DS</sub> = 20 mA**

Freq. GHz	NFO dB	Gamma Opt Mag	R <sub>N/50</sub>
2.0	0.4	.80	0.23
4.0	0.5	.54	0.22
6.0	0.7	.47	0.13
8.0	0.8	.27	0.17
12.0	1.1	.33	0.32
14.0	1.3	.42	0.38

**Electrical Specifications, T<sub>A</sub> = 25°C**

Symbol	Parameters and Test Conditions	Units	Min.	Typ.	Max.
NFO	Optimum Noise Figure: V <sub>DS</sub> = 2.5 V, I <sub>DS</sub> = 15 - 30 mA	dB		0.8	1.2
GA	Gain @ NFO: V <sub>DS</sub> = 2.5 V, I <sub>DS</sub> = 15 - 30 mA	dB		11.5	
P <sub>1 dB</sub>	Output Power @ 1 dB Gain Compression: V <sub>DS</sub> = 4 V, I <sub>DS</sub> = 40 mA	dBm		17.5	
G <sub>1 dB</sub>	1 dB Compressed Gain: V <sub>DS</sub> = 4 V, I <sub>DS</sub> = 40 mA	dB		8.5	
g <sub>m</sub>	Transconductance: V <sub>DS</sub> = 2.5 V, V <sub>GS</sub> = 0 V	mmho	25	55	
I <sub>DSS</sub>	Saturated Drain Current: V <sub>DS</sub> = 2.5 V, V <sub>GS</sub> = 0 V	mA	40	50	90
V <sub>P</sub>	Pinchoff Voltage: V <sub>DS</sub> = 2.5 V, I <sub>DS</sub> = 1 mA	V	-4.0	-1.5	-0.5

Notes: 1. Long leaded 35 package available upon request.  
2. Refer to PACKAGING section "Tape-and-Reel Packaging for Surface Mount Semiconductors".

ATF-13036 2-16 GHz  
Low Noise Gallium Arsenide FET

**Absolute Maximum Ratings**

Parameter	Symbol	Absolute Maximum <sup>1</sup>
Drain-Source Voltage	V <sub>DS</sub>	+5 V
Gate-Source Voltage	V <sub>GS</sub>	-4 V
Drain Current	I <sub>DS</sub>	I <sub>DSS</sub>
Power Dissipation <sup>2,3</sup>	P <sub>T</sub>	225 mW
Channel Temperature	T <sub>CH</sub>	175°C
Storage Temperature <sup>4</sup>	T <sub>STG</sub>	-65°C to +175°C

Thermal Resistance:  $\theta_{JC} = 400^\circ\text{C}/\text{W}$ ;  $T_{CH} = 150^\circ\text{C}$   
Liquid Crystal Measurement; 1  $\mu\text{m}$  Spot Size<sup>5</sup>

**Notes:**

1. Operation of this device above any one of these parameters may cause permanent damage.
2. Case Temperature = 25°C.
3. Derate at 2.5 mW/ $^\circ\text{C}$  for  $T_{CASE} > 85^\circ\text{C}$ .
4. Storage above +150°C may tarnish the leads of this package making it difficult to solder into a circuit. After a device has been soldered into a circuit, it may be safely stored up to 175°C.
5. The small spot size of this technique results in a higher, though more accurate determination of  $\theta_{JC}$  than do alternate methods. See MEASUREMENTS section for more information.

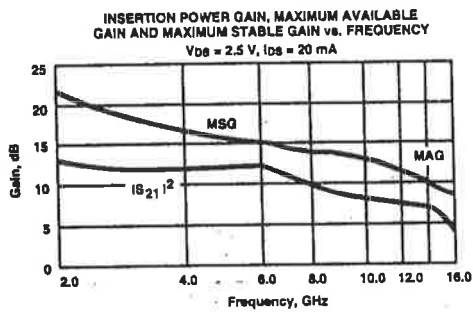
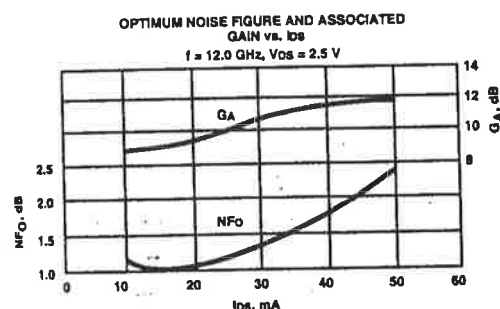
**Part Number Ordering Information**

Part Number	Devices Per Reel	Reel Size
ATF-13036-TR1	1000	7"
ATF-13036-TR2	4000	13"
ATF-13036-STR	1	STRIP

For more information, see "Tape and Reel Packaging for Semiconductor Devices", page 14-14.

**Typical Performance,  $T_A = 25^\circ\text{C}$**

(unless otherwise noted)



**Typical Scattering Parameters: Common Source,  $Z_0 = 50 \Omega$**

Freq. GHz	$S_{11}$		$S_{21}$			$S_{12}$		$S_{22}$		
	Mag	Ang	dB	Mag	Ang	dB	Mag	Ang	Mag	Ang
2.0	.96	-40	12.4	4.19	134	-28.0	.040	67	.56	-20
3.0	.88	-52	11.4	3.72	112	-25.5	.053	58	.58	-27
4.0	.81	-66	11.5	3.77	93	-22.7	.073	50	.55	-34
5.0	.68	-98	12.0	3.99	73	-20.1	.099	31	.43	-54
6.0	.55	-137	11.5	3.75	52	-19.0	.112	14	.30	-80
7.0	.53	-168	11.0	3.53	27	-18.1	.125	0	.21	-103
8.0	.51	161	10.3	3.27	2	-17.1	.139	-11	.14	-135
9.0	.51	120	10.2	3.25	-19	-16.1	.156	-25	.10	163
10.0	.56	84	9.2	2.87	-41	-16.1	.157	-43	.18	110
11.0	.60	50	8.3	2.61	-61	-16.2	.155	-55	.24	87
12.0	.62	44	7.8	2.45	-84	-16.7	.147	-62	.26	64
13.0	.64	36	7.3	2.32	-102	-17.0	.141	-73	.27	46
14.0	.67	16	6.6	2.14	-120	-17.9	.128	-85	.30	20
15.0	.73	-6	5.2	1.83	-139	-19.2	.110	-97	.36	-4
16.0	.77	-22	4.2	1.62	-157	-20.6	.093	-112	.39	-14

A model for this device is available in the DEVICE MODELS section.

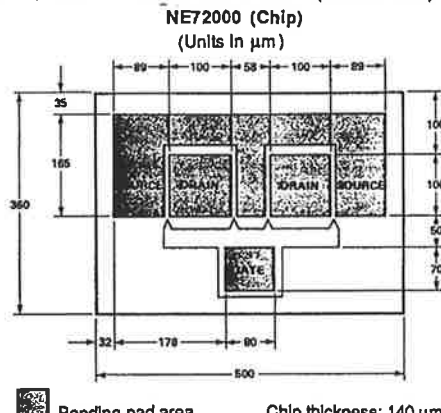
# NE720

## Low Cost General Purpose GaAs MESFET

### FEATURES

- LOW COST
- LOW NOISE FIGURE  
0.8dB at 4GHz  
1.7dB at 8GHz
- HIGH ASSOCIATED GAIN  
12.0dB at 4GHz  
9.0dB at 8GHz
- HIGH MAXIMUM AVAILABLE GAIN  
16.0dB at 4GHz  
12.0dB at 8GHz

### PHYSICAL DIMENSIONS (Units in mm)



Bonding pad area. Chip thickness: 140 µm

### DESCRIPTION AND APPLICATIONS

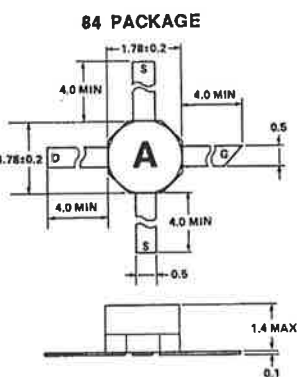
The NE720 is NEC's low cost 1.0µ recessed gate GaAs FET, offering a low noise figure and high gain through 8 GHz. It is designed for consumer applications.

The device is available as a chip (NE72000) and in two hermetically sealed stripline packages (NE72084 and NE72089A). The chip's gate and channel are glassivated with a thin layer of SiO<sub>2</sub> for mechanical protection. All bonding pads use a Ti-Pt-Au metallization system.

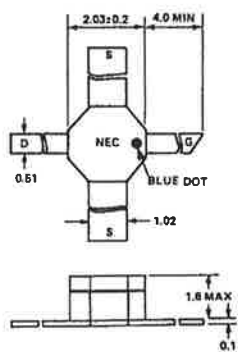
### ABSOLUTE MAXIMUM RATINGS (T<sub>A</sub> = 25°C)

SYMBOLS	PARAMETERS	UNITS	RATINGS
V <sub>DS</sub>	Drain to Source Voltage	V	5.0
V <sub>GDO</sub>	Gate to Drain Voltage	V	-6.0
V <sub>GSO</sub>	Gate to Source Voltage	V	-6.0
I <sub>GF</sub>	Gate Current	mA	4.0
I <sub>DS</sub>	Drain Current	mA	150
T <sub>ch</sub>	Channel Temperature	°C	175
T <sub>stg</sub>	Storage Temperature NE72084 NE72089A	°C	-65 to +125 -65 to +175

\* All dimensions typical unless noted.



### 89A PACKAGE



California Eastern Laboratories

**NE720, LOW COST GENERAL PURPOSE GaAs MESFET**

**ELECTRICAL CHARACTERISTICS (TA = 25°C)**

NE PART NUMBER EIAJ <sup>1</sup> REGISTERED NUMBER PACKAGE CODE			NE72000 CHIP			NE72084 2SK571 84			NE72089A 2SK354A 89A		
SYMBOLS	PARAMETERS AND CONDITIONS	UNITS	MIN	TYP	MAX	MIN	TYP	MAX	MIN	TYP	MAX
I <sub>DSS</sub>	Drain Current at V <sub>DS</sub> = 3V, V <sub>GS</sub> = 0	mA	30	60	150	30	60	150	30	60	150
V <sub>P</sub>	Pinch-off Voltage at V <sub>DS</sub> = 3V, I <sub>DS</sub> = 0.1mA	V	-0.8	-2.0	-4.0	-0.8	-2.0	-4.0	-0.8	-2.0	-4.0
g <sub>m</sub>	Transconductance at V <sub>DS</sub> = 3V, I <sub>DS</sub> = 10mA	mS	20	40	60	20	40	60	20	40	60
I <sub>GSO</sub>	Gate to Source Leakage Current at V <sub>GS</sub> = -5V	μA		1.0	10			10		1.0	10
R <sub>th</sub>	Thermal Resistance (c - a)	°C/W			170 <sup>5</sup>			400			400
P <sub>T</sub>	Total Power Dissipation	mW			500			300			300

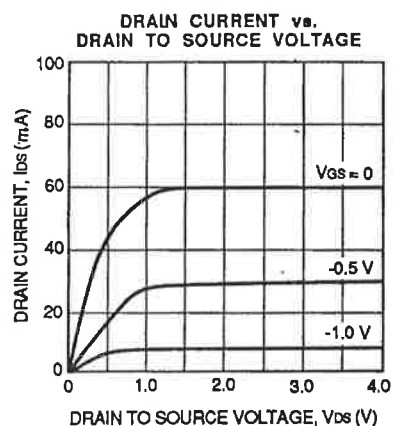
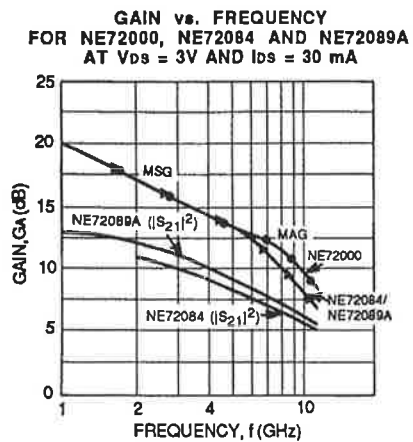
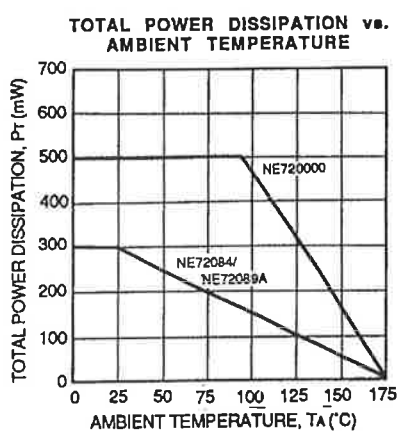
SEE NOTES ON PAGE 7.

**PERFORMANCE SPECIFICATIONS (TA = 25°C)**

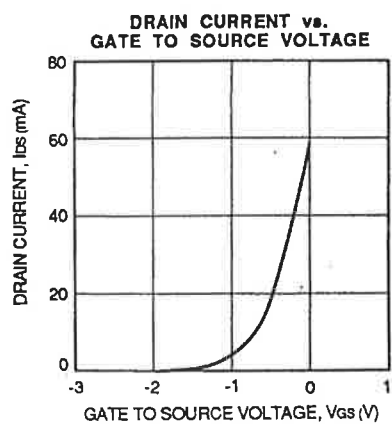
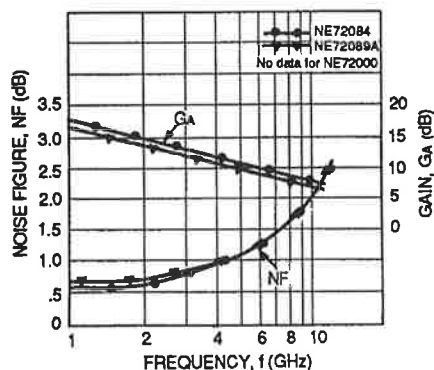
NE PART NUMBER EIAJ <sup>1</sup> REGISTERED NUMBER PACKAGE CODE			NE72000 CHIP			NE72084 2SK571 84			NE72089A 2SK354A 89A		
SYMBOLS	PARAMETERS AND CONDITIONS	UNITS	MIN	TYP	MAX	MIN	TYP	MAX	MIN	TYP	MAX
f <sub>max</sub>	Maximum Frequency Oscillation at V <sub>DS</sub> = 3V, I <sub>DS</sub> = 30mA	GHz		60			60			60	
MAG	Maximum Available Gain <sup>2</sup> at V <sub>DS</sub> = 3V, I <sub>DS</sub> = 30mA (Typ. I <sub>DS</sub> = 50% I <sub>DSS</sub> ) f = 2GHz f = 4GHz f = 8GHz f = 12GHz	dB		16.5 11.5			17.5 15 12 8			16.0 11.0	
NF <sub>opt</sub>	Optimum Noise Figure <sup>3</sup> at V <sub>DS</sub> = 3V, I <sub>DS</sub> = 10mA (Typ. I <sub>DS</sub> = 15% I <sub>DSS</sub> ) f = 2GHz f = 4GHz f = 8GHz	dB		1.0 1.7	1.4 <sup>4</sup>		0.6 0.8 2.0	1.4		1.0 1.7	1.4
G <sub>B</sub>	Associated Gain at NF at V <sub>DS</sub> = 3V, I <sub>DS</sub> = 10mA (Typ. I <sub>DS</sub> = 15% I <sub>DSS</sub> ) f = 2GHz f = 4GHz f = 8GHz	dB		11.0 9.0			15 12 8.5			11.0 8.5	
P <sub>1dB</sub>	Output Power at 1dB Compression Point at V <sub>DS</sub> = 4V, I <sub>DS</sub> = 30mA (Typ. I <sub>DS</sub> = 50% I <sub>DSS</sub> ) f = 4GHz	dBm		15.0			15.0			15.0	

SEE NOTES ON PAGE 7.

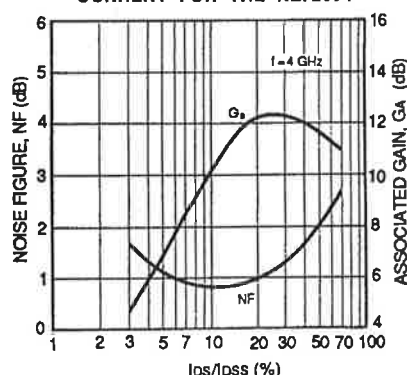
TYPICAL PERFORMANCE CHARACTERISTICS ( $T_A = 25^\circ\text{C}$ )



NOISE FIGURE, ASSOCIATED GAIN vs. FREQUENCY FOR THE NE72000, NE72084 AND NE72089A AT  $V_{DS} \approx 3\text{ V}$  AND  $I_{DS} = 10\text{ mA}$

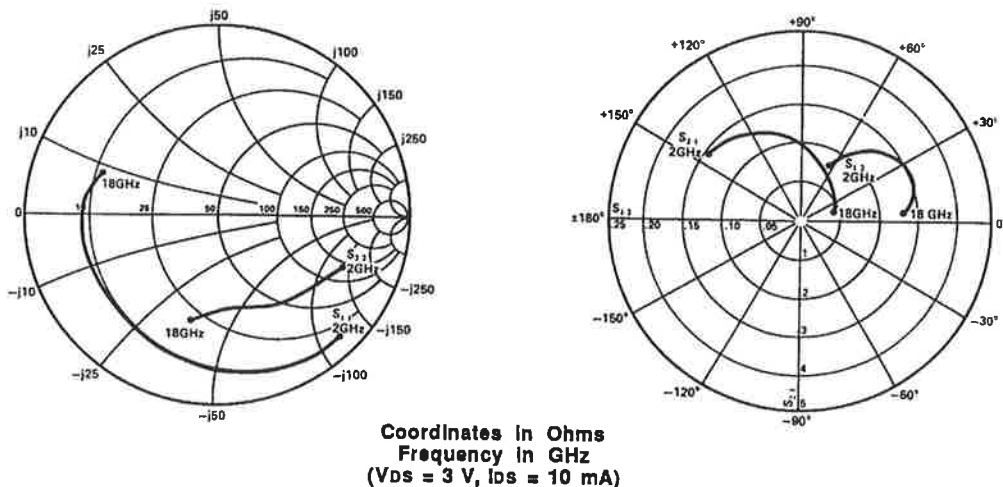


NOISE FIGURE, ASSOCIATED GAIN vs. RATIO OF DRAIN CURRENT AND ZERO GATE VOLTAGE CURRENT FOR THE NE72084



NE720, LOW COST GENERAL PURPOSE GaAs MESFET

NE72000 TYPICAL COMMON SOURCE SCATTERING PARAMETERS



S-MAGN AND ANGLE:

$V_{DS} = 3$  V,  $I_{DS} = 10$  mA

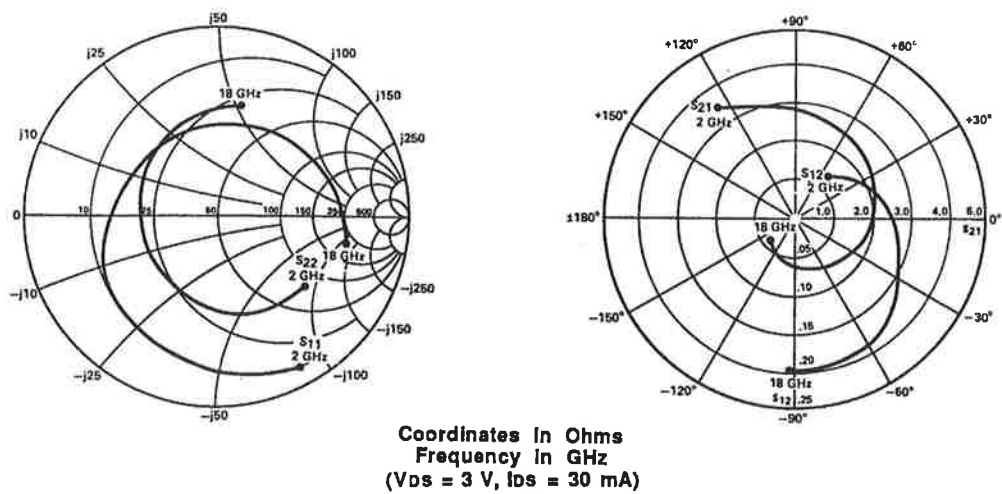
FREQUENCY (MHz)	S11		S21		S12		S22	
2000	.91	-44	2.95	144	.08	64	.71	-22
3000	.90	-63	2.81	132	.11	53	.68	-27
4000	.83	-81	2.47	113	.12	44	.62	-35
5000	.78	-96	2.27	105	.14	36	.58	-43
6000	.75	-108	2.08	97	.15	32	.56	-52
7000	.70	-119	1.83	87	.15	26	.55	-58
8000	.67	-130	1.65	79	.15	19	.55	-63
9000	.66	-140	1.49	72	.15	18	.56	-65
10000	.64	-152	1.37	64	.15	15	.56	-67
11000	.64	-158	1.24	59	.14	14	.54	-66
12000	.67	-165	1.18	54	.14	13	.54	-67
13000	.69	-168	1.11	49	.14	11	.51	-74
14000	.69	-175	1.11	44	.14	12	.54	-80
15000	.65	-178	.98	38	.13	9	.55	-86
16000	.66	174	1.02	33	.14	9	.53	-90
17000	.63	164	.96	26	.13	8	.56	-95
18000	.64	160	.86	21	.13	9	.50	-97

$V_{DS} = 3$  V,  $I_{DS} = 30$  mA

2000	.90	-49	3.61	143	.07	62	.85	-24
3000	.89	-70	3.39	130	.10	52	.81	-28
4000	.83	-88	2.91	117	.11	44	.55	-36
5000	.78	-103	2.63	104	.12	36	.51	-44
6000	.75	-116	2.37	97	.13	33	.49	-53
7000	.70	-126	2.08	87	.13	27	.49	-59
8000	.68	-137	1.87	79	.13	22	.49	-64
9000	.67	-148	1.67	73	.13	21	.51	-67
10000	.65	-158	1.53	65	.12	19	.51	-68
11000	.65	-164	1.37	60	.12	18	.49	-67
12000	.70	-171	1.32	55	.12	18	.47	-68
13000	.72	-174	1.23	51	.12	17	.47	-75
14000	.74	-180	1.22	46	.13	20	.49	-81
15000	.87	177	1.09	40	.12	17	.50	-87
16000	.69	169	1.12	36	.12	18	.50	-90
17000	.66	168	1.05	28	.13	18	.52	-96
18000	.67	156	.94	24	.12	20	.56	-98

**NE720, LOW COST GENERAL PURPOSE GaAs MESFET**

**NE72084 TYPICAL COMMON SOURCE SCATTERING PARAMETERS**



**S-MAGN AND ANGLE:**

$V_{DS} = 3$  V,  $I_{DS} = 10$  mA

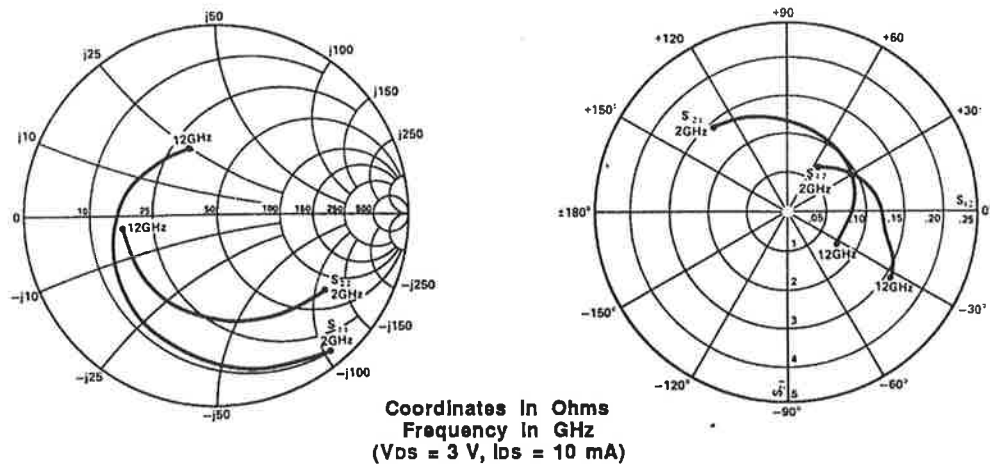
FREQUENCY (MHz)	S11	S21	S12	S22				
2000	.92	-54	2.91	130	.08	53	.69	-37
4000	.79	-102	2.47	85	.13	23	.81	-70
6000	.68	-141	2.19	49	.15	-0	.54	-100
8000	.53	-177	1.82	15	.15	-16	.47	-126
10000	.47	136	1.68	-17	.16	-30	.43	-159
12000	.48	89	1.45	-51	.16	-45	.45	164
14000	.52	49	1.22	-82	.17	-62	.49	131
16000	.61	14	1.03	-115	.18	-82	.58	98
18000	.66	-5	.81	-138	.18	-98	.64	77

$V_{DS} = 3$  V,  $I_{DS} = 30$  mA

2000	.91	-59	3.53	127	.07	54	.60	-37
4000	.76	-110	2.87	83	.10	26	.52	-69
6000	.65	-151	2.45	46	.12	8	.46	-97
8000	.52	171	2.02	14	.13	-4	.42	-122
10000	.49	124	1.82	-18	.15	-16	.38	-155
12000	.52	79	1.55	-50	.17	-31	.41	166
14000	.57	41	1.30	-82	.19	-51	.46	132
16000	.65	9	1.08	-114	.20	-74	.56	98
18000	.70	-10	.86	-136	.20	-91	.62	77

NE720, LOW COST GENERAL PURPOSE GaAs MESFET

NE72089A TYPICAL COMMON SOURCE SCATTERING PARAMETERS



S-MAGN AND ANGLE:

$V_{DS} = 3$  V,  $I_{DS} = 10$  mA

FREQUENCY (MHz)	S11		S21		S12		S22	
2000	.92	-52	2.94	130	.07	54	.68	-35
3000	.84	-75	2.62	108	.09	38	.63	-51
4000	.76	-95	2.34	90	.11	26	.59	-66
5000	.71	-113	2.18	72	.12	16	.58	-79
6000	.65	-131	2.02	56	.13	7	.56	-93
7000	.59	-146	1.86	41	.13	-1	.54	-105
8000	.55	-160	1.76	26	.13	-7	.54	-116
9000	.49	-177	1.68	13	.13	-12	.53	-129
10000	.44	165	1.66	-1	.14	-17	.53	-139
11000	.39	140	1.63	-19	.15	-26	.52	-154
12000	.37	112	1.55	-34	.16	-33	.51	-170

$V_{DS} = 3$  V,  $I_{DS} = 30$  mA

2000	.89	-58	3.76	127	.06	55	.60	-35
3000	.79	-82	3.27	105	.08	40	.56	-50
4000	.72	-103	2.88	86	.09	31	.53	-64
5000	.66	-121	2.61	69	.10	22	.51	-75
6000	.60	-139	2.38	54	.11	16	.50	-86
7000	.55	-155	2.18	38	.11	10	.50	-97
8000	.50	-170	2.04	24	.12	6	.50	-108
9000	.44	172	1.93	11	.12	2	.49	-118
10000	.40	152	1.89	-3	.14	-2	.50	-126
11000	.36	126	1.83	-20	.15	-11	.49	-138
12000	.35	99	1.72	-36	.16	-18	.48	-151

**NE720, LOW COST GENERAL PURPOSE GaAs MESFET**

**NE72084 TYPICAL NOISE PARAMETERS**

FREQ. (GHz)	NFopt (dB)	G <sub>a</sub> (dB)	Γ <sub>opt</sub>		Rn/50
			(MAG)	(ANG)	
1.0	0.55	17.5	0.90	15	0.52
2.0	0.60	14.5	0.81	38	0.49
4.0	1.00	11.5	0.74	59	0.39
6.0	1.30	9.5	0.66	102	0.30
8.0	1.70	8.5	0.49	130	0.24
10.0	2.15	7.5	0.32	172	0.18
12.0	2.50	6.5	0.26	-115	0.16
14.0	2.95	5.5	0.30	-54	0.13
16.0	3.30	4.7	0.26	-4	0.11
18.0	3.70	4.0	0.26	13	0.09

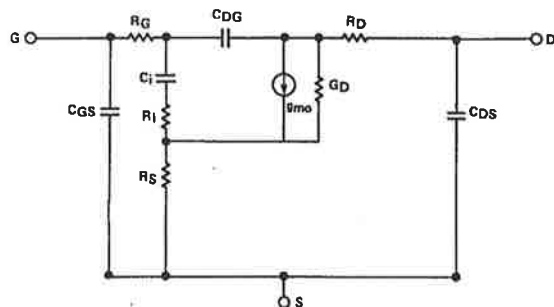
(V<sub>DS</sub> = 3 V, I<sub>DS</sub> = 10 mA)

**NE72089A TYPICAL NOISE PARAMETERS**

FREQ. (GHz)	NFopt (dB)	G <sub>a</sub> (dB)	Γ <sub>opt</sub>		Rn/50
			(MAG)	(ANG)	
1.0	0.60	17.5	0.76	13	0.68
2.0	0.75	14.5	0.73	36	0.58
4.0	1.00	11.5	0.65	68	0.42
6.0	1.30	9.0	0.53	100	0.28
8.0	1.70	8.5	0.42	138	0.19
10.0	2.05	7.0	0.31	175	0.15
12.0	2.50	6.5	0.25	-117	0.25

(V<sub>DS</sub> = 3 V, I<sub>DS</sub> = 10 mA)

**NE72000 EQUIVALENT CIRCUIT**



COMPONENT	VALUE
R <sub>G</sub>	0.57 Ω
C <sub>I</sub>	0.15 pF
R <sub>I</sub>	2.00 Ω
R <sub>S</sub>	2.00 Ω
C <sub>DG</sub>	0.03 pF
R <sub>D</sub>	2.00 Ω
C <sub>DS</sub>	0.015 pF
θ <sub>mo</sub>	40.0 (mS)
GD	2.0 (mS)
C <sub>GS</sub>	0.55 pF

**NOTES:**

1. Electronic Industrial Association of Japan.
2. Gain Calculations:  $MAG = \frac{|S_{21}|}{|S_{12}|} (k \pm \sqrt{k^2 - 1})$ ,  $k = \frac{1+|\Delta|^2 - |S_{11}|^2 - |S_{22}|^2}{2|S_{12}||S_{21}|}$ ,  $\Delta = S_{11}S_{22} - S_{12}S_{21}$
3. Typical values of noise figures are those obtained when 50% of the devices from a large number of lots were individually measured in a circuit with the input individually tuned to obtain the minimum value. Maximum values are criteria established on the production line as a "go-no-go" screening tuned for the "generic" type but not for each specimen.
4. RF performance is determined by packaging and testing 10 samples per wafer; wafer rejection criteria for standard devices is 2 rejects for 10 samples.
5. R<sub>th</sub> (channel to case) for chips mounted on a copper heatsink.

# Bibliography

- [1] Y.C. Chen, R. Lai, E. Lin, H. Wang, T. Black, H.C. Yen, D. Streit, W. Jones, P.H. Liu, R.M. Dia, T-W. Huang, P-P. Huang and K. Stamper, “A 94-GHz 130 mW InGaAs / InAlAs / InP HEMT High-Power MMIC Amplifier”, *IEEE Microwave and Guided Wave Letters*, vol. 7, no. 5, May 1997, pp. 133-135.
- [2] A.S. Gilmour, Jr., “*Microwave Tubes*”, (Artech, Boston, 1989).
- [3] T.A. Navarro and K. Chang, “*Integrated Active Antennas and Spatial Power Combining*”, (Wiley, New York, 1996).
- [4] E. Holzman and R. Robertson, “*Solid-State Microwave Power Oscillator Design*”, (Artech, Boston, 1992).
- [5] N. Camirelli and B. Baynaktarouglu, “Monolithic millimeter wave IMPATT oscillator and active antenna”, *IEEE Trans. on Microwave Theory and Techniques*, vol. 36, no. 12, Dec. 1988, pp. 1670-1676.

- [6] A. Vilcot and S. Tedjini, “Ground plane effects in monolithic millimetre-wave integrated circuits”, *IEEE Microwave and Guided Wave Letters*, vol. 3, Feb. 1993, pp. 32-34.
- [7] J.A. Navarro, Lu Fan and K. Chang, “Active inverted stripline circular patch antennas for spatial power combining”, *IEEE Trans. on Microwave Theory and Techniques*, vol. MTT-41, no. 10, Oct. 1993, pp. 1856-1863.
- [8] K. Chang, K.A. Hommer and G. Gopalakrishnan, “Active radiating element using FET source integrated with microstrip patch antenna”, *Electronics Letters*, vol. 24, no. 21, Oct. 1988, pp. 1347-1348.
- [9] J. Navarro, L. Fan and K. Chang, “Novel FET integrated stripline patch”, *Electronics Letters*, vol. 30, no. 8, April 1994, pp. 655-657.
- [10] R.D. Martinez and R.C. Compton, “High efficiency FET/microstrip-patch oscillators”, *IEEE Antennas and Propagation Magazine*, vol. 36, no. 1, Feb. 1994, pp. 16-19.
- [11] K. Kurokawa, “The single-cavity multiple-device oscillator”, *IEEE Trans. on Microwave Theory and Techniques*, vol. MTT-19, no. 10, Oct. 1971, pp. 793-801.
- [12] J.W. Mink, “Quasi-optical power combining of solid-state millimeter-wave sources”, *IEEE Trans. on Microwave Theory and Techniques*, vol. MTT-34, no. 2, Feb. 1986, pp. 273-9.
- [13] J. Bae, Y. Aburakanva, H. kondo, T. Tanaka and K. Mizuno, “Millimeter and sub-millimeter wave quasi-optical oscillator with Gunn diodes”, *IEEE Trans. on Microwave Theory and Techniques*, vol. MTT-41, no. 10, Oct. 1993, pp. 1851-1855.
- [14] L. Wandinger and V. Nalbandian, “Millimeter-wave power combiner using quasi-optical techniques”, *IEEE Trans. on Microwave Theory and Techniques*, vol. MTT-31, no. 2, Feb. 1983, pp. 189-193.

- [15] J. Lim and T. Itoh, “Two-dimensional quasi-optical power-combining arrays using strongly coupled oscillators”, *IEEE Trans. on Microwave Theory and Techniques*, vol. MTT-42, no. 4, April 1994, pp. 734-741.
- [16] Z.B. Popovic and D.B. Rutledge, “Diode grid oscillators”, *IEEE Antennas and Propagation Symposium*, 1988, pp. 442-445.
- [17] A. Materka and S. Mizushina, “A waveguide-cavity multiple-device FET oscillator”, *IEEE Trans. on Microwave Theory and Techniques*, vol. MTT-30, no. 8, Aug. 1982, pp. 1237-1241.
- [18] M. Rahman, T. Ivanov and A. Mortazawi, “26-MESFET spatial power combining oscillator”, *IEEE Microwave and Guided Wave Letters*, vol. 7, no. 4, April 1997, pp. 100-102.
- [19] Z.B. Popovic, R.M. Weikle, M. Kim and D.B. Rutledge, “A 100-MESFET planar grid oscillator”, *IEEE Trans. on Microwave Theory and Techniques*, vol. MTT-39, no. 2, Feb. 1991, pp. 193-200.
- [20] R.M. Weikle, M. Kim, J.B. Hacker, M.P. DeLisio, Z.B. Popovic and D.B. Rutledge, “Planar MESFET grid oscillators using gate feedback”, *IEEE Trans. on Microwave Theory and Techniques*, vol. MTT-40, no. 11, Nov. 1992, pp. 1997-2003.
- [21] M. Kim, E.A. Sovero, R.M. Weikle II, J.B. Hacker, M.P. DeLisio and D.B. Rutledge, “A 35 GHz HBT monolithic grid oscillator”, *Proc. SPIE 17th Int. Conf. on Infrared and Millimeter Waves*, R.T. Temkin, ed., 1992, pp. 402-403.
- [22] D.M. Pozar, “Considerations for millimeter wave printed antennas”, *IEEE Trans. Antennas and Propagation*, vol. AP-31, Sept. 1983, pp. 740-747.
- [23] D.W. Griffin and A.A. Sayyah, “Limitations of transistorised-grid oscillator-type quasi-optical transmitting arrays”, *Fifth Australian Symposium on Antennas*, CSIRO Division of Radiophysics, Sydney, Australia, February 1996.

- [24] R.F. Harrington, “*Time harmonic electromagnetic fields*”, (McGraw-Hill, New York, 1961).
- [25] E.H. Fooks and R.A. Zakarevicius, “*Microwave Engineering Using Microstrip Circuits*”, ch. 4, pp. 73-75, (Prentice-Hall, NJ, 1990).
- [26] K. Kurokawa, “Some Basic Characteristics of Broadband Negative Resistance Oscillator Circuits,” *Bell System Technical Journal*, vol. 48, July-August 1969, pp. 1937-1955.
- [27] S.C. Maas, “*Nonlinear Microwave Circuits*”, (Artech, Boston, 1988).
- [28] R. E. Collin, “*Foundations for microwave engineering*”, (2nd ed., McGraw-Hill, New York, 1992), ch. 12.
- [29] G.J. Palladino, “Two-Port Parameter Analysis Produces Negative Resistance”, *Microwave Journal*, April 1991, pp.106-113.
- [30] A.A. Sayyah and D.W. Griffin, “A graphically oriented automation of microstrip FET amplifier and oscillator design”, *to be submitted for publication.*\*
- [31] The Math Works, Inc., Cochichuate Place, 24 Prime Way, Natick, Mass. 01760.
- [32] G. Gonzales, “*Microwave Transistor Amplifiers Analysis and Design*”, (Prentice-Hall, N.J., 1984).
- [33] G.D. Vendelin, “*Microwave Circuit Design using Linear and Nonlinear Techniques*”, (Wiley, New York, 1990).
- [34] J.L. Kuester and J.H. Mize, “*Optimization Techniques with FORTRAN*”, (McGraw-Hill, New York, 1973).
- [35] K.C. Gupta , R. Garg and R.Chadha, “*Computer Aided Design of Microwave Circuits*”, (Artech, Boston, 1981), ch. 16-18.

---

\* Reproduced as Appendix G

- [36] Steven March, "Microstrip packaging: watch the last step", *Microwaves*, Dec. 1981, pp. 83- 94.
- [37] E. Yamashita and R. Mittra, "Variational method for the analysis of microstrip lines", *IEEE Trans. on Microwave Theory and Techniques*, vol. MTT-16, no. 4, April 1968, pp. 251-256.
- [38] E. Yamashita, "Variational method for the analysis of microstripline like transmission lines", *IEEE Trans. Microwave Theory and Techniques*, vol. MTT-16, no. 8, August 1968, pp. 529-535.
- [39] R. Mittra and T. Itoh, "Charge and potential distributions in shielded striplines", *IEEE Trans. Microwave Theory and Techniques*, vol. MTT-18, no. 3, March 1970, pp. 149-156.
- [40] R. Mittra, "*Computer Technique for Electromagnetics*", (Pergamon, New York, 1973), vol. 7, ch. 6.
- [41] K.C. Gupta, R. Garg, and I.J. Bahl, "*Microstrip Lines and Slot-Lines*", (Artech, Boston, 1979).
- [42] H.A. Wheeler, "Transmission line properties of parallel strips separated by a dielectric sheet," *IEEE Trans. Microwave Theory and Techniques*, vol. MTT-13, no. 2, 1965, pp. 172-185.
- [43] J.S. Rao and B.N. Das, "Analysis of asymmetric stripline by conformal mapping", *IEEE Trans. Microwave Theory and Techniques*, vol. MTT-27, no. 4, April 1979, pp. 299-303.
- [44] K.K. Joshi, J.S. Rao and B.N. Das, "Analysis of inhomogeneously filled stripline and microstripline", *IEE Proceeding*, vol. 127, pt. H, no.1, February 1980, pp. 11-14.
- [45] R.A. York and Z.B. Popovic (editors), "*Active and Quasi-Optical Arrays for Solid-State Power Combining*", (Wiley, New York, 1997).

- [46] C. C. Su and J. M. Guan, "Finite-difference analysis of dielectric loaded cavities using the simultaneous iteration of the power method with the Chebyshev acceleration technique," *IEEE Trans. on Microwave Theory and Techniques*, vol. MTT-42, no. 10, Oct. 1994, pp. 1998-2006.
- [47] J. P. Webb, "The finite-element solution of three-dimensional electromagnetic problems," *IEEE Trans. on Microwave Theory and Techniques*, vol. MTT-33, no. 7, July 1985, pp. 635-639.
- [48] S. Akhtarzad and P. B. Johns, "Solutions of Maxwell's equations in three space dimensions and time by t.l.m. method of numerical analysis," *Proc. Inst. Elec. Eng.*, vol. 122, Dec. 1975, pp. 1344-1348.
- [49] R. E. Collin, "*Field Theory of Guided Waves*", (2nd ed., McGraw-Hill, New York, 1991).
- [50] K. Kurokawa, "*An Introduction to the Theory of Microwave Circuits*", (Academic Press, New York, 1969).
- [51] K. Kurokawa, "The expansions of electromagnetic fields in cavities," *IRE Trans. on Microwave Theory and Techniques*, April 1958, pp. 178-187.
- [52] A.S. Omar and K. Schunemann, "A new approach to the analysis of inhomogeneously filled cavities", in *Proc. 18th EuMC*, Stockholm, 1988, pp. 527-533.
- [53] A. Jostingmeier and A. S. Omar, "Analysis of inhomogeneously filled cavities coupled to waveguides using VIE formulation", *IEEE Trans. on Microwave Theory and Techniques*, vol. MTT-41, June / July 1993, pp. 1207-1214.
- [54] A. Jostingmeier and A.S. Omar, "Analysis of the scattering by dielectric bodies using the SIE formulation", *IEEE Trans. on Microwave Theory and Techniques*, vol. MTT-42, no. 3, March 1994, pp. 471-480.

- [55] C. A. Balanis, “*Advanced Electromagnetics*”, (John Wiley, New York, 1989), ch. 8, pp. 394-410.
- [56] F. E. Gardiol, “*Introduction to Microwaves*”, (Artech, Boston, 1984), ch. 3, pp. 125.
- [57] J. L. Altman, “*Microwave Circuits*”, (Van Nostrand, NJ 1964), ch. 1, pp. 36-39.
- [58] T. Rozzi, and M. Mongiardo, “E- plane steps in rectangular waveguide”, *IEEE Trans. on Microwave Theory and Techniques*, vol. MTT-39, August 1991, pp. 1279-1288.
- [59] H. Platzelt and F. Arndt, “Double-plane steps in rectangular waveguide and their application for transformers, irises, and filters,” *IEEE Trans. on Microwave Theory and Techniques*, vol. MTT-30, May 1982, pp. 771-776.
- [60] G. V. Eleftheriades, A. S. Omar, L. P. B. Katehi and G. M. Rebeiz, “Some important properties of waveguide junction generalised scattering matrices in the context of the mode matching technique”, *IEEE Trans. on Microwave Theory and Techniques*, vol. MTT-42, October 1994, pp. 1896-1903.
- [61] G. V. Eleftheriades, W. Y. Ali-Ahmad, L. P. B. Katehi and G. M. Rebeiz, “Millimeter-wave integrated-horn antennas: Part I - Theory”, *IEEE Trans. on Microwave Theory and Techniques*, vol. MTT-39, November 1991, pp. 1575-1581.
- [62] N. Marcuvitz, “*Waveguide Handbook*”, (McGraw-Hill, New York, 1951).
- [63] G. Matthaei, L. Young, and E. M. T. Jones, “*Microwave Filters, Impedance-Matching Networks, and Coupling Structures*”, (McGraw-Hill, New York, 1964).
- [64] H. Abe, “A GaAs MESFET self bias mode oscillator”, *IEEE Trans. on Microwave Theory and Techniques*, vol. MTT-34, January 1986, pp. 167-172.

- [65] R.G. Rogers, “*Low Phase Noise Microwave Oscillator Design*”, (Artech House, Norwood, M.A., 1991).
- [66] P.H. Ladbroke, “*MMIC Design GaAs FETs and HEMTs*”, (Artech House, Norwood, M.A., 1991).
- [67] M.J. Bailey, “PHEMT devices offer high power density and efficiency”, *Microwaves & RF*, vol. 36, Feb. 1997, pp. 61-70.